

NPS ARCHIVE  
1965  
BUXCEY, S.

ACOUSTIC DETECTION OF MICROBUBBLES AND  
PARTICULATE MATTER NEAR THE SEA SURFACE

STANLEY BUXCEY  
JAMES E. McNEIL  
ROBERT H. MARKS, JR.

**DUDLEY KNOX LIBRARY  
NAVAL POSTGRADUATE SCHOOL  
MONTEREY, CA 93943-5101**

U.S. NAVAL POSTGRADUATE SCHOOL  
MONTEREY, CALIFORNIA











ACOUSTIC DETECTION OF MICROBUBBLES AND  
PARTICULATE MATTER NEAR THE SEA SURFACE

\* \* \* \* \*

Stanley Buxcey

James E. McNeil

Robert H. Marks, Jr.



ACOUSTIC DETECTION OF MICROBUBBLES AND  
PARTICULATE MATTER NEAR THE SEA SURFACE

by

Stanley Buxcey

Lieutenant Commander, Royal Canadian Navy

James E. McNeil

Flight Lieutenant, Royal Canadian Air Force

Robert H. Marks, Jr.

Lieutenant, United States Navy

Submitted in partial fulfillment of  
the requirements for the degree of

MASTER OF SCIENCE  
IN  
ENGINEERING ELECTRONICS

United States Naval Postgraduate School  
Monterey, California

1 9 6 5

~~1965~~  
~~1965/8~~

THE ARCHIVE  
1965  
BUXCEY, S.

ACOUSTIC DETECTION OF MICROBUBBLES AND  
PARTICULATE MATTER NEAR THE SEA SURFACE

by

Stanley Buxcey

James E. McNeil

Robert H. Marks, Jr.

This work is accepted as fulfilling  
the thesis requirements for the degree of

MASTER OF SCIENCE

IN

ENGINEERING ELECTRONICS

from the

United States Naval Postgraduate School





## ABSTRACT

A pulse-echo system using an electrostatic transducer and steel reflector was operated over the frequency range 24-192 Kcps in the sea and in the laboratory. Excess attenuations from 0.15 to 1.1 db/M due to absorption and scattering by inhomogeneities were made over the full frequency range with a maximum error of less than 0.05 db/meter. Backscattering at sea was detected in the frequency range 24-60 Kcps with an average scattering cross-section per unit volume of  $400 \text{ cm}^2/\text{m}^3$  at a depth of 10 feet. Scattering was not detected above 60 Kcps. Variation of sound velocity with frequency was measured from 24-192 Kcps. The accuracy of these values was 0.03 percent for frequencies over 40 Kcps. Results are compared and it is postulated that;

(1) below 60 Kcps the absorption and scattering was due to microbubbles of radius greater than 50 microns, and

(2) above 60 Kcps minute plankton caused absorption without significant scattering.



## TABLE OF CONTENTS

Section	Title	Page
1.	Introduction	1
2.	Instrumentation	2
3.	Attenuation Measurements	10
4.	Detection of Backscatter	39
5.	Detection of Veleocity Shift	82
6.	Data Evaluation	95
7.	Conclusions	108
8.	Acknowledgements	109
9.	Bibliography	110
Appendix I	Electrostatic Transducer	113
Appendix II	Signal Gate	147
Appendix III	Transmit-Receive Switching Section	152
Appendix IV	System Characteristics	154
Appendix V	Equipment Specifications	156
Appendix VI	Test Locations	160
Appendix VII	Velocity Shift Computer Program	163
Appendix VIII	Envelope Detector and Echo Counter	176
Appendix IX	Time Marker	180
Appendix X	Extracts from N.E.L. Tower Log with Temperature and Oxygen Data	183
Appendix XI	Effect of Scatterer Position on Scattering Signal	185



## LIST OF ILLUSTRATIONS

Figure		Page
2.1	Power Amplifier Outputs at 40 Kcps and 200 Kcps	4
2.2	Block Diagram of Transmit Section	5
2.3	Block Diagram of Transmit-Receive Switching Section	6
2.4	Receiver Output while Transmitting	7
2.5	A Receiver Output Display at 100 Kcps	7
2.6	Block Diagram of Receiver Section	8
2.7	Electronics Setup at N.E.L. Tower	9
3.1	Photographs Obtained During the Calibration of the System	11
3.2	Graph: Pulse Amplitude vs Echo Number	13
3.3	Graph: Pulse Amplitude or $\langle P \rangle_{rms}$ vs Distance.	16
3.4	Graph: Distance, $d$ vs $a^2/\lambda$	17
3.5	Photographs at 192 Kcps	19
3.6	System Diagram	19
3.7	System mounted at N.E.L. Tower	20
3.8	Graph: Echo Amplitude vs Polarizing Voltage	22
3.9	Graph: Attenuation vs Sample Number at 60 Kcps.	22
3.10	Graph: Standard Attenuation vs Frequency	26
3.11	Graph: Attenuation vs Frequency: Algae in Anechoic Tank	29
3.12	Graph: Attenuation due to Sea-Water vs Frequency	31
3.13-3.16	Graphs: Attenuation: Variation with Time and Depth at 40, 60, 96 and 152 Kcps	32,33, 34,35



3.17	Graph: Attenuation: Variation with Depth at 192 Kcps	36
4.1	Comparison of Scattering and Geometrical Cross-Sections	40
4.2	Graph: Ratio of Scattering Cross-Section at Resonance to Geometrical Cross-Section	41
4.3	Graph: Scattering Cross-Sectional Area for Resonant Bubbles at Sea Level	42
4.4	System Output at 60 Kcps	43
4.5	Scatter Amplitude Experiment	44
4.6	Constructed Backscatter from Bubbles	45
4.7	Echoes 3 and 4 at 34 Kcps	47
4.8	Divergent Field Situation	48
4.9	Pulse Correction Situation	50
4.10	Geometry of Isotropic Scattering Correction Factor	52
4.11	Graph: Signal Level vs Frequency: Example of Smoothing Technique	59
4.12	Apparatus at N.E.L. Tower	60
4.13	Apparatus with Deflectors in Place	61
4.14	Tank Interference at 16.5 Kcps	62
4.15-4.17	Scatter Signal Voltage vs Frequency	65,66,67
4.18-4.20	Total Scattering Cross-Section vs Frequency	68,69,70
4.21	Graph: Scattering Cross-Section vs Time	71
4.22-4.24	Graphs: Bubble Density vs Frequency	72,73,74
4.25-4.27	Graphs: Bubble Volume Concentration vs Frequency	75,76,77
4.28-4.29	Graphs: Scattering Cross-Sections vs Depth - 40 Kcps	78,79
4.30	Scattering Cross-Section vs Depth at 50 Kcps	80





4.31	Scattering Cross-Section vs Depth at 35.7 Kcps	81
5.1	Sound Velocity Shift in Sea Water Containing Bubbles in the Glotov, Kolobaev and Neuimin Distribution	85
5.2	Block Diagram of Envelope Detector and Echo Counter	88
5.3	Block Diagram of Time Marker	89
5.4	Typical Display at 60 Kcps	89
5.5	Calibration Curves for Two Transducers	91
5.6	Measuring Points	92
5.7	Signals from Non-parallel Reflector	93
6.1 a & b	Extinction Cross-Section of Sea Water vs Frequency	97,
6.2	Bubble Volume Concentration of Figure 4.25	98
6.3	Bubble Volume Concentration of Figure 3.12	102
6.4	Bubble Volume Concentration of Figure 4.27	103
6.5	Velocity of Sound vs Frequency, San Diego	106
6.6	Velocity of Sound vs Frequency, Monterey Bay	107
I.1	Electrostatic Transducer Cross-Section	119
I.2	Front View of Finished Transducer	120
I.3	Rear View of Finished Transducer	120
I.4	Face Deterioration due to Water Penetration	121
I.5	Transmitting Sensitivity of Electrostatic Transducer	127
I.6	Transmitting Sensitivity of Electrostatic Transducer	128
I.7	Receiving Response of Electrostatic Transducer	129
I.8	Transducer Mounting Detail	132



I.9	Transducer Capacitance vs Depth (N.E.L.)	134
I.10	Transducer Capacitance vs Depth (Anechoic Tank)	135
I.11	Transducer Impedance vs Frequency	136
I.12-18	Directivity Patterns for Electrostatic Transducer	140, 141, 142, 143, 144, 145, 146
II.1	Signal Gate Circuit Diagram	148
II.2	Signal Gate Outputs	150
II.3	Maximum Gate Input Without Distortion	151
II.4	Signal Gate Voltage Transfer Ratio	151
III.1	Transmit-Receive Switching Section Diagram	153
IV.1	System Signal plus Noise to Noise Ratio vs Frequency	155
VI.1	N.E.L. Tower, looking West	162
VI.2	N.E.L. Tower, Closeup showing Transducer Mounting	162
VII.1	Velocity Shift Computer Program Flow Diagram	167
VIII.1	Detector Output	177
VIII.2	Echo Counter and Detector Diagram	178
VIII.3	Proposed Improved Echo Counter	179
IX.1	Distribution of Travel Time Measurements	182
XI.1	Sphere at Position 1	185
XI.2	Analysis of Photograph 1	186
XI.3	Sphere at Position 2	187
XI.4	Arrangement for Scatterer Position Experiment	189



## LIST OF TABLES

Table		Page
3.1	Attenuation Calibration Confidence Levels	24
4.1	Divergent Field Correction Factors	50
4.2	Total Correction Factors	55
6.1	Maximum Particle Radius for Absorption without Scattering	99
I.1	Transducer Sensitivity Change with Depth	139



## 1. Introduction

It has been found that the behavior of sound upon being reflected from the surface of the ocean does not agree with theory, particularly for angles of incidence away from the normal. One of the possible explanations for this disagreement is the presence of small bubbles or other particulate matter near the surface. Theory and laboratory experience have shown that a small concentration of bubbles in water would be particularly effective in causing backscattering, attenuation, and changes in sound velocity. It is the purpose of this project to experimentally determine the presence of microbubbles and other scatterers and absorbers near the ocean surface.

A basic pulse-echo system [28] consisting of an open arrangement of an electrostatic piston transducer facing a reflector was used to determine attenuation, scattering and velocity dispersion at two field locations described in Appendix VI. The three types of measurements were then used in order to interpret the sources of absorption and scattering of sound at frequencies ranging from 24 Kcps to 200 Kcps, in sea states one and two, and primarily at a depth of ten feet.





## 2. Instrumentation.

The instrumentation used in this project consists of four main sections; a transmitting section, a receiving section, a transmit-receive switching section, and a transducer section. Each will be described briefly.

The transmit section takes a sinusoidal signal, gates it to form wave pulses, and then amplifies these wave pulses. The wave pulses are added to a direct current polarizing voltage and then applied to the electrostatic transducer through the transmit-receive switching section. Typical transmitter outputs are shown in figure 2-1. A block diagram of the transmit section may be found in figure 2-2.

The transmit-receive switching section utilizes a signal diode network and an electronic switch to isolate the transmitter from the receiver. Figure 2-3 is a block diagram of this section. Figure 2-4 shows the receiver output while transmitting.

The receiving section consists of an electronic filter and oscilloscope display with amplification before and after the filter. Figure 2-5 is an example of a receiver output display. Figure 2-6 is a block diagram of the receiving system.

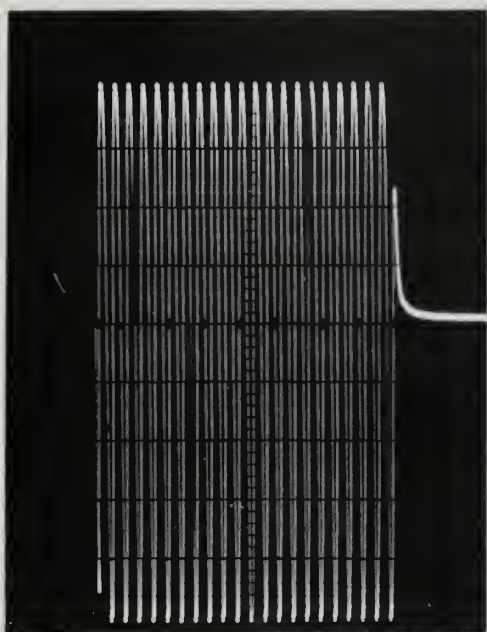
The transducer section consists of a 24 cm diameter wide-band electrostatic piston transducer and a parallel 30 cm steel reflector located 76 centimeters along the axis from the transducer. A complete description of the design, construction and characteristics of the electrostatic transducer is given in Appendix I.

Figure 2-7 shows the electronics set up at the Naval Electronics



Laboratory Tower. Manufacturer's specifications for the commercial equipment used in the entire system may be found in Appendix V. The overall system characteristics are given in Appendix IV.





Power Amplifier Output

at 40 MHz

100 ns/cm horizontal

10 volts/cm vertical

Power Amplifier Output

at 200 MHz

100 ns/cm horizontal

10 volts/cm vertical

Figure 2-1

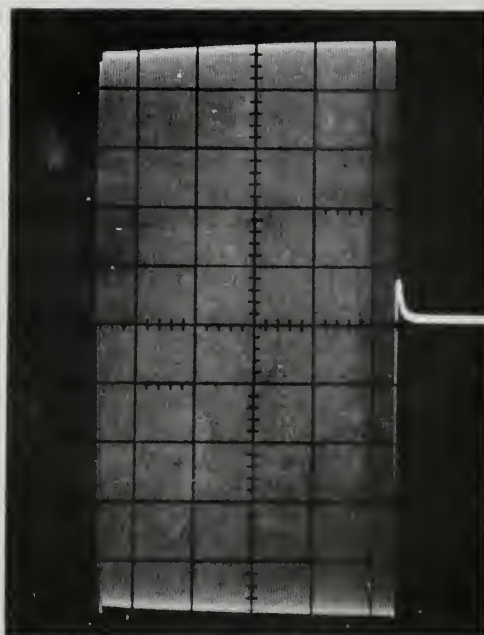




Figure 2-2  
Transmit Section

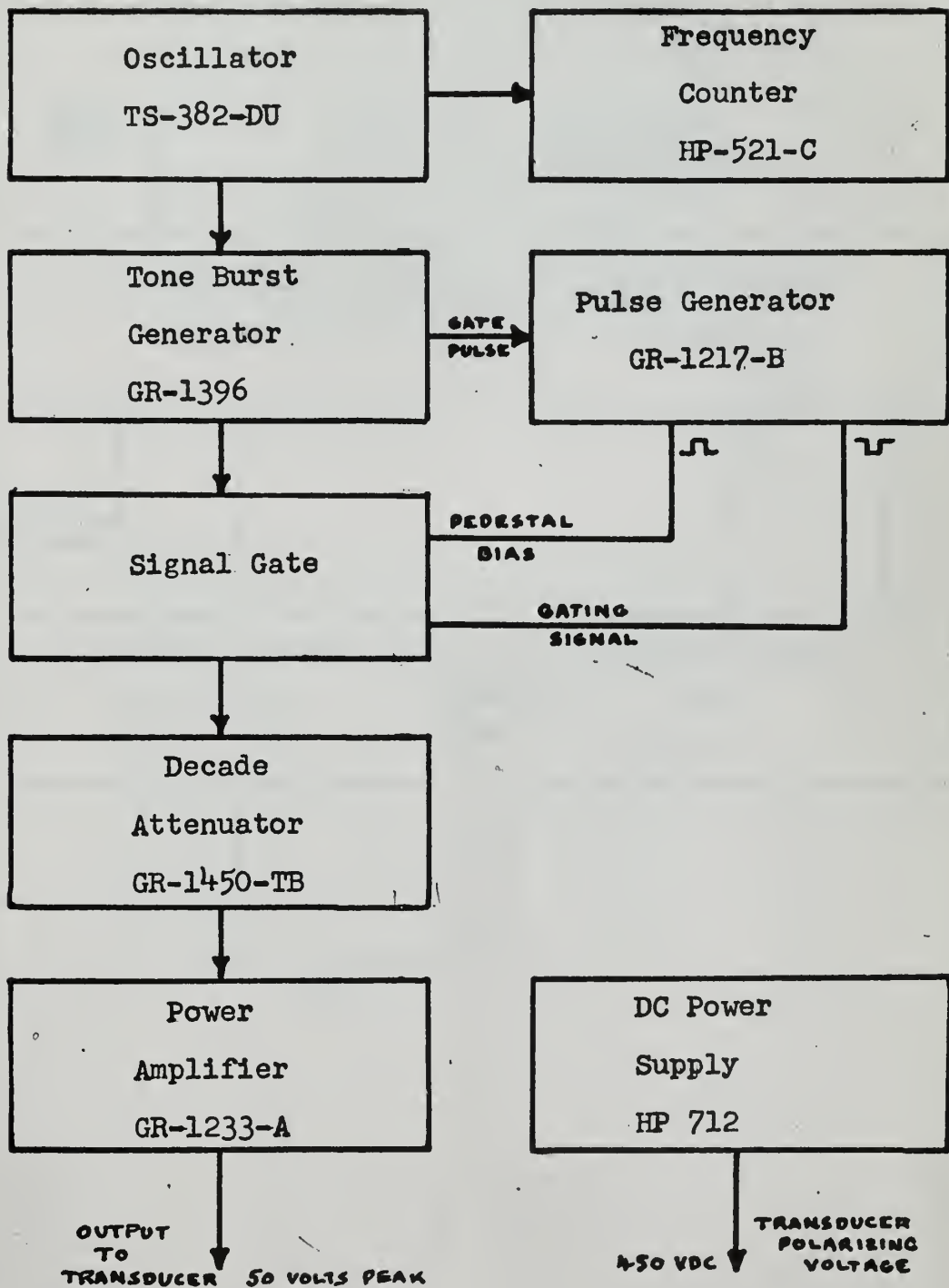
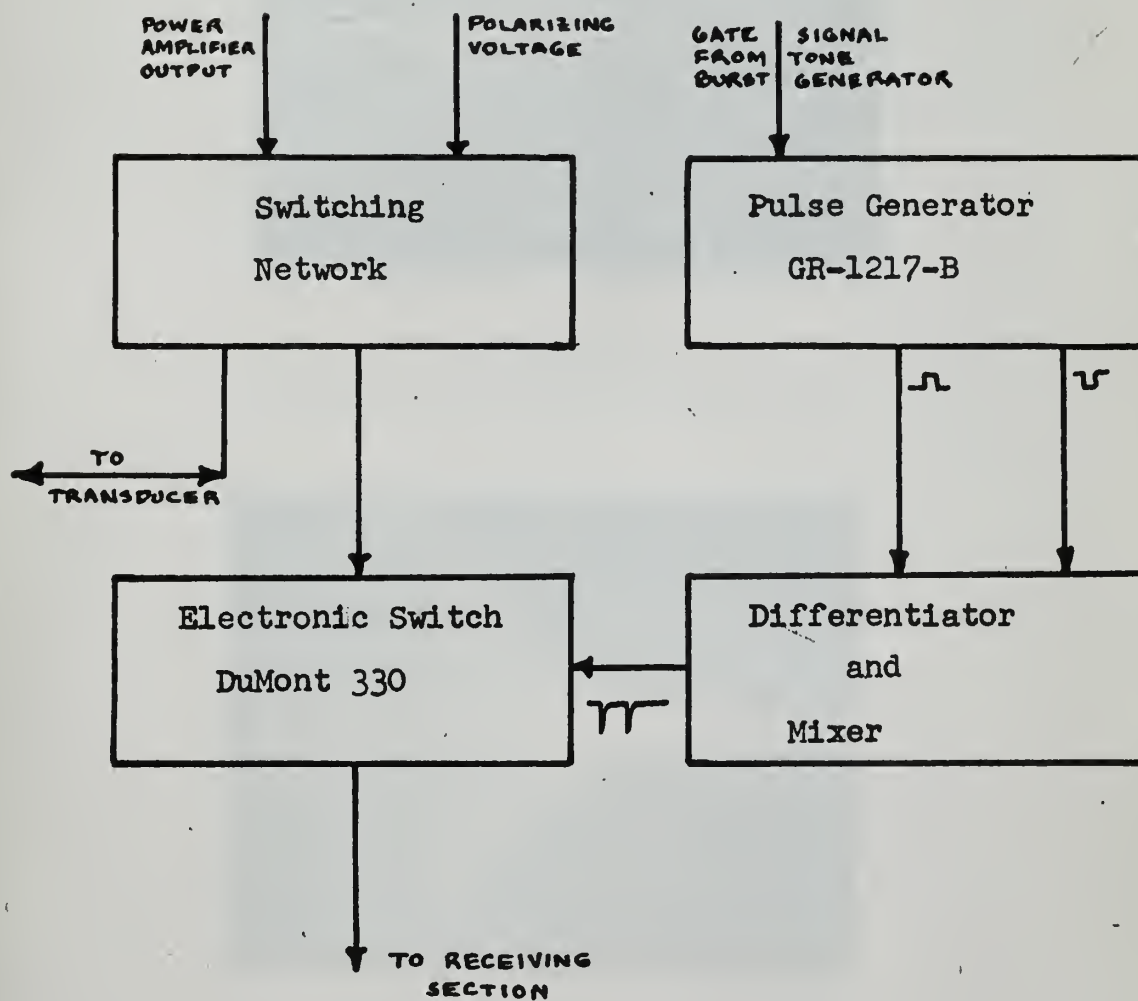






Figure 2-3  
Transmit-Receive Switching Section





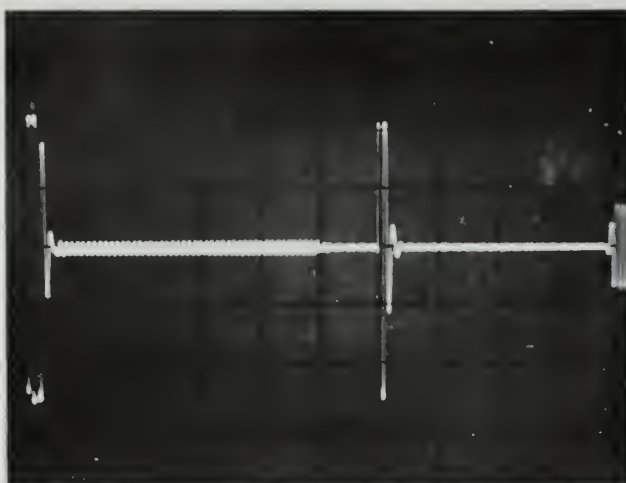


Figure 2-4  
 A receiver output with 100 MHz

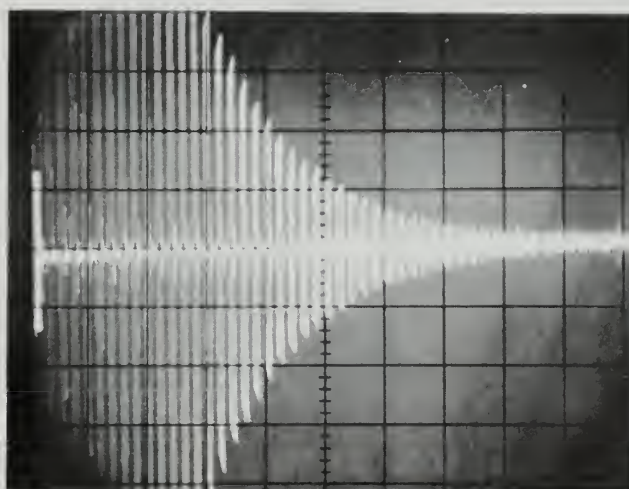
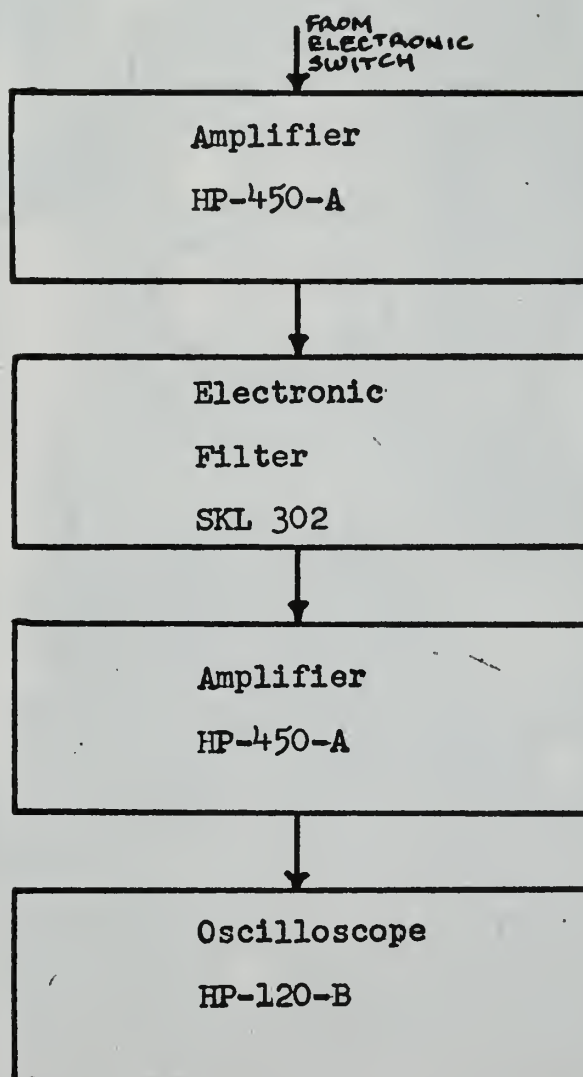


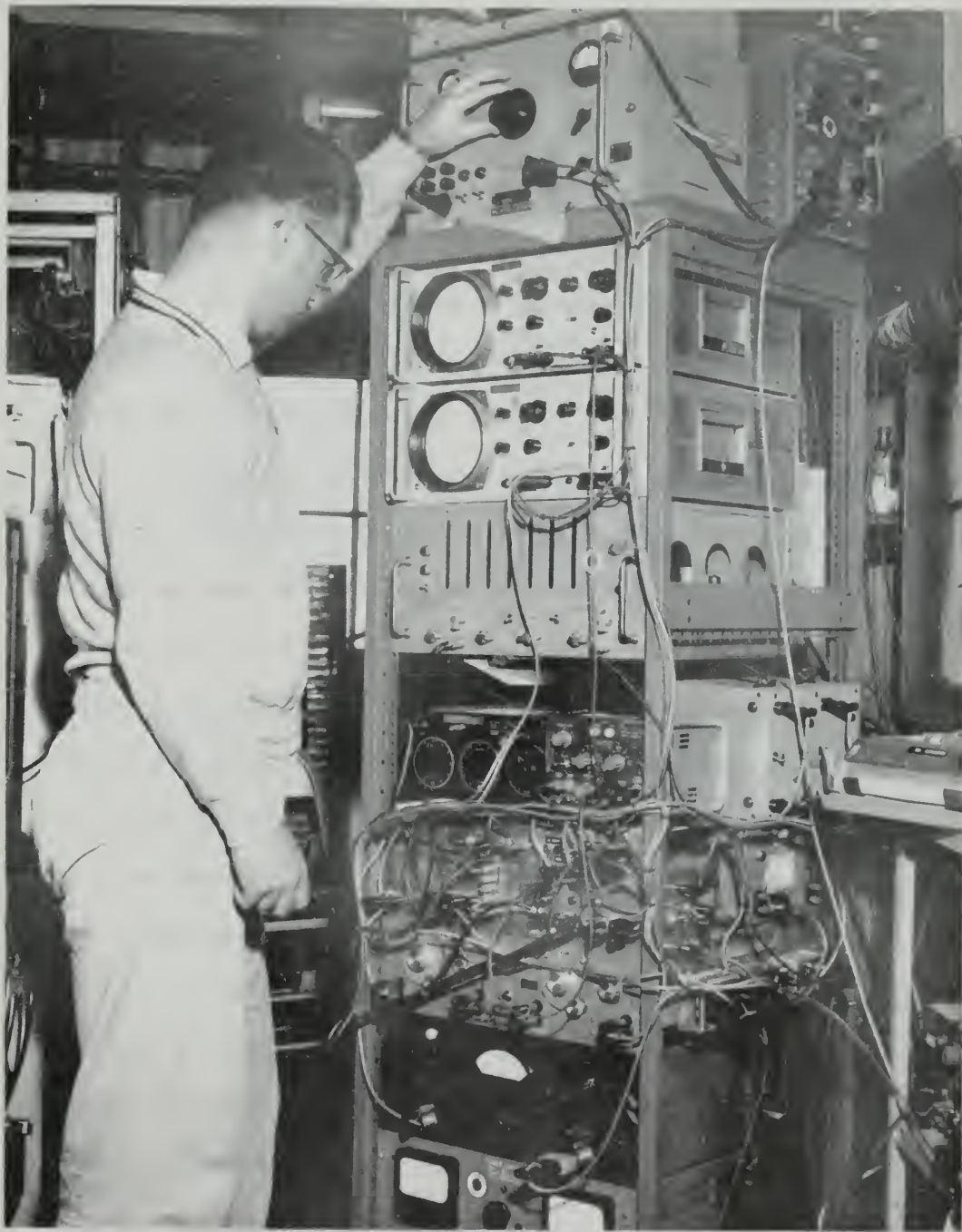
Figure 2-5  
 A receiver output display at 100 MHz



Figure 2-6  
Receive Section











### 3. Attenuation Measurements

#### a. Basic Principle.

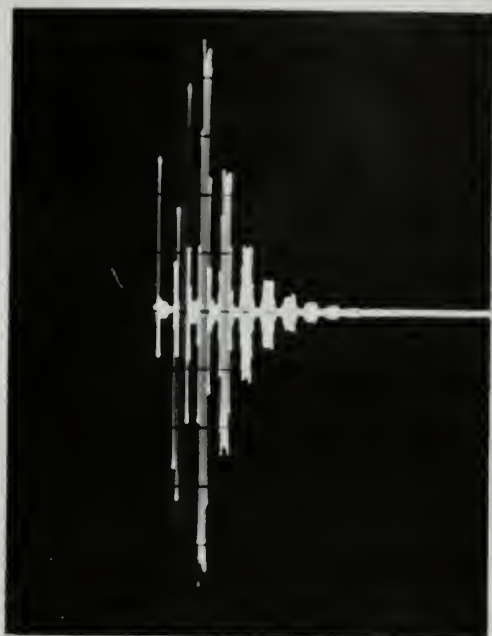
An Electrostatic transducer was gated to emit a short pulse and then electronically switched to receive the successive echoes returned from a reflector placed 76.4 cms. in front of it. Photographs of the pulse echo return are shown in Fig. 3.1. In all cases the gain of the oscilloscope was adjusted so that the amplitude of the second echo was approximately 10 cm. when measured on the oscilloscope face.

Successive echoes were reduced in amplitude by three types of loss; divergence, imperfect reflection at the reflector and the transducer and attenuation in the medium. This attenuation in the medium was due to scattering and absorption by inhomogeneities, in addition to the conventional absorption of the medium itself. The object was to measure the excess attenuation loss in the sea. For all media studied, in the frequency range 24-192 Kcps, this medium loss was smaller than the reference system loss due to reflection and divergence.

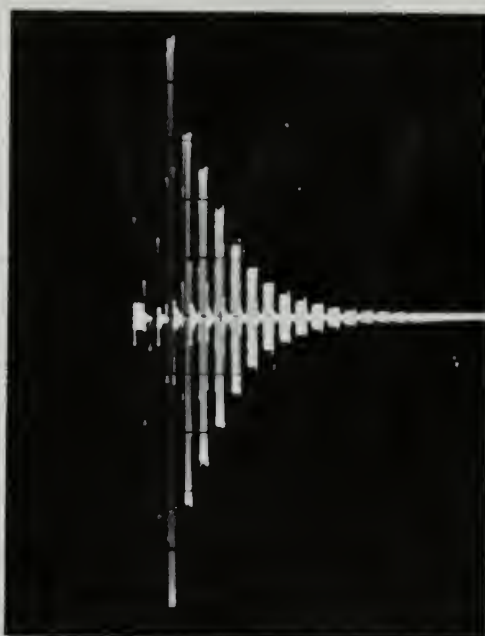
At the lower frequencies, below approximately 60 Kcps, divergence loss was very great so that the number of pulses which could be measured was smaller than that desirable for graphical work. However graphs were drawn for frequencies as low as 24 Kcps and used for the calculation of attenuation.

Fig. 3.1 shows photographs from the minimum usable frequency of 24 Kcps to the maximum frequency at which it was possible to operate the equipment satisfactorily, 240 Kcps.

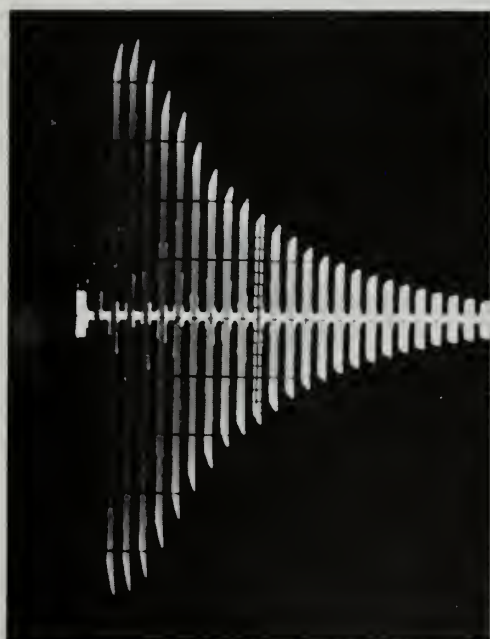




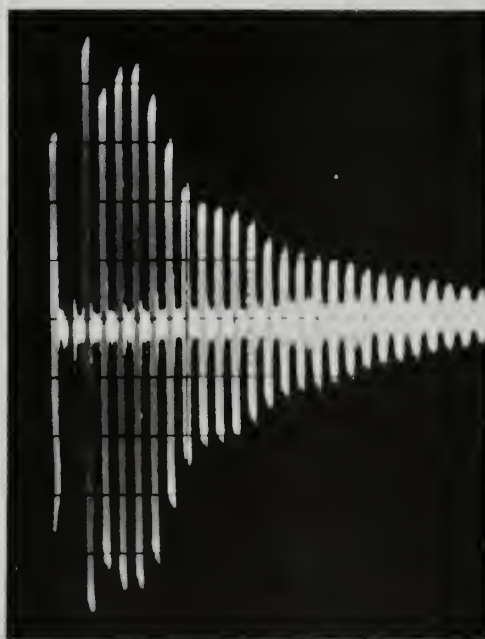
a) 24Kcps.



b) 48 Kcps.



c) 96Kcps.



d) 240 Kcps.

Fig. 3.1

Photographs obtained during the calibration of the system.



Higher frequency operation will require the use of an amplifier capable of delivering an undistorted input to the transducer at the frequency of interest and a filter capable of operation at that frequency. As can be seen from Fig. 3.1 d, noise made the accurate measurement of pulse amplitude increasingly difficult above 200 Kcps.

b. Interference Effects

Interference effects are illustrated by Fig. 3.2 which shows pulse amplitude (logarithmic scale) against echo number (linear scale). These effects are superimposed upon the straight line decay and increase in amplitude with echo number

In this case the interference was not due to mechanical misalignment which gives similar graphs but to the development of a crack at the edge of the transducer. As the aluminum exposed by the crack reacted with the water and was eaten away, the electrostatically driven surface was no longer circular and the piston like behaviour was impaired. The interference effects became worse with time as can be seen by comparing the 1725 and 1753 curves beyond the tenth echo.

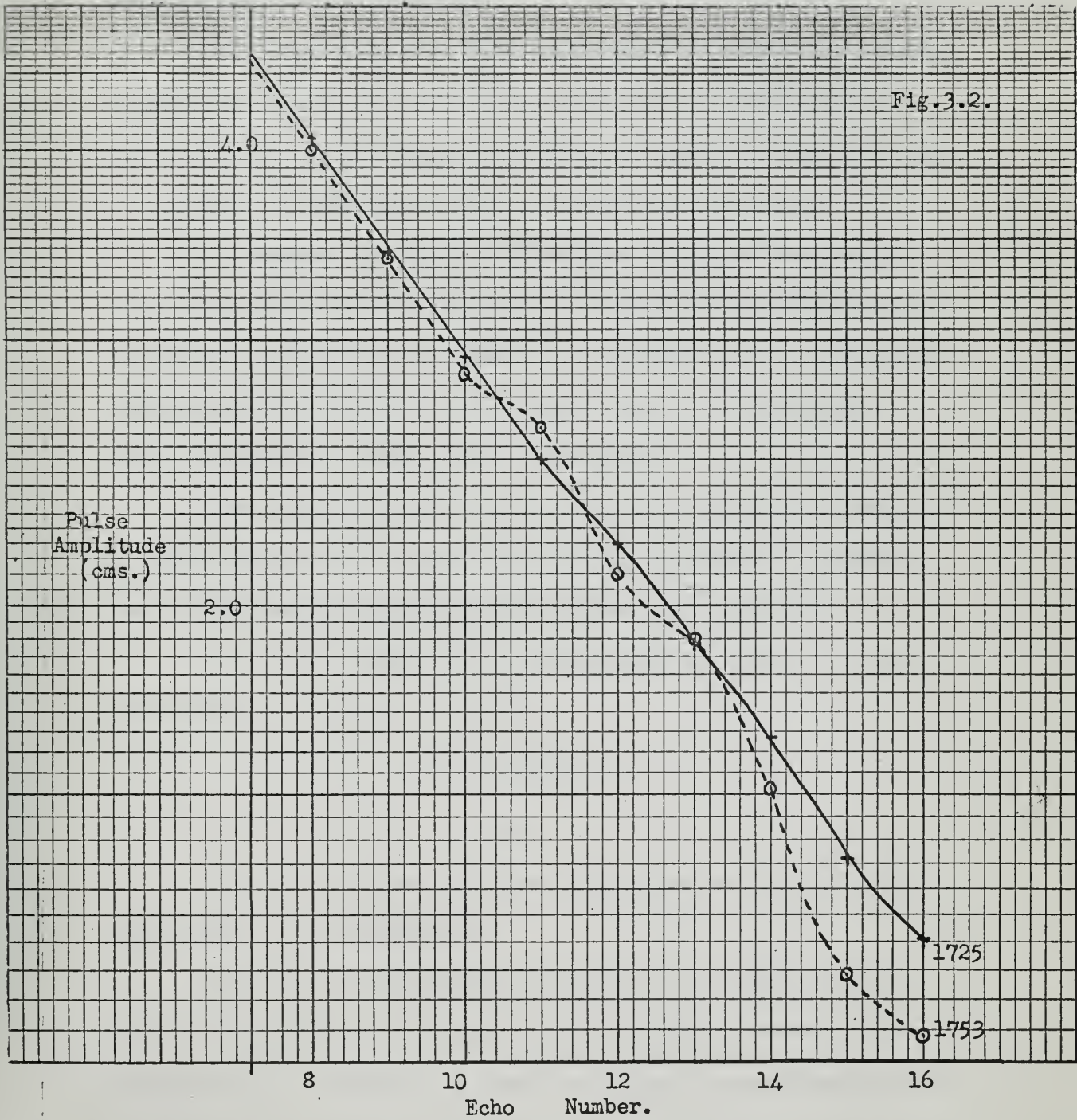
c. Diffraction Effects - Comparison with Theory

Seki, Granato and Truell [23] have used a pulse echo system to investigate diffraction effects in the ultrasonic field of a quartz crystal acting as a piston source and verify William's [27] theory. Our pulse echo system differs in that the pulse is repeatedly reflected from a reflector the same size as the source. At first thought, the method appears equivalent (assuming perfect reflection) to the direct radiation from a piston. In fact, the





Fig. 3.2.







physics more closely approaches the condition of a sound beam that is passed through a series of apertures. At each aperture there will be a new diffraction (near) field. This problem has not been solved, to our knowledge.

The comparison with William's theory is solely for interest. It must be emphasised that the determination of attenuation by subtracting the calibration-slope from the sea-data-slope bypasses the problem of diffraction that is being discussed here.

To compare our field pattern with Seki's we have started with his data for  $ka = 50$  (curve a). This curve was then modified to include the loss due to imperfect reflection at the transducer and reflector (Section I) and yielded curve b. It was assumed that this loss was independent of frequency.

The comparison experimental data used was that of Section H, calibration of the system, since at the frequency of interest the theoretical absorption by fresh water was negligible.

The active radius of the transducer was 12 cms so that, at 96 Kcps

$$\begin{aligned} ka &= \frac{2\pi f a}{c} \\ &= 49 \end{aligned}$$

This is so close to 50 that the variation in diffraction field due to it is negligible.

It was also determined that at 96 Kcps  $a^2/\lambda$  was 93.5 cms so that the distance travelled by the sound waves between echoes was  $1.64 a^2/\lambda$ . Curve c was then drawn with echo amplitude plotted



against distance travelled by sound in units of  $a^2/\lambda$ . Different starting heights are used for a) and c) to preserve clarity.

When d, the distance to the first pulse of the straight line section of the graph was plotted against  $a^2/\lambda$  for the frequencies between 24 and 240 Kcps the straight line of Fig. 3.4 was obtained. Its equation was

$$d = 1.25 + 13.8 a^2/\lambda$$

This distance is the range beyond which the attenuation in db is proportional to the distance travelled.

The dashed line for  $2a^2/\lambda$  also shows that diffraction effects and significant divergence losses occurred for beyond the nominal end of the near field.

Diffraction effects varied between transducers and changes have been observed in a single transducer as shown by Fig. 3.5.

The additional noise in photograph 3.5a is due to a wide band width setting on the electronic filter. Despite the changes in early pulse amplitudes, graphs of pulse amplitude against echo number yielded straight lines which were of the same slope within the limits of accuracy of the experiment (0.06 db/m).

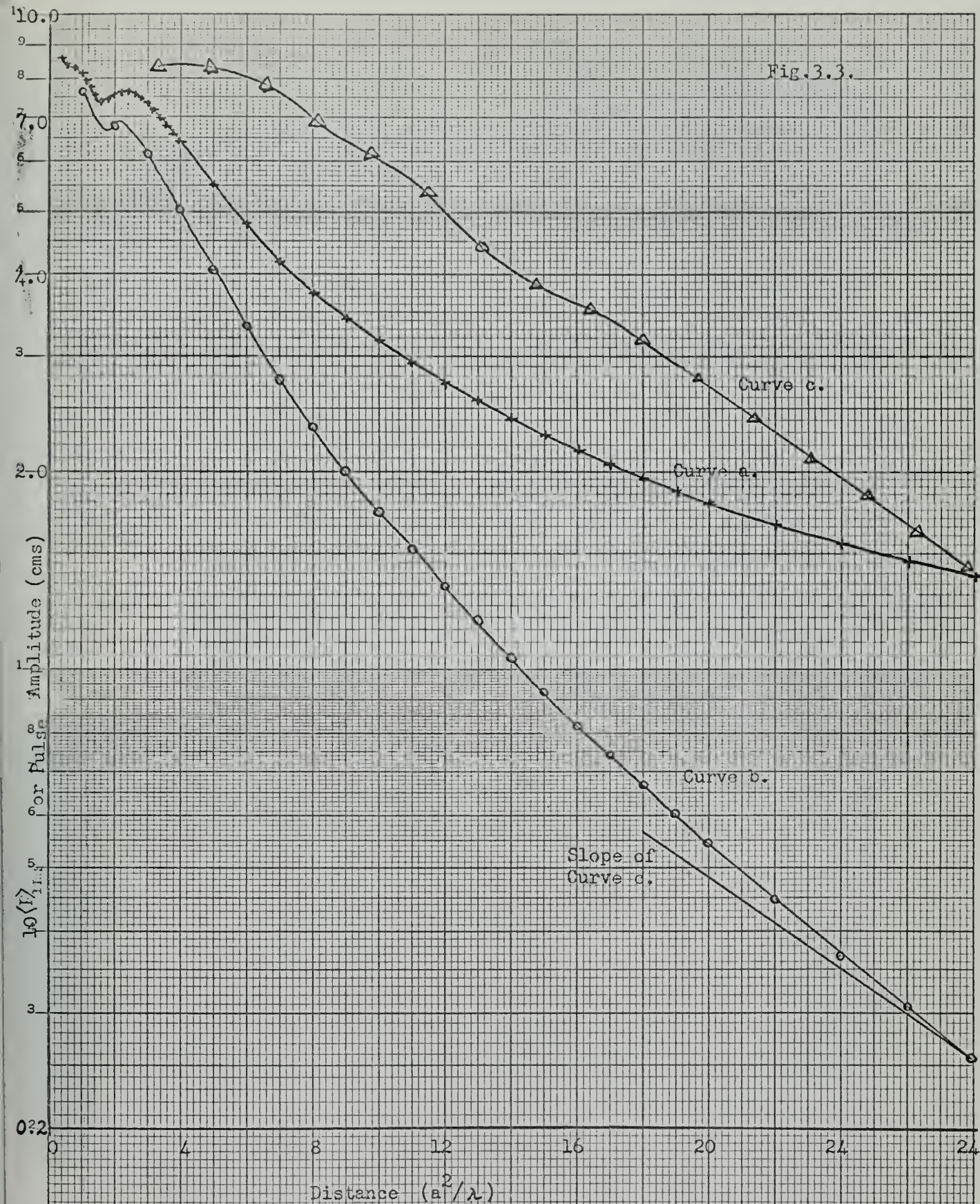
#### d. System Alignment.

To prevent interference effects of the type shown in Fig. 3.2 it was necessary to align the transducer and reflector so that their faces were as nearly parallel as possible. As shown in Fig. 3.6 the transducer mount could be moved along the direction labelled "h" and rotated about its supporting arm, while the reflector was mounted on three adjusting bolts so that its direction might be





Fig.3.3.



Curve a ; Seki data ext rapolated.

Curve b ; Seki data modified by additional reflection loss.

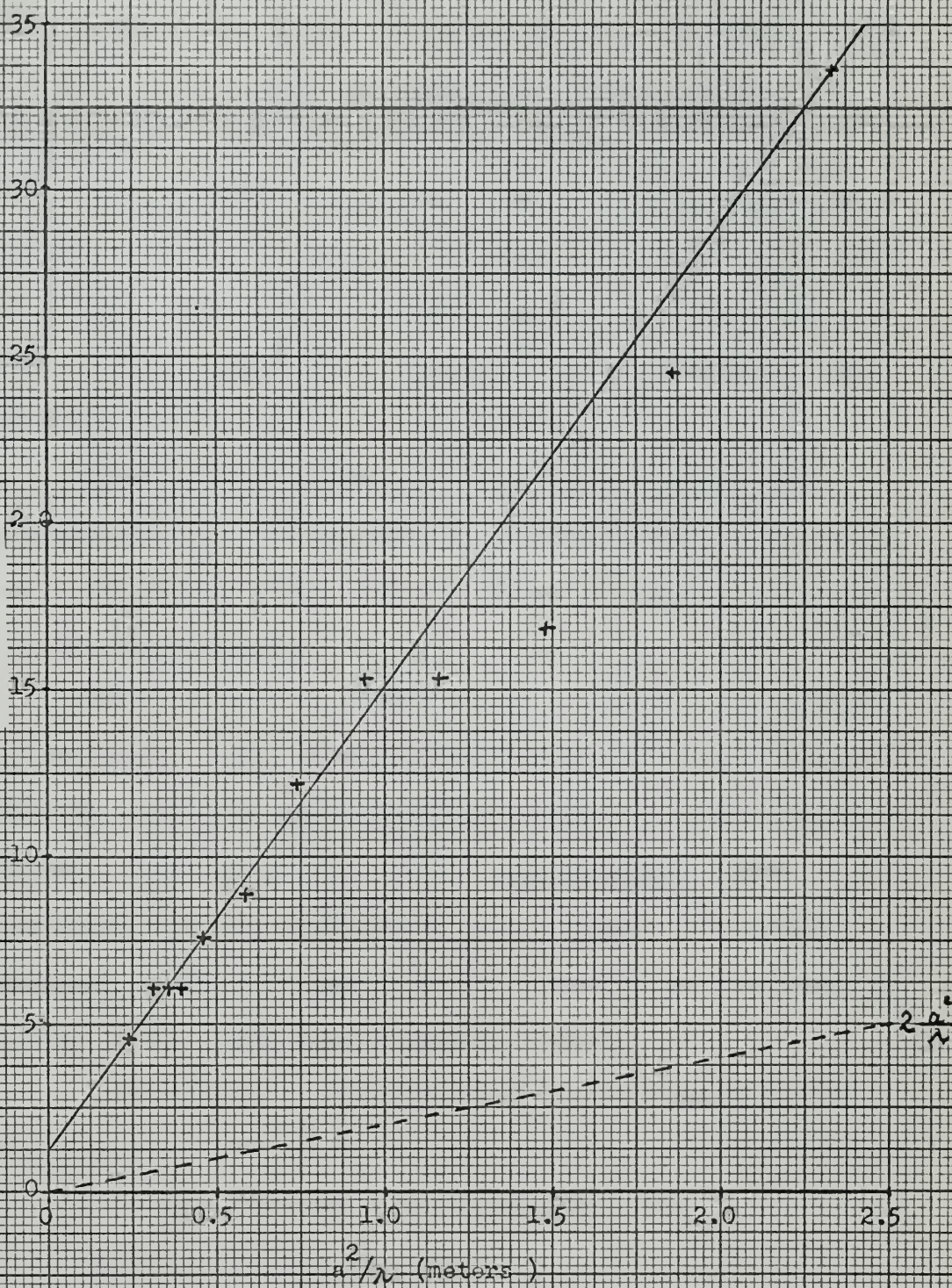
Curve c ; Experiment al results.





Fig. 3.4.

Distance to  
first echo on  
linear  
attenua tion  
section, d.  
(meters)







adjusted both vertically and horizontally.

The initial mechanical alignment was made by adjusting the transducer mount and the reflector until the distances "s" and "d" were the same between all corresponding points on the circumferences of the transducer and reflector.

The system was then placed in water and operated at 192 Kcps when gross misalignment was indicated by a decay pattern much more irregular than those illustrated in Fig. 3.5. Minor adjustments were then made at this frequency, the most sensitive within the normal operating range of the equipment.

When a photograph had been taken and a plot of pulse amplitude against frequency found to yield an ultimate straight line as in curve c of Fig. 3.3, the system was regarded as being satisfactorily aligned.

This procedure was difficult under laboratory conditions and proved more difficult while operating from the N.E.L. Tower, where the system was mounted as shown in Fig. 3.7. Since the transducer mount was easily rotated, despite locking screws, handling difficulties prevented the maintenance of the accurate alignment needed for higher frequency operation, when working from the U.S.N.P.G.S. Oceanographic Research Vessel.

It is therefore recommended that the mounting should be redesigned so that it can be adjusted accurately in the laboratory and then transported safely to the observation site.

#### e. Choice of Reflector Material

To keep reflection loss as low as possible reflectors of



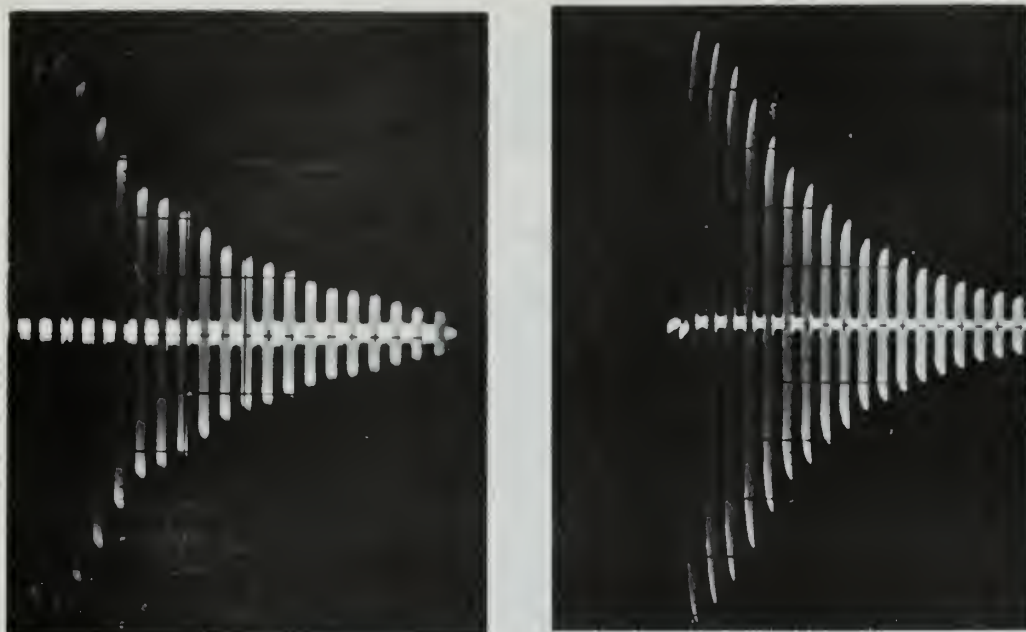


Fig. 3.5.

Photographs obtained at 192 fps. using the same transducer in the same tank containing the same water.

a) 10 Mar. 1131.

b) 11 Mar. 0915.



Fig. 3.6.



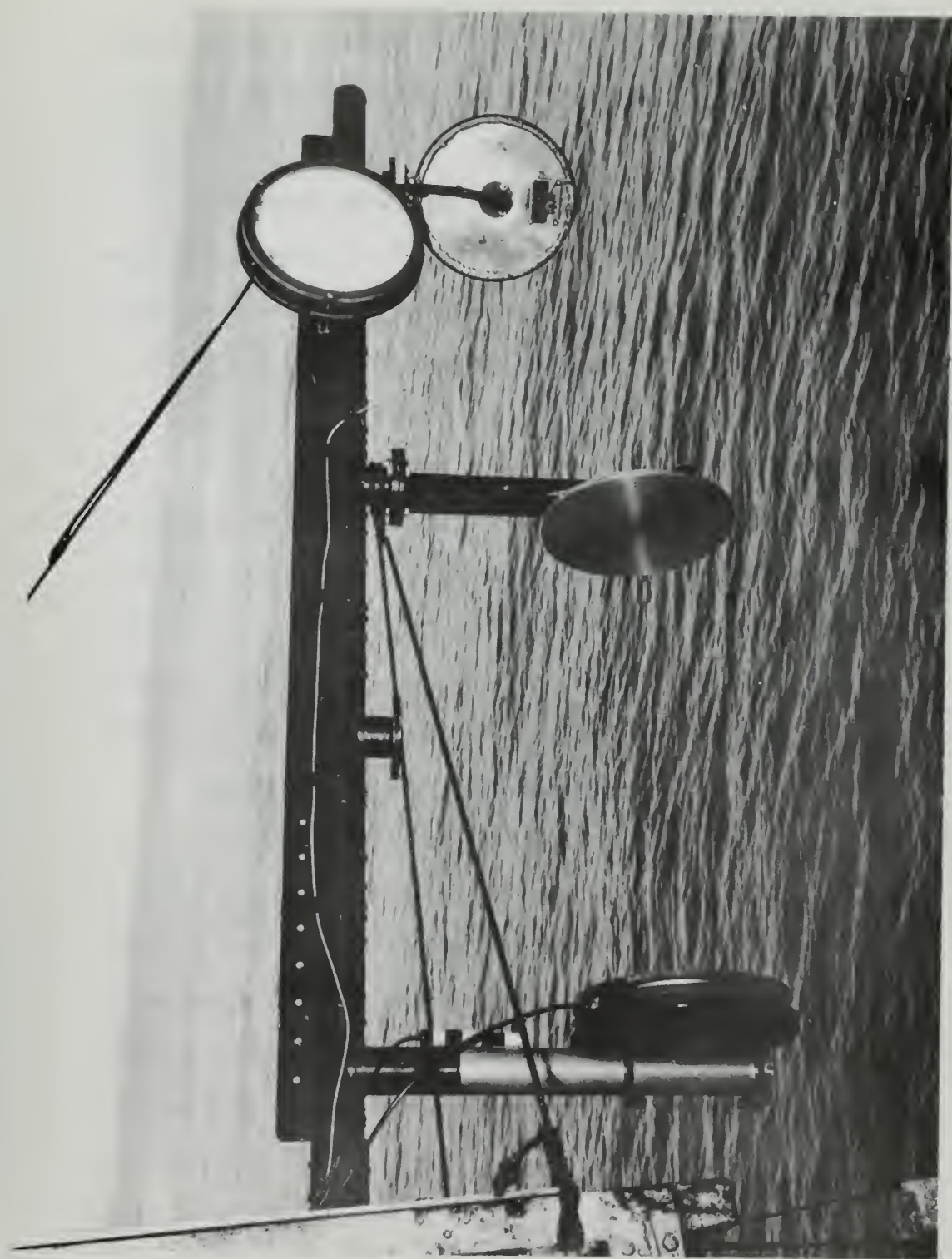


Fig. 2.7.

System mounted at U.S.N.S. A. Thomas, San Diego Bay.

(Courtesy of the U.S. Navy.)





steel, styrofoam and corprene were made and used in succession. With a polarising voltage of 200 V. and an input drive of 20 V. peak at 60 Kcps applied to the transducer, the amplitudes of the first echo were: steel, 33 mv.; styrofoam, 31 mv.; corprene, 25 mv.

The steel reflector was therefore selected; it had the additional advantage of mechanical strength so that its reflection coefficient would not be altered by compression as its depth increased.

f. Selection of Operating Voltage

After the reflector had been selected the polarising voltage and input drive were varied and the first echo amplitude observed, the results being as shown in Fig. 3.8. On the basis of this graph it was decided to apply a polarising voltage of 450 V., the maximum which would be accurately set with the power supply in use, and to use an input drive of up to 50 V peak. This input drive was reduced at higher frequencies to maintain a better input pulse shape.

g. Determination of Standard Deviation.

In order to determine whether variations in the field data were due to the medium or the system and to establish the confidence level for the calibration, the mean and standard deviation were determined at 60 Kcps and 192 Kcps. A series of photographs was taken as rapidly as possible to minimize changes in the tank water and equipment. The attenuations were then determined from each photograph.





2.0

For each polarising voltage  
the applied signal had an  
amplitude which was 10%  
of the polarising voltage.  
Frequency was 60 Kcps.

1.6

1.2

0.8

0.4

0

0

100

200

300

400

500

First Echo  
Amplitude.  
Volts p-p.

Polarising Voltage (volts)

Fig. 3.3. Echo Amplitude vs Polarising Voltage.

1.70

Attenuation.

1.60

1.50

0

5

10

15

20

25

(db./meter)

Sample  
Mean

Sample Number.

Fig. 3.9. Attenuation vs Sample Number at 60Kcps.





60 Kcps Result. (27 samples)

$$\text{Mean } \bar{X} = 1.62. \text{ db/meter}$$

$$\sum_{j=1}^{27} (X_j - \bar{X})^2 = 1.58 \times 10^{-2} \text{ (db/meter)}^2$$

$$\text{Variance } S^2 = 6.10 \times 10^{-4} \text{ (db/meter)}^2$$

$$\text{Standard Deviation } S = 0.025 \text{ db/meter}$$

192 Kcps Result. (26 samples)

$$\text{Mean } \bar{X} = 0.89 \text{ db/meter}$$

$$\text{Standard Deviation } S = 0.015 \text{ db/meter}$$

Fig. 3.9 shows the attenuation in db/m vs sample number at 60 Kcps. The sample points are distributed in much the same way as some of the field data, particularly that in which depth and frequency were held constant while photographs were taken at 2 minute time intervals. The noise was not significantly different in the field. The field curves have therefore been smoothed by up to twice the standard deviation for system noise.

h. Calibration of System.

Knowing the mean and standard deviation at 60 and 192 Kcps, it was desirable to determine the number of photographs to be taken at each frequency to ensure that the error was less than 1% at a satisfactory confidence level. Since the standard deviation was somewhat worse at 192 Kcps than at 60 Kcps all calculations were performed at the higher frequency.

When  $n$  is the number of observations

$\epsilon$  is the permissible error

$s$  is the standard deviation



and  $k_{\frac{\alpha}{2}}$  is from standard normal tables

$$\frac{\sqrt{n} \epsilon}{s} = k_{\frac{\alpha}{2}}$$

so that for specific values of  $n$ ,  $k_{\frac{\alpha}{2}}$  can be determined and the confidence level found.

NUMBER OF OBSERVATIONS	CONFIDENCE LEVEL
n	%
5	76
6	81
8	86

Table 3.1

From the results shown in the above table it was decided to take six photographs and establish a confidence level of better than 80%.

In preparation for the calibration a sonar tank with a capacity of about 10,000 gals. was emptied, washed down and then refilled with tap water to which an algicide had been added. After filtering for one day to remove particulate matter, the tank was allowed to stand for four days so that any bubbles of air produced by the filling might rise to the surface or be absorbed in the water.

Six exposures were then made at the frequencies of interest and used to establish the standard values for attenuation due to the system in bubble-free fresh water.

At all frequencies the pulse amplitudes for the first and last photographs were measured from pulse 2 until they became too



small for valid measurement or the last pulse on the photograph had been measured. These pulse amplitudes were then plotted against echo number as before to determine the straight line section of the graph after which measurements from the other four photographs were confined to this section of the graph.

From graphs of the form shown in Fig. 3.3, curve c it was possible to determine the pulse amplitude  $P_n$  at the beginning of the straight line or extrapolated beyond it and a second pulse amplitude  $P_{n+m}$ ,  $m$  bounces beyond  $P_n$  but still large enough to be measured accurately. Then loss  $m$  bounces =  $20 \log \frac{P_n}{P_{n+m}}$  db.

From this the loss in db/bounce was calculated and then converted to db/meter. knowing that the separation between the transducer and reflector was 76.4 cms.

The results of this determination yielded the curve shown in Fig. 3.10. Apparently algae were still causing excess attenuation centered about 150 Kcps. So that excess attenuations could be determined from the field data the dashed line was drawn in and has been treated as the standard reference attenuation due to divergence and reflection loss.

#### i. Reflection Losses.

If the attenuation loss at 240 Kcps is used to measure the reflection coefficient of the system, divergence losses may be neglected since the linear section of the graph used to calculate attenuations corresponds to great distances from the source.

Minimum measured attenuation = 0.87 db/bounce  
where the path length for one bounce is 1.53 meters.

At the frequency of 240 Kcps





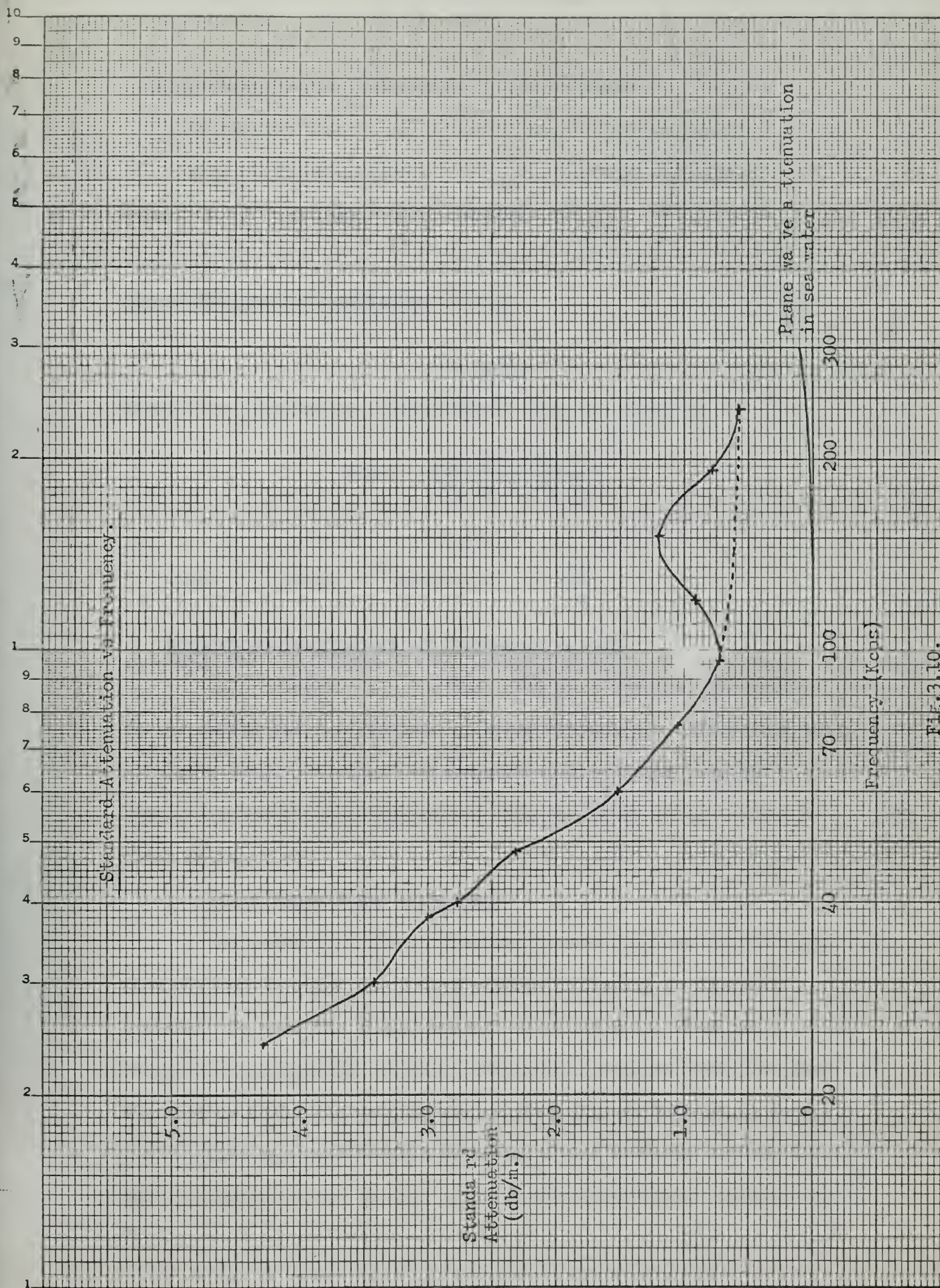


Fig. 3.10.





Absorption due to fresh water 0.02 db/meter

Absorption/bounce due to fresh water = 0.03 db/meter

Total Reflection Loss = 0.84 db/bounce

$$10 \log_{10} \frac{I_1}{I_2} = 0.84$$

$$\begin{aligned} \text{System Reflection Coefficient} &= \frac{I_2}{I_1} \\ &= \underline{0.83}. \end{aligned}$$

Theoretical Reflection Coefficient of steel is given by

$$\begin{aligned} \text{Steel} &= \left( \frac{\rho_2 c_2 - \rho_1 c_1}{\rho_2 c_2 + \rho_1 c_1} \right)^2 \\ &= 0.94 \end{aligned}$$

$$\text{since } \alpha_{\text{steel}} \times \alpha_{\text{transducer}} = \frac{I_2}{I_1}$$

Reflection Coefficient of transducer = 0.88.

This determination has only been made for one transducer.

If the reflection coefficients of other transducers differ from this, erroneous values of excess attenuation will be found when the standard attenuation is subtracted from the field determination of total attenuation.

#### j. Fresh Water Algae Experiment

The anechoic tank was drained, washed down and refilled and then allowed to stand for 5 days without filtering or chemical treatment so that the algae present could develop. Previous absorption experiments had shown evidence of bubbles after two days standing so that this waiting period also allowed bubbles to escape.

Although considerable attenuation was measured between 120 and 200 Kcps as shown in Fig. 3.11, no back-scattering (Section 4)



was detected nor did velocity measurements (Section 5) indicate any dispersion.

A sample was taken with a plankton net and an analysis and count kindly performed by Dr. E. C. Haderlie of Monterey Peninsula College, the algae population being:

Desmids (20-40 $\mu$ ) population	= 20 x 10 <sup>3</sup> /liter
Ceratium Dinoflagellates ( $\sim$ 90 $\mu$ ) population	= 0.4/liter
Volvox (100 $\mu$ ) population	= 0.2/liter

This experiment showed that phyto-plankton were capable of producing considerable attenuation without detectable scattering or dispersion at selected frequencies. Whether there were minute bubbles associated with the photosynthesis of the plankton could not be determined.

k. Absorption in San Diego Bay

Attenuation photographs were obtained at known times and depths. Using the Precision Scientific Company Galvanic Bell Oxygen Analyser simultaneous observations of temperature and oxygen content of the water were obtained from a thermistor and oxygen electrode mounted on the equipment as shown in Fig. 3.7. The Winkler tests needed to calibrate the oxygen electrode were kindly performed by Mr. F. Crowe and Mr. J. T. Hart of the Scripps Field Annex.

The photographs were analysed and graphs drawn to determine the total attenuation. From these results the attenuations due to the system were subtracted leaving the attenuation due to the medium, as shown in Figs. 3.12 to 3.17.





# Attenuation vs Frequency - Algae in Anechoic Tank.

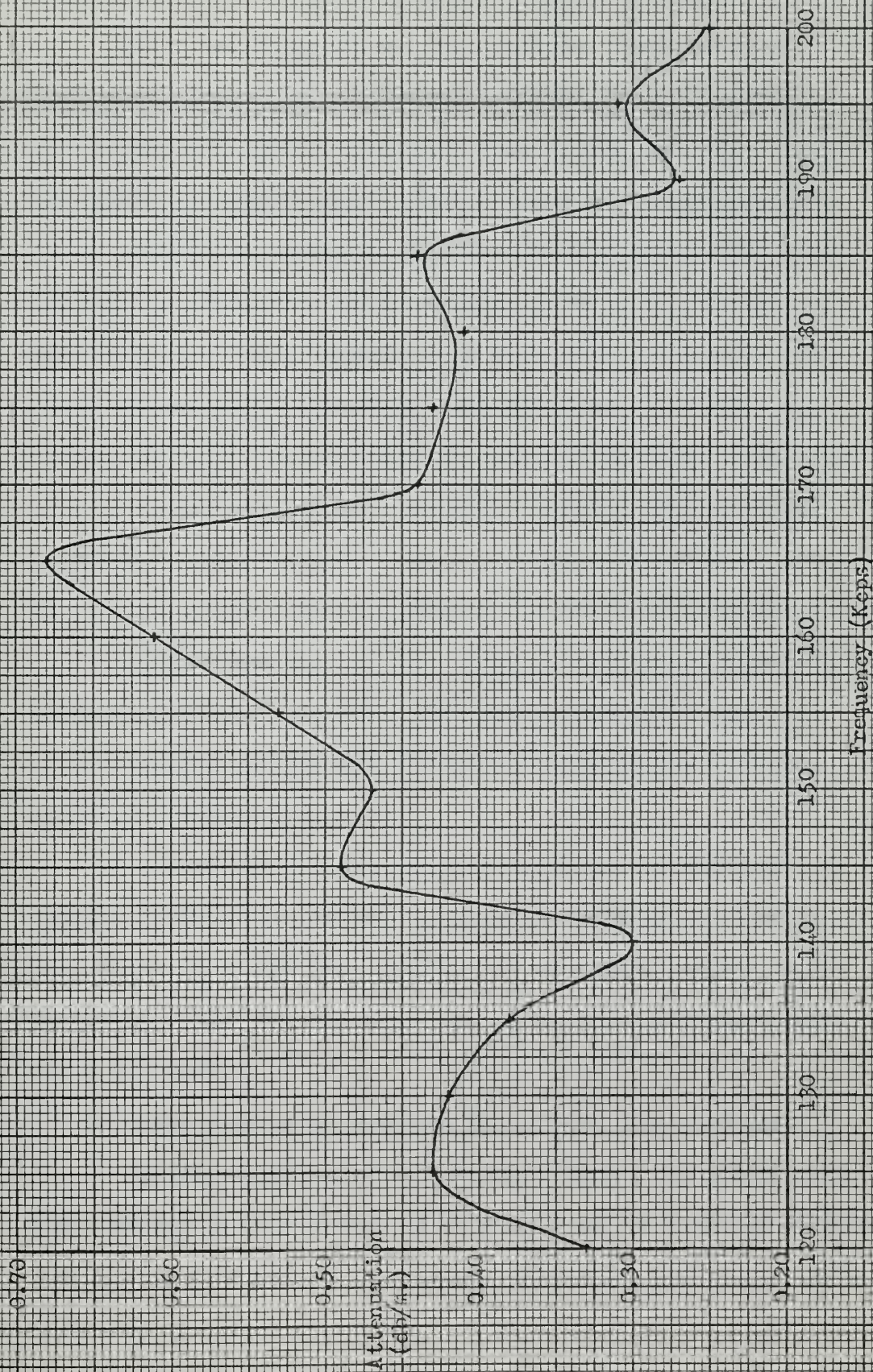


Fig. 2.11





There was little change in attenuation over a 30 min. period when observations were made at a fixed frequency.

When the frequency was fixed and the depth varied a consistent attenuation pattern was produced, which appeared to move slowly with time. Additional observations over 24 hr. periods are needed to confirm that a diurnal change was being observed.

Small bubbles may be generated during the daylight hours causing the attenuation at frequencies above 96 Kcps to increase during the day. After sunset these bubbles would no longer be generated but would be absorbed into the water or coalesce into larger bubbles so reducing high frequency attenuation (See Fig. 3.16) . Their coalescence into larger bubbles would increase attenuation below 96 Kcps. as shown in Figs 3.13 and 3.14, where the evening attenuations are greater than the morning attenuations.

At 152 Kcps and 192 Kcps there was a definite relationship between absorption and depth, with maximum absorption near the surface suggesting that the absorbers were organisms requiring light for photosynthesis.

Attenuation did not correlate with either temperature or oxygen content of the water. However, the water was isothermal (in general  $\pm 0.05^{\circ}\text{C}$  or  $\pm 0.10^{\circ}\text{C}$ ) and the oxygen content varied little from 100% saturation so that these quantities could have had little effect.

#### 1. Comparison of Attenuation Values with Published Data.

In the experimental work a short sound pulse passed many times through a small volume of water so that the measured attenuation was that of a very short path length and was independent of depth,





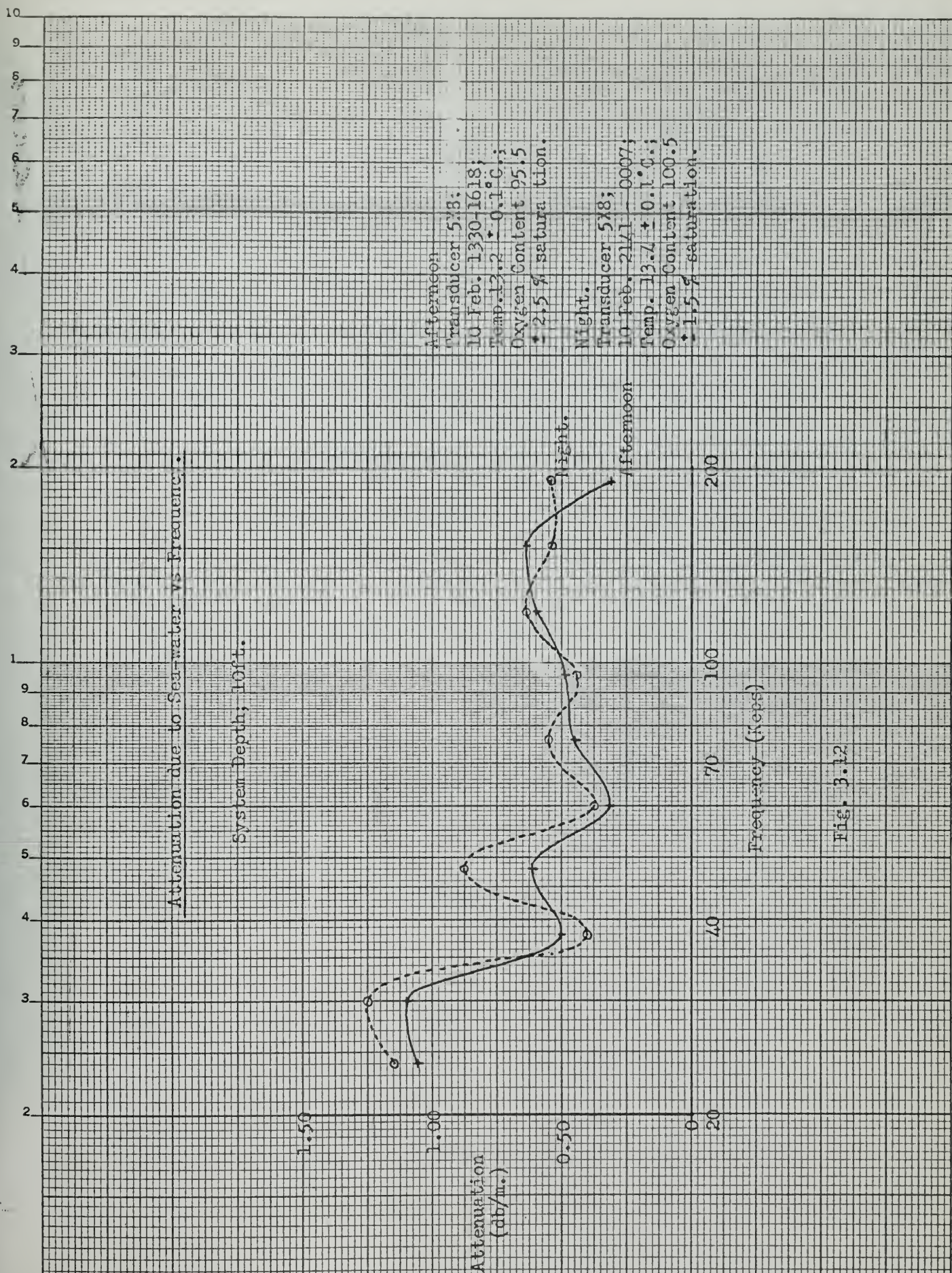


Fig. 3.12





40 Kcps.

Fig.3.13.

Variation with Time.

0.40

0.30

(db/m.)

0.20

1220

Lapsed Time (mins.)

Transducer 5K3; 10 Feb.; Depth 25 ft.;

Temp.  $13.05 \pm 0.05^\circ\text{C}$ ; Oxygen Content  $90 \pm 2\%$  saturation.

1.00 Variation with Depth.

110

0.50

100

0.60

Oxygen Content;  
(% saturation)  
10 Feb.

Attenuation

(db/m.)

0.20

80

Depth (ft.)

Morning: Transducer 24; 15 Feb., 0923 - 0942;  
Temp. Isothermal at  $12.9^\circ\text{C}$ . ;  
Oxygen Content,  $98 \pm 2\%$  saturation.

Evening: Transducer 5K3; 10 Feb., 1323 - 1355;  
Temp.  $13.25 \pm 0.05^\circ\text{C}$ . ;  
Oxygen Content, As Shown.

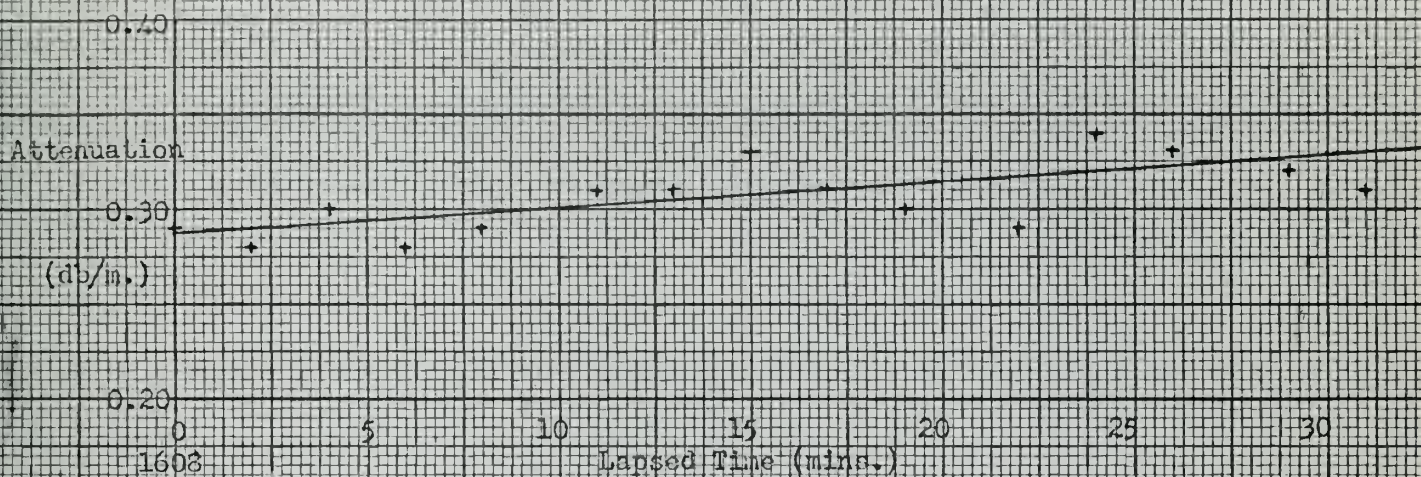




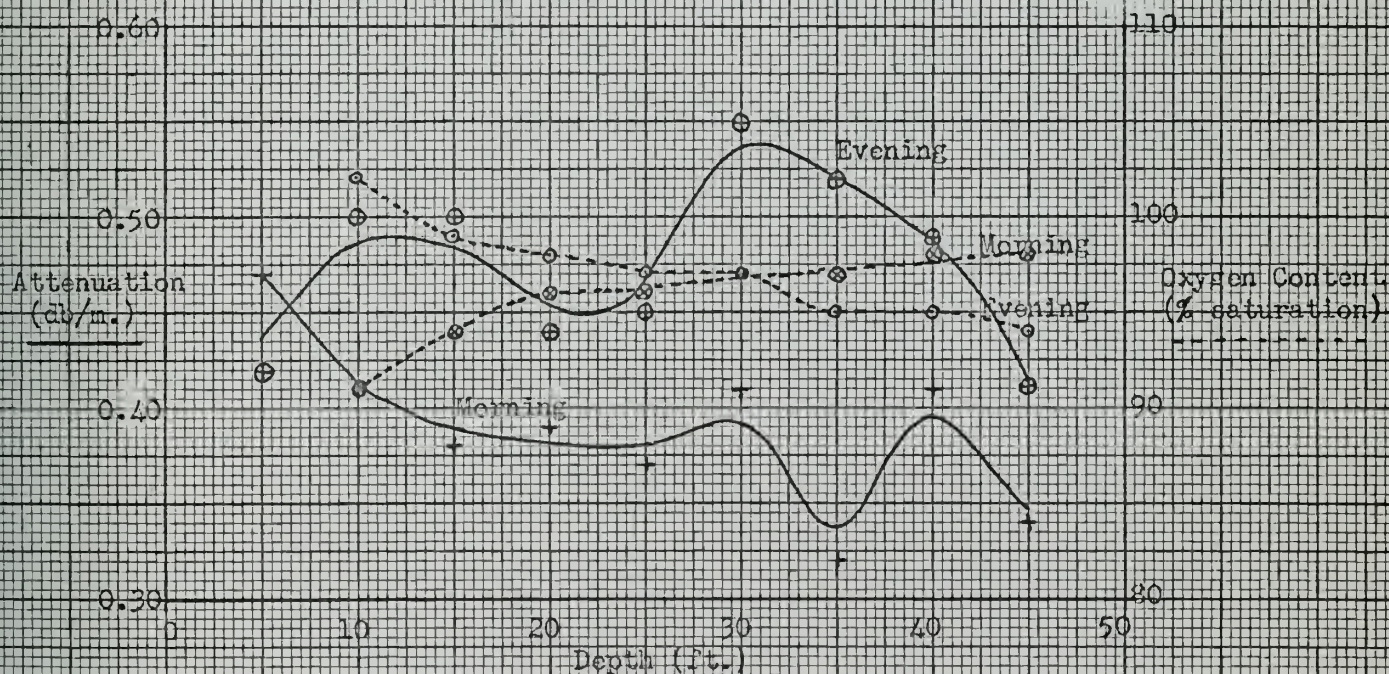


60 Kcps.

Fig. 3.14

Variation with Time.

1608  
 Transducer 24; 15 Feb.; Depth 25 ft.;  
 Temp., Isothermal at 13.1°C.; Oxygen Content, 95 ± 1% saturation.

Variation with Depth.

Morning: Transducer 24; 15 Feb., 0950 - 1100;  
 Temp., Isothermal at 12.9°C.

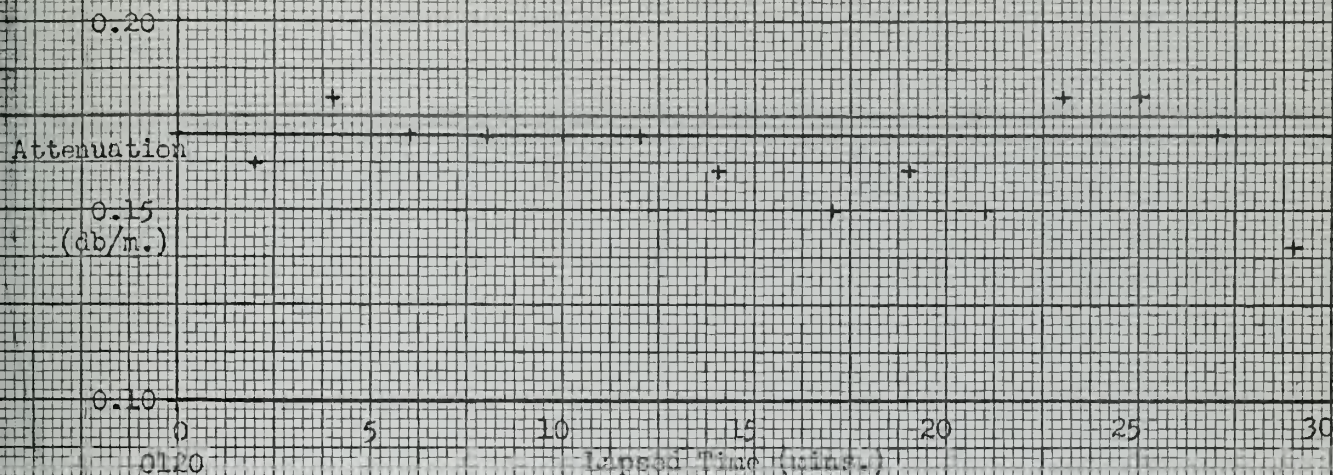
Evening: Transducer 5X8; 10 Feb., 1913 - 2005;  
 Temp., 13.25 ± 0.05°C.







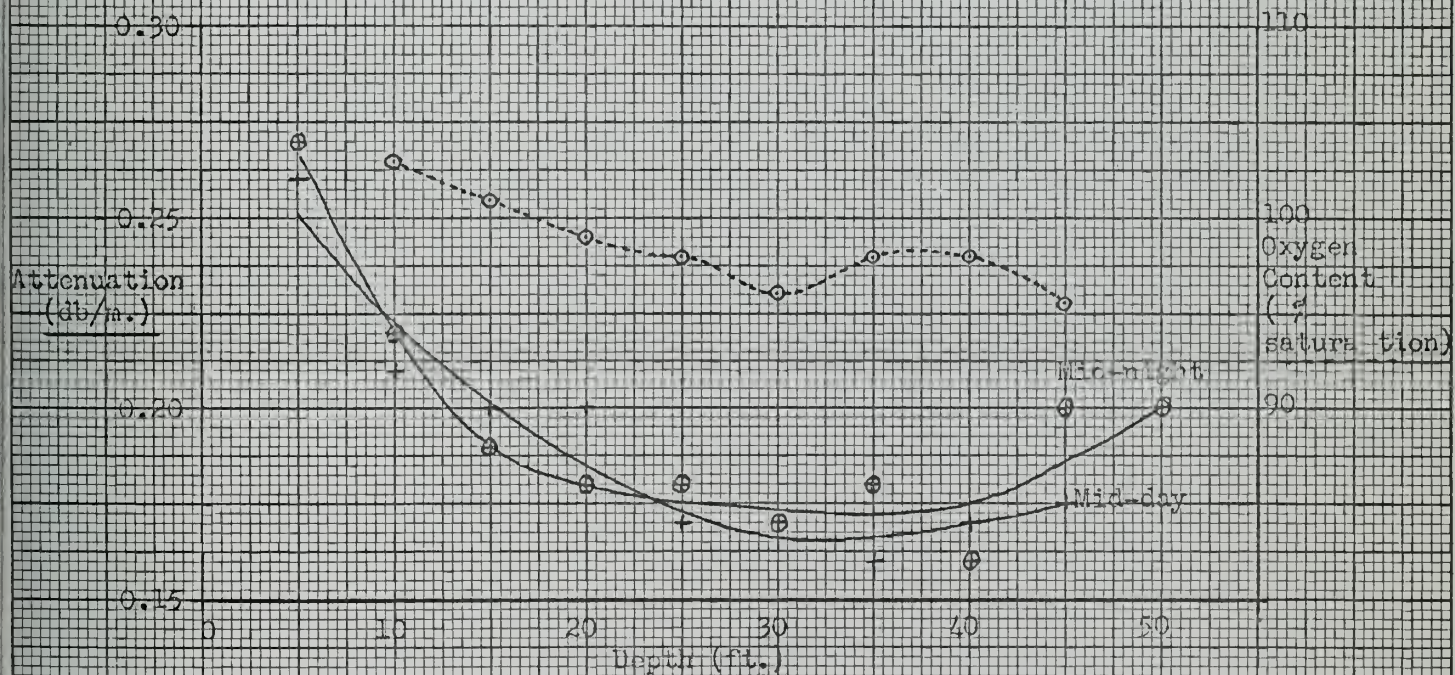
## Variation with Time.



Transducer 24; 16 Feb.; Depth 25 ft.;

Temp., isothermal at 13.0°C.; No oxygen data available.

## Variation with Depth.



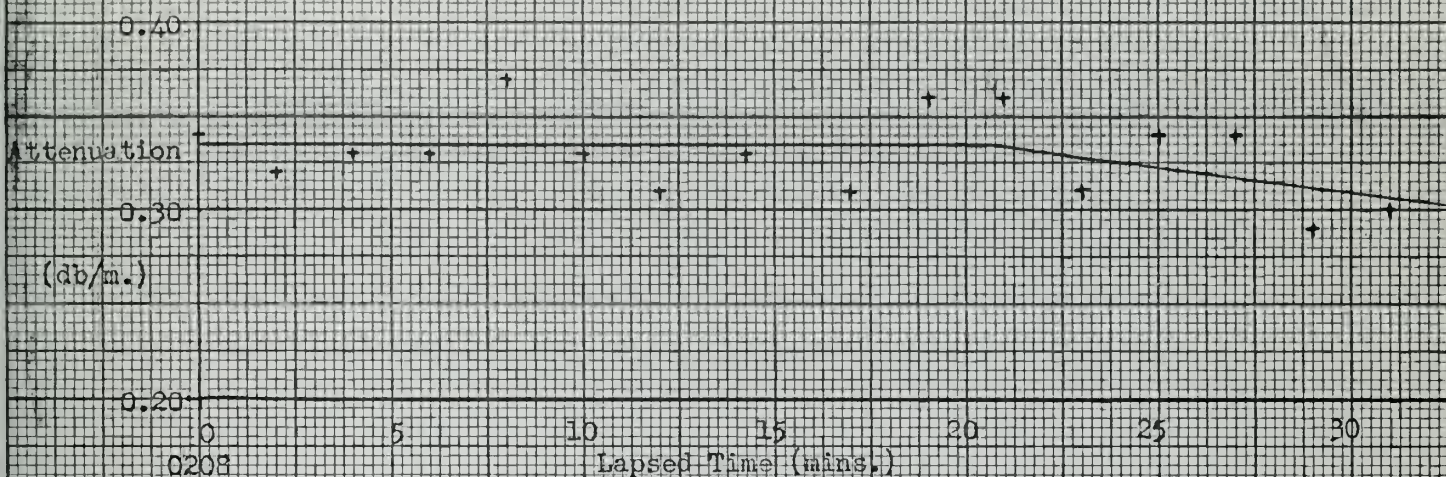
Mid-day : Transducer 24; 12 Feb., 1155 - 1218;  
 Temp., 13.25 ± 0.05°C.;  
 Oxygen Content as shown.

Mid-night : Transducer 24; 16 Feb., 0120 - 0151;  
 Temp., 13.05 ± 0.05°C.;  
 No oxygen data available.





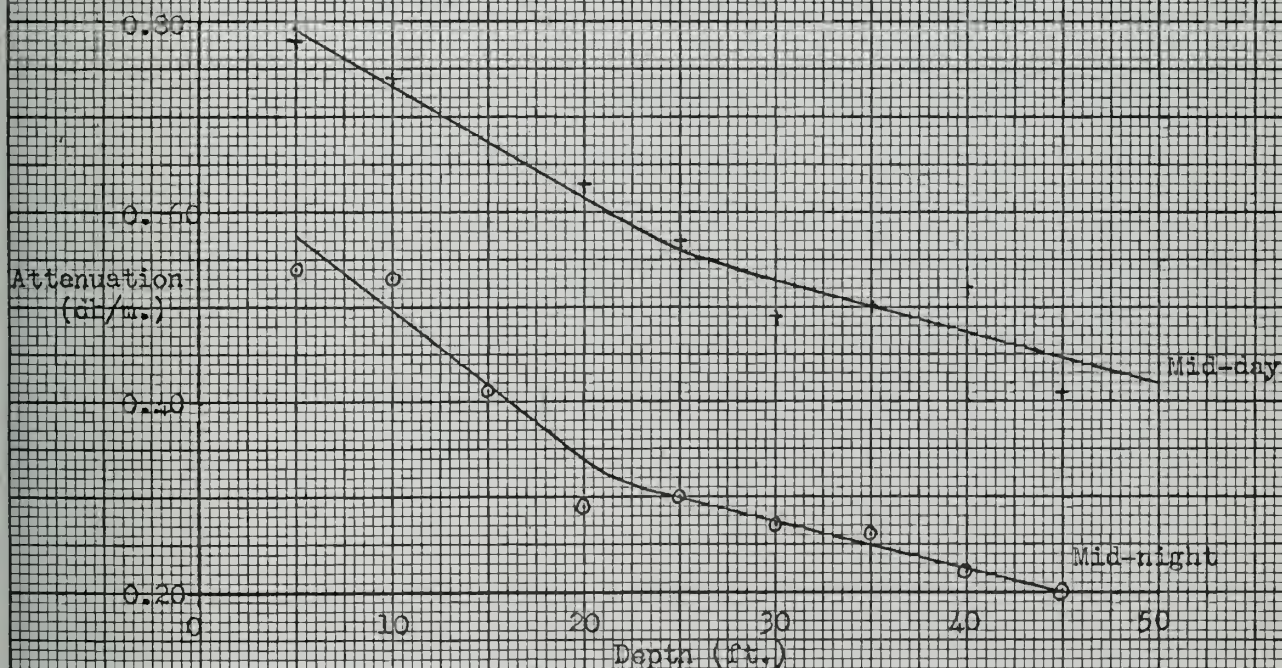
## Variation with Time.



0208

Transducer 24; 16 Feb., Depth 25 ft.;  
Temp.,  $12.9 \pm 0.1^\circ\text{C}$ .; No oxygen data available.

## Variation with Depth.

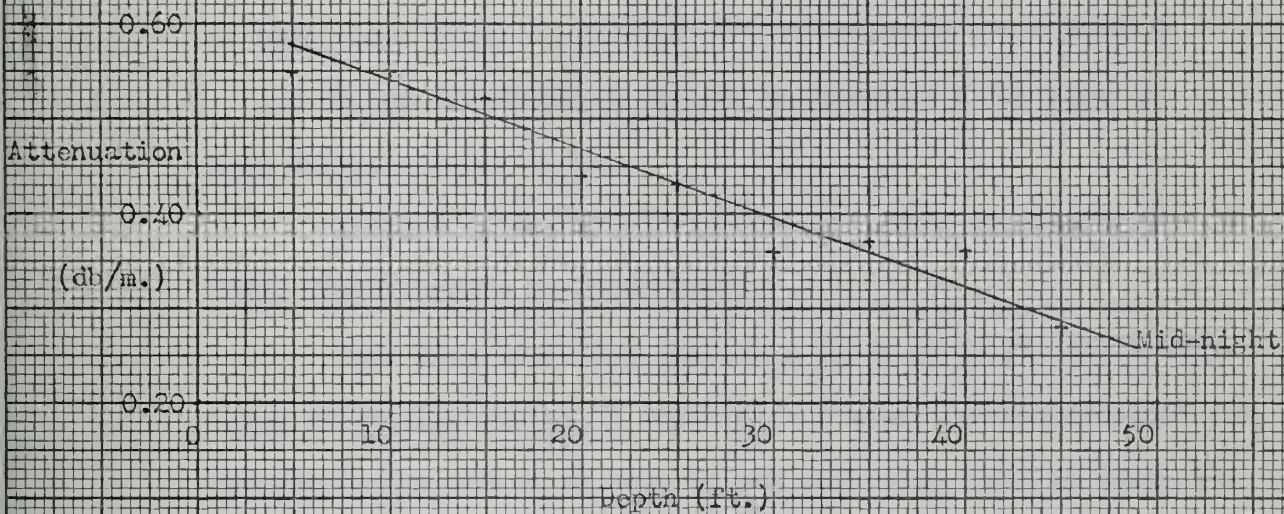


Mid-day : Transducer 24; 12 Feb., 1224 - 1253;  
Temp.,  $13.15 \pm 0.05^\circ\text{C}$ .;  
Oxygen Content  $94 \pm 2\%$  saturation.

Mid-night : Transducer 24; 16 Feb., 0028 - 0045;  
Temp.,  $13.05 \pm 0.05^\circ\text{C}$ .;  
No oxygen data available.





192 Kops.Variation with Depth.

Transducer 24 ; 16 Feb., 0006 - 0024;

Temp., 13.09  $\pm$  0.15 C.;

No oxygen data available.





surface and bottom effects. The data published in Physics of Sound in the Sea, Part 1, Transmission, measures loss over thousands of yards where the attenuation was effected by the surface and the bottom, temperature gradients and the relative depth of the transmitter and hydrophone in use.

If Fig. 14, Pl02, graph of average transmission anomalies in isothermal water is examined the attenuation of 24 Kcps is

$4.5 \text{ db/kyd} = 0.0049 \text{ db/m}$  and the attenuation at 60 Kcps is  $12.5 \text{ db/kyd} = 0.014 \text{ db/m}$ .

Similar values of attenuation are given in Kinsler and Frey, "Fundamentals of Acoustics".

From Fig. 3.12 from data at a depth of 10 ft. the average value of attenuation at 24 Kcps was 1.1 db/m. about 220 times the accepted value and at 60 Kcps it was 0.35 db/m, only 25 times the accepted figure.

Our data was obtained in an environment which would have been unsuitable for longer path transmission loss determinations because of its shallowness. If our near surface operation was made in water with many more bubbles and much more plankton than would be found in a deep water experiment abnormally high attenuations would certainly result.

The only previous work giving attenuations of the same order of magnitude is that of Hansen and Barham [9] who used tanks resonant at 7.9 Kcps in the laboratory and 2.7 Kcps in the sea to determine attenuation by measuring reverberation time. Working in "red water"





areas they found attenuations greater than the maximum measurable with their equipment, 0.405 db/m at both frequencies. Although the order of magnitude of their results agrees with ours it must be pointed out that

- a) their equipment measures absorption not scattering and absorption
- b) their equipment measured absorption for plankton, not for bubbles and plankton.

Other possible explanations of our "high" value of absorption have been considered:

- 1) Cavitation loss: This is rejected because our maximum S.P.L. was 70 db re 1  $\mu$ bar whereas cavitation would require S.P.L. of 120 db. re 1  $\mu$ bar at the surface and greater than 120 db. re 1  $\mu$ bar as depth increased.
- 2) There may have been undetected bubbles attached to our transducer or reflector. This possibility cannot be completely rejected, although the self-consistency of our data suggests that it is an unlikely explanation.



#### 4. Detection of Backscatter.

##### a. Theory.

A great deal of work has been done in the study of scatterers in a sound field. The scattering cross-sections ( $\sigma_s$ ) of small solid or liquid particles is much less than the geometrical cross-section for  $kR \ll 1$ ;

$$kR = 2\pi R/\lambda$$

where  $R$  = Radius of the scatterer.

$\lambda$  = wave length of the sound.

This represents the well known condition of Rayleigh scattering where the scattered intensity is proportional to the fourth power of the frequency.

The scattering cross-section also depends on the density and elasticity of the particle and the medium; the characteristic impedance of the scatter material ( $\rho_s c_s$ ) must be different from that of the medium for scattering to occur.

Figure 4.1 illustrates the variation of  $\sigma_s$  with  $kR$  for the two extreme cases of heavy, rigid sphere and an ideal air bubble.

When  $kR$  is greater than 2, both curves coincide and show oscillations about the mean value of unity for ratio  $\sigma_s/kR^2$ .



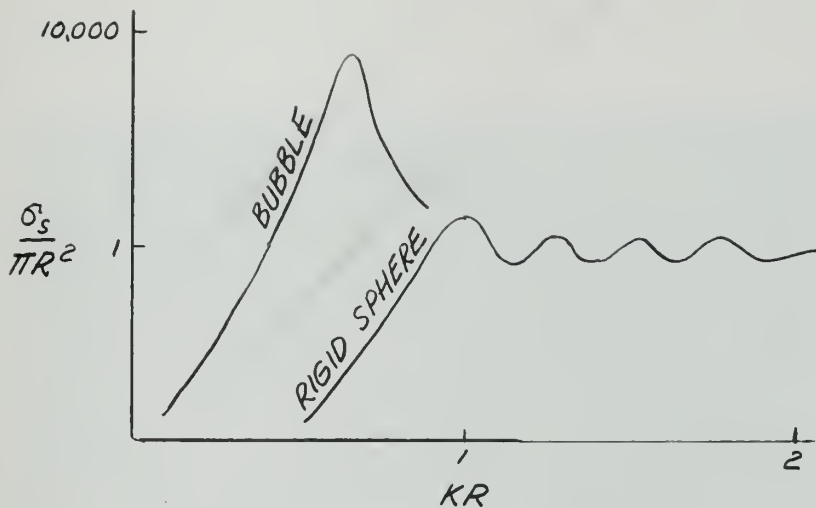


Figure 4.1  
Comparison of  
Scattering and  
Geometrical Cross-  
Sections.

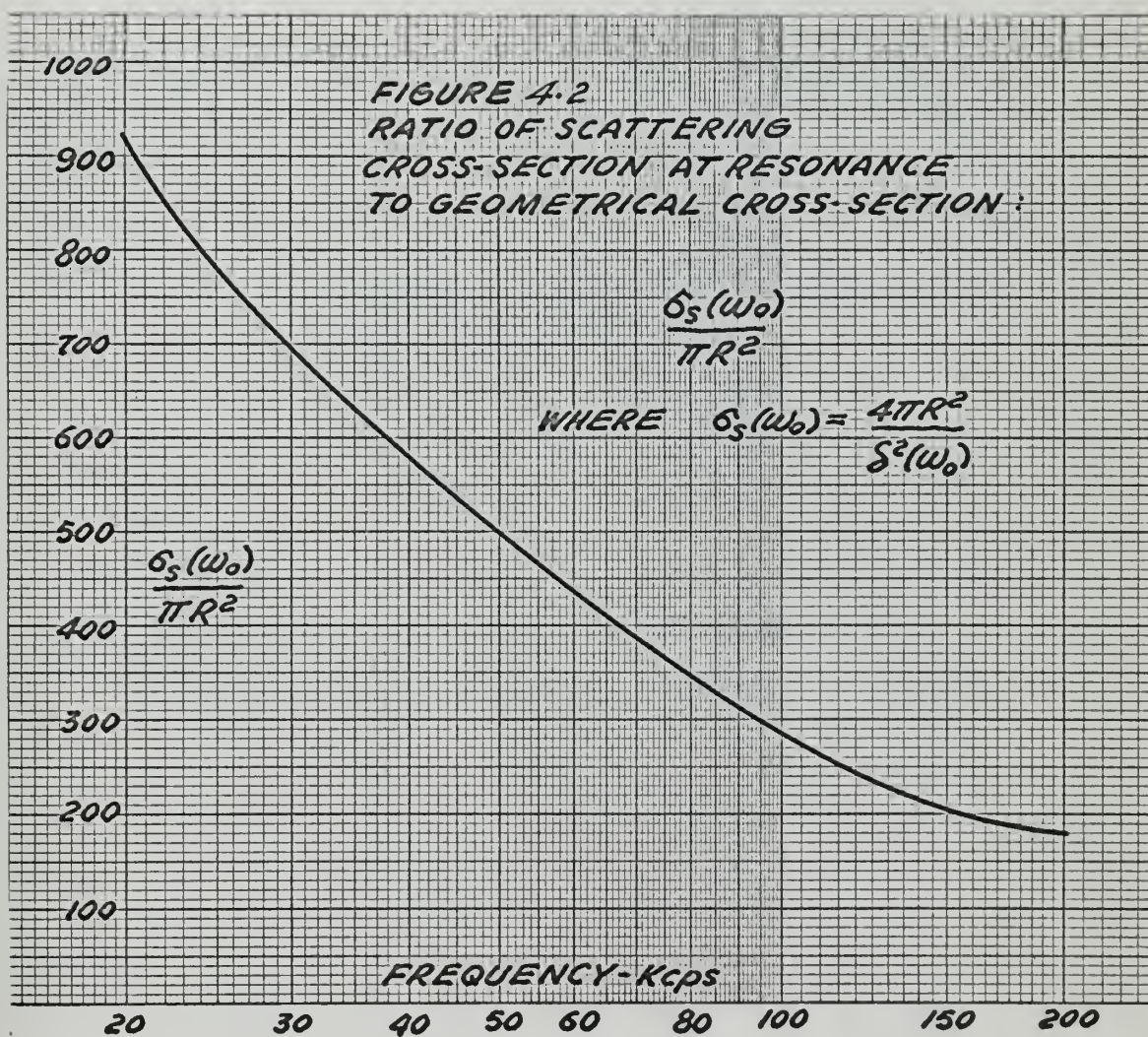
It was assumed that only those bubbles at or near resonance are the cause of any significant backscatter at any particular frequency. This is so because the  $Q$  of the bubble is of the order of 10 and the effective scattering cross-section at resonance is enormously greater than the geometrical cross-section of the bubble

$$\frac{\sigma_s(w_0)}{\text{Cross-Sectional Area}} = \frac{\frac{4\pi R^2}{S^2(w_0)}}{R^2} = \frac{4\pi}{\bar{S}^2(w_0)}$$

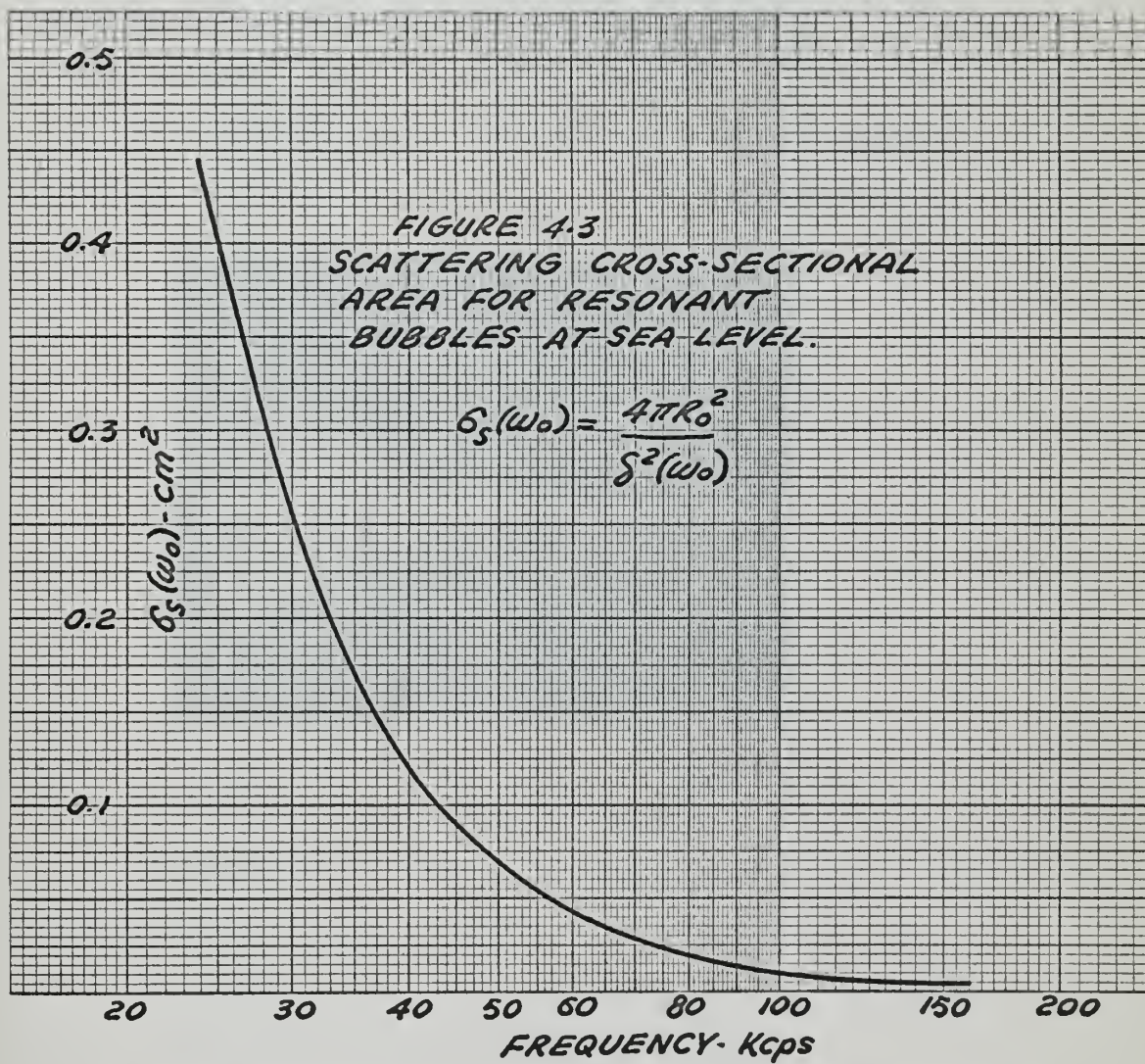
Where  $S$  is the bubble damping constant due to shear viscosity, thermal conductivity and resadiation as described by Devin [4]. This relative scattering cross-section is plotted in Figure 4.2 and varies from 918 to 178 at frequencies of 20 Kcps and 200 Kcps respectively, the frequency range of the apparatus.















$\epsilon(\omega_0)$  is given by:

$$\epsilon(\omega_0) = \frac{4\pi k_0^2}{\epsilon^2(\omega_0)}$$

A curve showing  $\epsilon(\omega_0)$  for the frequency range of interest is given in Figure 4.3.

#### b. Procedure.

The pulse-echo system gives an output which is a decaying wavetrain of echoes; a typical output is that shown in Figure 4.4.

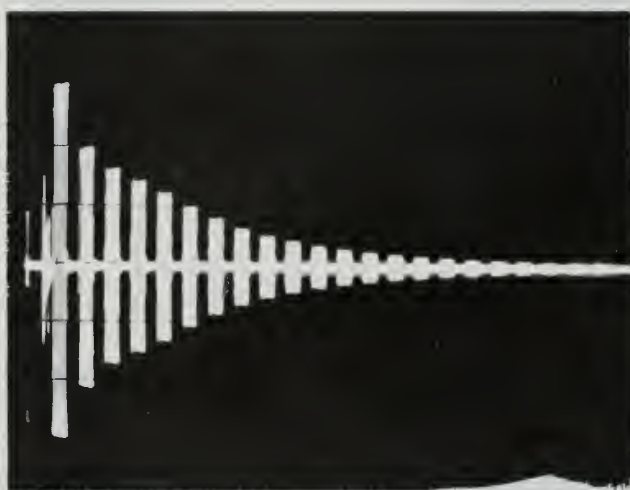


Figure 4.4  
System output at 60 kc/s

To investigate the existence of backscatter a portion of the wavetrain containing two successive echoes was expanded and observed in detail, that is beyond  $\frac{D^2}{\lambda}$  so that the field would be more nearly uniform over the entire volume.

The pattern for the amplitude of the back scattered energy from resonant bubbles was studied in the laboratory by introducing bubbles into the water, (approximately 500 bubbles of about 60









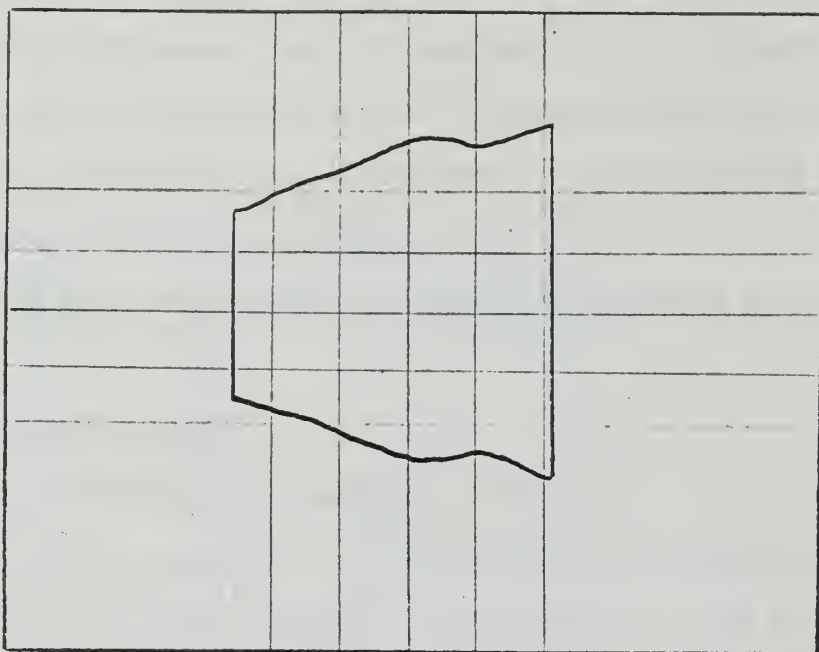


Figure 4.6  
Constructed Backscatter from Bubbles.

Figure 4.5(a) shows the region with system reverberant noise only while Figure 4.5(b) shows the increased amplitude detected when bubbles were introduced. When the noise is subtracted from the signal-plus-noise the difference is a measure of the back-scattered energy from the bubbles; this is plotted in Figure 4.6.

The photos of Figure 4.5 serves also to indicate the difficulty of extracting bubble scatter evidence in the presence of reverberant scatter from the anechoic tank walls as well as the system supports.

An experiment was conducted in the laboratory using a 1.5 inch diameter styrofoam sphere to determine the effect of scatter position on signal. The experiment showed that the signal level changed by no more than 10% as the sphere was moved throughout the volume,





thus indicating the relative uniformity of the field. For this sphere and the frequency used the resulting  $ka$  of 4 indicated that the scattering cross-section should be approximately equal to the geometrical cross-section; the experiment verified this and confirmed the validity of the technique used.

The scatterer position experiment is described in Appendix XI.

### c. Data Processing.

#### 1. Correction for Electronic Noise.

The backscatter is to be evaluated from the amplitude  $H$  of Figure 4.7. First, however, it is necessary to use the average of the reflector echos  $A$  and  $B$  (Figure 4.7) as a measure of the amplitude which would be obtained if a "perfect" reflector were at the midpoint of the system.

Hence:

$$\frac{A + B}{2} = R \approx \text{the interpolated echo level for a perfect plane reflector.}$$

In a similar manner the amplitude of  $H$  midway between the two echos can be associated with the amplitude of the scatter, that is:

$$H \rightarrow S_{st} = \text{the total scattering cross-section in the insonified volume, including the equivalent scattering cross-section of the system noise.}$$

Assuming incoherent signal and noise we have;

$$\begin{aligned} H^2 &= E_o^2 + N^2 \\ E_o &= \sqrt{H^2 - N^2} \end{aligned} \quad (4.1)$$



where  $N$  is the measured system electronic noise voltage (3.53 mv) and  $E_0$  is the scatter signal voltage.

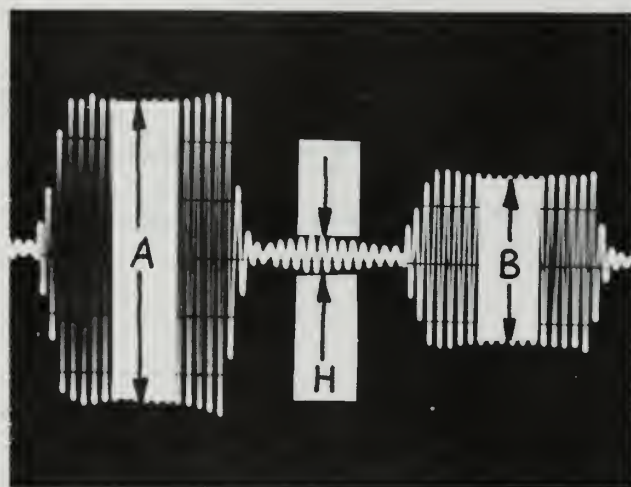


Figure 4.7 Echoes 3 and 4 at 34 Mcps

Since the area of the reflector (5) is known, the proportionality can be made:

$$\left( \frac{\text{Scattering Cross-Section within Cylinder Volume}}{\text{Reflection Area}} \right) \propto \left( \frac{\text{Scatter Signal Voltage}}{\text{Average Reflector Echo Voltage}} \right)^2$$

or  $\frac{\sigma_{st}}{V} \propto \left( \frac{E_0}{N} \right)^2$

$$\sigma_{st} \propto V \left( \frac{E_0}{N} \right)^2 \quad (4.2)$$

$\sigma_{st}$  is the total scattering cross-section of the transducer/reflector volume ( $V$ ); to normalize this to a unit volume  $\sigma_{st}$  is divided by  $V$ ;

$$\sigma_s = \frac{\sigma_{st}}{V}$$



$$S_s \propto \frac{S}{V} \left( \frac{E_0}{R} \right)^2 \quad (4.3)$$

In this investigation  $S_s$  is expressed in  $\text{Gm}^2/\text{m}^3$ .

## 2. Correction for Divergent Field.

The fact that the transducer radiation pattern changes with frequency results in the insonified volume being a variable as the frequency is changed.

Consider the situation as shown in Figure 4.8

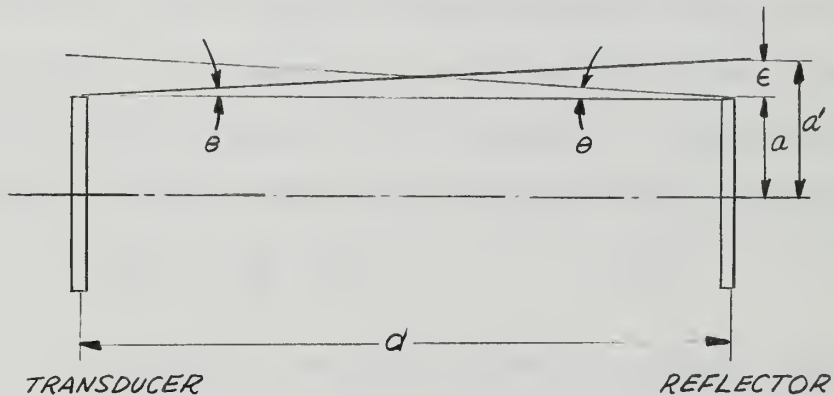


Figure 4.8. Divergent Field Situation.

A pulse leaving the transducer backscatters as it sweeps over the truncated conical volume created by the divergence angle  $\theta$  (for this experiment  $30^\circ < \theta < 90^\circ$ ). The fractional increase in volume over that of the original cylindrical volume becomes:





$$\frac{\Delta V}{V} \approx \frac{\frac{\epsilon}{2} d [2\pi(a + \frac{\epsilon}{2})]}{\pi a^2 d} = \frac{d^2 \tan \theta [2\pi(a + \frac{d}{2} \tan \theta)]}{\pi a^2 d}$$

$$\frac{\Delta V}{V} \approx \frac{\pi a d^2 \tan \theta}{\pi a^2 d}$$

$$\frac{\Delta V}{V} \approx \frac{d}{a} \tan \theta \quad (4.4)$$

The reflected pulse approaching the transducer also diverges and causes forward scatter from bubbles; the forward scatter from the cylindrical volume will be hidden in the main echo but the forward scatter from outside the cylinder will arrive later due to the longer path length and will appear between echos. This divergent region from the reflector is subtended by the same angle  $\theta$  thereby doubling the fractional volume increase:

$$\frac{\Delta V}{V} \approx \frac{2d}{a} \tan \theta \quad (4.5)$$

The ratio of effective volume to cylinder volume becomes:

$$\frac{V'}{V} = 1 + \frac{2d}{a} \tan \theta \quad (4.6)$$

The angle  $\theta$  is taken to that of the half power half beam width and is given by:

$$\theta = \sin^{-1} 0.0212\lambda \approx 0.0212\lambda \quad (4.7)$$

Because backscatter actually comes from the larger volume  $V'$  the scattering cross-section per unit volume requires a correction factor of:



$$K_1 = \sqrt{\frac{1}{\frac{V'}{V}}} = \sqrt{\frac{V}{V'}}$$

and (4.3) becomes:

$$S_s = \frac{S}{V} \left( \frac{K_1 E_0}{R} \right)^2 \quad (4.8)$$

The range of Divergent Field connection factors is given in Table 4.1 for frequencies between 20 Kcps and 60 Kcps.

Table 4.1 Divergent Field Connection Factors ( $K_1$ )

Frequency (Kcps)	$K_1$
20	0.600
30	0.676
40	0.730
50	0.764
60	0.794

### 3. Correction for Pulse Duration.

Consider the two successive pulse as in Figure 4.9

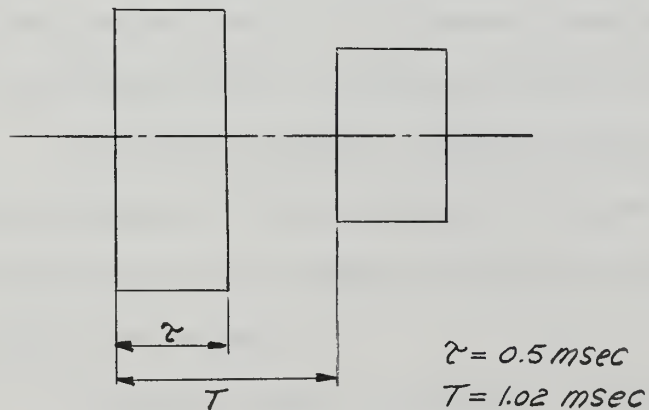


Figure 4.9 Pulse Correction Situation





During the time of the pulse ( $\tau$ ) any backscattered energy will be obscured by the much greater level of the pulse, to correct for this a comparison is made between energy levels rather than power levels, assuming that the scatter power is spread over the full time between the pulses (T.)

Then 4.8 becomes:

$$S_s = \frac{S}{V} \left( \frac{K_1 E_0}{R} \right)^2 \left( \frac{T}{\tau} \right)$$

In general for this experiment:

$$K_2 = \sqrt{\frac{T}{\tau}} = 1.43$$

$$\text{so } S_s = \frac{S}{V} \left( \frac{K_1 K_2 E_0}{R} \right)^2 \quad (4.10)$$

#### 4. Correction for Isotropic Scattering

Because the scattering from any resonant bubbles will be isotropic in nature the transducer will only intercept a portion of the spherical scatter in an amount depending on the position of the bubble within the transducer/reflector volume.

In order to obtain a correction factor for this effect it was necessary to obtain a value for the mean solid angle subtended at the transducer assuming a homogeneous distribution of bubbles within the volume.

Consider a bubble at position P in Figure 4.10.



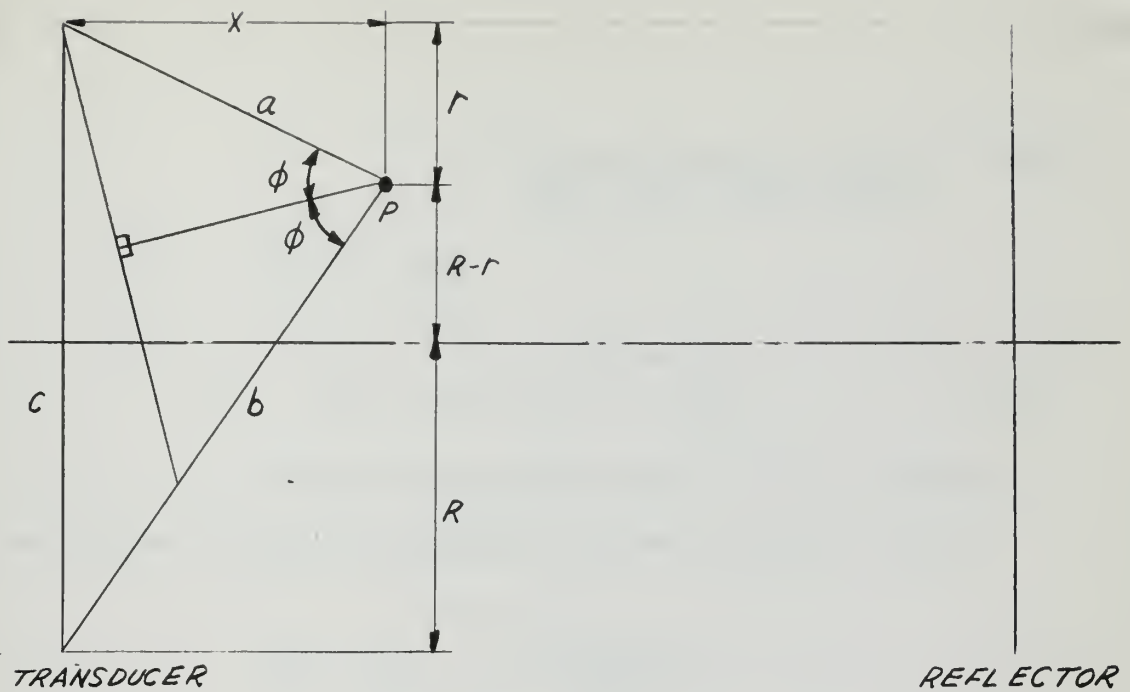


Figure 4.10  
Geometry of Isotropic Scattering Correction Factor

The solid angle  $\Omega$  is given by:

$$\Omega = 2\pi (1 - \cos\phi) \quad (4.11)$$

and

$$\cos\phi = \sqrt{\frac{1}{2} + \frac{\cos 2\phi}{2}}$$

From the Law of Cosines:

$$\cos 2\phi = \frac{a^2 + b^2 - c^2}{2ab}$$

$$\text{where: } a^2 = (R-r)^2 + X^2$$

$$c^2 = 4R^2$$

$$b^2 = X^2 + (R+r)^2$$

$$\text{hence: } \Omega = 2\pi \left(1 - \sqrt{\frac{1}{2} + \frac{\cos 2\phi}{2}}\right) \quad (4.12)$$

expanding:

$$\cos 2\phi = \frac{X^2 + r^2 - R^2}{\sqrt{r^2 X^2 - 27.2rX + X^4 + 34200 - 370r^2 + r^4 + \dots}}$$



$$\frac{1}{+27.2 rX^2 + r^2X^4 + 370 X^2} \quad (4.13)$$

$$\cos 2\phi = \frac{2B}{A}$$

$$\Omega = 2\pi \left( 1 - \sqrt{\frac{1}{2} + \frac{B}{A}} \right) \quad (4.14)$$

To find the mean solid angle  $\bar{\Omega}$  it is necessary to perform a double integration in the two variables  $r$  and  $X$ :

$$\bar{\Omega} = 2\pi \int_{r=0}^R \int_{X=0}^L \frac{\Omega r dr dx}{\pi R^2 L}$$

$$\bar{\Omega} = \frac{2}{R^2 L} \int_{R=0}^R \int_{X=0}^L \Omega r dr dX$$

Substituting the expression for  $\Omega$  :

$$\bar{\Omega} = \frac{4\pi}{R^2 L} \int_{X=0}^L \int_{r=0}^R r \left( 1 - \sqrt{\frac{1}{2} + \frac{B}{\sqrt{A}}} \right) dr dx \quad (4.15)$$

Substituting the values:  $R = 13.6$  cm

$L = 76.4$  cm





$$\bar{\Omega} = \frac{1}{1124} \int_{x=0}^{76.4} \int_{r=0}^{13.6} r \left( 1 - \sqrt{\frac{1}{2} + \frac{B}{\sqrt{A}}} \right) dr dx$$

$$\bar{\Omega} = 2\pi - \frac{1}{1124} \int_0^{76.4} \int_0^{13.6} r \sqrt{\frac{1}{2} + \frac{B}{\sqrt{A}}} dr dx \quad (4.16)$$

An approximate value was obtained for  $\bar{\Omega}$  by finding the mean value of  $\Omega$  along the axis, (for the case  $r=0$ ).

$$\text{Hence: } A \approx X^4 + 34200 + 370X^2$$

$$B \approx (X^2 R^2)^{\frac{1}{2}}$$

Substituting appropriate values gave:

$$\bar{\Omega} \approx 0.5 \pi$$

To find the total scattering cross-section per unit volume it was necessary to multiply the experimentally obtained values by  $K_3$  where

$$K_3 = \frac{\text{Total Spherical Solid Angle}}{\bar{\Omega}} = \frac{4\pi}{0.5\pi} = 8$$

##### 5. Tank Calibration for Reverberation.

For various data runs  $S_g$  can be calculated and plotted as a function of frequency. In general, however, there was an unknown amount of interference due to the transducer support structure. An attempt to correct for this a number of calibration runs were made in the USNPGS anechoic tank. It was found that most of the reverberant level measured in the anechoic tank was due to scattering from the tank itself. Orientation of the transducer-reflector had a substantial effect on background and so the curve of background reverberation obtained in the "calibration" over-



corrects. The magnitude of the correction curve was considerably less than the signal levels and any correction was less than 10%.

#### 6. Summary of Corrections for Backscatter Analysis.

Combining all the correction factors (4.10) becomes:

$$S_s = \frac{S}{V} K_3 \left( \frac{K_1 K_2 E_0}{R} \right)$$

$$\text{finally: } S_s = \frac{S}{V} \left( \frac{K E_0}{R} \right) \quad (4.18)$$

$$\text{where } K = K_1 K_2 \sqrt{K_3}$$

Values for K over the frequency range 20-60 Kcps are given in Table 4.2.

Table 4.2 Total Correction Factor (K).

Frequency (Kcps)	K
20	2.42
30	2.73
40	2.95
50	3.09
60	3.21

It must be conceded that the number and magnitude of the corrections that have been discussed above lend uncertainty to the final calculation of scattering cross-section per unit volume. The writer feels that the final correction itself may be in error by a factor perhaps as great as two. This error factor will reflect in all values of scattering cross-sections which follow.

#### d. Analysis of Data

An analysis is now carried out assuming that the scattering cross-sections obtained were due only to the presence of bubbles; this permits calculation of the maximum bubble density and volume concentration for any particular datum.





corrects. The magnitude of the correction curve was considerably less than the signal levels and any correction was less than 10%.

#### 6. Summary of Corrections for Backscatter Analysis.

Combining all the correction factors (4.10) becomes:

$$S_s = \frac{S_{K3}}{V} \left( \frac{K_1 K_2 E_0}{R} \right)$$

$$\text{finally: } S_s = \frac{S}{V} \left( \frac{K E_0}{R} \right) \quad (4.18)$$

$$\text{where } K = K_1 K_2 \sqrt{K_3}$$

Values for K over the frequency range 20-60 Kcps are given in Table 4.2.

Table 4.2 Total Correction Factor (K).

Frequency (Kcps)	K
20	2.42
30	2.73
40	2.95
50	3.09
60	3.21

It must be conceded that the number and magnitude of the corrections that have been discussed above lend uncertainty to the final calculation of scattering cross-section per unit volume. The writer feels that the final correction itself may be in error by a factor perhaps as great as two. This error factor will reflect in all values of scattering cross-sections which follow.

#### d. Analysis of Data

An analysis is now carried out assuming that the scattering cross-sections obtained were due only to the presence of bubbles; this permits calculation of the maximum bubble density and volume concentration for any particular datum.



From classical theory [22], the total scattering cross-section per unit volume is given by:

$$S_s = \int_0^{\infty} \frac{4 R^2 n(R) dR}{\left[\left(\frac{W_0}{W}\right)^2 - 1\right]^2 + \delta^2} \quad (4.19)$$

Where  $n(R)dR$  is the number of bubbles per unit volume which have a radius between  $R$  and  $R+dr$ .

An approximate evaluation of  $S_s$  is carried out by substituting the small quantity.

$$R = \frac{W_0}{W} - 1 = \frac{R}{R_0} - 1 \text{ and } dR = \frac{dR}{R_0}$$

and integrating:

$$S_s \approx 4\pi R_0^3 n(R) \int_{-R}^R \frac{(1 - \frac{R}{R_0})^2 dR}{\left[\left(\frac{R}{R_0} - 1\right)^2 + \delta^2\right]} \quad (4.20)$$

The integrand is simplified by dropping higher order terms of the small quantity  $R$  so that we need only consider:

$$\int_{-R}^R \frac{dR}{4R^2 + \delta^2} \approx \frac{1}{\delta} \tan^{-1} \frac{2R}{\delta} = A \quad (4.21)$$

if we assume  $\delta \approx 0.1$

then  $A \approx 10 \tan^{-1} 20R$

$$A_{\max} = 15.7$$

if we let  $R = 0.05$

$$A \approx 7.83$$

$$\text{and } \frac{A}{A_{\max}} = \frac{7.83}{15.7} \approx 0.50$$



In other words, the bubbles within 5% of the resonant size will cause 50% of the observed scattering cross-section per unit volume ( $S_s$ ).

The 5% bandwidth was used in the determination of the number of bubbles per unit volume with radii between  $r$  and  $r + dr$  (hereafter called "bubble density" =  $n(R)dr$ ) and the ratio of bubble air volume to water volume (hereafter called "bubble volume concentration" =  $U(R)dr$ ).

The bubble density over any of the 5% increments of frequency is:

$$n(r)dr = \frac{\frac{S_s}{2}}{\delta(W_0)} \quad (4.22)$$

where  $\delta_s(W_0)$  is the resonant scattering cross-section of a single bubble as shown in Figure 4.3.

$$\delta_s(W_0) = \frac{4\pi R_0^2}{\delta^2}$$

Hence

$$n(R)dr = \frac{\delta_s \delta^2}{8\pi R_0^2} \quad (4.23)$$

The bubble volume concentration over the same frequency increment is:

$$U(R)dr = \frac{4}{3}\pi R_0^3 n(R)dr \quad (4.24)$$

Data was taken in San Diego Bay using the USN-NEL oceanographic Research Tower as an equipment platform and in Monterey Bay using the USNPGS Hydrographic Research Vessel.





The variables considered in gathering the scattering data were: depth, frequency, time, day/night comparison and sea state. It was found that the system was frequency limited to a range of 20 Kcps to 60 Kcps when using this technique; the oscillator had a lower limit of  $\sim 20$  Kcps and above 60 Kcps the signal to noise ratio deteriorated to a point of unusability.

Most of the data were gathered at a depth of 10 feet which seemed to be the optimum depth for scatter detection without being influenced by wave action and surface effects.

In measuring the signal level it was found that there were interference or reverberation effects associated with the configuration of the apparatus; this is discussed in Section 4.E.

The interference resulted in a standing wave type pattern being superimposed on the signal due to scattering; because of this the measuring technique used was to find and measure all the signal maxima and minima as frequency was varied; when all the points were plotted against frequency a smoothing technique was used to approximate the signal due to scattering alone. Examples of the field data and related "smooth" curve are shown in Figure 4.11.

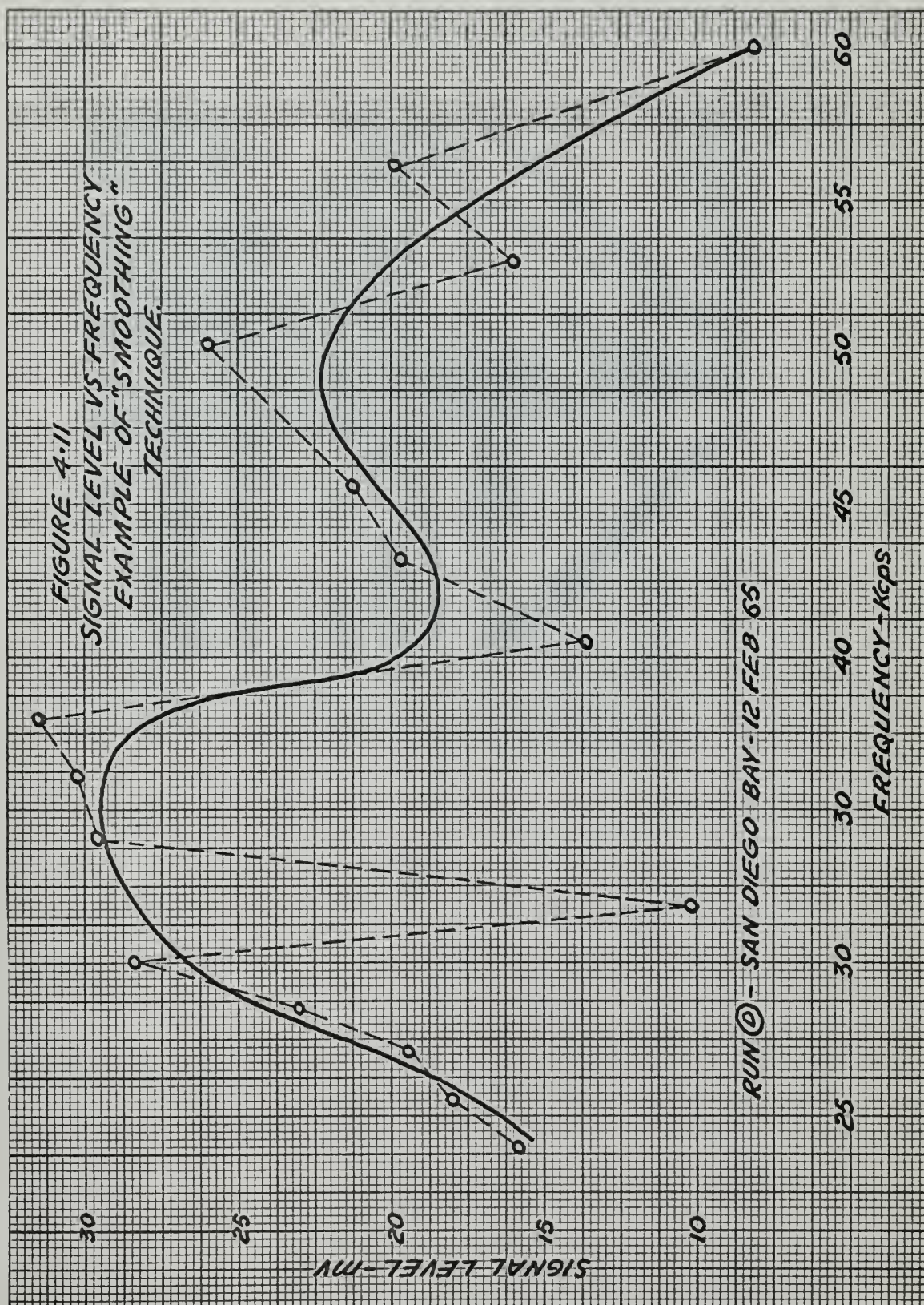
The "smooth" curve is used as the basis for subsequent curves.

#### e. Interference Problems.

All the data gathered from the NEL Oceanographic Research Tower suffered from spurious scattered radiation. Leaks of interference were spaced at about 5 Kcps intervals; this indicated the possibility of an interfering source about 1 foot from the















... and ... in the ...  
 tank ... , ...  
 previously ... , ...  
 utilized ...  
 manufactured and ... in Figure 4.13.

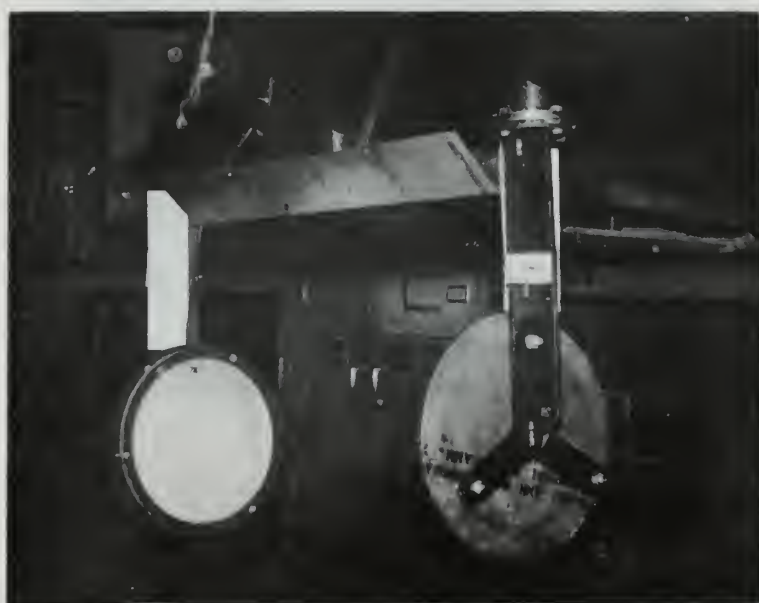


Figure 4.13 Apparatus with Reflectors in Place

There was no appreciable improvement with the addition of the horse hair ... as it was concluded that the interference was in part at least from the tank itself; further investigation confirmed this and it became apparent that the signal depended a great deal ... of the ... of the ...  
 this and all other ... were ...  
 uencies; evidence of ... interference from the ...



in Figure 4.14.

The arrow in Figure 4.14 indicates an echo from the tank walls coming in after the desired echo train and attenuated.

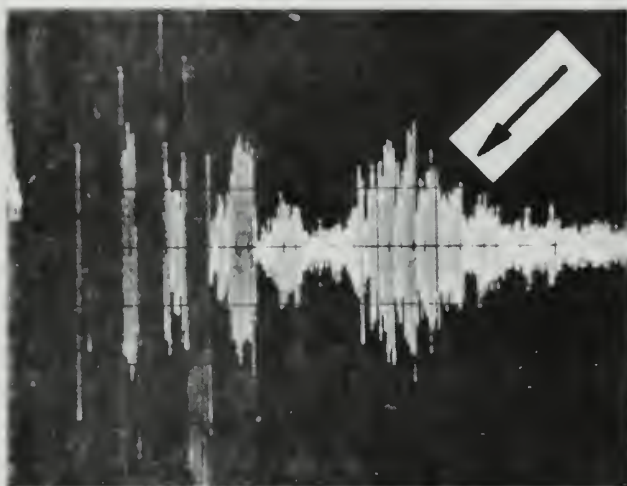


Figure 4.14 Tank interference at 10.5 kc/s

Since the interference could not be eliminated the max/min-smoothing technique described in section 4.5 was adopted as the best way to cope with the problem.

#### f. results.

Signal voltages for five frequency runs are plotted in Figures 4.15 to 4.17 and the resulting scattering cross-sections are plotted in Figures 4.18 to 4.20.

From these two sets of curves it can be generally concluded that a higher scattering cross-section results from a higher sea state and that the scattering level is greater at night up to about 46 kc/s, beyond which the day scattering level is the greater. The





latter observation might be explainable by phytoplankton photosynthesis during the day with emission of the smaller bubbles which coalesce after dark, decreasing the number of small bubbles and increasing the number of large bubbles which rise during the night and disappear with daylight again; there might also be a vertical movement of bubbles fixed to plankton during the night.

A 24 hour observation at 40Kcps (Figure 4.21) with readings every hour confirmed the increased scattering activity during the dark hours at this frequency; the scattering level rose sharply between 2000 and 0800 hours.

Assuming that the scattering is due solely to bubbles the "bubble" density curves for runs A to E are plotted in Figure 4.22 to 4.24. In all cases the density distributions peak between 38 Kcps and 47 Kcps; this is in general agreement with the work done by Glotov, Kolobaev and Neumim [6] in which it was observed that the distribution of wind-initiated bubbles peaked at 45 Kcps. The comparison may even be better when one considers that the Glotov experiment was done in a tank with "clean" sea water whereas the investigation of this paper concerns bubbles in the ocean which may be attached to particulate matter which would tend to increase the bubble mass, reducing the resonant frequency and shifting the distribution peak to a lower frequency.

There is approximately a 4:1 ratio between the highest and lowest density peaks observed.

The corresponding "bubble" volume concentration for runs A to E are shown in Figures 4.25 to 4.27.



A number of runs (F to L) were conducted to determine the variation of back-scatter with depth. Figures 4.28 and 4.29 show comparative day/night data at 40 Kcps; in general there is a drop-off with increasing depth. The drop-off at night is less pronounced and the night scatter is less near the surface. At 50 Kcps however (Figure 4.30) the night scatter level is greater than the day level at all depths and in both cases the level is essentially unchanged with depth indicating that bubbles of this size (radius = 64 microns) are more evenly distributed in the medium than the 40 Kcps bubbles (radius = 80 microns) which are more concentrated near the surface.

The depth run in Monterey Bay (Figure 4.31) indicated that there was little change in the scattering level to a depth of 56 feet at a frequency of 35.7 Kcps. However, there was no data between the surface and 10 feet where the level was probably higher. Another reason for the apparent lack of scattering drop off with depth is the fact that these data were taken in a condition of sea state 1 whereas most of the previous data were for sea state 2 conditions in which it would be expected that there would be more activity near the surface, particularly at such a low frequency.

Referring to the total scattering cross-sections per unit volume as plotted in Figures 4.18 to 4.20 the mean attenuation due to the "bubbles-only" assumption is approximately 1.0 db per meter in the frequency range 30 to 60 Kcps; this figure is obtained by using the expression [22] ;

$$a = 4.34 \left( \frac{\delta}{\delta_r} \right) S_s \quad \text{db/meter}$$





(A) x SAN DIEGO BAY-15 FEB 65 @ 1412-1453 SEA STATE 2  
 (B) o SAN DIEGO BAY-15 FEB 65 @ 2106-2200

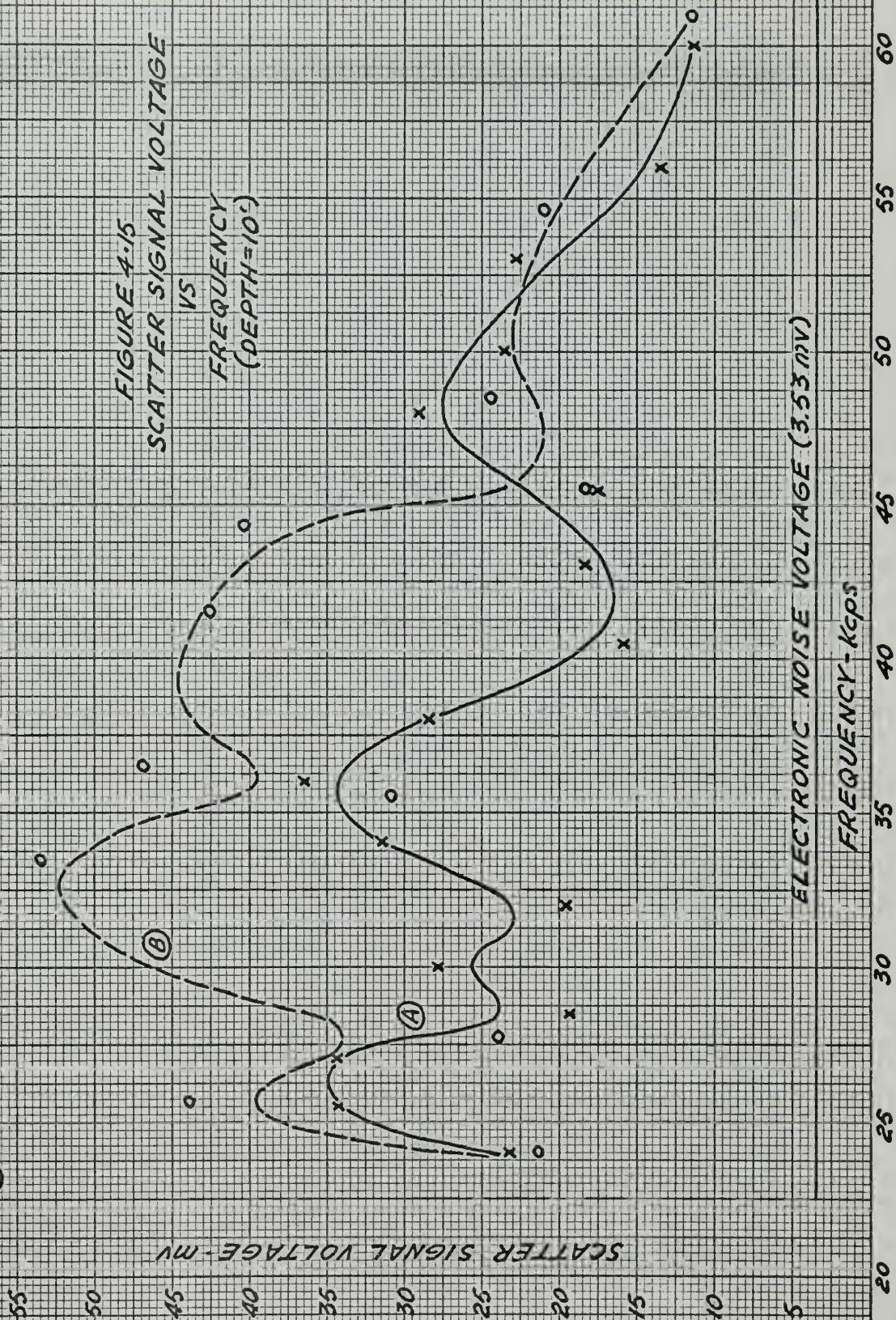
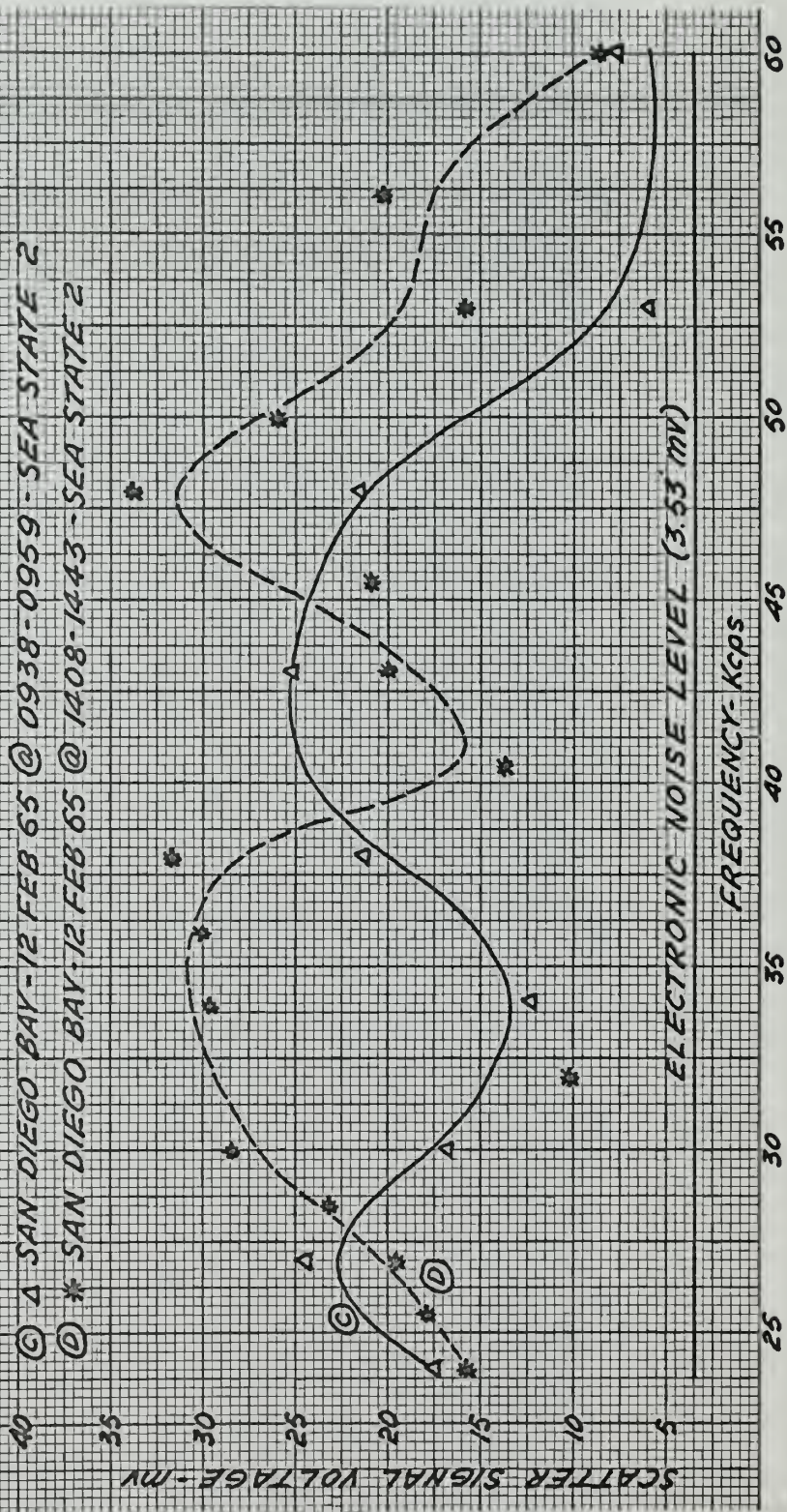




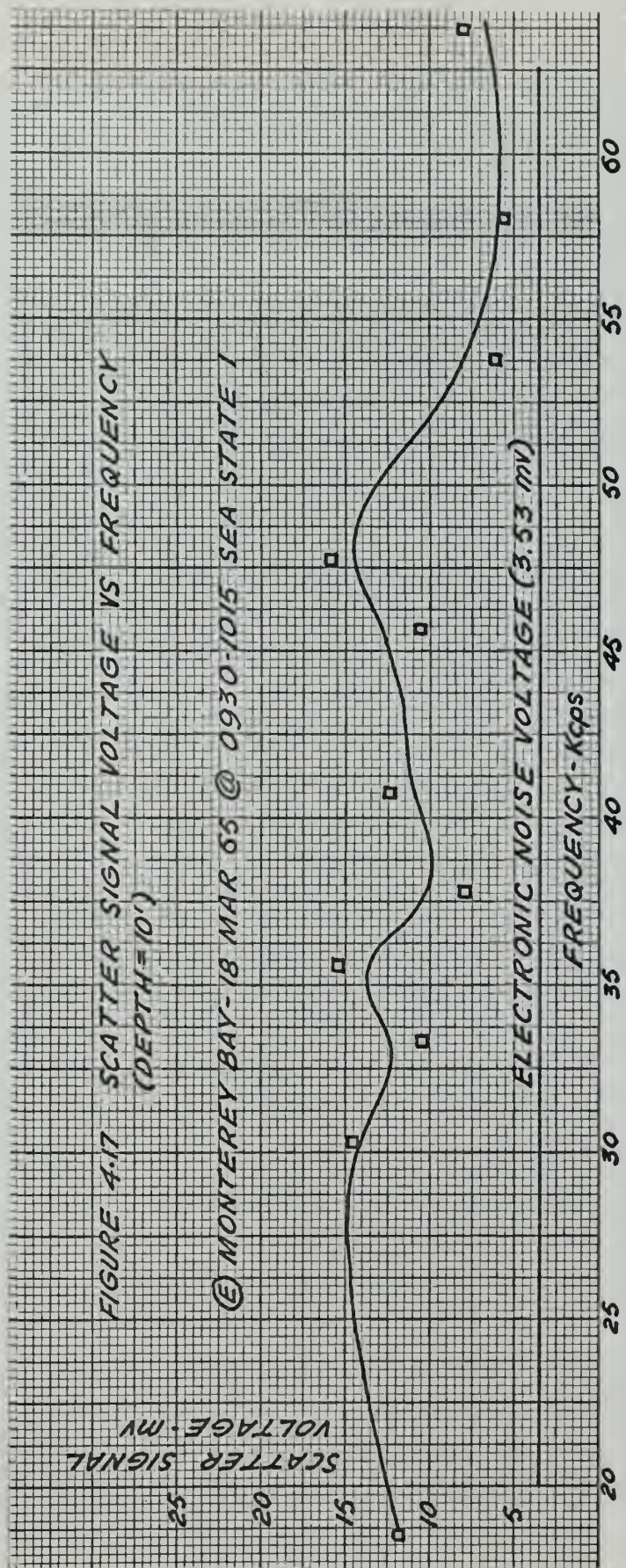


FIGURE 4-16 SCATTER SIGNAL VOLTAGE VS FREQUENCY  
(DEPTH=10')



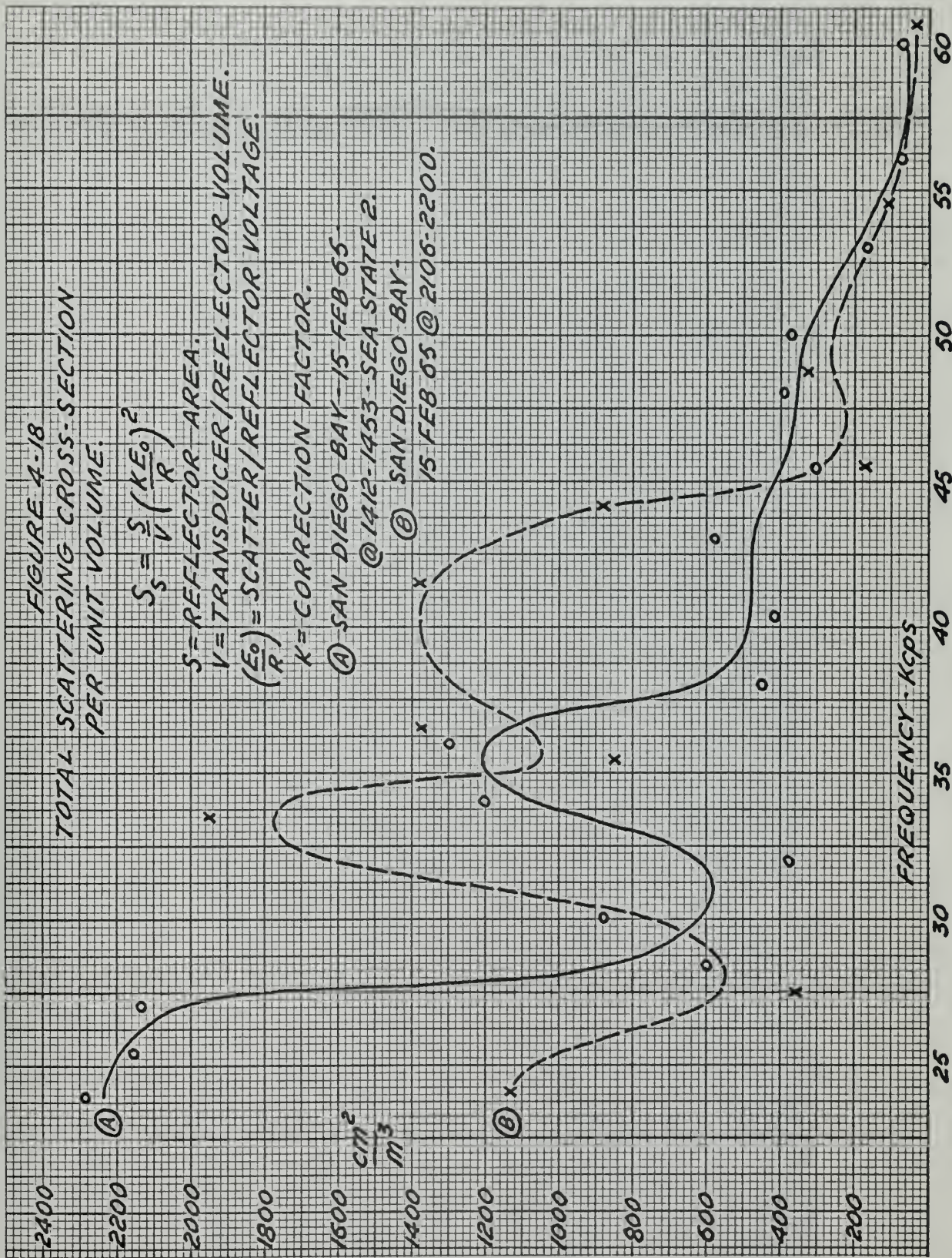






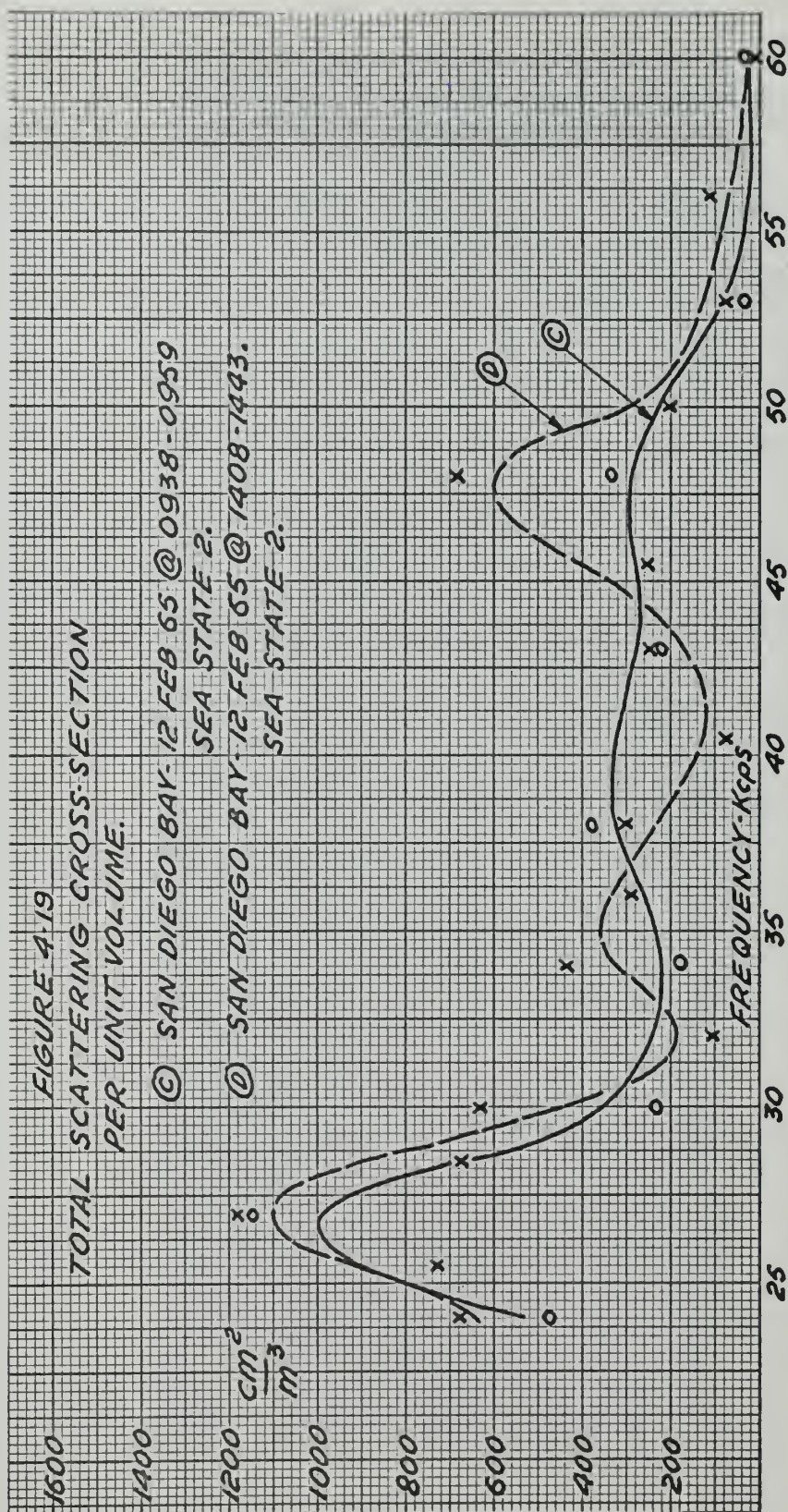
















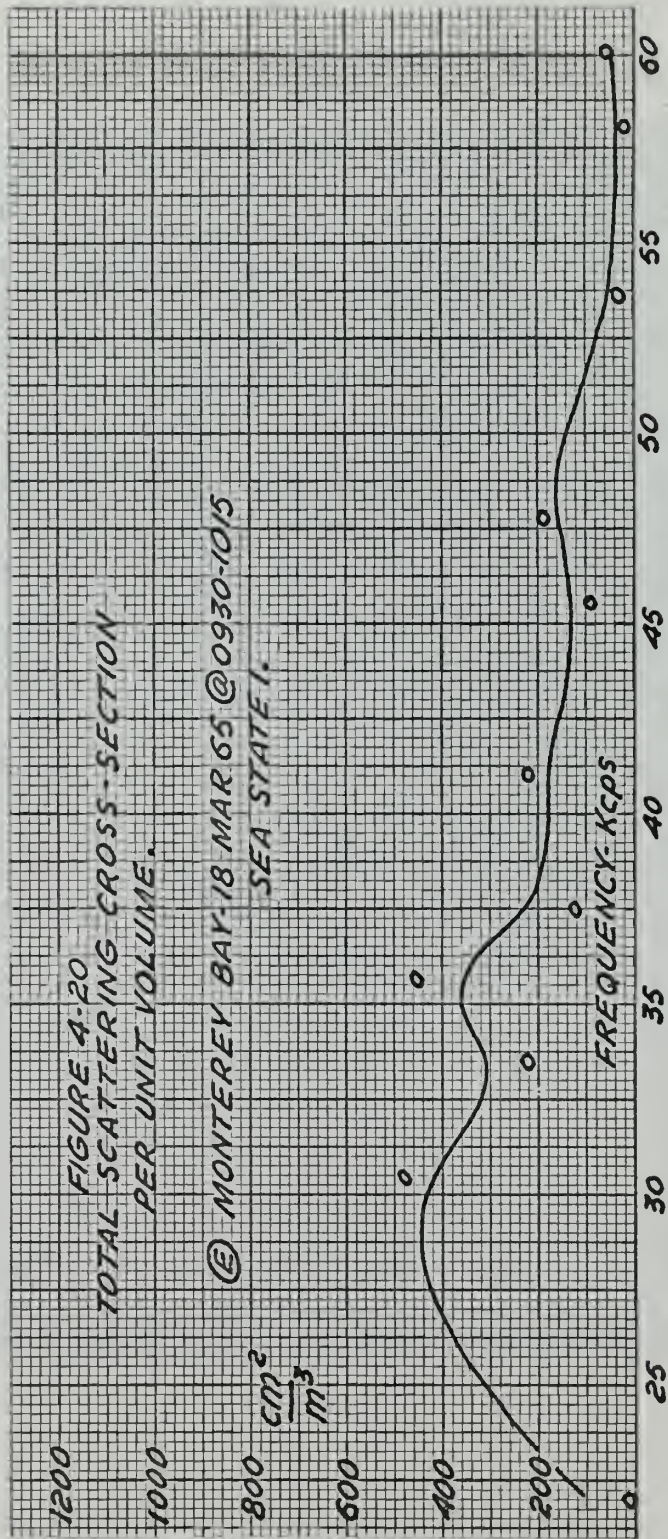
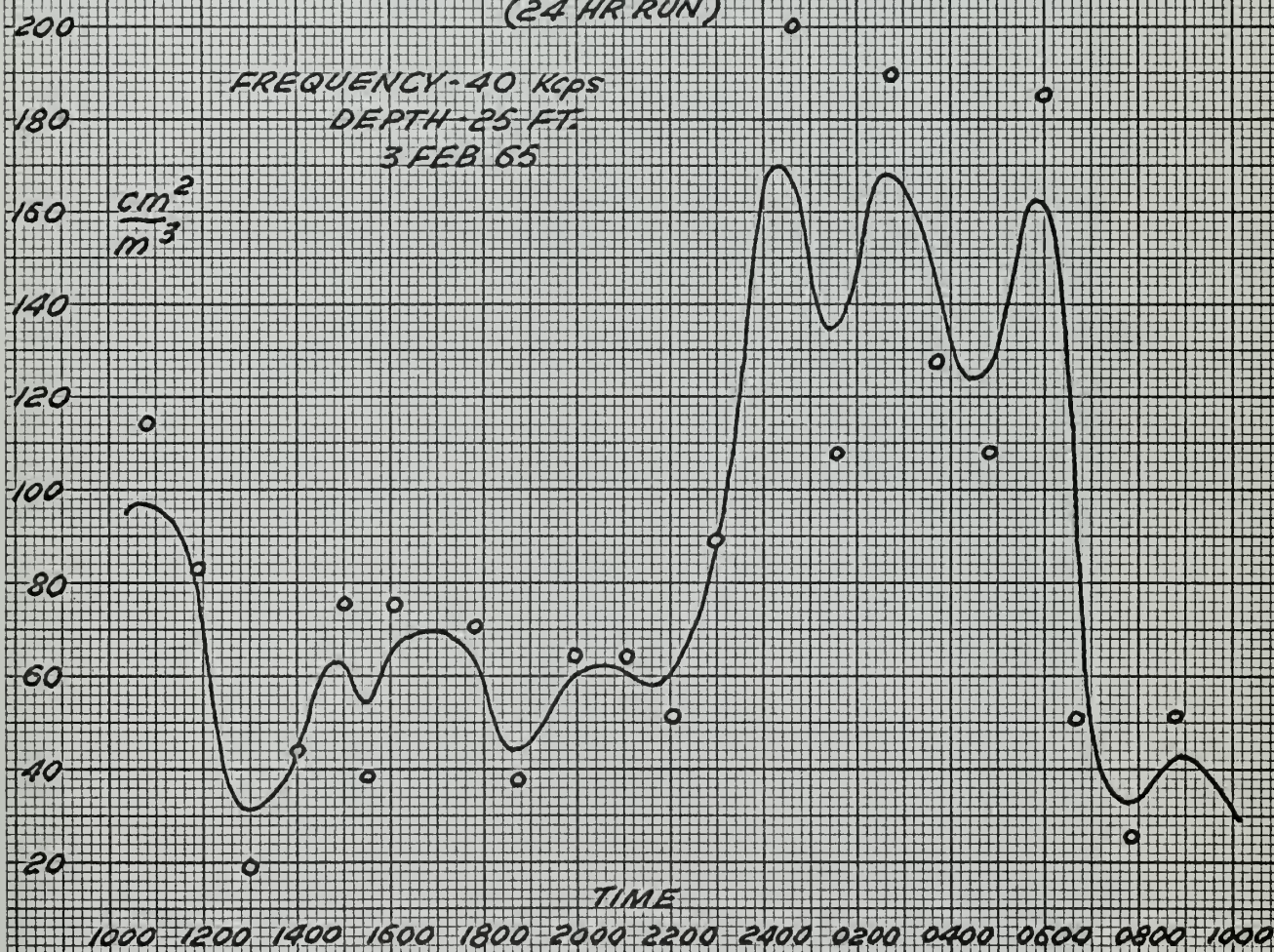




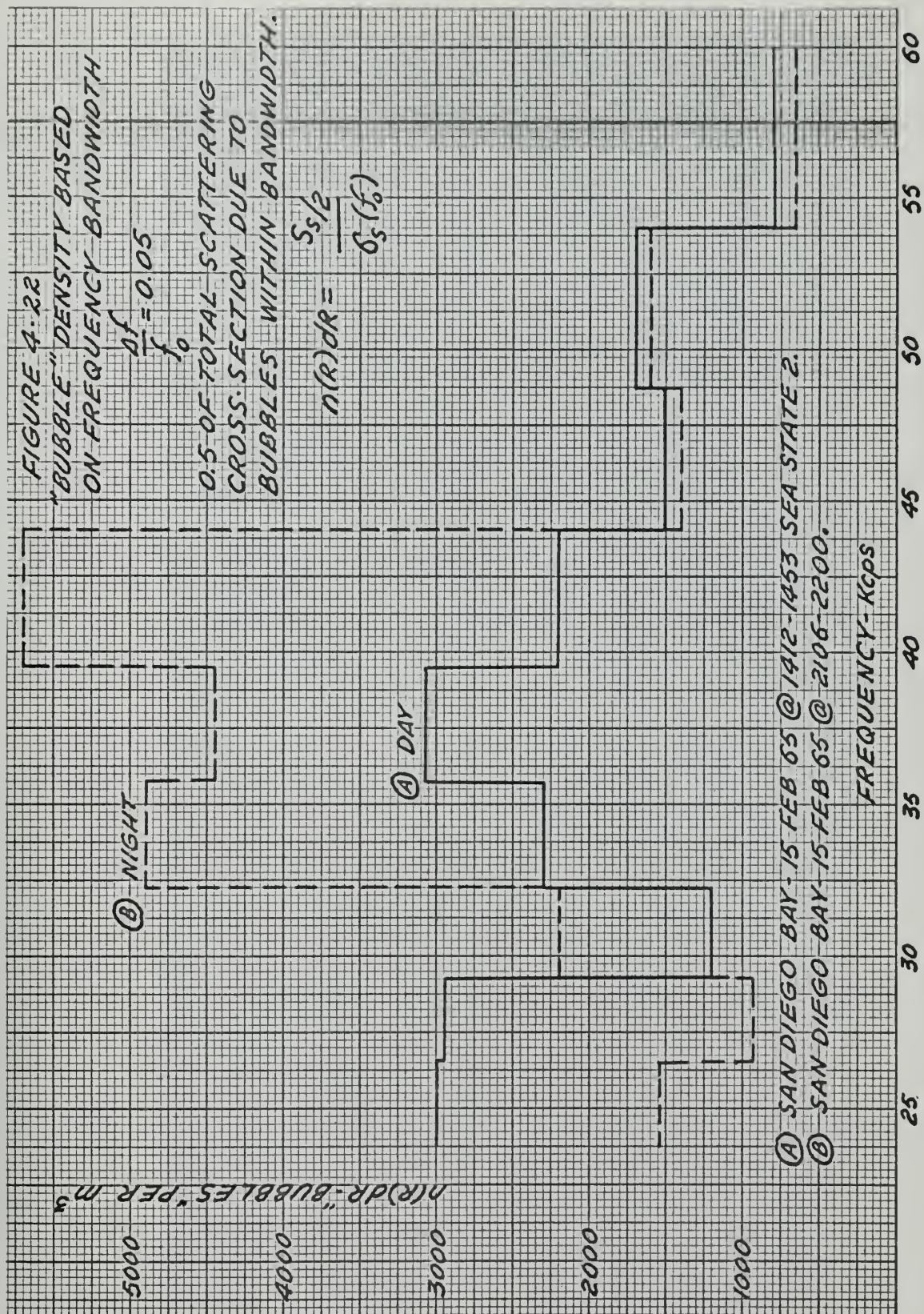


FIGURE 4-21  
SCATTERING CROSS-SECTION  
VS  
TIME  
(24 HR RUN)



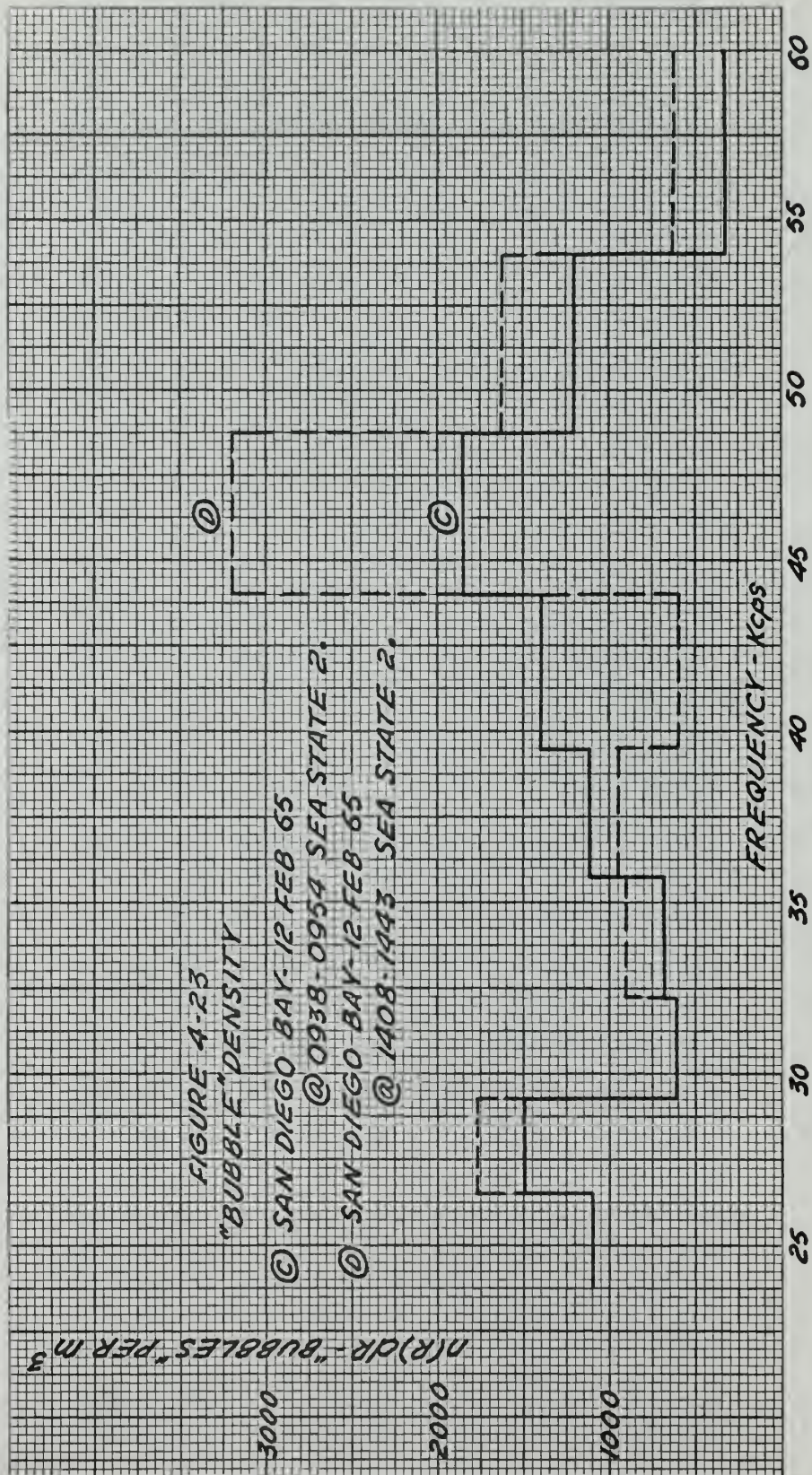






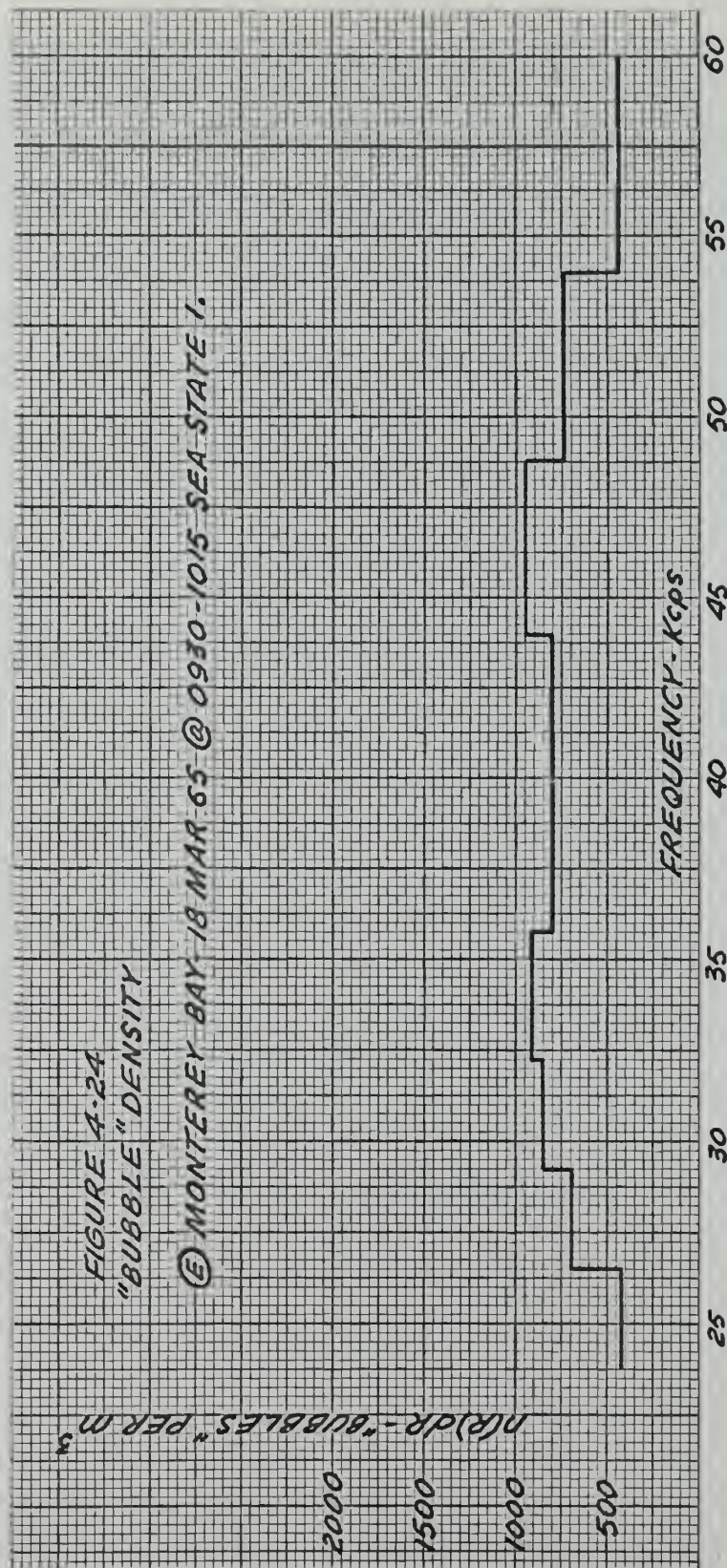






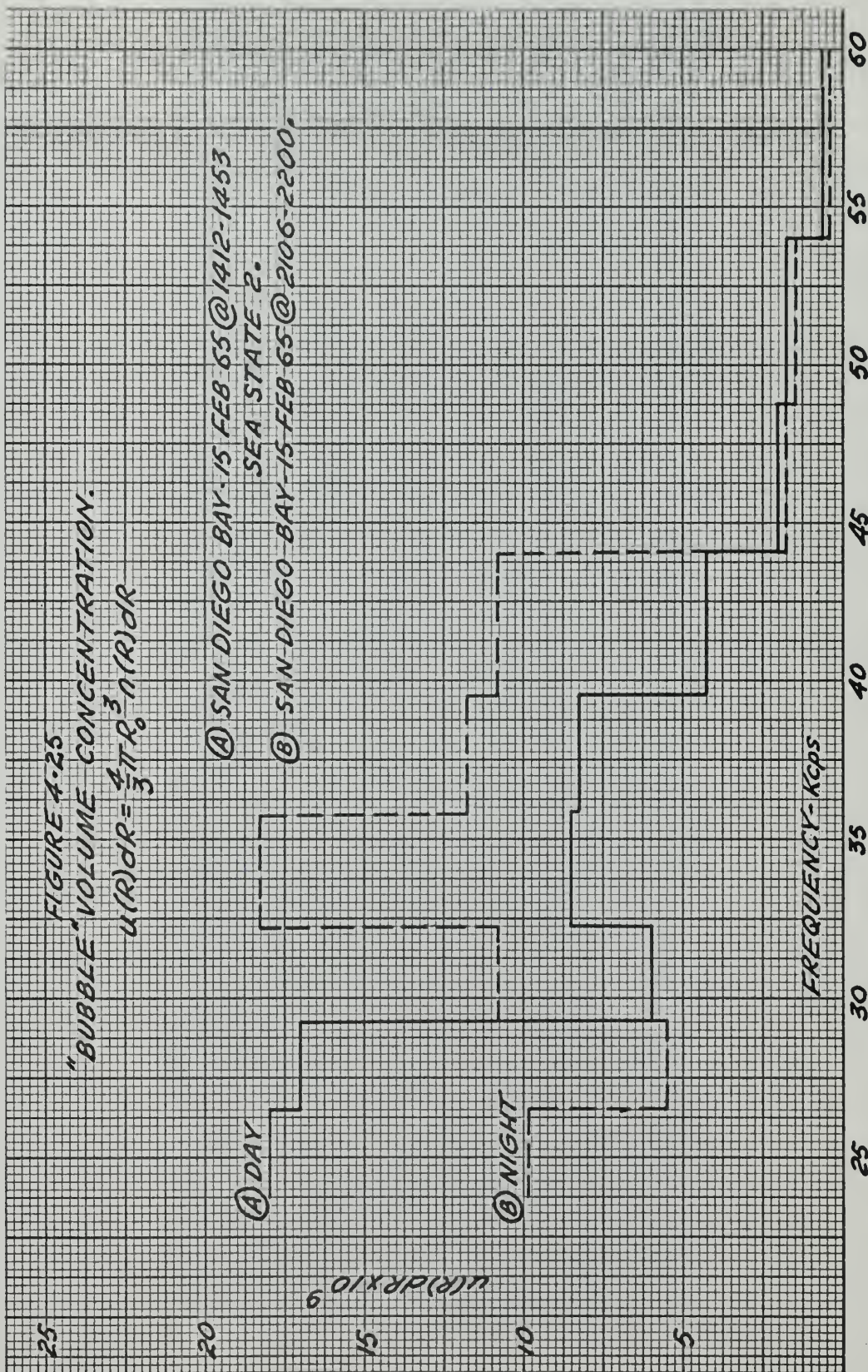






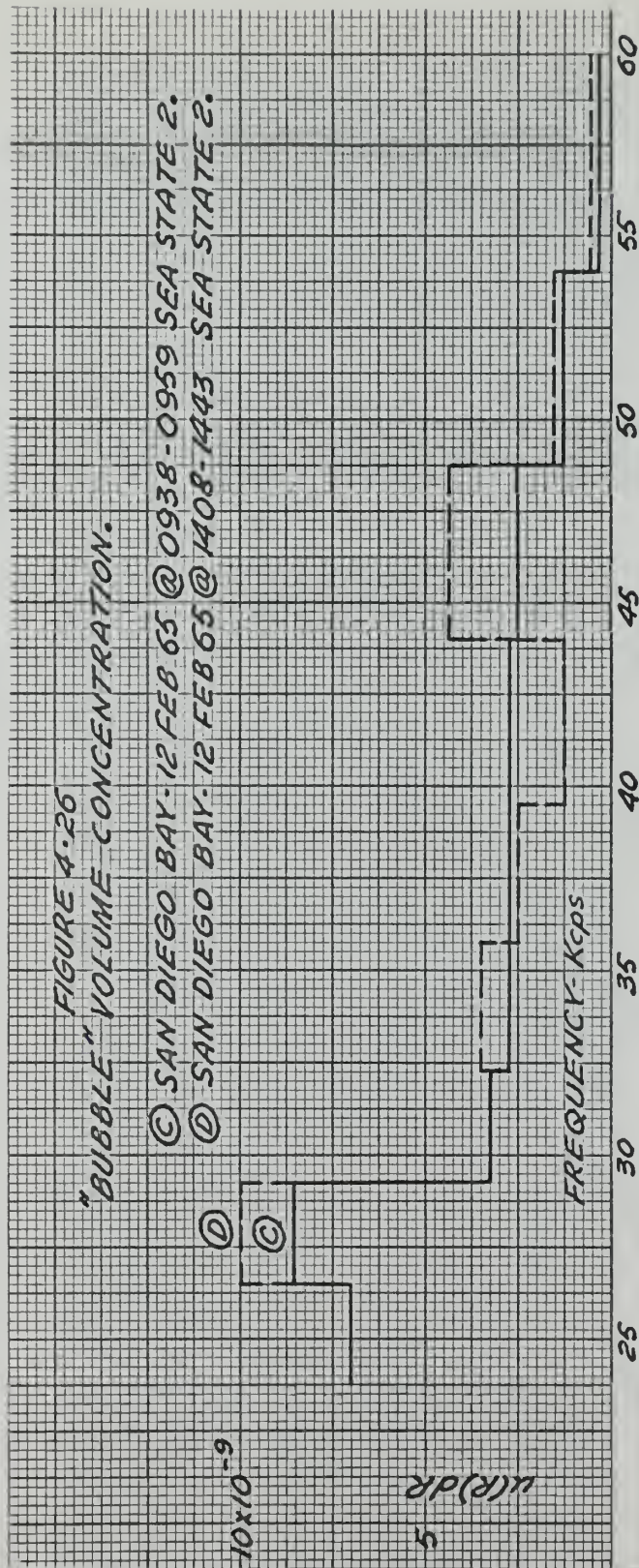




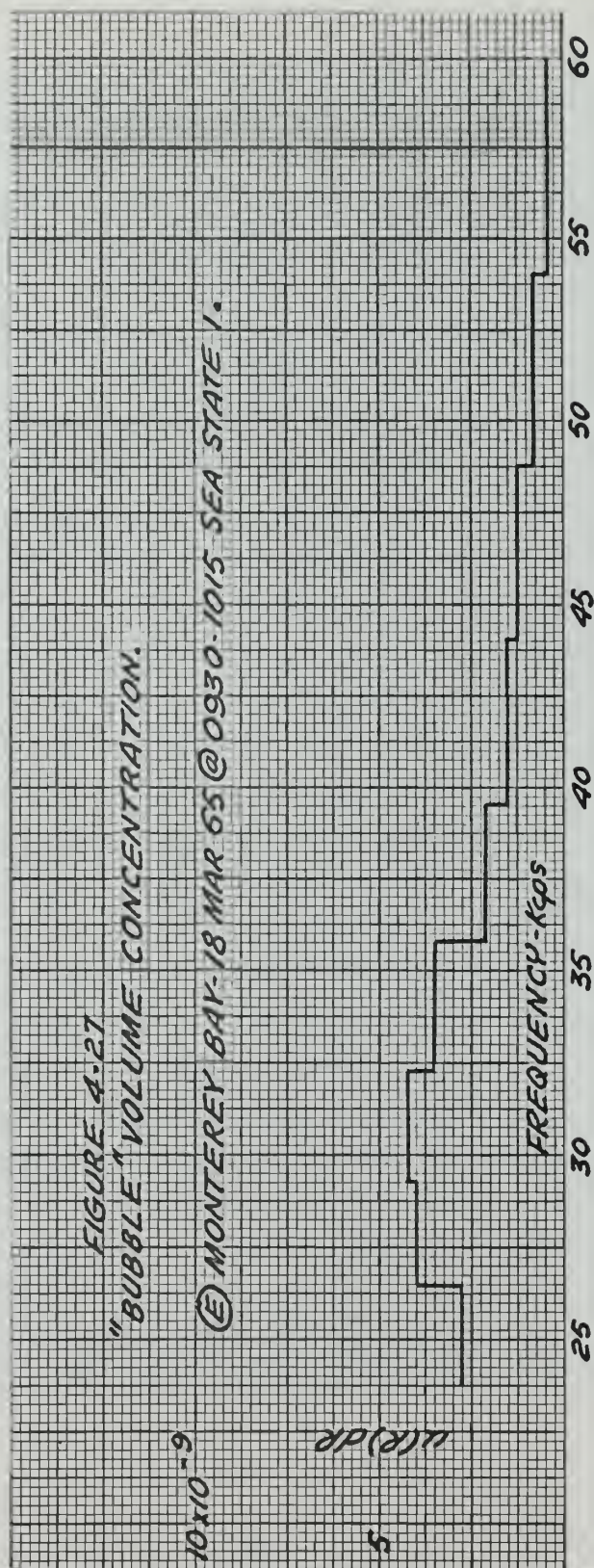








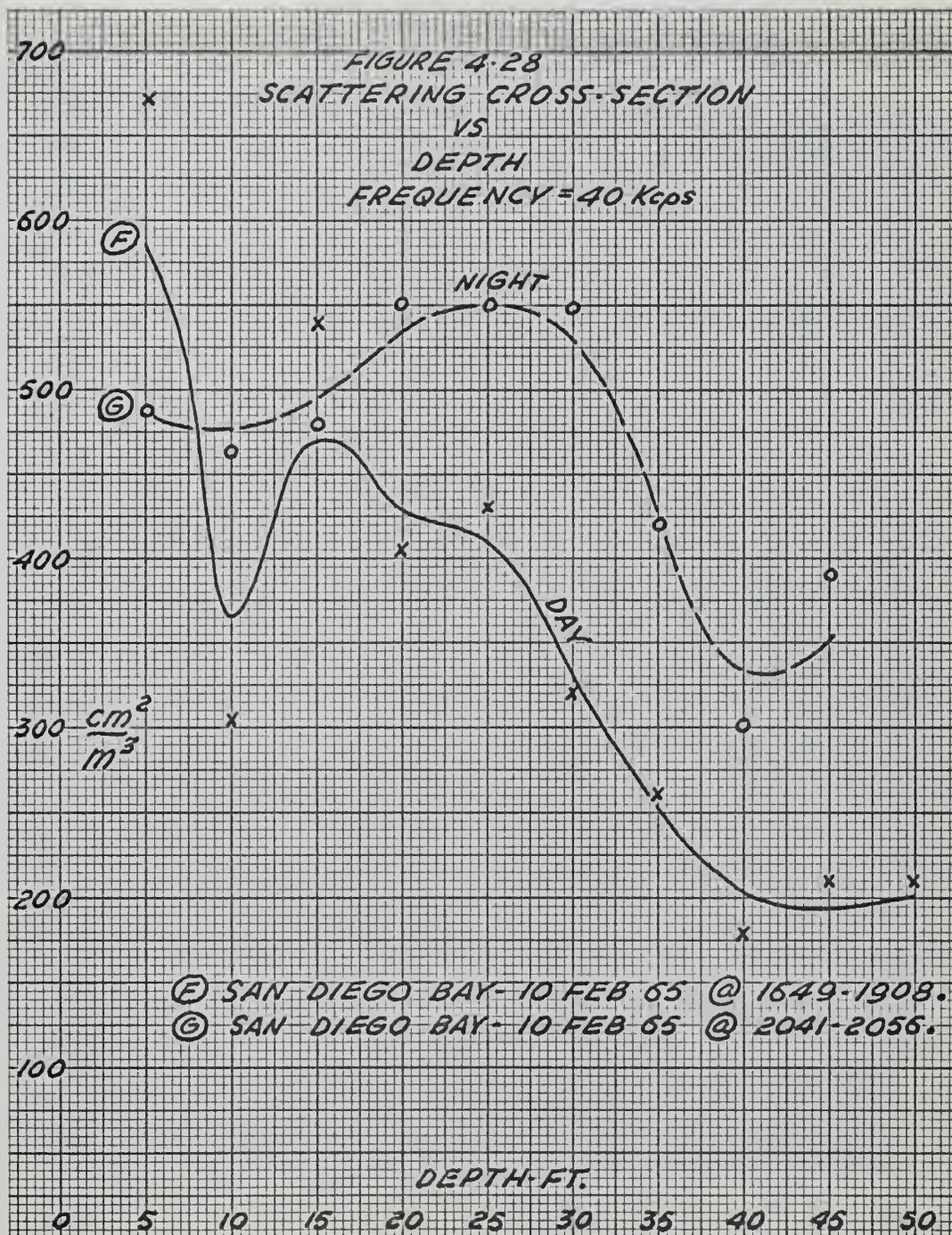




(E) MONTEREY BAY-18 MAR 65 @ 0930-1015 SEA STATE 1.

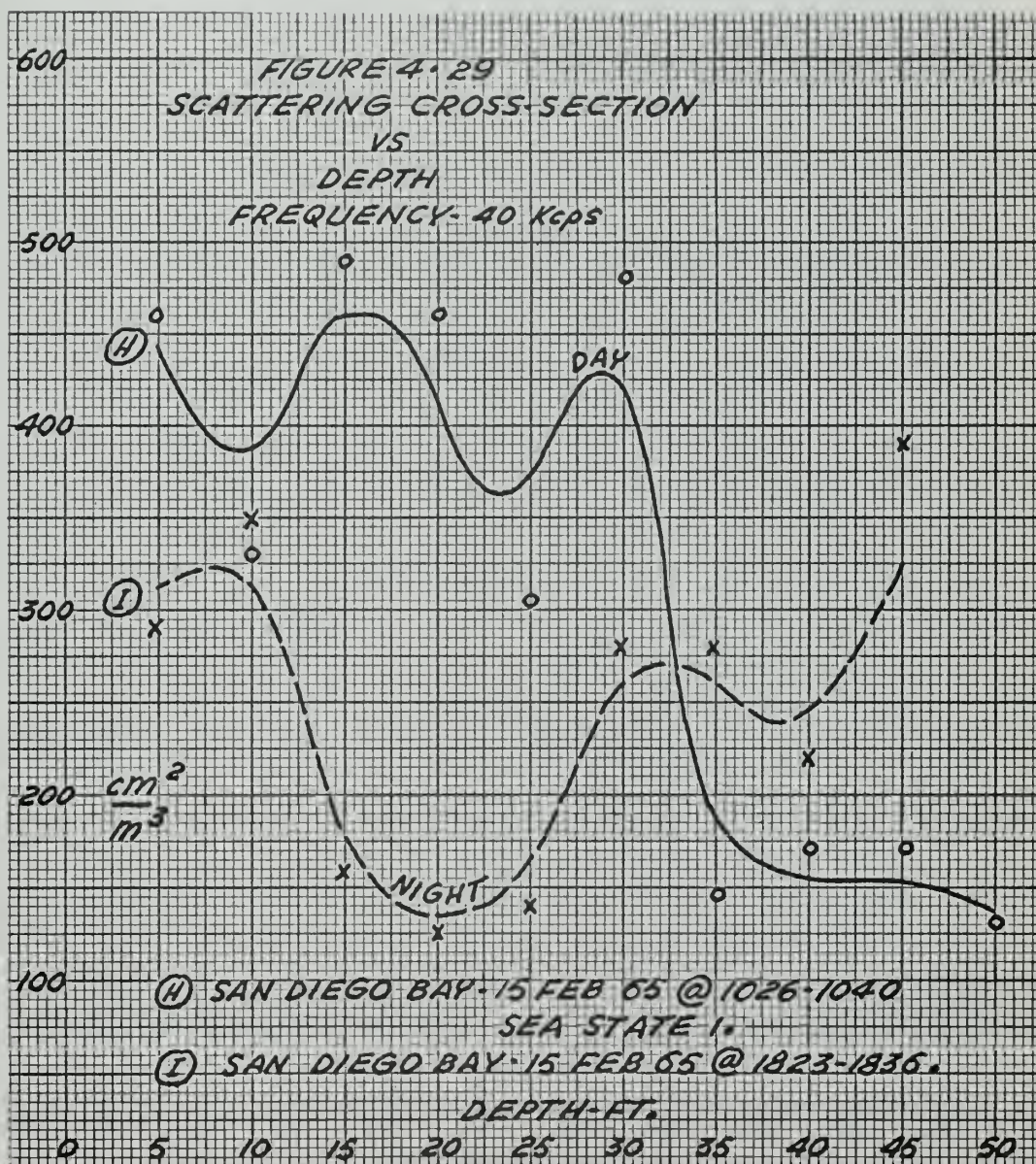






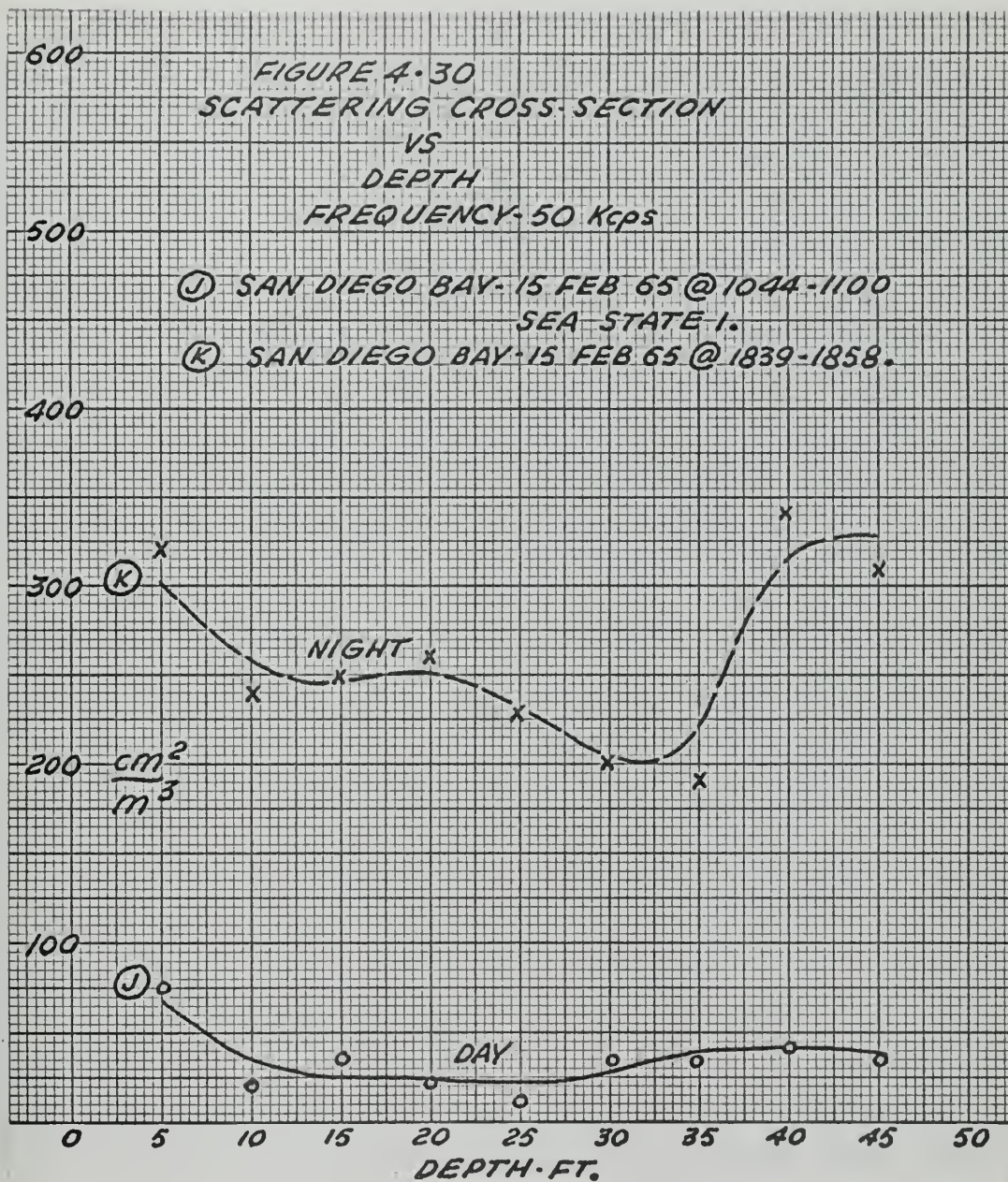






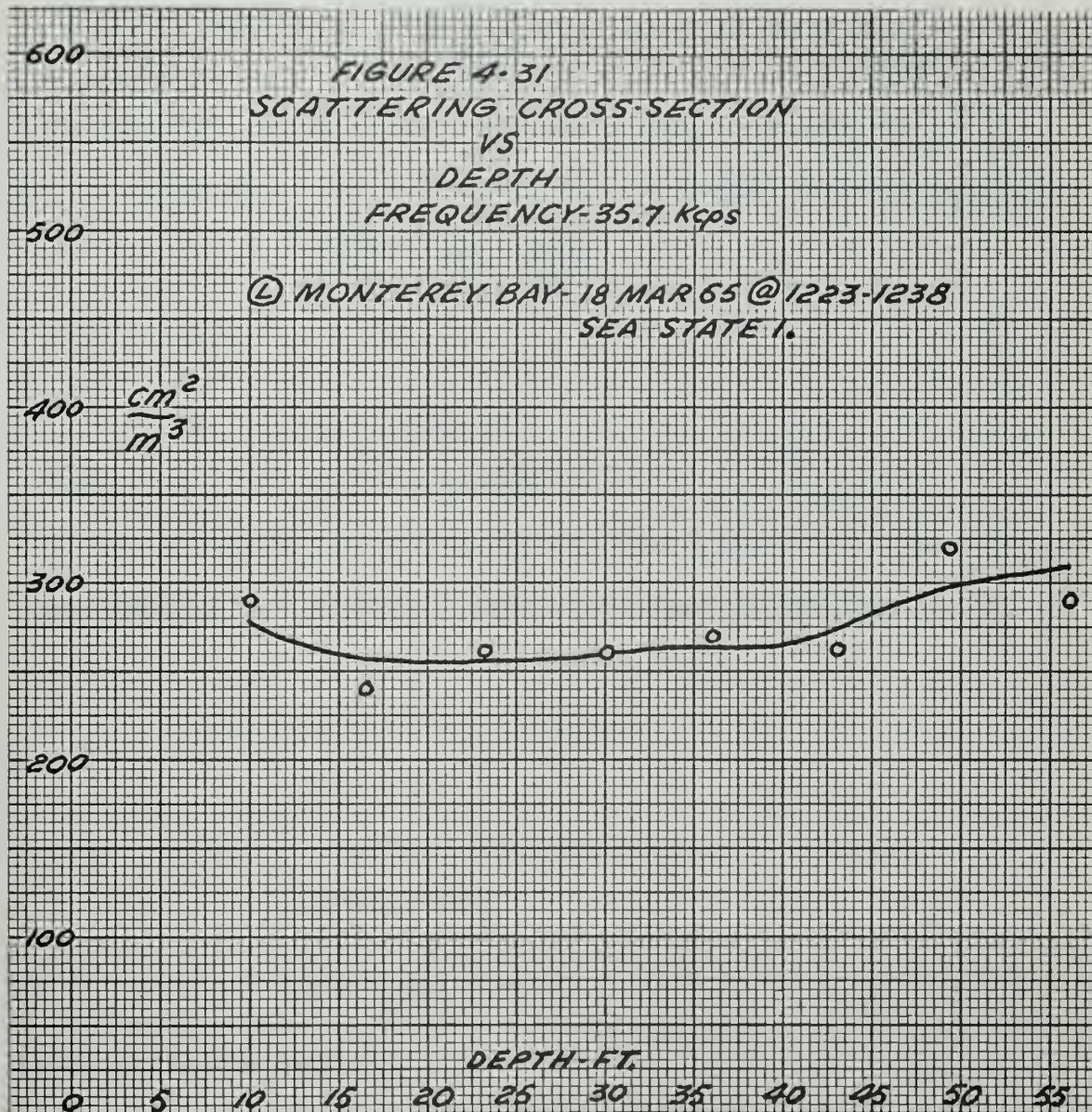














## 5. Velocity Measurements.

### a. Brief Theory.

The basic properties of a liquid that control the velocity of sound through the liquid are compressibility,  $K$ , and density,  $\rho$ . The sound velocity can be expressed as

$$C = 1 / \sqrt{K\rho} \quad (5-1)$$

This equation can be derived from the equation of state [21].

The plane wave solution to the one-dimensional wave equation,

$$\frac{\partial^2 \xi}{\partial x^2} = \frac{k^2}{\omega^2} \frac{\partial^2 \xi}{\partial t^2},$$

can be written

$$\xi = A e^{-kx} e^{j\omega t}$$

where  $k = \alpha + j\beta = \frac{\omega}{c}$  (5-2)

It can be seen that  $\alpha$  will describe the attenuation of the wave with increasing  $x$ , and  $\beta$  will describe the propagation constant of the wave.

If we substitute a complex  $K$ ,

$$K = a + jb$$

into equation 5-1 and then combine equation 5-1 with 5-2 we obtain

$$\beta = \omega \sqrt{a\rho}$$
$$C = \frac{1}{\sqrt{a\rho}} \quad (5-3)$$

For bubble free water

$$a = 1/\rho c_0^2$$

where  $c_0$  is the sound velocity in bubble free water.

Since we are looking for the effect of small bubbles in small





concentrations we will assume that the density of water with bubbles is not different from that without bubbles. With this in mind, if we have an equation for the compressibility of water with bubbles, we can calculate the velocity of sound through bubbly water. Meyer and Skudrzyk have derived such an equation for bubbles of a particular size [20].

$$\kappa' = \frac{3V}{\rho R^2 \omega_0^2} \left[ \frac{\frac{\omega_0^2}{\omega^2}}{\frac{\omega_0^2}{\omega^2} - 1 + j d \frac{\omega_0}{\omega}} \right]$$

where

$V$  = The volume concentration of bubbles in water = ratio of  
volume of air in bubbles to volume of water

$\rho$  = water density

$\omega_0$  = bubble resonant frequency

$\omega$  = frequency (independent variable)

$R$  = bubble radius

$d$  = bubble damping factor

$\kappa'$  = added compressibility due to bubbles in water.

The real part of  $\kappa'$  is

$$a' = \frac{3V}{\rho R^2 \omega_0^2} \left[ \frac{\frac{\omega_0^2}{\omega^2} - 1}{\left( \frac{\omega_0^2}{\omega^2} - 1 \right)^2 + d^2 \frac{\omega_0^2}{\omega^2}} \right] \quad (5-4)$$



The velocity in bubble water is then

$$c = \frac{1}{\sqrt{(a+a')\rho}} = \frac{c_0}{\left[ 1 + \frac{3V}{R^2\omega_0^2} \frac{\frac{\omega_0^2}{\omega^2} - 1}{\left(\frac{\omega_0^2}{\omega^2} - 1\right)^2 + d^2 \frac{\omega_0^2}{\omega^2}} \right]^{\frac{1}{2}}} \quad (5-5)$$

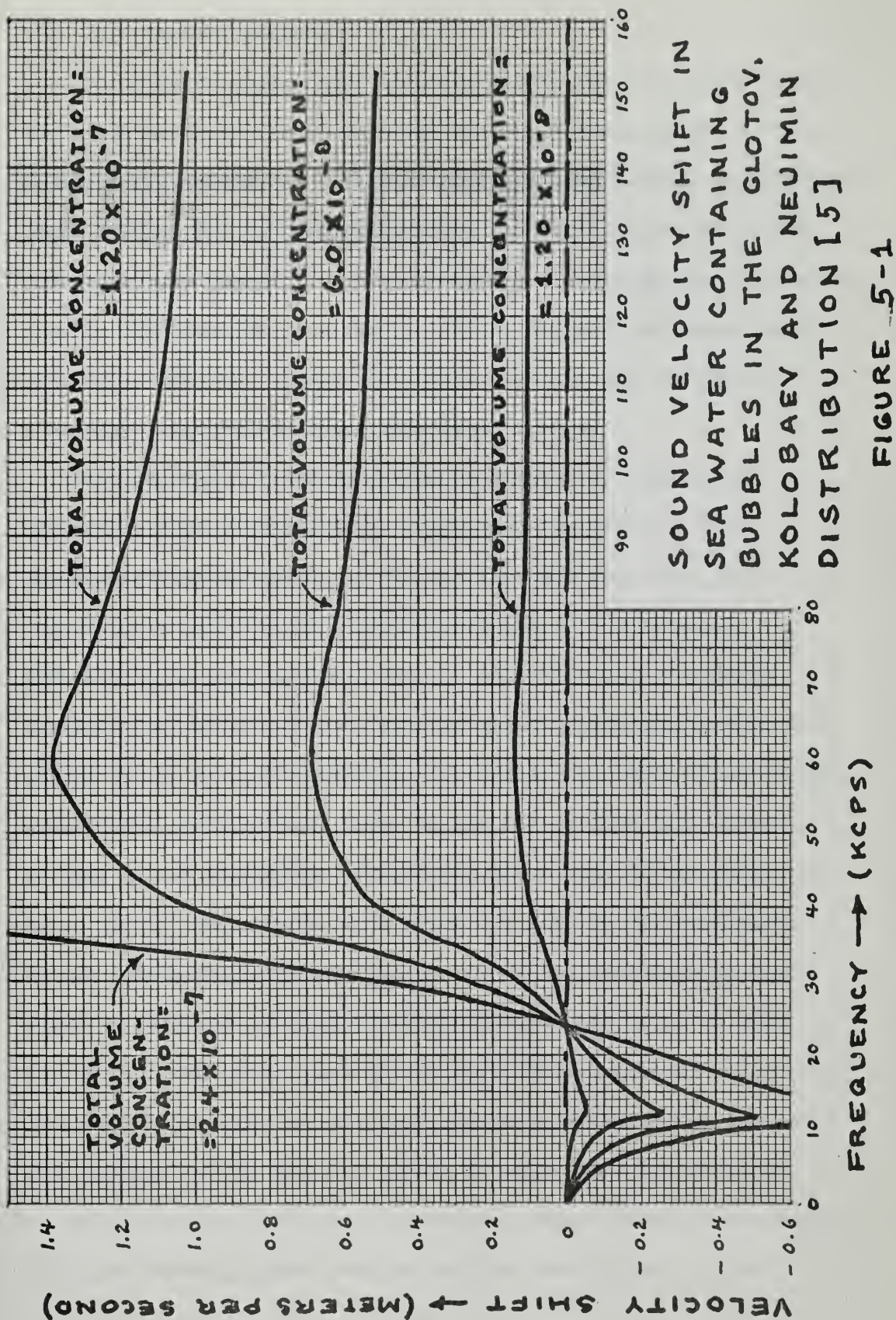
Fox Curley, and Larsen have obtained experimental data that qualitatively confirm Meyer and Skudrzyk's equation for a distribution of bubbles centered at 60 microns radius and ranging from 20 to 120 microns radius. This bubble distribution constituted 0.02 percent of the water volume. [6]

If we know the volume distribution of bubbles over a range of sizes we can integrate equation 5-4 over  $R$  (note that  $\omega_0 = f_c(R)$ ) and substitute the new  $a'$  total into equation 5-5 to determine velocity as a function of frequency.

This was done using a CDC 1604 computer and the results for various distributions are shown in figure 5-1. The computer program is presented in Appendix Vii. The volume distributions put into the computer were divided such that volume concentration values were assigned to discrete bands of bubble sizes. The band width used was 20 microns. An alternative method of incrementing the bubble volume distribution would be to assign volume concentration values to discrete bands of bubble resonant frequencies. The former method was used because it appears more often in the literature. [5, 22, 26]









## 5.2 Experimental Methods.

In order to determine dispersion due to bubbles in the ocean the velocimeter used must meet the following requirements. First, it must have continuous frequency coverage from 10 Kcps to 200 Kcps; these frequencies are determined from the characteristics of dispersion curves shown in figure 5-1 that are computed from the bubble density distribution observed by Glotov, Kolobaev and Neuimin. [5] Second, it must be quickly and easily read in order to sweep the frequency range before ocean conditions change.

Any dispersion experiment will be limited by temperature inhomogeneities in the ocean. Liebermann has measured these inhomogeneities at depths of 100-200 feet and found a typical temperature variation of  $.05^{\circ}\text{C}$  occurring over a correlation distance of 60 centimeters. This is equivalent to a velocity variation of 0.2 M/S or 0.01 percent occurring during an average period of 0.6 seconds assuming a current of two knots flows by the transducer. Similar data taken at the sea surface as a function of time is not available. Figure 5-1 shows that if the velocity error due to temperature is of order 0.2 M/S the smallest total volume concentration of bubbles in the Glotov distribution that could be detected in ocean velocity measurements would be about  $6 \times 10^{-8}$ . . . Salinity inhomogeneities could account for a variation of 1.23 M/S per part per thousand change in salinity but whether such changes can be expected during an experiment is not known.

Of the various methods for measuring sound velocity the time of flight method appears best suited for this project in that





frequency can be changed continuously without changing the physical dimensions of the transducer assembly and the same basic pulse echo system can be used in making attenuation and backscattering measurements as well. A variation on the time of flight technique, the "sing around" technique could not be used because it would require major changes in electronic systems settings thereby precluding simultaneous velocity, attenuation, and backscattering measurements. [8] Also the "sing around" technique is not accurate in a dispersive medium. Time of flight measurements have been made in the laboratory by Greenspan and Tschiegg with accuracies of one part in 30,000 or .003 percent. [7]

Two different techniques for measuring time of flight have been tried. Each will be described below.

#### Envelope Detector and Echo Counter

In this technique the time interval is measured from the start of the main bang to the start of a preselected echo. Figure 5-2 is a block diagram of the system.

The advantage of this technique lies in its ease of operation and reading. The one megacycle counter gives an instantaneous reading of travel time. In the laboratory, travel time readings to the sixth echo were obtained. This provided a reading resolution of one microsecond in about 6300 microseconds or about 0.016 percent. However, the reading was sensitive to frequency and echo amplitude changes as well as velocity so that the accuracy of the velocity value was about 5%. A discussion of this error and a possible remedy may be found in Appendix VIII.





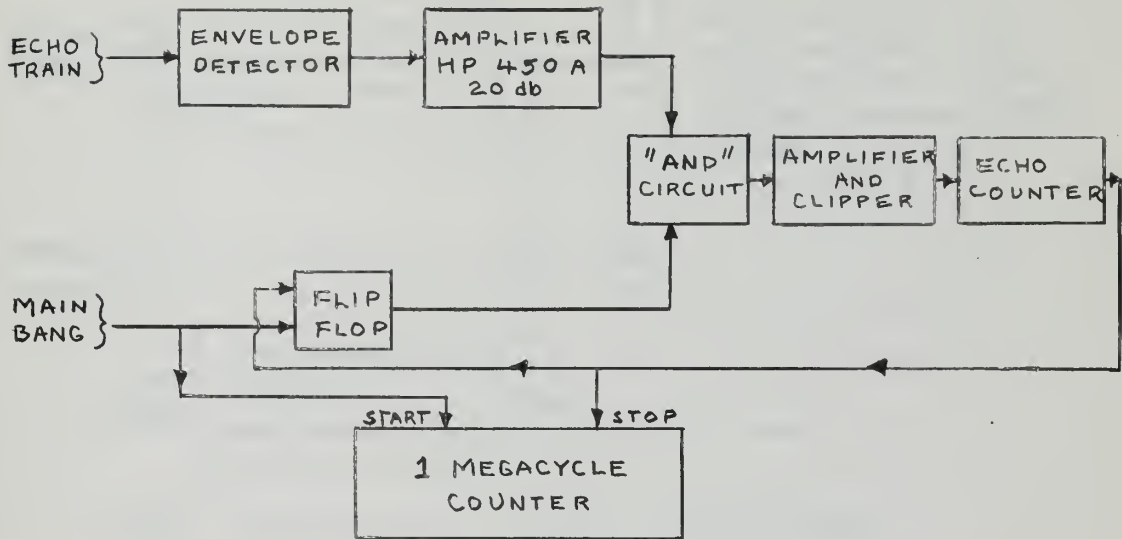


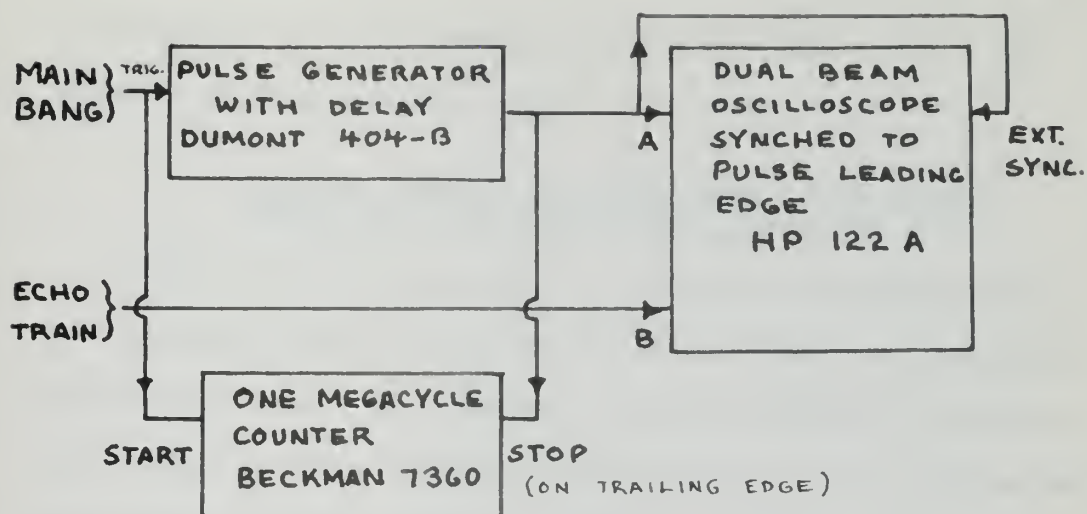
Figure 5-2  
Block diagram of envelope detector and echo counter.

#### Time Marker.

This system provides an oscilloscope display similar to that of a radar range marker on an expanded scale "A" scope. Figure 5-3 is a block diagram of the system. Figure 5-4 is a typical display provided by this system. Appendix IX presents a detailed description of the system.

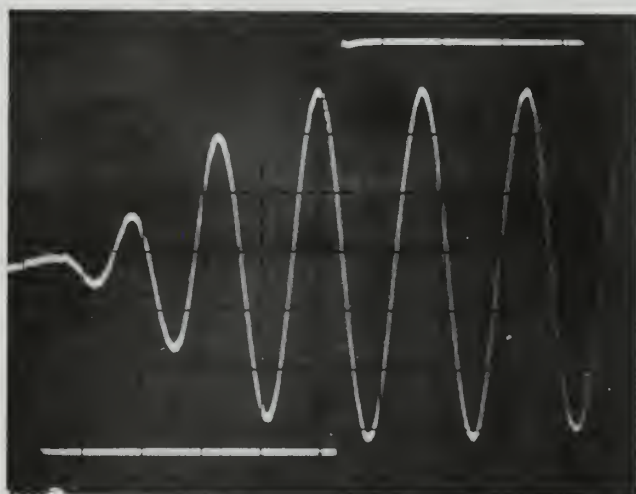
The time marker system appeared very attractive because of the precision with which measurements could be made. When measuring travel time to the 11th echo a reading resolution of one part in 10,000 was possible.





TIME MARKER BLOCK DIAGRAM

FIGURE 5-3



TYPICAL DISPLAY AT 60 KCPS

FIGURE 5-4





The method of measurement was as follows. Time was measured to an easily identifiable point on the first echo. The time was then measured to the corresponding point on a later echo. The velocity was then obtained from

$$c = \frac{\text{distance traveled from first echo to later echo}}{\text{travel time from first echo to later echo}}$$

Difficulty was encountered in identifying the proper point on the later echo that corresponded to the previously selected point on the first echo. It is believed that this difficulty may have been caused by phase shift upon reflection from the transducer and misalignment of the transducer reflector apparatus. The error due to phase shift upon reflection was determined from travel time data taken in an anechoic tank filled with water believed to be non-dispersive<sup>1</sup>. Figure 5-5 is plotted from such data and used as calibration curves for data taken using the same transducers. It should be noted that the rapid apparent change of travel time with frequency at low frequencies will cause low frequency determination of travel time to be inaccurate. This effect, due to transition from stiffness to resistance control in the transducer is reflected as a phase shift which is a function of frequency.<sup>2</sup> Any lack of parallelism causes extra cycles to appear in front of late echoes at high frequencies. This ambiguity in echo leading edge due to misalignment is a function of frequency which makes it difficult to follow the preselected point on late echoes as frequency is

<sup>1</sup>See Section 3H for a discussion of tank preparation.

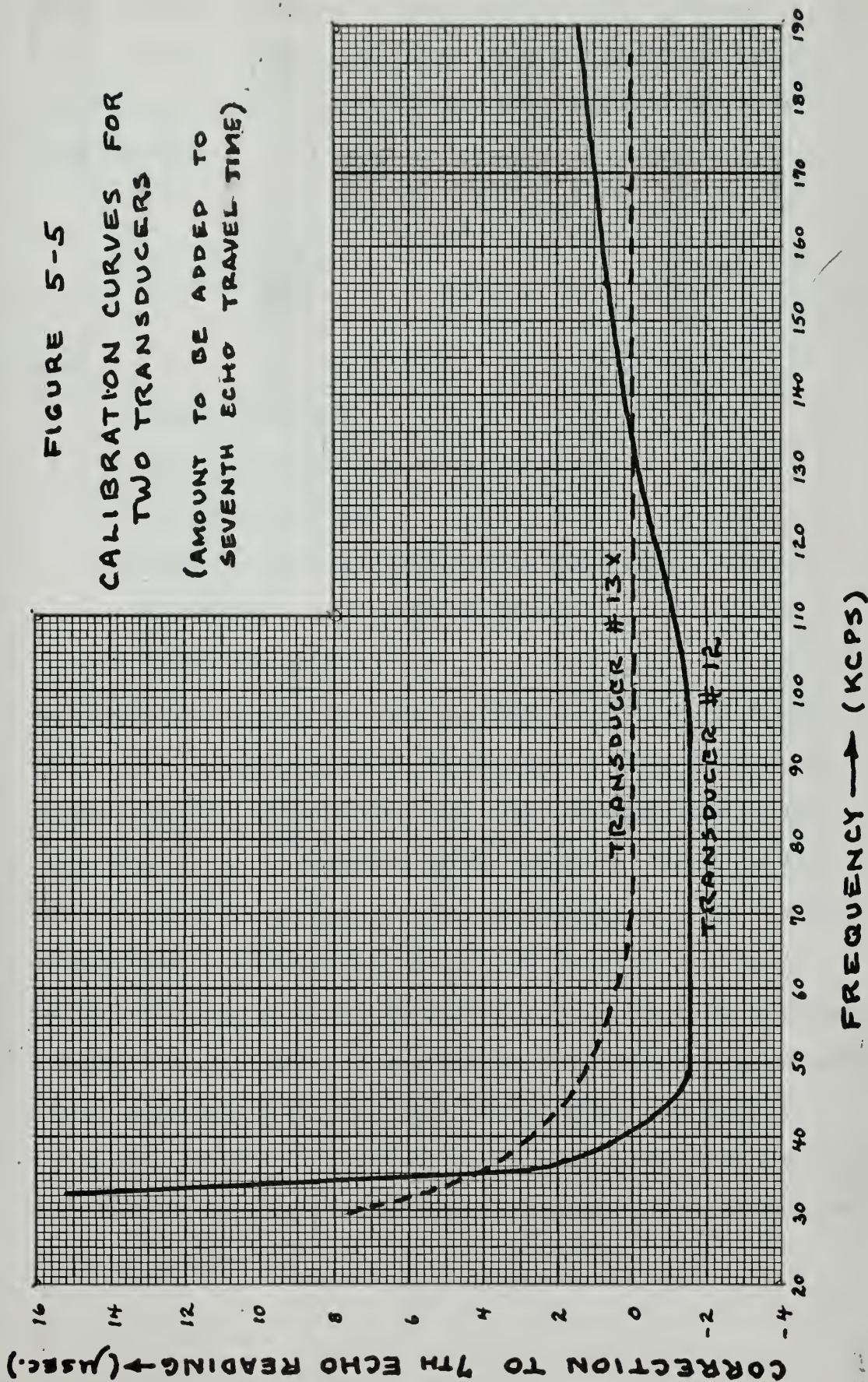
<sup>2</sup>See Appendix I for a discussion of this transition.



FIGURE 5-5

CALIBRATION CURVES FOR  
TWO TRANSDUCERS

(AMOUNT TO BE ADDED TO  
SEVENTH ECHO TRAVEL TIME)







If the measuring point on the later echo does not correspond to the measuring point on the first echo, the measured velocity plotted as function of frequency in a non-dispersive medium will be of the form

$$c = \frac{d}{T_0 + \frac{K}{f}} \quad (5-6)$$

where

$c$  = Measured velocity

$d$  = distance traveled

$T_0$  = correct travel time

$K$  = Error in selecting corresponding point on later echo  
(in cycles or fractions of cycles)

$f$  = signal frequency

By fitting curves generated from equation 5-6 for various values of  $K$  to the experimental curve, an approximate value for  $K$  can be obtained from the curve of best fit. The measuring point on the later echo can now be corrected by the amount  $K$ . Figure 5-6 illustrates the above discussion. Lack of parallelism is not a source of error **once**  $K$  is determined. Figure 5-7 shows how the signals received from all points on the reflector will always add to present a signal that represents an echo from an effective parallel reflector located some average distance from the transducer that does not change with frequency. The error due to uncertainty in this distance will cause an error of 0.96 M/S per millimeter; this error does not change with frequency.





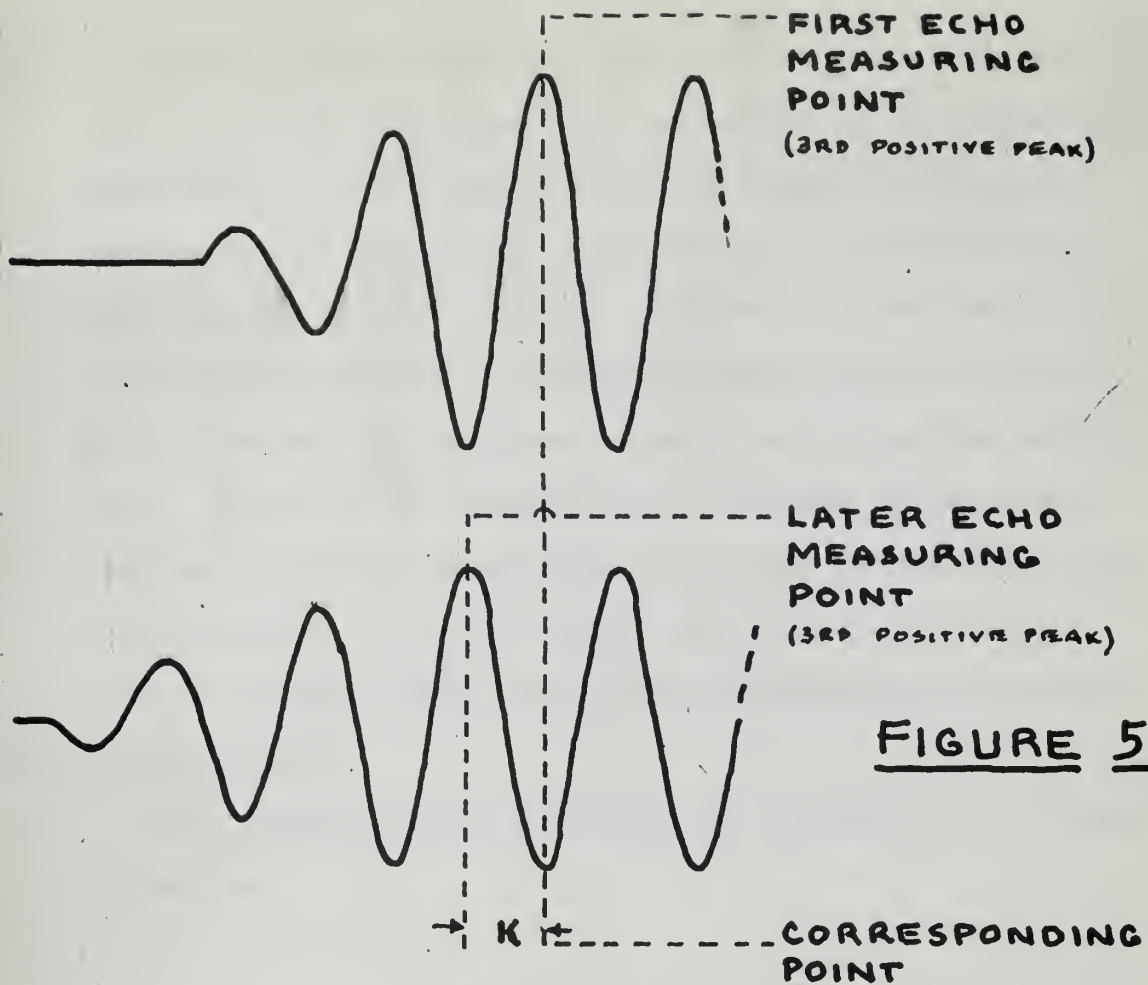


FIGURE 5-6

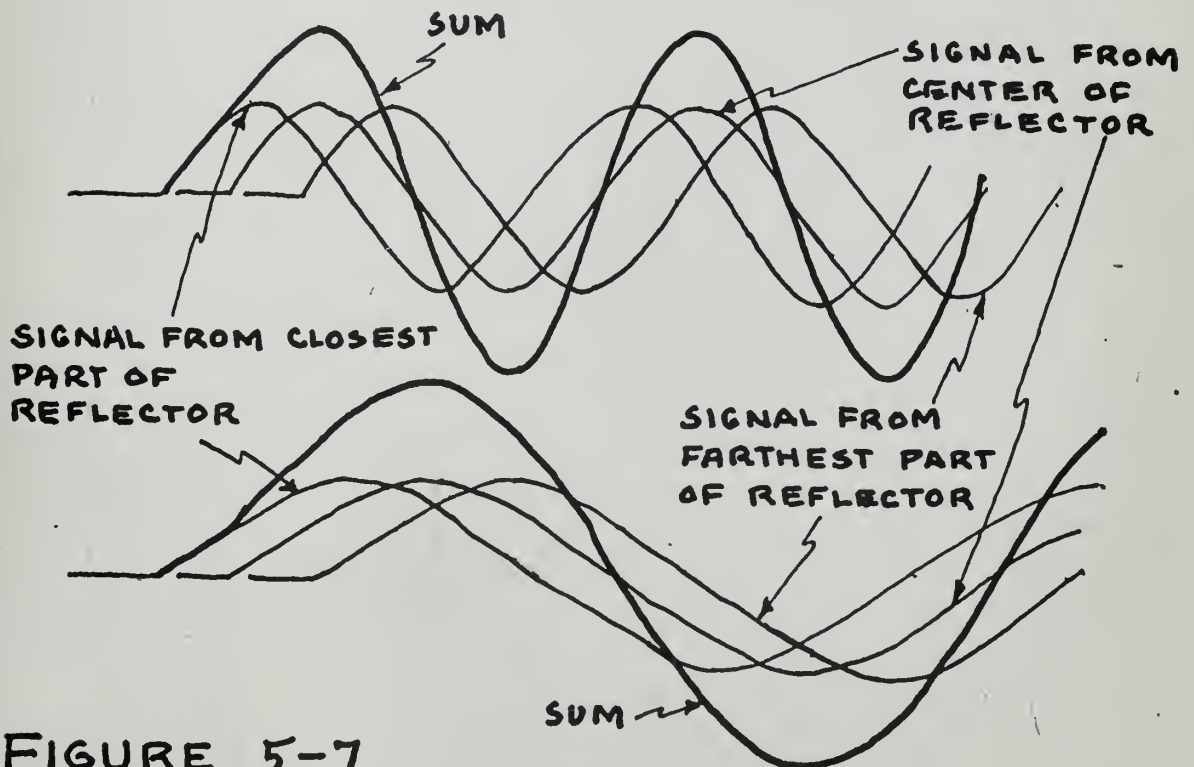


FIGURE 5-7



Reading error may be caused by instability in the delay and pulse width in the pulse generator, instability in the oscilloscope synchronizing circuit, instability in the trigger points in the counter and rise time of the trailing edge of the delayed pulse which was used as the time marker. The rise time error was eliminated by consistently taking measurements with the desired point on the echo one centimeter below the top of the time marker pulse. Errors due to instability were determined by taking many readings at a few selected points and plotting distribution curves. The distribution curves are shown in figure IX-1. The reading error as determined from these curves is conservatively estimated as .03 percent.

The field measurements of velocity are discussed in the following section.





## 6. Data Evaluation.

### A. a) Comparison of attenuation and back-scattering data.

To compare the data obtained in Sections 3 and 4 it is convenient to convert both to the equivalent extinction cross-section using the relationships developed in Physics of Sound in the Sea [18] .

The basic attenuation relationship is

$$\begin{aligned} a &= + 4.34 \sigma_e N(R) \\ &= + 4.34 S_e, \end{aligned}$$

where  $a$  is the attenuation measured in db/meter

$\sigma_e$  is the extinction cross-section of a single bubble

$N(R)$  is the number of bubbles of required radius and

$S_e$  is the total extinction cross-section.

Then using the experimental data

$$\underline{S_e = 0.23a \text{ m}^{-1} .}$$

To determine  $S_e$ , given  $S_s$ , the basic relationship for a single bubble is

$$\frac{\sigma_s}{\sigma_e} = \frac{KR}{S}$$

but  $KR = \delta_r$  so that replacing the single bubble case by that for multiple bubbles,

$$\underline{S_c = \frac{\delta}{\delta_r} S_s,}$$

where  $\delta$  is the total damping constant

and  $\delta_r$  is the radiation of damping constant.



### A. b) Experimental Results

Fig. 6.1a shows the extinction cross-sections calculated from scattering cross-section and data obtained directly from attenuation measurement. In view of the small initial signal return from the scatterers and the large number of correction factors applied, agreement between the curves is satisfactory.

Since no scattering is observed above 60 Kcps it is believed that the effect of microbubbles is negligible above that frequency. This implies that bubbles of radius less than 50 microns are rapidly dissolved while bubbles of greater than 50 micron radius, possibly attached to particles, are persistent.

Attenuation at frequencies higher than 60 Kcps is probably due to some mechanism other than scattering and absorption by microbubbles. This is believed to be absorption by minute plankton with negligible scattering.

Fig. 6.1b shows extinction cross-section as a function of frequency and indicates the frequency ranges over which the effects of microbubbles and plankton are dominant.

### A. c) Conditions for Absorption without Scattering.

Data both from the sea and from the fresh water algae experiment have shown considerable attenuation where no scattering was detected, so that bubbles cannot play a major part in this process at these frequencies.

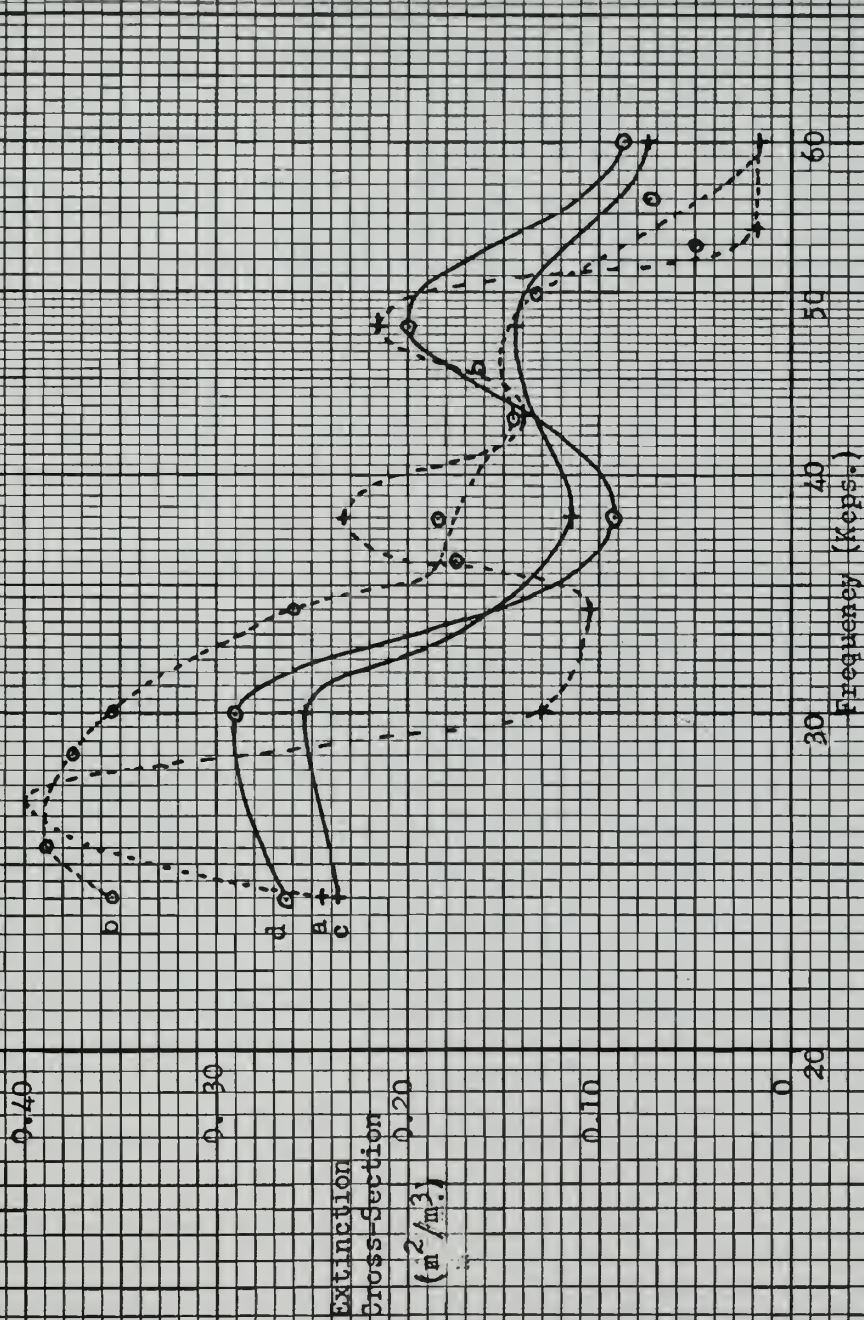
Meister and St. Laurent [19] have made a study of the absorption due to algae in the frequency range 15-27 mcps and concluded that scattering was not a mechanism for absorption. They also concluded that the excess structural viscosity due to the





# Extinction Cross-Section of Sea Water vs Frequency

Site: U.S.N.E.L. Tower, San Diego Bay.



Scattering Cross-Section data

a) 12 Feb. 1965, 0938 0954.

b) 12 Feb. 1965, 1708 - 1743.

Attenuation data

c) 10 Feb. 1965, 1330 1618.

d) 10 Feb. 1965, 2141 - 2353.

Fig. 6.1







Fig. 6 2.

Mean Extinction Cross-section vs Frequency.

The extinction cross-sections were calculated from the mean at ten stations obtained on the U.S.N.R.L. Tower, San Diego, 10 Feb. Depth, 10 ft.

plankton

microbubbles

Frequency (Kcps)

0.40

0.20

0.20

0.10

0.10

0.20

40

70

100

200

Extinction  
Cross-section  
( $m^{-1}$ )





algae behaved in the same manner as the structural viscosity present in the liquid.

Lax and Feshback [13] show that for particles sufficiently small with respect to a wavelength absorption will be dominant and scattering will be negligible. This occurs when  $ka < 0.1$ , where  $a$  is the particle radius

$$\text{and } k = \frac{2 \pi f}{c}$$

The maximum radius for absorption without scattering is

$$\begin{aligned} \frac{a}{\phantom{a}} &= \frac{0.1 c}{2 \pi f} \\ &= \underline{2.4 \times 10^4 / F \text{ microns}} \end{aligned}$$

where  $F$  is frequency in Kcps.

This gives the maximum particle radius for absorption with negligible scattering at the frequencies shown in the table.

Frequency Kcps	a max microns
24	1,000
30	800
38	630
48	500
60	400
76	320
96	250
120	200
152	160
192	125

Table 6.1

Both these studies confirm that plankton could give attenuation without scattering over the frequency range of the measurements, but neither suggests a mechanism which would make the absorption a function of frequency, although definite





attenuation peaks were obtained in the fresh water algae experiment.

B. a) Bubble distribution from data.

To determine the volume of air per volume of water, assuming the attenuation to be due to bubbles, use was again made of the N.D.R.C. relationships [18].

$$\text{If } R \text{ is given by } \frac{dR}{R_0}$$

where  $R_0$  is the radius of the bubble resonant at the frequency of interest, the fraction,  $p$ , of the total extinction cross-section which is due to bubbles between  $R - dr$  and  $R + dr$ , is

$$p = \frac{\frac{1}{\delta} \tan^{-1} \frac{2R}{\delta}}{\frac{\pi}{2\delta}}$$

$$= \frac{2}{\pi} \tan^{-1} \frac{2R}{\delta}$$

Then the attenuation due to bubbles in this range is simply  $pa$ .

Defining  $u(R) dR$  as the volume of air per unit volume for the bubbles under consideration

$$pa = 1.50 \times 10^{+3} u(R) \text{ db/meter}$$

$$u(R) = 6.67 \times 10^{-4} pa$$

$$\underline{u(R) dR} = 2 u(r) dr$$

$$= \underline{1.33 \times 10^{-3} pa dr.}$$

Bubble distribution and volume concentration bases on scattering data were illustrated in detail in section 4.f. but certain curves are repeated here for comparison with the distribution and concentrations obtained from the attenuation data.



Figure 6-2 shows bubble volume concentration obtained from scattering data in San Diego Bay while figure 6-3 shows the bubble volume concentrations needed to produce the attenuations shown in Figure 3-12. The bubbles of radius less than 50 microns are not believed to exist in significant amounts.

Figure 6-4 shows the bubble volume concentrations obtained from scattering data in Monterey Bay.

#### C. Comparison of velocity and backscattering data.

Velocity data was taken at the two locations as described in Appendix VI. The data were taken with the intention of comparing with velocity data at the same time utilizing the computer program of appendix VII.

Unfortunately the DuMont 404 B pulse generator was not available when taking data at the N.E.L. tower in San Diego. A GR 1217-A pulse generator was used instead. Its relatively unstable pulse width caused considerable horizontal jitter reducing the reading accuracy to about 0.07 percent. Figure 6-5 shows velocity data and simultaneous data derived from scattering data taken at the N.E.L. tower. The broken line is the bubble free velocity. It was chosen so that the computed dispersion curve best fits the data points. It was not possible to determine the bubble free velocity because simultaneous salinity readings were not taken for substitution into the empirical formula for sound velocity in sea water. [11] The data for figure 6-5 were taken on 15 February 1965 in mid afternoon and corresponds to figure 4-25 and 6-1.





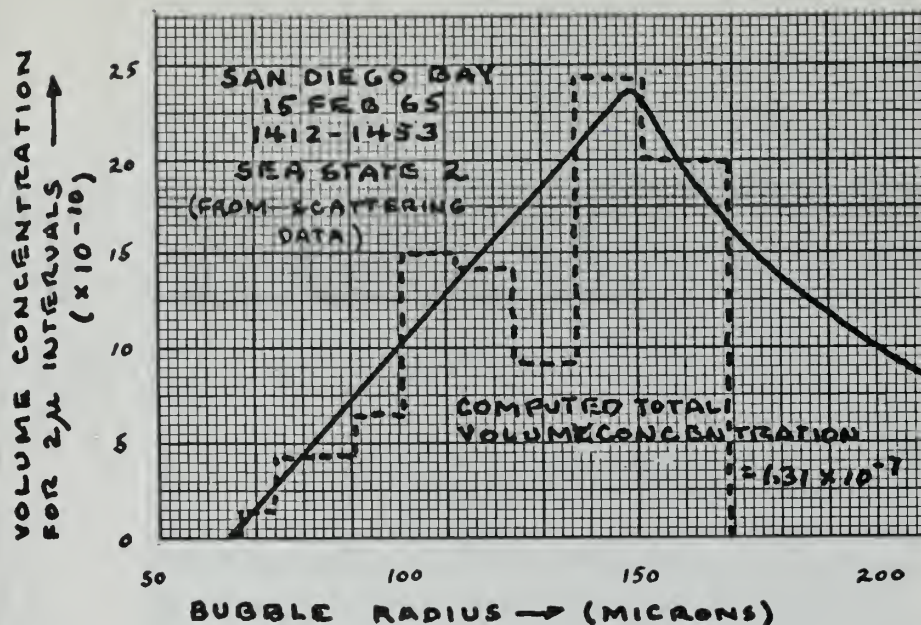


FIGURE 6-2 BUBBLE VOLUME CONCENTRATION OF FIGURE 4-25 NORMALIZED TO TWO MICRON INCREMENTS. (SOLID CURVE IS APPROXIMATION USED IN COMPUTER.)

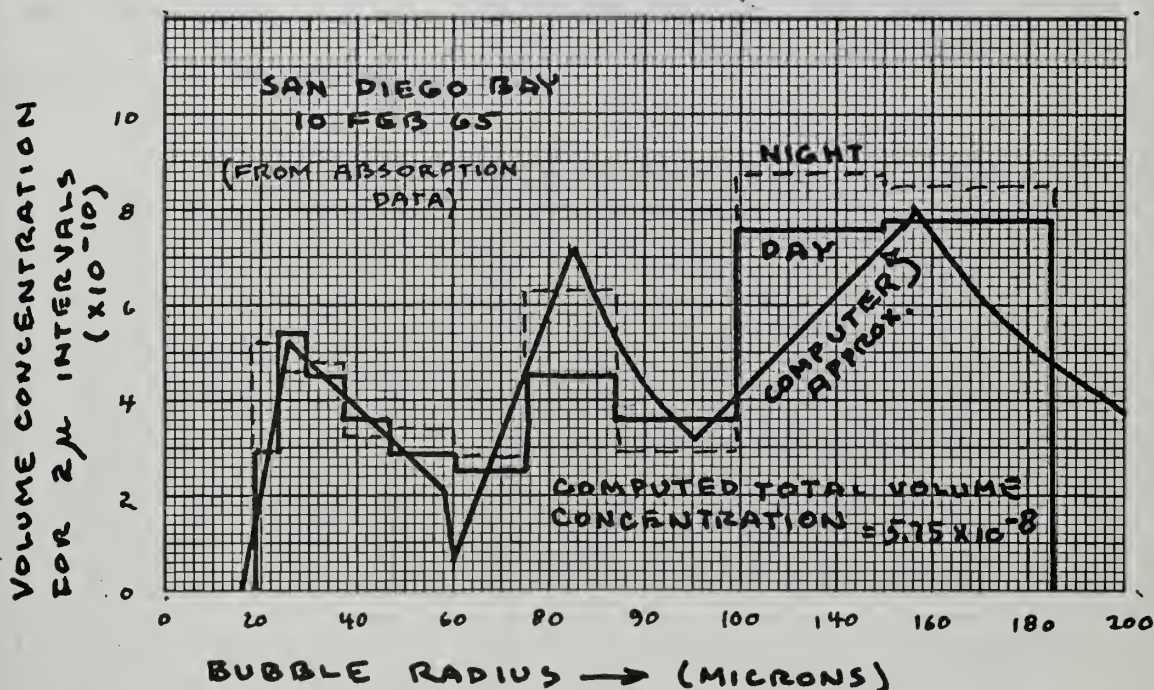


FIGURE 6-3 BUBBLE VOLUME CONCENTRATION OF FIGURE 3-12 NORMALIZED TO TWO MICRON INCREMENTS.





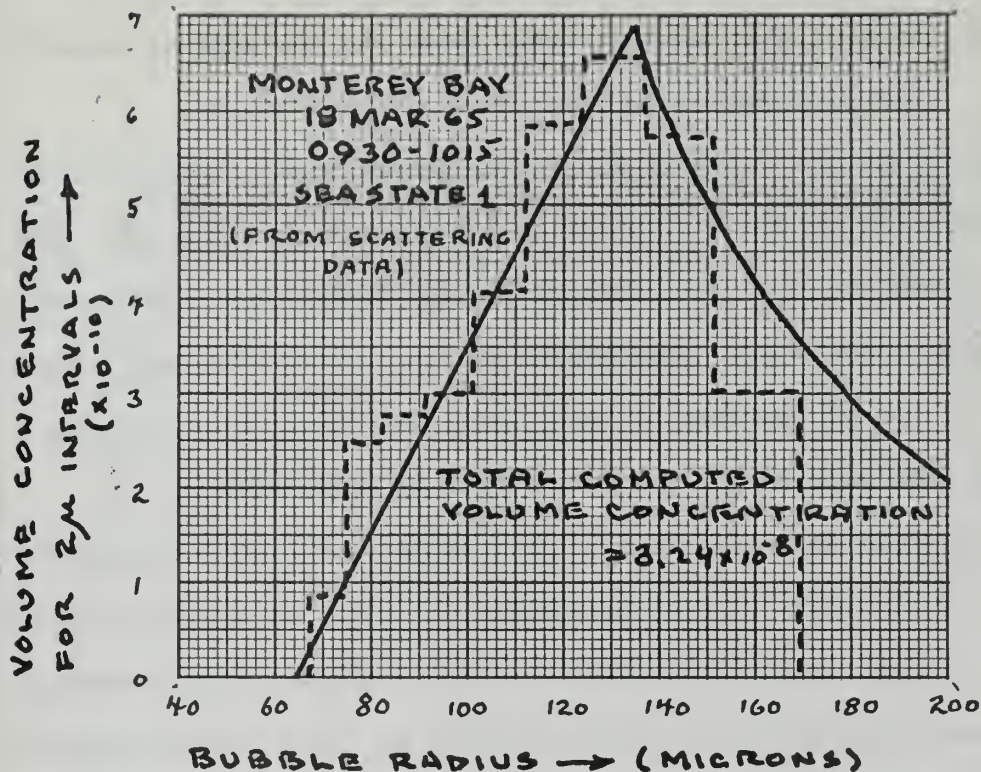


FIGURE 6-4 BUBBLE VOLUME CONCENTRATION OF FIGURE 4-27 NORMALIZED TO TWO MICRON INCREMENTS. (SOLID CURVE IS APPROXIMATION USED IN COMPUTER.)



Attenuation data was not taken simultaneously with velocity data.

Figure 6-6 is a dispersion curve computed from scattering data taken on the morning of 18 March 1965 in Monterey Bay. The points appearing on Figure 6-6 are velocity data points taken at the same time. Again, since salinity was not known the bubble free velocity can not be determined. Attenuation data as a function of frequency were not taken in Monterey Bay.

Examination of figures 6-5 and 6-6 reveals that the velocity data do not disagree with the velocity dispersion curves obtained from scattering and attenuation data. Unfortunately the largest velocity shifts in these dispersion curves occur at frequencies below the low frequency limit of the velocity measuring apparatus. This could be remedied by using a transducer which has a flat response that extends to lower frequencies. It is the transition from stiffness to resistance control (about 4.0 Kcps in the present transducers) that produces a phase shift which prevents accurate measurement.

Examination of figures 5-1, 6-5 and 6-6 reveals that the shape of the dispersion curves obtained from the Glotov bubble distribution and the various bubble distributions obtained in this paper are very similar. Also the velocity shift from bubble free velocity changes very little with changing frequency above 80 Kcps. If we assume a Glotov distribution and take one velocity measurement at, say, 80 Kcps we can obtain the total bubble volume concentration for the entire distribution by substituting the





measured velocity,  $V$  into equation 6-1

$$\text{Vol. Conc.} = 9.71 (V - V_0) \times 10^{-8} \quad (6-1)$$

which is derived from figure 5-1 at 80 Kcps. This equation requires a knowledge of  $V_0$  the bubble free velocity which, according to figure 5-1, should be obtained below three Kcps. Unfortunately the instrumentation described in this paper is not operable below 20 Kcps. However, this single measurement technique could be useful in studying the decay of bubbles in a wake with time by simply assuming the terminal velocity measurement is the bubble free velocity,  $V_0$ .



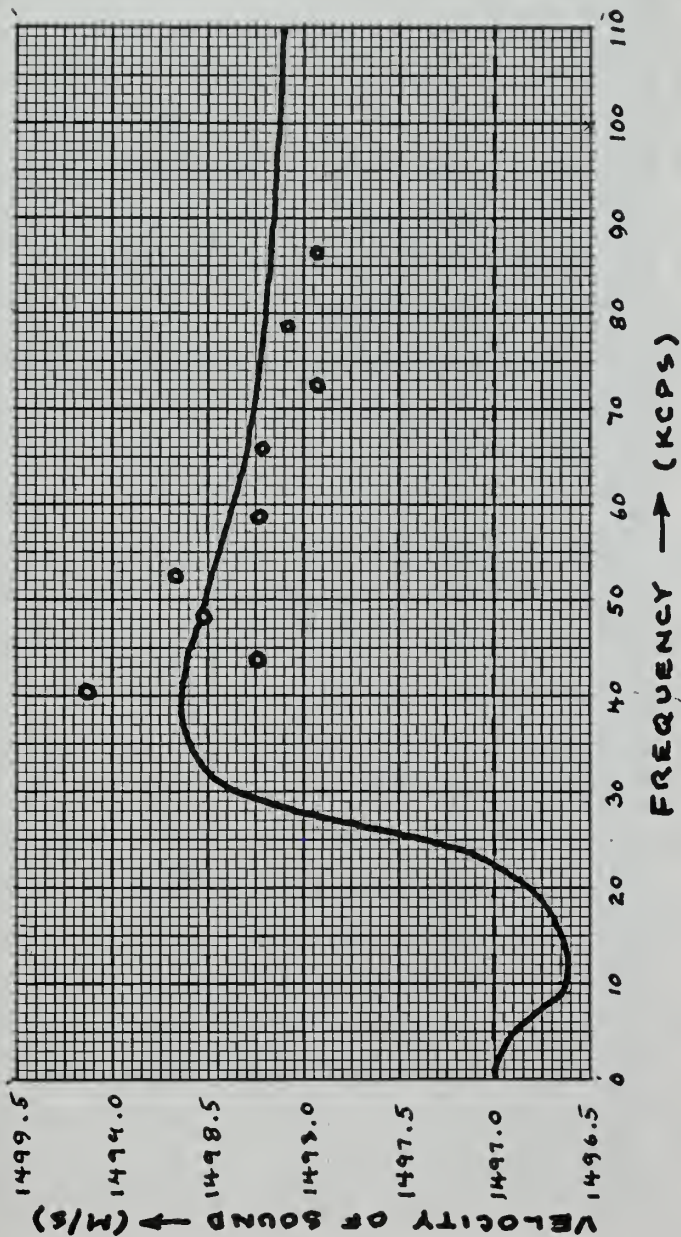


FIGURE 6-5 COMPARISON OF MEASURED  
VELOCITY AND VELOCITY SHIFT COMPUTED  
FROM SCATTERING DATA OF FIGURE 4-25  
(SOLID CURVE IS COMPUTED CURVE)



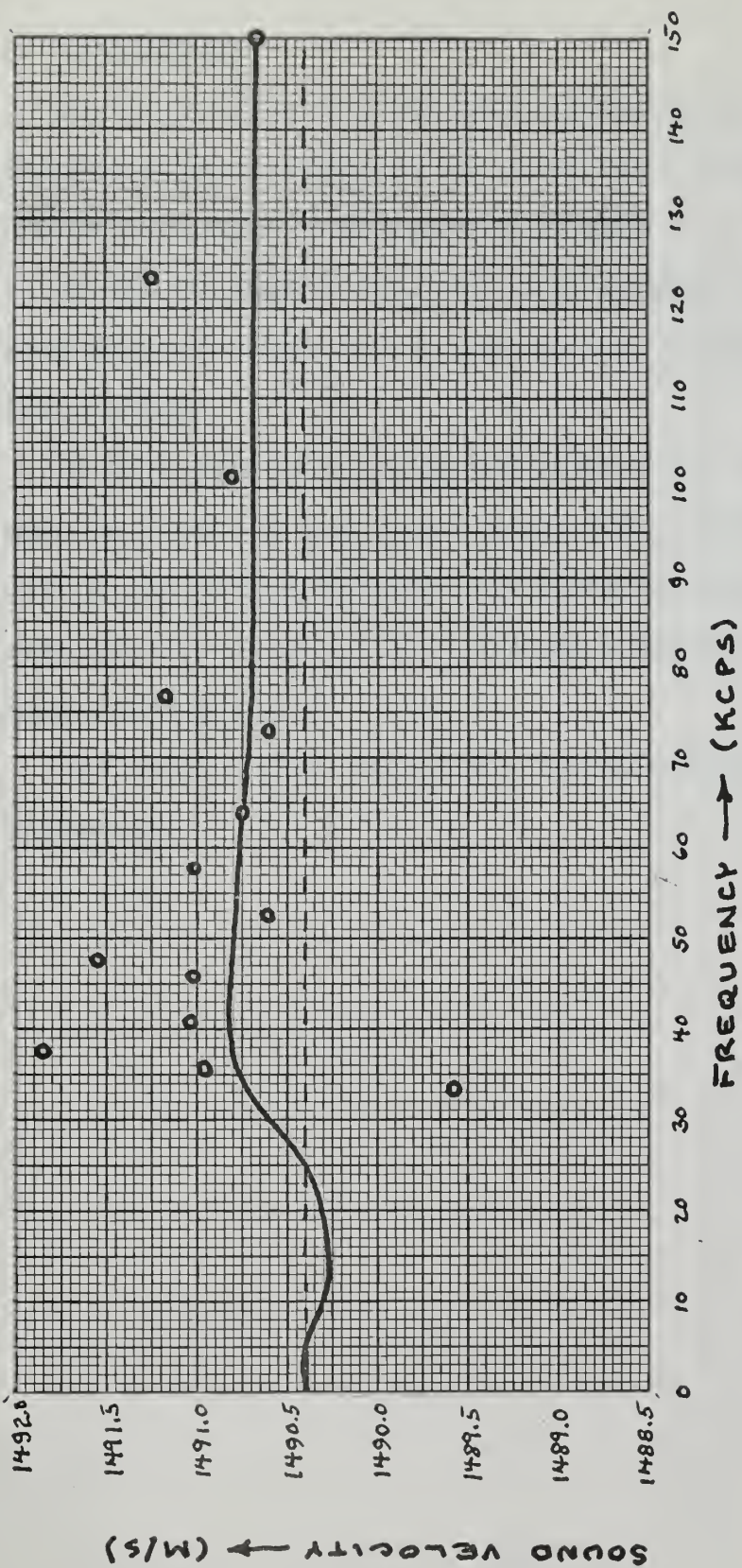


FIGURE 6-6 COMPARISON OF MEASURED VELOCITY AND VELOCITY SHIFT COMPUTED FROM SCATTERING DATA OF FIGURE 4-27 (SOLID CURVE IS COMPUTED CURVE)





## 7. Conclusions.

It is postulated that the total attenuation measured at sea at frequencies below 60 Kcps is due to bubbles, the effect of the bubbles increasing as frequency is reduced.

At all frequencies there will be attenuation with negligible scattering due to plankton of size  $ka < 0.1$ . This effect is dominant above 60 Kcps.

It is impossible to assess the effect of any suspended inorganic material in the sea since its acoustic effect would be the same as that of plankton (algae-type). Since the San Diego sea water was very clear it is assumed that there was a negligible amount of suspended particles.

The velocity shift measurements do not disagree with the above hypothesis.



## 8. Acknowledgements.

The writers wish to express their appreciation to Professor Herman Medwin of the Physics Department, U. S. Naval Postgraduate School for his guidance in the experimental work, to Mr. Robert Moeller, Mr. Harold Whitfill and Mr. Michel O'Day of the USNPG for their help in the construction and acquisition of equipment and to Lt. D. Basham and staff of the Electronics Department for logistic support.

Thanks are also due to personnel of the U. S. Navy Electronics Laboratory and in particular to Dr. E. C. LaFond and staff, Dr. C. J. Kreiger and staff, Mr. D. Fraughton, Mr. Charles Green and staff and Mr. Henry Spreckelmeyer.

In addition, the writers are indebted to Dr. Rakestraw and Mr. Snodgrass of the Scripps Institute of Oceanography for valuable conversations.





9. Bibliography.

1. Albers, V. M. Underwater Acoustics Handbook. The Pennsylvania State University Press, 1960.
2. Anderson, V. C. Sound Scattering from a Fluid Sphere. JASA, v.22, no. 4, December 1949; 426-431.
3. DelGrosso, V. A. Systematic Errors in Ultrasonic Propagation Parameter Measurements, Part I-Effect of Free Field Diffraction. NRL Report 6026, January 29, 1964.
4. Devin, C. Jr. Survey of Thermal, Radiation, and Viscous Damping of Pulsating Air Bubbles in Water. JASA, v. 31, December 1959: 1654-1667.
5. Fox, F. E., Curley, S. R. and Larson, G. S. Phase Velocity and Absorption Measurements in Water Containing Bubbles. JASA, v. 27, no. 3, May 1955: 534-539
6. Glotov, V. P., Kolobaev, P.A. and Neuimin, G. G. Investigation of the Scattering of Sound by Bubbles Generated by an Artificial Wind in Sea Water and the Statistical Distribution of Bubble Sizes. Soviet Physics-Acoustics, v.7, Apr. - June. 62: 341-345.
7. Greenspan, M. and Tschiegg, E. Speed of Sound in Water by a direct Method. Journal of Research of National Bureau of standards, v.59, no.4, October 1957: 249-254.
8. Greenspan, M. and Tschiegg, E. Sing-Around Ultrasonic Velocimeter for Liquids. The Review of Scientific Instruments, V.28, no. II, November 1957: 897-901.
9. Hansen, P. G. and Barham, E. G. Resonant Cavity Measurements of the Effects of "Red Water" Plankton on the Attenuation of Underwater Sound. Limnology and Oceanography, v.7, January 1962: 8-13.
10. Hickling, R. An Analysis of Echoes from a Solid Elastic Sphere in Water. California Institute of Technology, Report No. 85-20, March 1962.
11. Kinsler, L. E. and Frey, A. R. Fundamentals of Acoustics. Wiley and Sons Inc., 1962.
12. Kuttruff, H. and Wille, P. Absoluteichung Verschiedenartiger Wasserscallwandler im Bereich von 5 bis 250 KHz. Acoustica, v.12, no. 6, 1962: 410-421.



13. Lax, . and Feshback, . Absorption and Scattering for Impedance Boundary Conditions on Spheres and Circular Cylinders. JASA, v.20, no.2, March 1948: 109-124.
14. Liebermann, L. Air Bubbles in Water. JAP, v.28, no.2, February 1957: 205-211.
15. Liebermann, L. The Effect of Temperature Inhomogenities in the Ocean on the Propagation of Sound. JASA, v.23, September 1951: 563-570.
16. McMillan, D. R. and Lagemann, R. T. A Precision Ultrasonic Interferometer for Liquids and Some Velocities in Heavy Water. JASA, v.19, November 1947: 956-960.
17. McSkimin, H.J. Empirical Study of the Effect of Diffraction on Velocity of Propagation of High Frequency Ultrasonic Waves. JASA, v.32, November 1960: 1401-1404.
18. NDCR Technical Reports, Div. 6, Vol. 8, Part IV, page 466.
19. Meister, and St. Laurent, Ultrasonic Absorption and Velocity and Water Containing Algae in Suspension. JASA, v.32, no. 5, May 1960: 556-559.
20. Meyer, E. and Skudrezyk, . Sound Absorption and Sound Absorbers in Water. NAVSHIPS 900.164, v.1, 1 December 1950.
21. Officer, C. B. Introduction to the Theory of Sound Transmission. McGraw-Hill, 1958.
22. Physics of Sound in the Sea. Division 6, v.8, NDRC Summary Technical Reports, 1945.
23. Seki, H., Granato, A. and Truell, R. Diffraction Effects in the Ultrasonic Field of a Piston Source and their Importance in the Accurate Measurement of Attenuation. JASA, v.28, no.2, March 1956: 230-238.
24. Stenzel, H. On the Disturbance of a Sound Field Brought About by a Rigid Sphere. Elektrische Nachrichten Technik, V. 15, 1938: 71-78.
25. Urick, R. J. and Hoover, R. M. Backscattering of Sound from the Sea Surface. JASA, V.28, no. 6, November 1956: 1038-1042.
26. Vitro Laboratories. Microbubble Persistence (A Preliminary Research Report), by W. R. Turner, Tech. Note TN-N4329/12960, January 1960.



27. Williams, A.O. The Piston Source at High Frequencies. JASA, v.23, no. 1, January 1951: 1-6.
28. Zimdar, R.E., Barnhouse, P.D. and Stoffel, M.J. Instrumentation to Determine the presence and Acoustic Effect of Microbubbles near the Sea Surface. USNPGS Thesis, 1964.
29. LaFond, E.C. Enlarging an Oceanographic Research Tower, Naval Research Reviews, May 1962.
30. Patterson, G. Use of Hytech Salinometer and Summer Salinities 1964. USNEL Oceanographic Data Report No. 6, 1964.
31. Ward, J. R. General Graph Output Subroutine. USNPGS Computer Center, February 1964.
32. Buxcey, S. Use of an Acoustical Interferometer for Wake Detection. USNPGS Research Paper, 1965.





## APPENDIX I

### The Electrostatic Transducer

#### A. Brief Theory

Electrostatic transducers have been described in the literature by a number of individuals.

To arrive at the expected forms of the receiving and transmitting sensitivities the following derivation is presented starting with the equation of motion for any point localized mechanical system with an applied periodic force:

$$\frac{md^2x}{dt^2} + \frac{R_m dx}{dt} + sx = F_e e^{j\omega t} \quad (I-1)$$

where  $x$  is the displacement.

$m$  is the mass.

$R_m$  is the mechanical resistance.

$s$  is the stiffness

$F$  is the force applied.

If the displacement is simple harmonic then:

$$x = \bar{x} e^{j\omega t}$$

and (I-1) becomes:

$$-\bar{x}\omega^2 m + j\bar{x}\omega R_m + \bar{x}s = F \quad (I-2)$$

Considering the transducer as a receiver a substitution can be made for the force:

$$F = PA$$

where  $P$  is the pressure

$A$  is the area of transducer face



and further, if a large polarizing voltage is applied such that the total charge is essentially constant, then the signal voltage developed (V) is approximately proportional to the displacement X:

$$V = kX$$

hence:

$$-kVw^2m + jkVwRm = kVs = PA$$

$$-Vw^2m + jVwRm + Vs = \frac{PA}{k} \quad (I-3)$$

Microphone sensitivity is given by:

$$M = \frac{V}{P}$$

so:

$$-Mw^2m + jMwRm + Ms = \frac{A}{k} = \text{constant} \quad (I-4)$$

We have three terms that indicate three distinct and different regions of operation:

(a) Low frequency or stiffness controlled region:

$$Ms \approx \text{constant}$$

$$M \approx \text{Constant}$$

(b) High frequency or mass controlled region:

$$Mw^2m \approx \text{Constant}$$

$$M \approx \frac{\text{Constant}}{w^2}$$

In this region the response should fall off at a rate of 12 db per octave with increasing frequency.

(c) Mid-frequency or resistance controlled region:

$$MwRm \approx \text{Constant}$$

$$M \approx \frac{\text{Constant}}{w} \quad (I-5)$$





In this region the hydrophone response should fall off at a rate of 6 db per octave.

The E/S transducer with its large diameter to wavelength ratio is assumed to be operating in this region over the frequency range of the investigation (20 Kcps to 200 Kcps).

Considering the same region, one way of expressing the transmitting sensitivity is:

$$S_i = \frac{P}{I}$$

where I is the driving current for constant voltage V,  
but since:

$$I = \omega CV$$

where C is the capacitance of the transducer

$$S_i = \frac{P}{\omega CV} \quad \text{but from (I-5)} \quad V \approx \frac{P}{W} \quad (\text{constant})$$

$$\text{so } S_i \approx \frac{\text{Constant}}{C} = \text{constant}$$

Another way of expressing the transmitting sensitivity is:

$$S_v = \frac{P}{V}$$

where V is the driving voltage for constant current.

Since

$$V = \frac{I}{\omega C}$$

$$S_v = \frac{P\omega C}{I} \quad \text{but from (I-5)} \quad V \approx \frac{P(\text{Constant})}{W}$$

$$S_v = \omega (\text{Constant}) \quad (\text{I-7}) \approx \frac{I}{\omega C} (\text{constant})$$



In this case the transmitting sensitivity should increase with frequency by 6 db per octave.

The calibration data obtained for 5 transducers is in agreement with the resistance-control assumption and the conclusions of equations (I-5), (I-6) and (I-7).

Looking at equations (I-5 and (I-6) it can be seen that the impedance of the transducer should also be frequency dependent:

$$\text{from (IV-5)} \quad M = \frac{V}{P} \approx \frac{\text{constant}}{w}$$

$$\text{from (IV-6)} \quad S_i = \frac{P}{I} \approx \text{Constant}$$

$$\text{Impedance} = Z = \frac{V}{I} = \frac{V/P}{I/P} = \frac{\text{Constant}/w}{1/\text{Constant}}$$

$$Z \approx \frac{\text{Constant}}{w} \quad (\text{I-8})$$

This is to be expected since the E/S transducer is no more than a capacitor.

## B. Design and Construction

### 1. General

Reference is made to Figure I-1 which shows a cross-sectional view of the transducer. The fixed electrode is the aluminum plate while the movable electrode is the thin aluminum film on the outer side of the mylar; the one mil mylar constitutes the solid dielectric. The electrical circuit is completed by means of a coaxial cable connected to the two electrodes by means of the screw terminal and silver painted area shown on the diagram. A small air cushion exists between the fixed electrode and the mylar; the concentric grooves in the aluminum plate add to the air cushion and increase the sensitivity by adding compliance to the system.



By means of the air chamber in the back of the transducer pressure equalization is obtained which makes the sensitivity independent of depth. Such pressure equalization was described by Kuttruff and Wille (12 ); there will of course be a limiting depth for any given size of chamber but one of the transducers constructed for this investigation was successfully operated at a depth of 40 meters with no apparent change in sensitivity.

The transducer diameter of 24 cm is equivalent to 8 wavelengths at 50 kcps; this was considered satisfactory and made for a convenient handling size.

Many hours were spend in developing techniques for the construction of a satisfactory transducer; so many subtle details were involved in the final technique that a step by step procedure is outlined in Appendix I-B.2.

Once the mylar was bonded to the plexiglass rim a coating was required to protect the thin aluminum film from the action of the sea water. Such a coating has negligible effect on the transducer performance provided that its mass is not significant, its thickness is much less than a quarter wavelength, and it does not contain air bubbles. In practice a coating of Epon 828 of thickness 0.35 to 0.40 mm was consistently obtained; this more than satisfied the quarter wavelength criterion even at the upper limit frequency of 200 Kcps. The response curves obtained for several transducers showed that the added mass of the coating did not effect the resistance-control assumption described earlier.





In determining the resonant frequency, resistance and stiffness of the system it was assumed:

$$R_w \approx S \text{ at } 20 \text{ Kcps}$$

$$R = R_m + R_r$$

$$R_m \ll R_r$$

$$R \approx R_r$$

where  $S$  is the stiffness

$R_m$  is the mechanical resistance

$R_r$  is the radiation resistance

$$\text{for } ka \gg 1 \rightarrow R_r = \rho_0 c \pi a^2 = 2.05 \times 10^5$$

$$\text{hence: } S \approx R_r = 4.1 \times 10^9 \frac{\text{Newtons}}{\text{Meter}}$$

The resonant frequency is given by:

$$W_o = \sqrt{\frac{S}{M_o + M_r}}$$

where  $M_o$  is the measured mass of the radiator = 0.0228 kg.

$M_r$  is the added mass due to the radiation reactance.

$$\text{let } W_o = \frac{S}{M_o} = 4.24 \times 10^6$$

For a piston in the range  $Ka \gg 1$ ,  $M_r \ll M_o$

hence the resonant frequency is:

$$f_o = 680 \text{ Kcps}$$

Front and rear views of a finished transducer are shown in Figures I-2 and I-3 respectively.

The greatest difficulty encountered was in maintaining a water-tight seal for the face; if water penetrated the protective epoxy coating it would attack the aluminum film and gradually



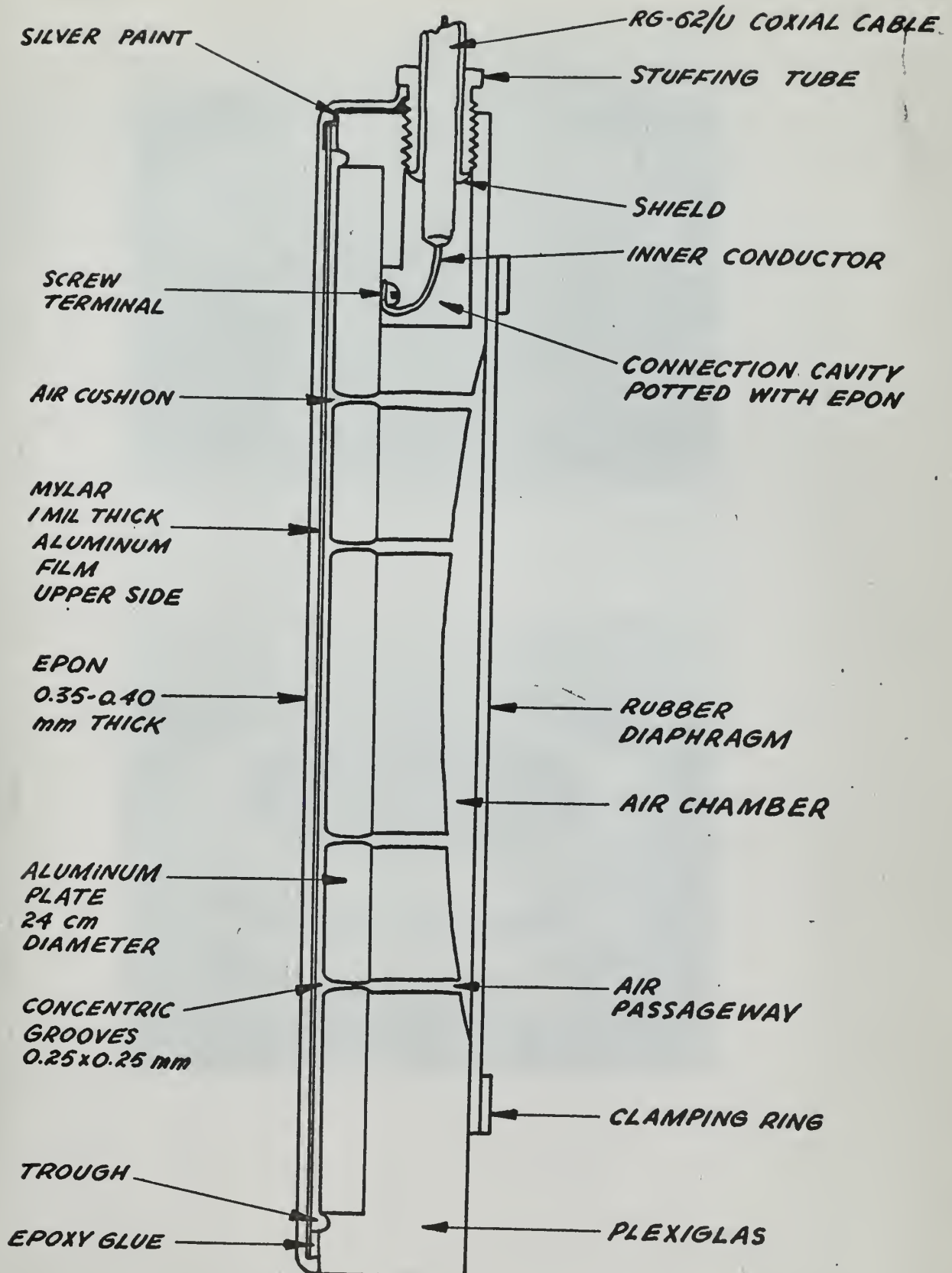


FIGURE I-1 ELECTROSTATIC TRANSDUCER CROSS-SECTION







Figure I-1 Front View of finished Transducer



Figure I-2 Rear View of finished Transducer





Figure 1-4 Piece Interior with due to water penetration



reduce the effective area of the transducer. An example of face deterioration due to water penetration is shown in Figure I-4, a photograph of the face removed from transducer 4 after about a week of operation in the sea.

Two different resins were used in constructing the transducers, Shell Epon 828 and Shell Epon 1004. Operationally, there was little difference but the 828 was used in most cases because of its easier handling qualities. Both epons are described in Appendix I-B.3.

## 2. Construction Procedure

### Problem Statement:

- (1) To provide sufficient tension in the mylar face while the adhesive is drying,
- (2) To keep water from getting in under the rubber pressure-compensating diaphragm,
- (3) To seal the face so that the water cannot react with the aluminum coating on the mylar,
- (4) To keep the contained air from being forced out through the coaxial cable,
- (5) To provide a good electrical contact between the mylar aluminum film and the outer conductor of the coaxial cable.

### Construction Procedure:

- (1) The following is a step by step procedure for the final stage construction of the transducer using Figure I-1 diagram as a reference.
- (2) The area around the stuffing tube hole is coated





with silver paint and allowed to dry.

(3) The coaxial cable must be fitted to the transducer by means of the stuffing tube. The cable is fed thru the stuffing tube, the shielding layed back and soldered to the body of the stuffing tube; the thread of the stuffing tube is coated with neoprene before insertion; the portion of the thread that protrudes after tightening must be left bare so that a good electrical connection can be made to the aluminum film on the face.

(4) After the stuffing tube connection is tightened, the center conductor can be formed into a loop and connected to the aluminum plate by means of the provided screw.

(5) Since the "connection cavity" provides a path for the air to be forced out it is filled with Epon; this effectively seals off the contained air.

(6) Epon is spread on the back of the transducer on the area which will be directly under the diaphragm claming ring; this ensures a good seal when the diaphragm is in place.

(7) A sheet of rubber is placed over the back of the transducer and the clamping ring placed in position; holes are punched thru the rubber when the pre-drilled holes of the ring are lined up with the holes in the transducer back; the rubber is stretched during this operation and held taunt while the ring is tightened down. The excess rubber can be trimmed off with a knife.

(8) The ring area is coated with Epon to complete the sealing of the back. The transducer is left to dry 24 hours.

(9) A piece of mylar out to size is placed on the



aluminum frame with the aluminum film facing up; an ohmmeter should be used to determine which side is the aluminum side since it is difficult to determine this visually.

(10) The mylar is stretched over the frame by means of strips of electrical plastic tape adhered to the mylar and pulled down and over the edge of the frame. Care should be taken to keep the tape off that part of the mylar within the area of the frame hole.

(11) The frame is put aside and a film of Epoxy Glue applied to the outer ring of the transducer between the edge and the aluminum plate (or edge of trough if later model).

(12) The frame is fitted over the transducer so that the mylar rests on the face; the edges are pressed to ensure good contact with the epoxy glue, the frame is then weighted to ensure tension in the mylar while the glue dries; this setup should be left overnight.

(13) The mylar can be roughly cut away to enable removal of the frame; the mylar is then "cut back" from the edge about one eighth of an inch leaving an outer ring of plexiglas.

(14) Silver paint is not applied to the exposed threads of the stuffing tube and spread down over the front edge of the transducer and over a small area of the aluminum film. Making small grooves in the edge at the area where the paint is to be applied helps in providing a good electrical contact. Once the silver paint has dried a continuity check should be made with an ohmmeter.

(15) A mixture of Epon is prepared and spread over the face of the transducer, which has been placed on a steady, level surface, by means of a corrugated cardboard "spreader" about 4"x5" (any material which will not scratch the aluminum film will suffice).





The Epon can be spread over the entire face quite uniformly with minimum thickness; care must be taken to ensure that there are no pinholes exposing the aluminum and that the coating is spread right to the edge of the transducer.

(16) After the Epon has dried the capacitance of the transducer can be measured on a bridge; it should be  $\geq 0.005$  uf.

(17) The transducer is now ready for use.

### 3. Epon Characteristics

Epons 828 and 1004 were both used in transducer construction with curing Agent U; both were satisfactory but the Epon 828 being a liquid was easier to use and became the preferred coating. The characteristics of the Epons are as follows:

Epon 828: A pourable liquid at room temperature; widely used in wet lay-up laminating, casting and the pathing of electrical equipment, and in formulating adhesives for bonding wood, plastics, metal and glass to themselves and to each other; its low viscosity makes it attractive for contact pressure and vacuum bag laminating at room temperature.

Epon 1104: Supplied as a solid resin and requires a solvent such as Acetone. Combines flexibility, adhesion and toughness with good chemical resistance properties.

Curing Agent U: Provides fast cure at room temperature; has short pot life and low toxicity; gives strong lamination.



$$\begin{aligned} \text{Mixtures (by weight):} \quad & \frac{828}{\text{Agent U}} = \frac{5}{1} \\ & \frac{1004}{\text{Agent U}} = \frac{19}{1} \end{aligned}$$

## C. Characteristics

### 1. Response

With the help of the NEL Transducer Evaluation Center (TRANSDEC) calibration data was obtained for 5 of the 6 transducers taken to San Diego for field measurements.

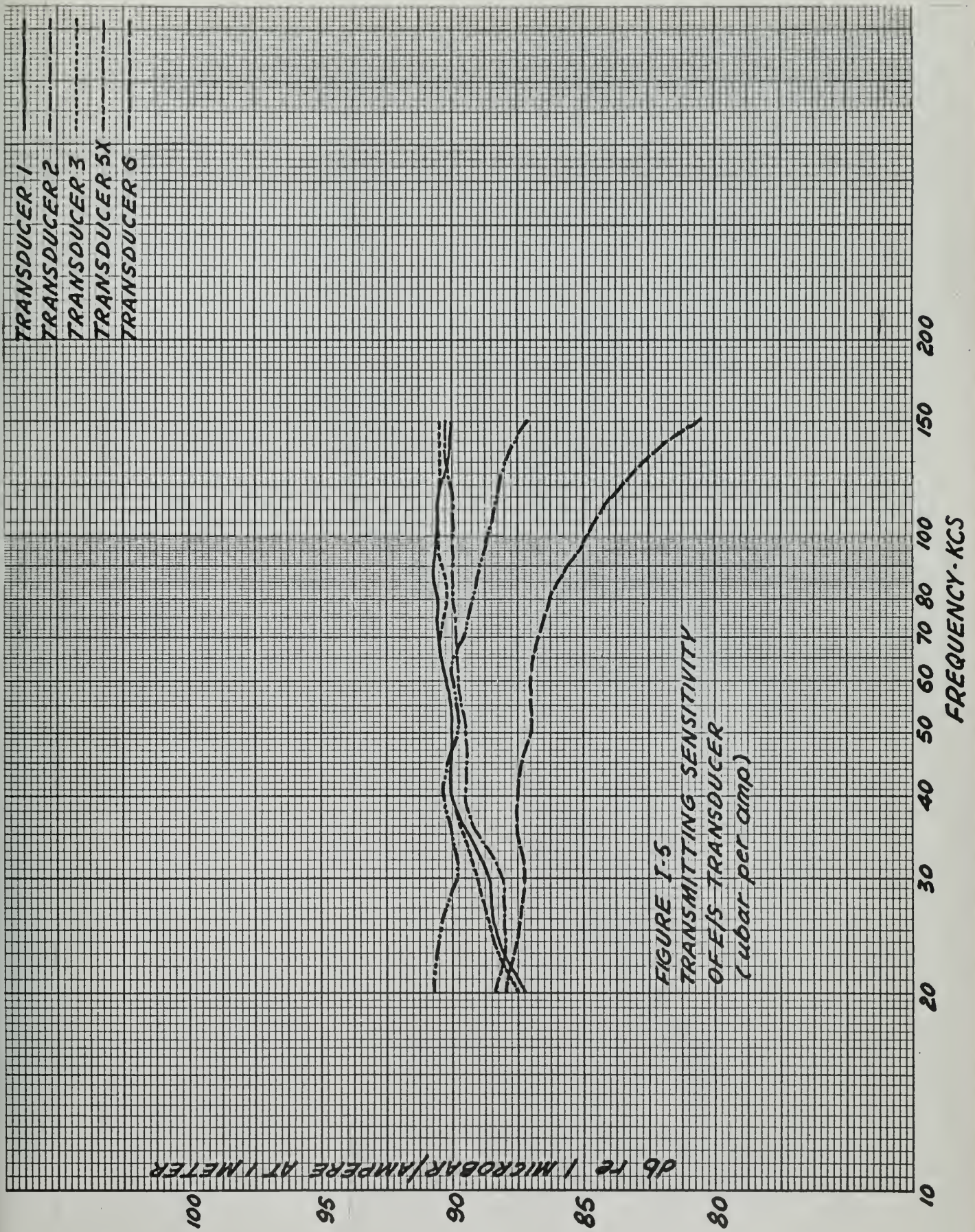
The equations developed in Appendix I-A indicated that the transmitting sensitivity with respect to driving current, in microbars of pressure at one meter per ampers input should be a constant in the resistance controlled region; Figure I-5 shows such curves for the 5 transducers calibrated and with the exception of transducer 6 are within 1.5 db of the 89 db level throughout the 20 Kcps to 150 Kcps frequency range of the calibration.

The transmitting sensitivity can also be expressed in terms of microbars per volt and as was shown in Appendix I-A the sensitivity should vary directly as the frequency or increase at a rate of 6 db per octave; Figure I-5 shows that such is the behavior for all 6 transducers.

The receiving response should, from the developed theory, vary inversely as the frequency or fall at a rate of 6 db per octave. Figure I-7 shows that the 6 db per octave behavior is followed reasonably well although the fall rates of transducers 5X and 6 is slightly different from that of the other 3 transducers in that the slopes of the response curves are slightly different. This

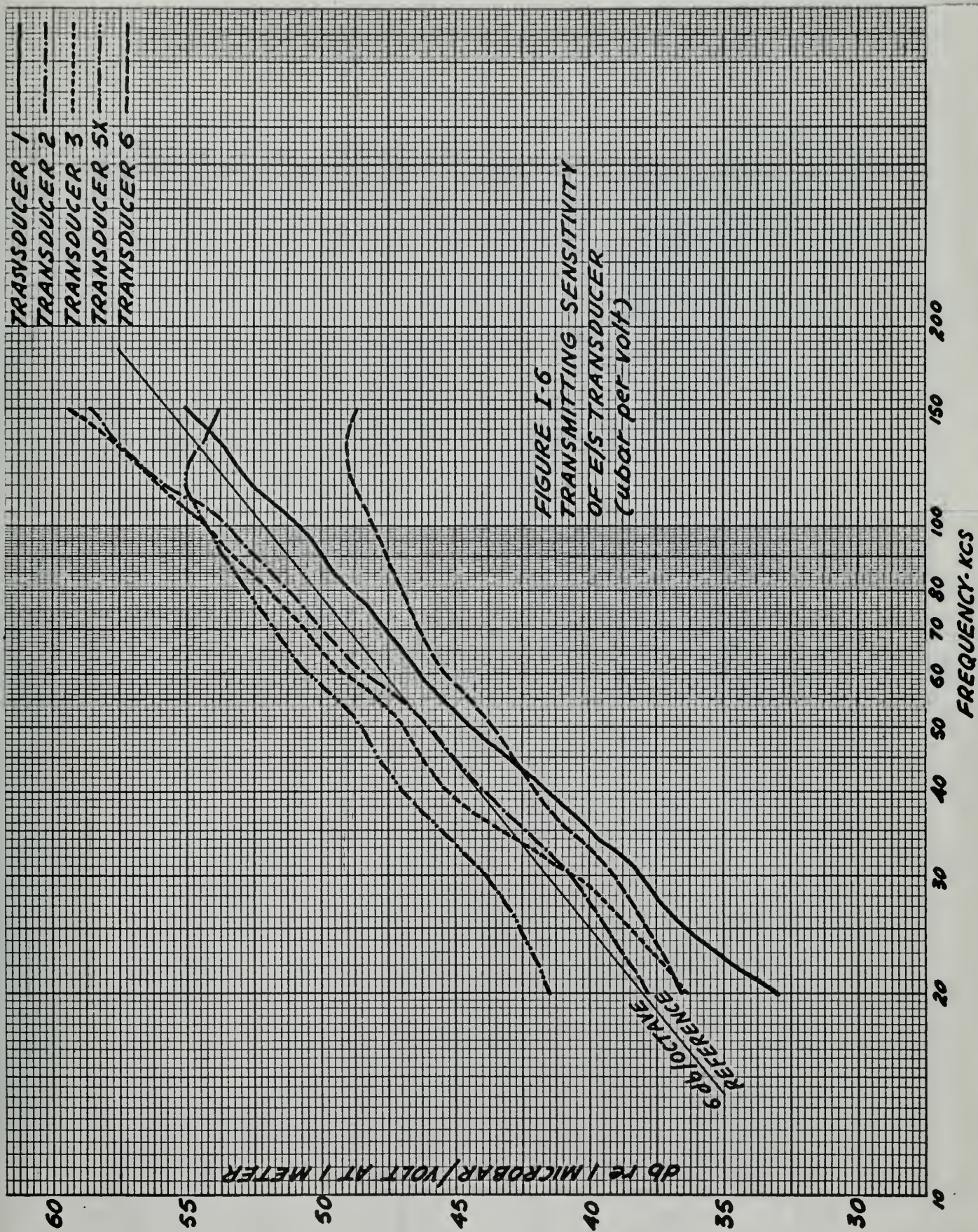






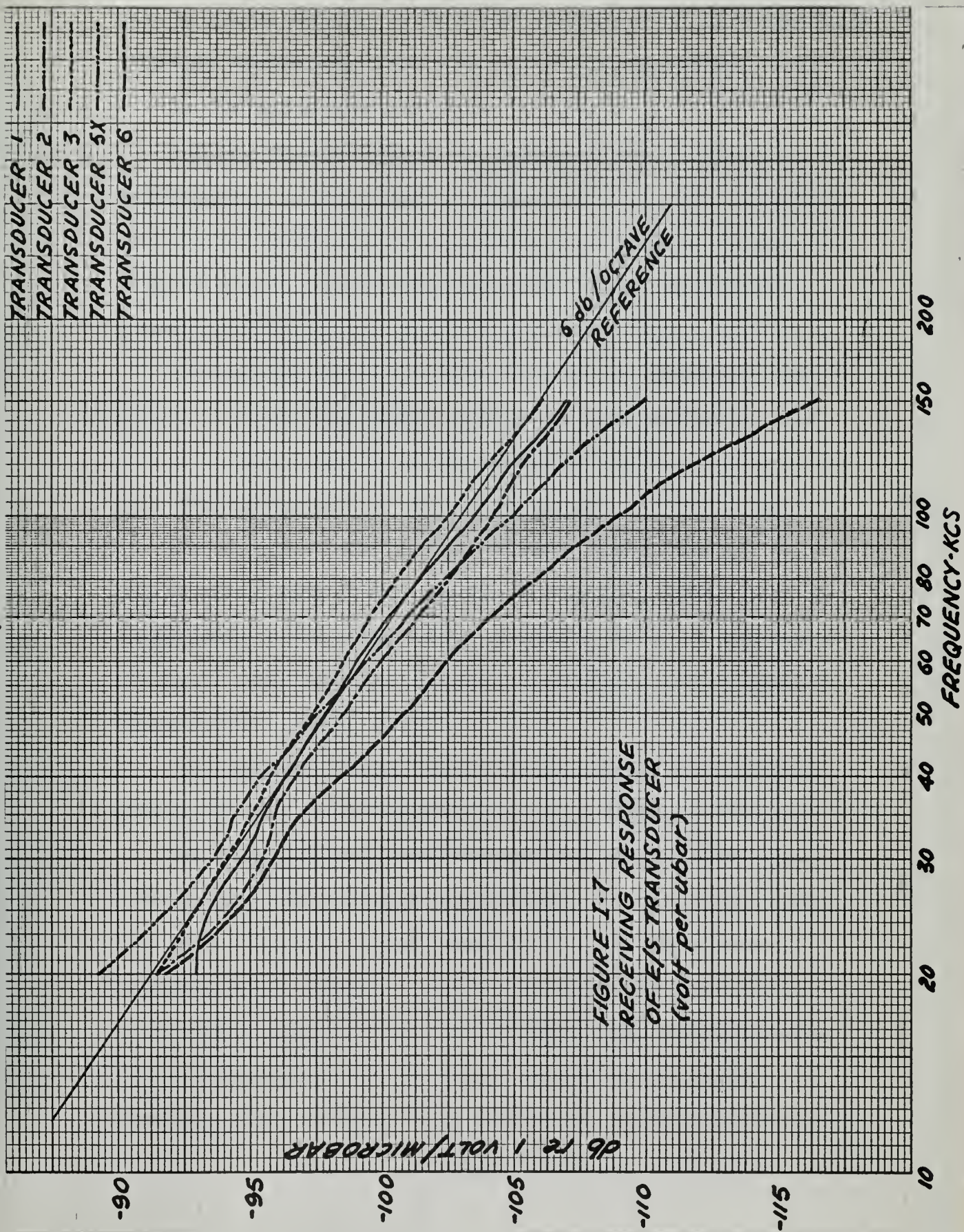
















must be attributable to the fact that transducers 5X and 6 were faced with Epon 828 while 1, 2 and 3 were faced with Epon 1004.

## 2. Radiation Characteristics

The fact that the transducer diameter is quite large ( 8 wavelengths at 50 Kcps) makes it highly directive. The directivity patterns for the 5 transducers calibrated are shown in Figures I-12 to I-18; for all 5 were calibrated at 60 Kcps and in addition patterns for transducer 3 were obtained at 100 Kcps and 150 Kcps.

In comparing the radiation behavior of the transducers with that of the ideal flat piston three things were considered: the effective radius, the db differences between the main lobe and the first side lobes, and the directivity index.

The calculated effective piston radii ranged from 12.5 to 15.5 cm with a mean of 13.2 cm; this was slightly greater than the actual radius of 12 cm and is not surprising since the face must be subject to some flexing action which results in a pattern normally expected from a larger piston.

The directivity index ranged from 29.7 db to 31.8 db with a mean of 30.5 db; the theoretical value for a piston is 29.6 db.

The db difference between the main lobe and the first side lobes proved to be much more inconsistent. The differences ranged from 10.6 db to 16.6 db with a mean of 13.8 db. The theoretical difference for a piston is 17.6 db. In seeking an explanation it would seem that the fact that two different epons were used in the face construction would be a factor, but the two transducers closest to the theoretical value (16.6 db and 16.2 db) had different



faces, so some other non-obvious feature of the construction must be at fault; the thickness of the epon at the edges which varied from the mean thickness by as much as 15% might be a significant factor. The variation in the epon thickness and the fact that the epoxy glue was sometimes squeezed in over the edge of the aluminum plate thereby distorting the circular shape of the radiator slightly accounts for most of the assymetry in the radiation patterns.

In use all the back radiation portions of the directivity patterns were probably suppressed by the rigid steel mounting plate. The mounting can be seen in Figure I-8.

### 3. Capacitance and Impedance Characteristics.

The electrostatic transducer, like the condenser microphone, is a device that depends for its operation on the value of capacitance between a fixed plate and a stretched membrane which in this case is the aluminum film on the mylar.

As in any capacitor:

$C \propto 1/d$  where  $d$  is the separation between plates. For the E/S transducer the dielectric is made up of the mylar and the air cusion in series so that the capacitance  $C$  is given by:

$$\frac{1}{C} = \frac{1}{C_M} + \frac{1}{C_A}$$

where  $C_M$  is the capacitance due to the mylar part of the dielectric.

$C_A$  is the capacitance due to the air part of the dielectric.



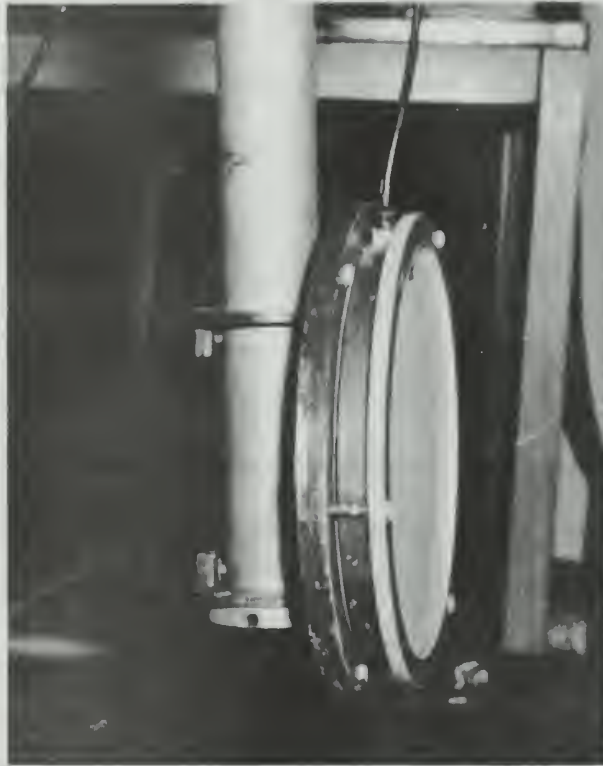


Figure 1 - Transducer Mounting Details





finally

$$C = \frac{K_m \epsilon_0 A}{(d_A K_m + d_m)} \quad (I-9)$$

where  $K_m$  is the dielectric constant for mylar = 3

$\epsilon_0$  is the permittivity of free space =  $8.85 \times 10^{-12}$

$A$  is the area of the aluminum plate =  $4.53 \times 10^{-2} \text{ m}^2$

$d_A$  is the thickness of the air cushion

$d_m$  is the thickness of the mylar =  $2.54 \times 10^{-5} \text{ m}$  (1 mil)

Using a measured value of capacitance at a depth of 10 feet it was found that the thickness of the air cushion at that depth was  $1.88 \times 10^{-5} \text{ m}$  (0.741 mil).

It was found that the value of capacitance increased with water depth due to compression of the air cushion; the increase was quite rapid to 5 feet and then leveled off to a linear increase of approximately 100 uuf per foot of depth. If the pressure compensation system were perfect the capacitance would not change at all with depth but such a system would require an exact combination of back diaphragm and mylar membrane stiffness relationships.

Capacitance data taken at the NEL Tower to a depth of 45 feet is plotted in Figure I-9. Curve data between the surface and 5 feet is only approximate due to difficulties created by wave action.

Shallow-water data was later gathered in the USNPGS anechoic tank; this data is plotted in Figure I-10.





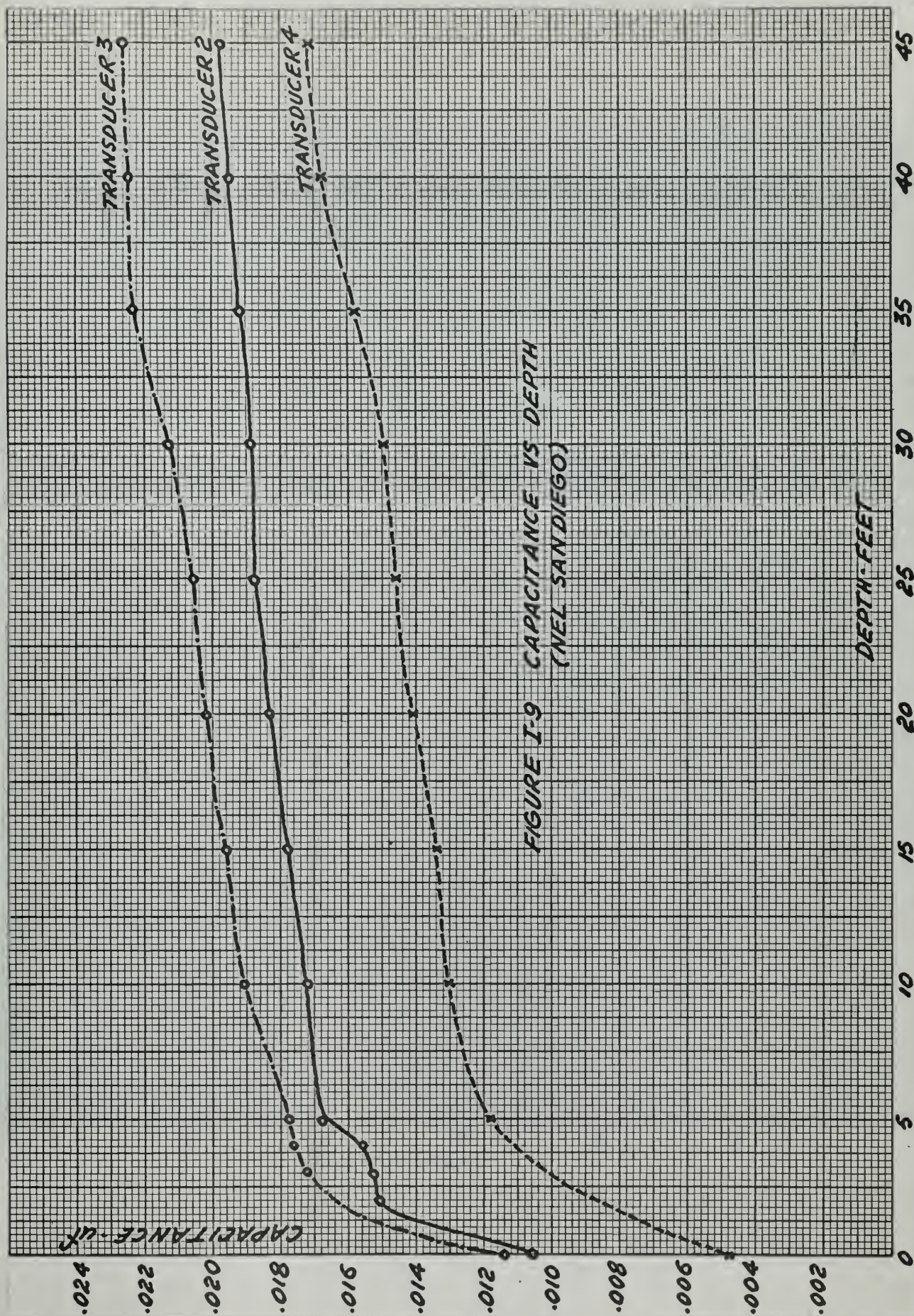
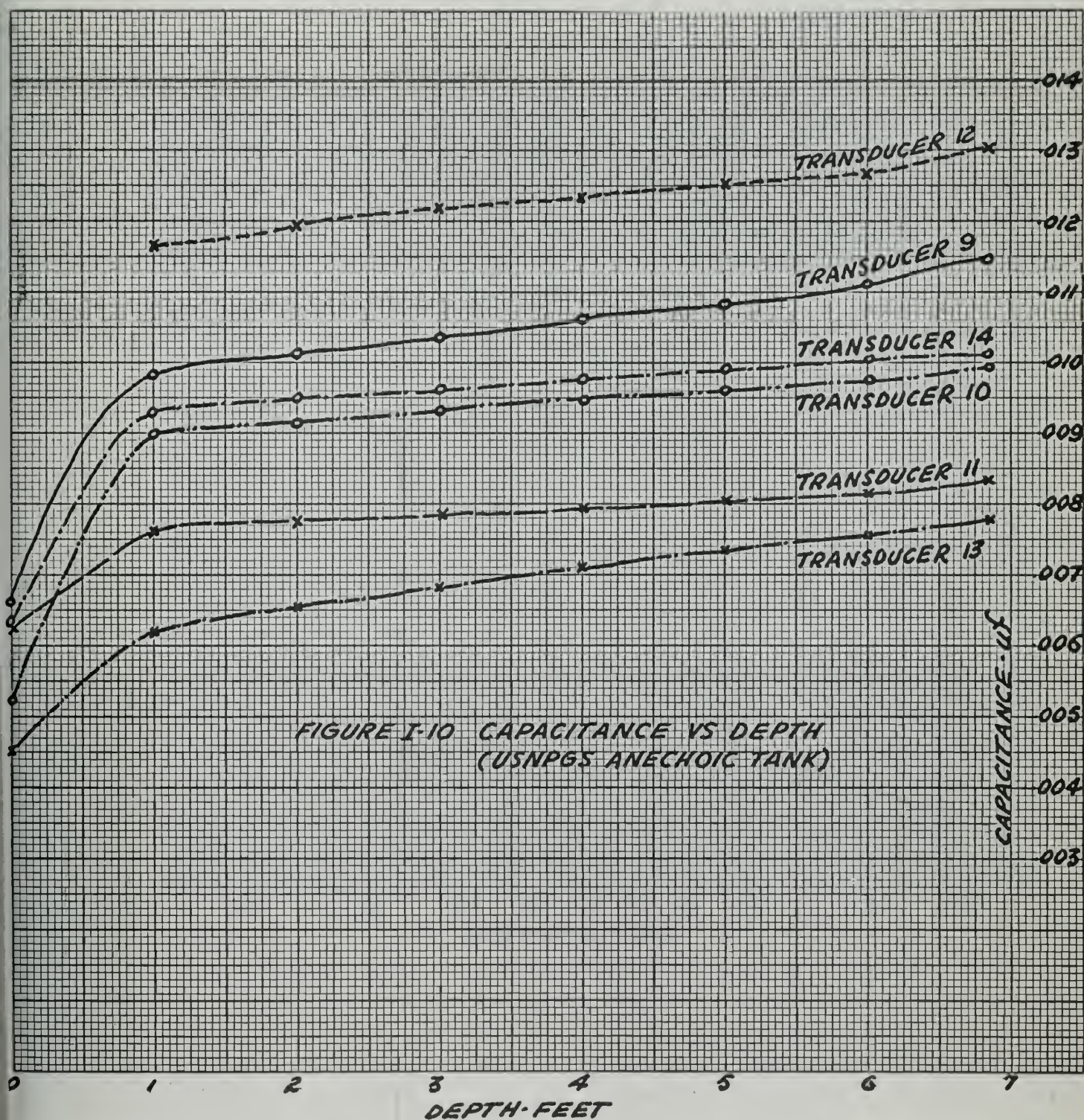


FIGURE I-9 CAPACITANCE VS DEPTH  
(NEL SANDIEGO)

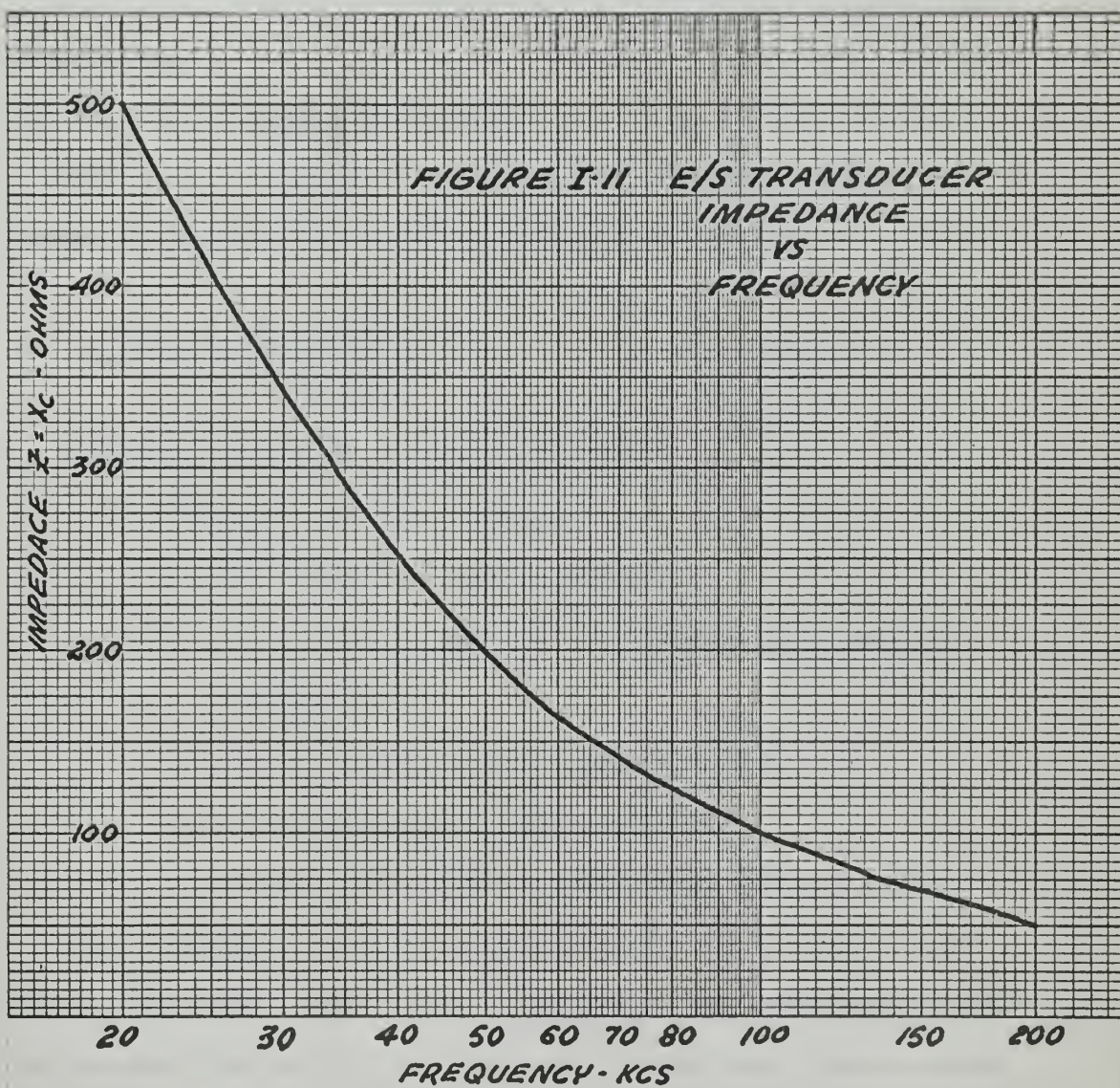














The impedance of the E/S transducer depends solely on the value of capacitance discussed above. A curve showing impedance variation over the frequency range of interest is plotted in Figure I-11 using the average value of capacitance at 10 feet from Figure I-9.

#### D. Factors Affecting Sensitivity

The receiving sensitivity of the E/S transducer depends on a number of factors which can be expressed as follows:

$$\text{Sensitivity} = M \propto \frac{E_0^2 a_e^2 E}{dT Z_{me}} \quad (\text{I-10})$$

where  $E_0$  is the dc polarizing voltage

$a_e$  is the effective radius

$E$  is the source pulse amplitude

$d$  is the spacing between the aluminum plate and the aluminum film.

$T$  is the tension in the stretched mylar.

$Z_M$  is the mechanical input impedance.

$e$  is the charging factor associated with the mylar

The polarizing voltage  $E_0$  was maintained at 450 volts (upper limit of available power supply) throughout the investigation while the source pulse voltage ( $E$ ) used was 50 volts peak; these values gave an approximate 10:1 ratio and ensured that harmonic distortion would be minimized.

The ratio  $E_0/d$ , the electric field intensity, will increase with depth as the air cushion is compressed as described earlier;





such action increases the sensitivity.

In construction of the transducer pre-stretching the mylar determined the value of the tension  $T$ ; this was a compromise situation since the stiffer the mylar was the more the transducer behaved like an ideal flat piston and it is also a factor in the pressure compensation system; on the other hand increasing  $T$  decreases the sensitivity as shown in (I-10).

Increasing the depth increases the mechanical input impedance  $Z_m$  which tends to decrease the sensitivity, however the increase of electric field intensity with depth is the dominant factor so that the overall effect of increased depth is an increase in sensitivity, disregarding the pressure-equalization system.

It was found that there was a charging factor ( $e$ ) associated with the mylar due to the polarizing voltage  $E_0$ . For a given polarity of  $E_0$  for a period of time would have a neutralizing effect so that if the polarity was again reversed there was an observable increase in sensitivity. This effect did not present any major problem and did not have any noticeable effect on the data as long as the polarity remained unchanged for the duration of a data taking period.

In addition to all of the above, the fact that the capacitance is depth sensitive as described earlier, means that wave action could also be a factor affecting sensitivity, particularly if the transducer is operated close to the surface. As an example of this effect consider the following:



Wave velocity = 10 knots

Wave period = 3 sec

Wave amplitude = 6 ft (crest to trough)

For a wave train equivalent to 20 msec the maximum change in depth for the period of the wavetrain works out to be  $\sim 0.1$  ft; the resulting sensitivity changes are tabulated in Table I-1.

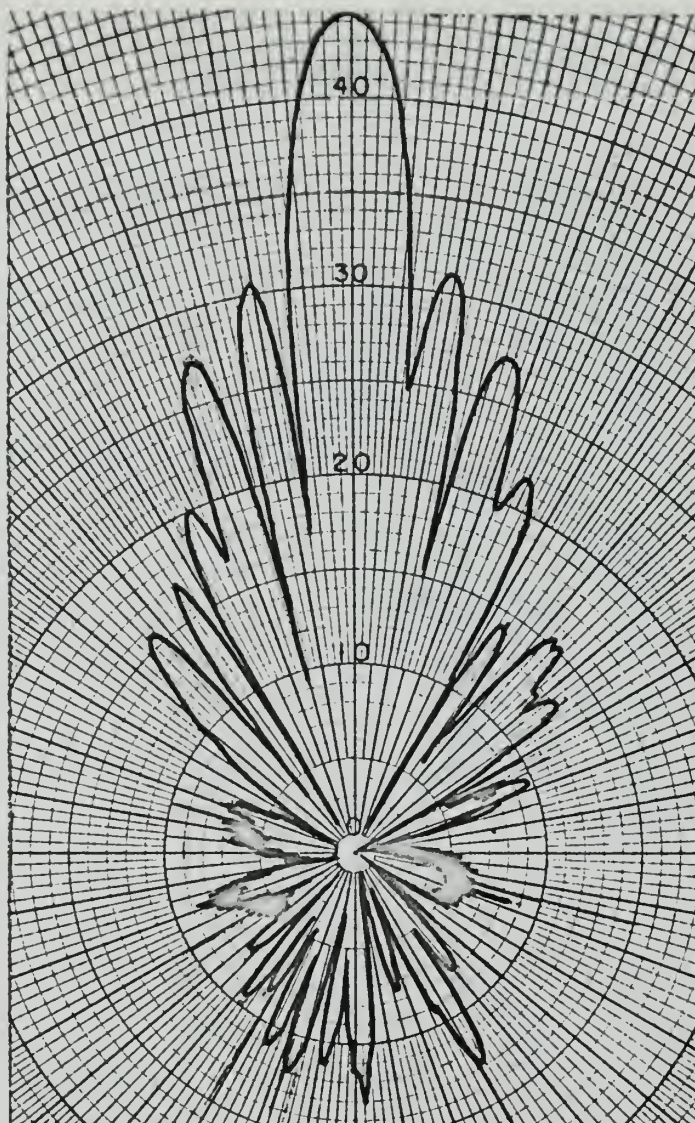
Table I-1

Depth-ft	C-uuf	C-uuf	M
5	15400	45	.0260 db
10	16400	10	.0054 db
20	17500	10	.0050 db
40	19600	10	.0044 db

Since the transducer was always operated at depths of 10 feet or greater the above effect was not significant in this investigation.







1 db per radial division

Effective Radius 12.5 cm

Frequency 60 KCS

1st Side Lobes Down 13.5 db

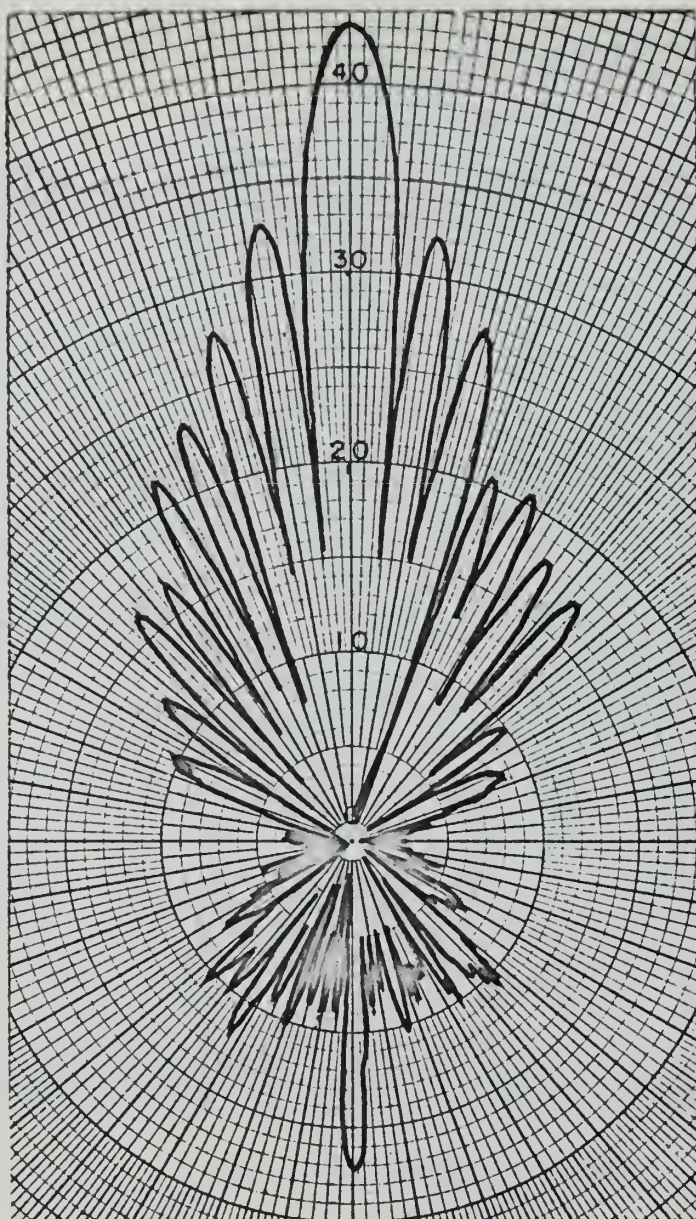
Test Distance 8 meters

Directivity Index 29.9 db

Depth 6.1 meters

Figure 1 - 12 Directivity Pattern-Transducer No. 1





Effective Radius 15.5 cm

Frequency 60 KCS

1st Side Lobes Down 10.6 db

Test Distance 8 meters

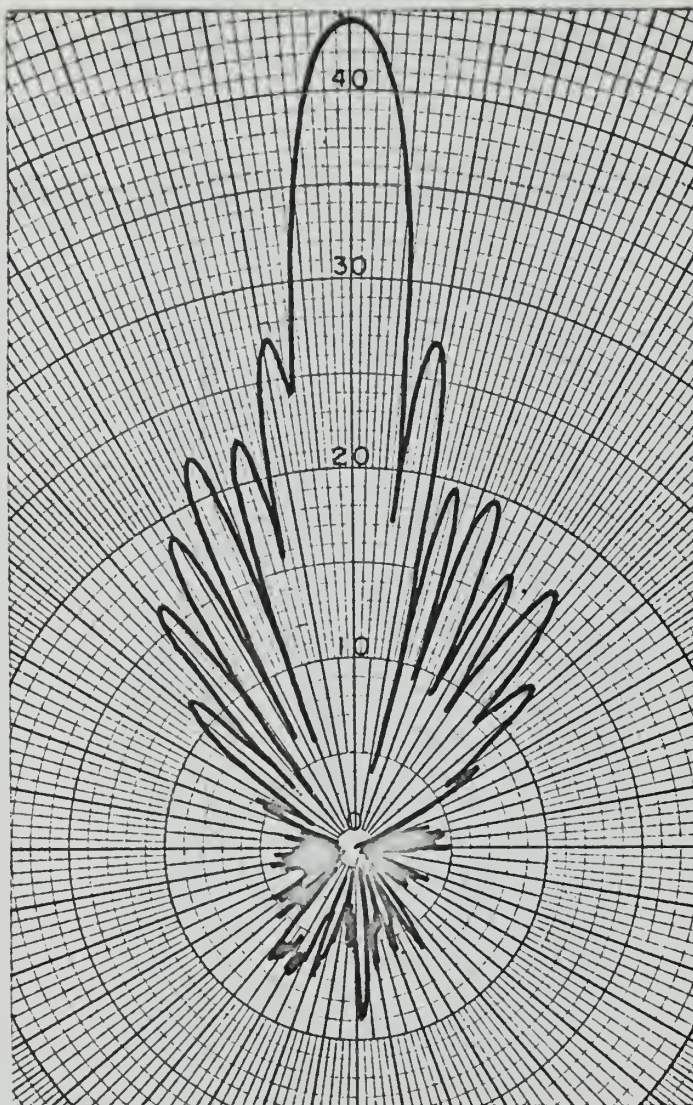
Directivity Index 31.8 db

Depth 6 meters

Figure I-13 Directivity Pattern-Transducer No. 2







1 db per radial division

Effective Radius 12.3 cm

Frequency 60 KCS

1st Side Lobes Down 16.6 db

Test Distance 6 meters

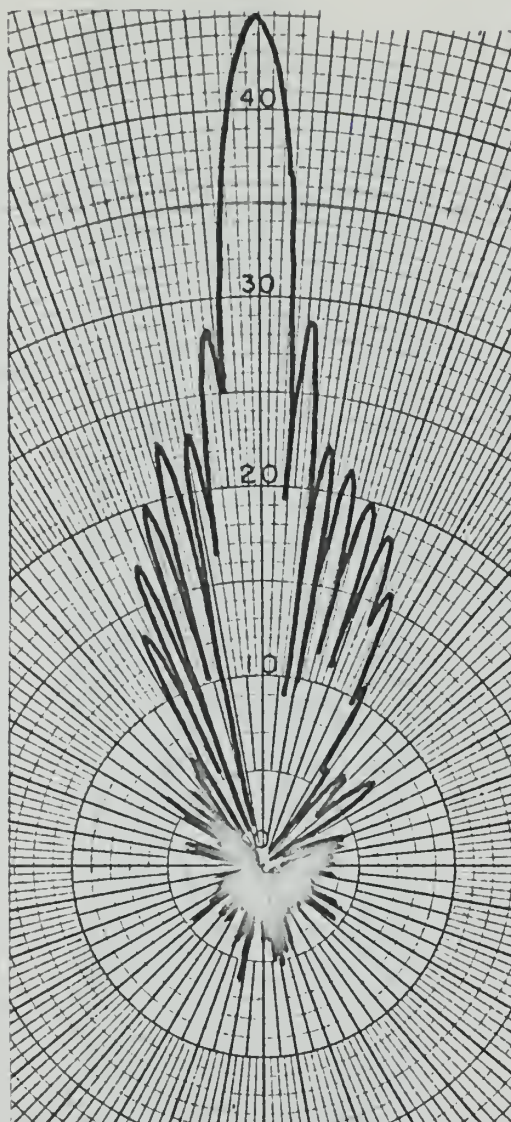
Directivity Index 29.7 db

Depth 6.1 meters

Figure I-14 Directivity Pattern-Transducer No. 3







1 db per radial division

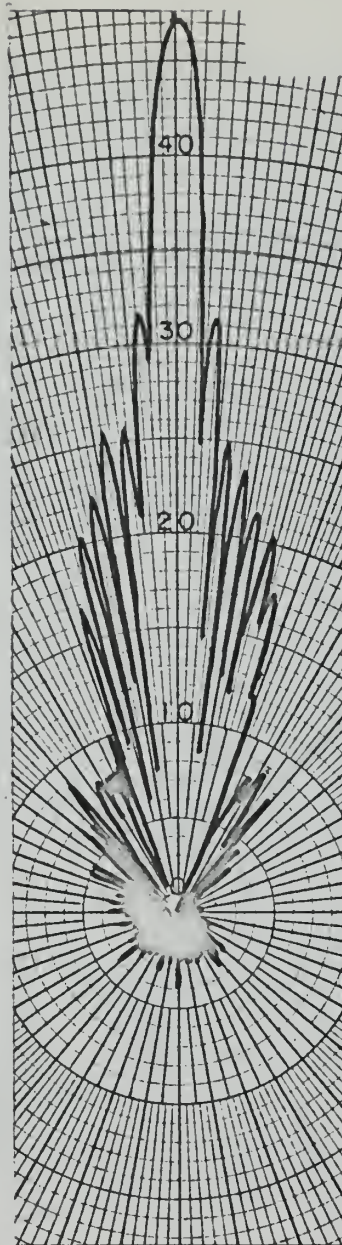
Frequency 100 KCS

Test Distance 8 meters

Depth 6.1 meters

Figure I-15 Directivity Pattern-Transducer No. 3





1 db per radial division

Frequency 150 KCS

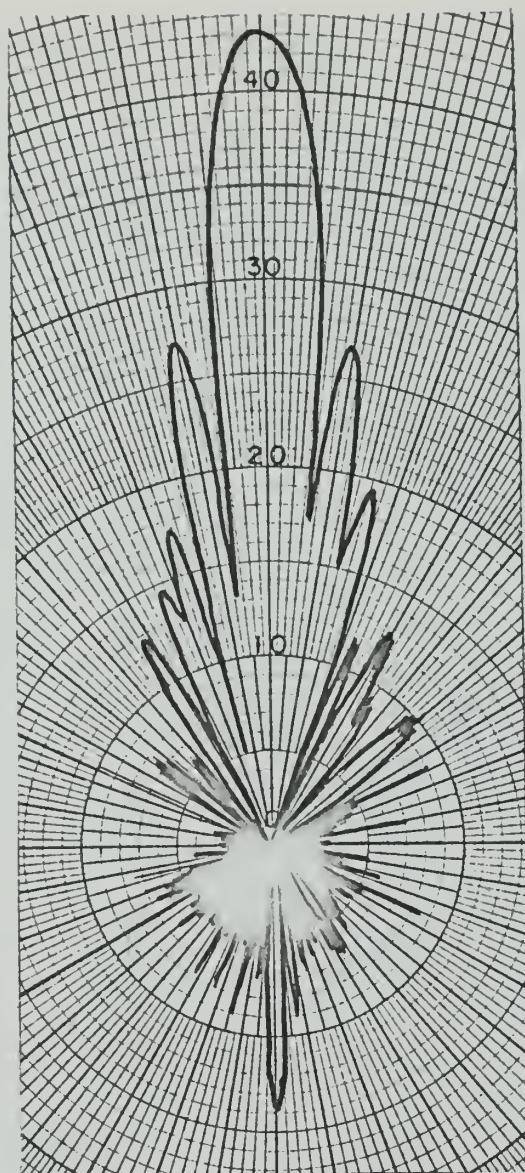
Test Distance 8 meters

Depth 6.1 meters

Figure I-16 Directivity Pattern-Transducer No. 3







1 db per radial division

Effective Radius 12.3 cm

Frequency 60 KCS

1st Side Lobes Down 16.2 db

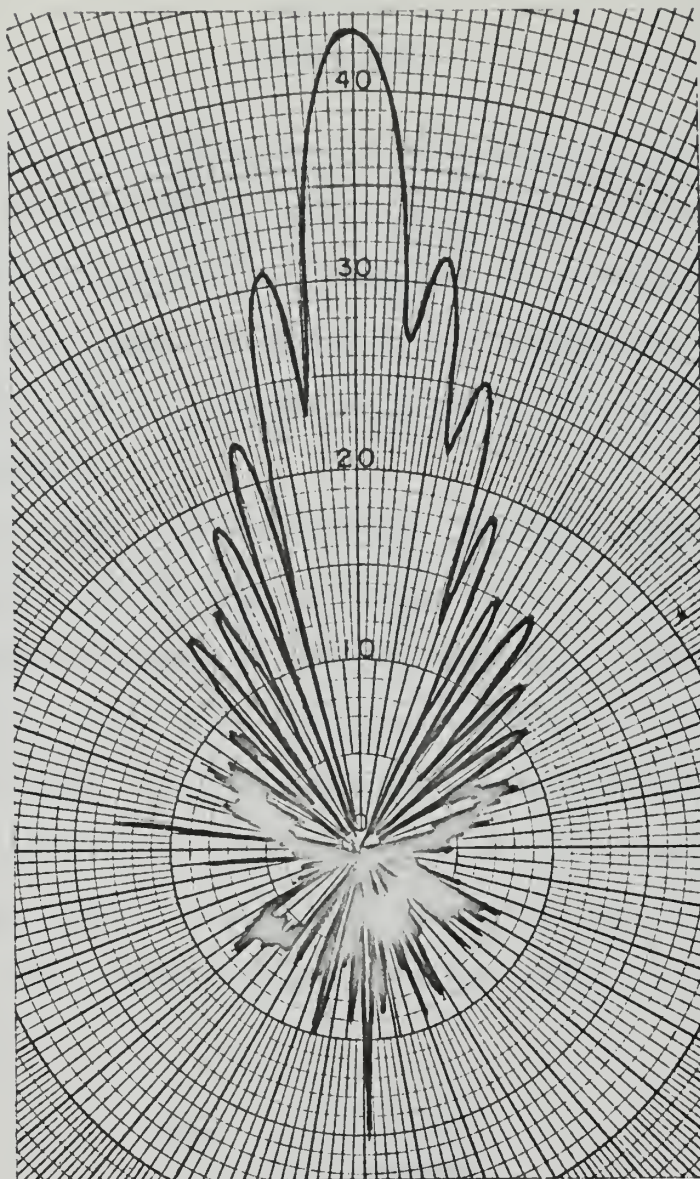
Test Distance 8 meters

Directivity Index 29.7 db

Depth 6.1 meters

Figure I-17 Directivity Pattern-Transducer No. 5X





1 db per radial division

Effective Radius 13.5 cm

Frequency 60 KCS

1st Side Lobes Down 12.2 db

Test Distance 8 meters

Directivity Index 30.6 db

Depth 6.1 meters

Figure I-18 Directivity Pattern-Transducer No. 6



## APPENDIX II

### SIGNAL GATE

This circuit utilizes a General Radio 1217-B Pulse Generator to gate an AC input signal. When used in conjunction with the General Radio 1396-A Tone Burst Generator, it provides an additional 50 db separation of on and off signals and it provides more flexibility in controlling pulse width. The circuit is shown in Figure II-1.

The gate consists of two sections. The first section is a common emitter amplifier whose collector bias voltage is supplied by the negative terminals of the pulse generator. The width of the collector bias pulse determines the width of the resulting wave pulse output. The bias resistors are adjusted for maximum gain. Since high gain is the principal means for obtaining a high on/off signal ratio a high gain transistor was used for this amplifier. The forward DC current transfer ratio for the 2N1380 is listed as

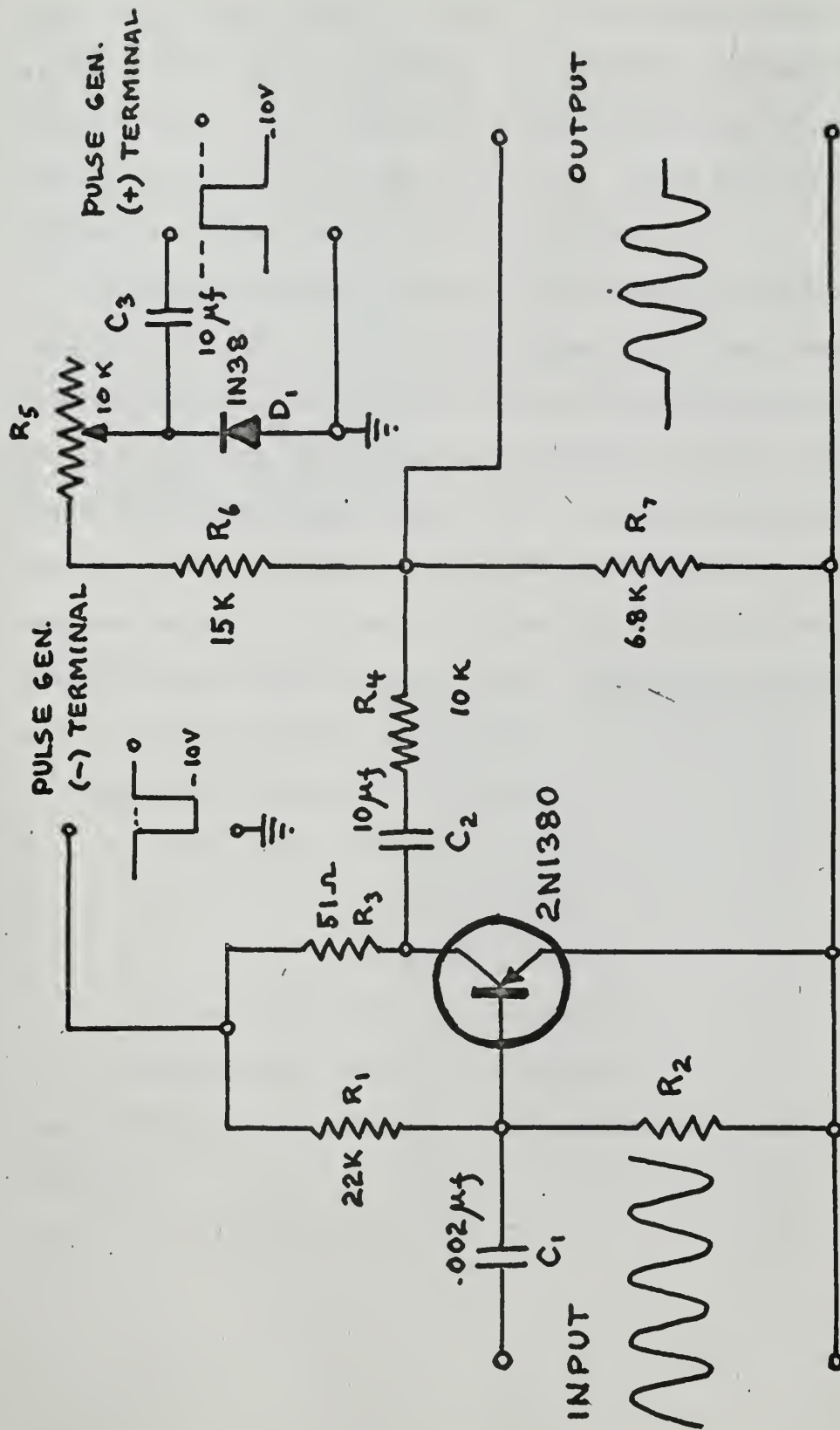
$$\begin{array}{rcl} & 30 \text{ minimum} \\ h_{FE} & = & 100 \text{ typical} \\ & 300 \text{ maximum} \end{array}$$

The purpose of  $C_1$  is to present a high impedance to the signal generator and provide DC isolation. The value of  $C_1$  was determined by decreasing it until the peaks of the first cycle of a 200 Kcps wave pulse were the same amplitude as the subsequent peaks.

The collector output voltage contains a negative five volt pedestal which is removed by the second section.  $C_3$  and  $D_1$  clamp







SIGNAL GATE CIRCUIT DIAGRAM  
FIGURE II - 1



the "plus" output of the General Radio 1217-B pulse generator so that the minimum value of the pulse is zero at the cathode of  $D_1$ . This positive going pulse is added to the wave pulse thereby nullifying the negative pedestal.  $R_5$  provides a fine control of the pedestal height. The addition is accomplished by the resistive network consisting of  $R_4$ ,  $R_5$ ,  $R_6$ , and  $R_7$ . Figure II-2 shows typical wave pulse outputs at 40 and 200 Kcps.

For optimum performance the collector bias pulse amplitude should be adjusted so that the gated signal is clipped symmetrically when the amplifier is overdriven. Then the oscillator amplitude should be adjusted for maximum output amplitude without clipping. These adjustments should be made every time the frequency is changed. When time does not permit following this procedure, the pulse generator should be set once at ten volts and the oscillator amplitude set as shown in Figure II-3. This shorter procedure will cost a few db in on/off signal ratio.

Brief specifications are as follows:

On/off ration = 61 db at 25 Kcps

56 db at 60 Kcps

45 db at 200 Kcps

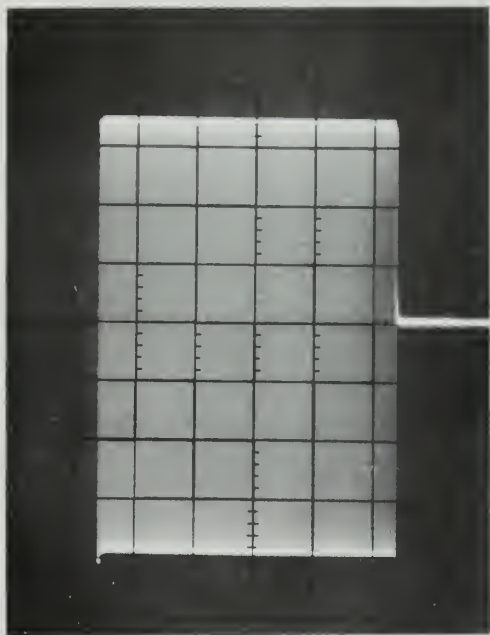
Minimum pulse width = 5 microseconds

Maximum pulse width = 8 milliseconds

Figure II-4 shows the variation of voltage transfer ratio with frequency.







Signal to be output

at 200 MHz

original--100 /cm

original--100 /cm

(0. 100 /cm)

(0. 100 /cm)

original--100 /cm

original--100 /cm

original--100 /cm

original--100 /cm

Signal to be output

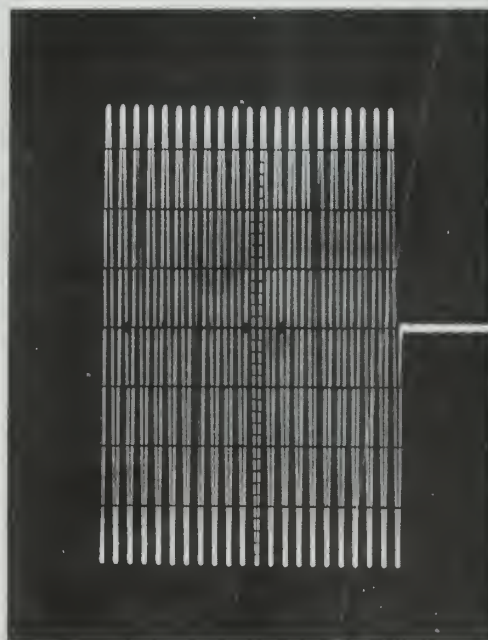
at 200 MHz

original--100 /cm

original--100 /cm

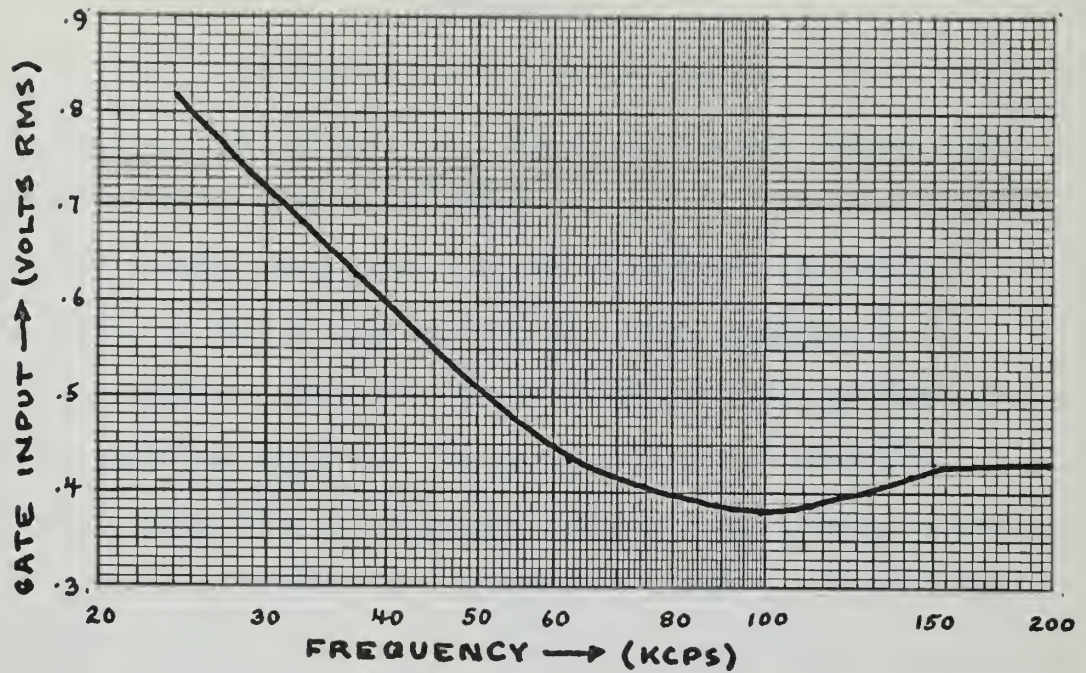
original--100 /cm

(0. 100 /cm)



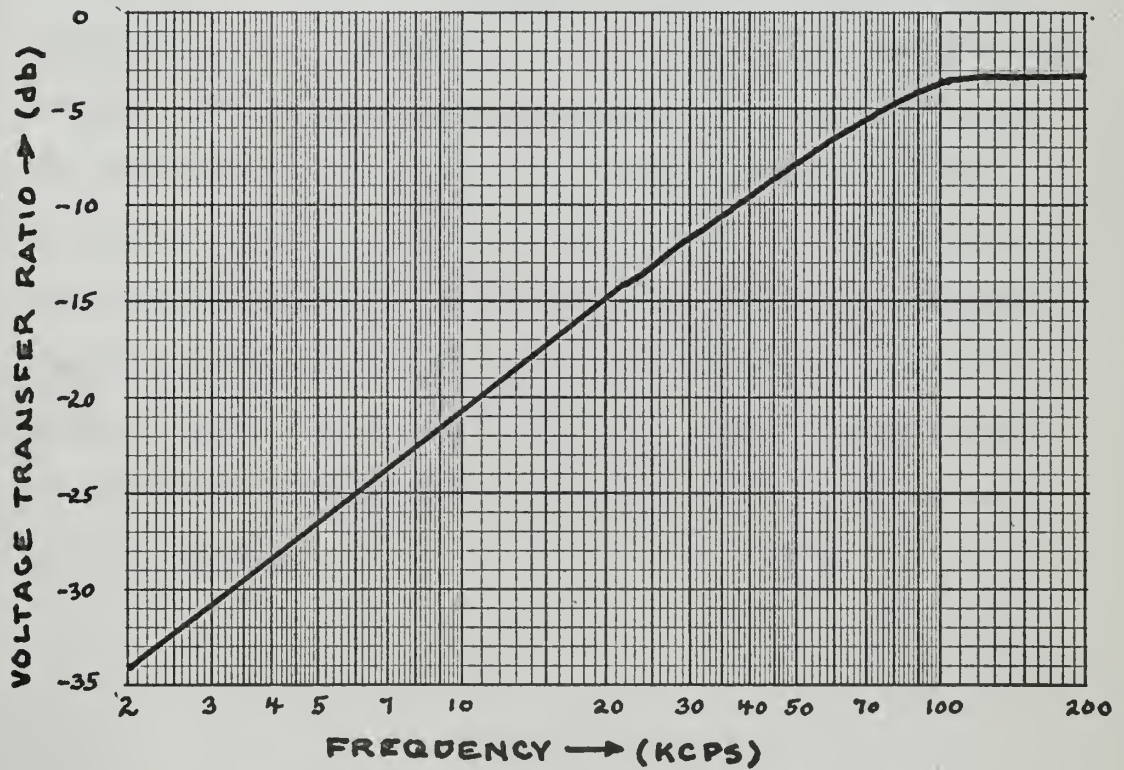
Signal to be





MAXIMUM GATE INPUT WITHOUT DISTORTION

FIGURE II-3



VOLTAGE TRANSFER RATIO ( $E_{out}/E_{in}$ )

FIGURE II-4



## APPENDIX III

### TRANSMIT-RECEIVE SWITCHING SECTION

This section isolates the transmitter from the receiver using three networks. See figure III-1.

The network consisting of  $D_1$  and  $D_2$  offers a low series impedance to high voltage signals and a high impedance to low voltage signals. Therefore the echo signals do not see the low power amplifier impedance.  $R_2$  and  $C_1$  isolate the polarizing voltage supply from the AC signal voltages. The network consisting of  $D_3$  and  $D_4$  presents a low impedance to ground for high voltage signals and a high impedance to ground for low voltage signals. The main bang therefore appears across  $R_1$ . Several volts of main bang to appear across  $D_3$  and  $D_4$  which seriously saturates the filter, amplifiers, and oscilloscope display thus making the electronic switch necessary. The network at the output of the GR-1217-A pulse generator differentiates both pulse generator outputs and clips the resulting positive pulses. The remaining negative pulses trigger the electronic switch so that channel A is on during the main bang and channel B is on at all other times. The switching transients appearing at the output of the electronic switch are shown in Figure 2-4. They were not wide enough to saturate the receiver. The transmit-receive switching section provides about 60 db of rejection.





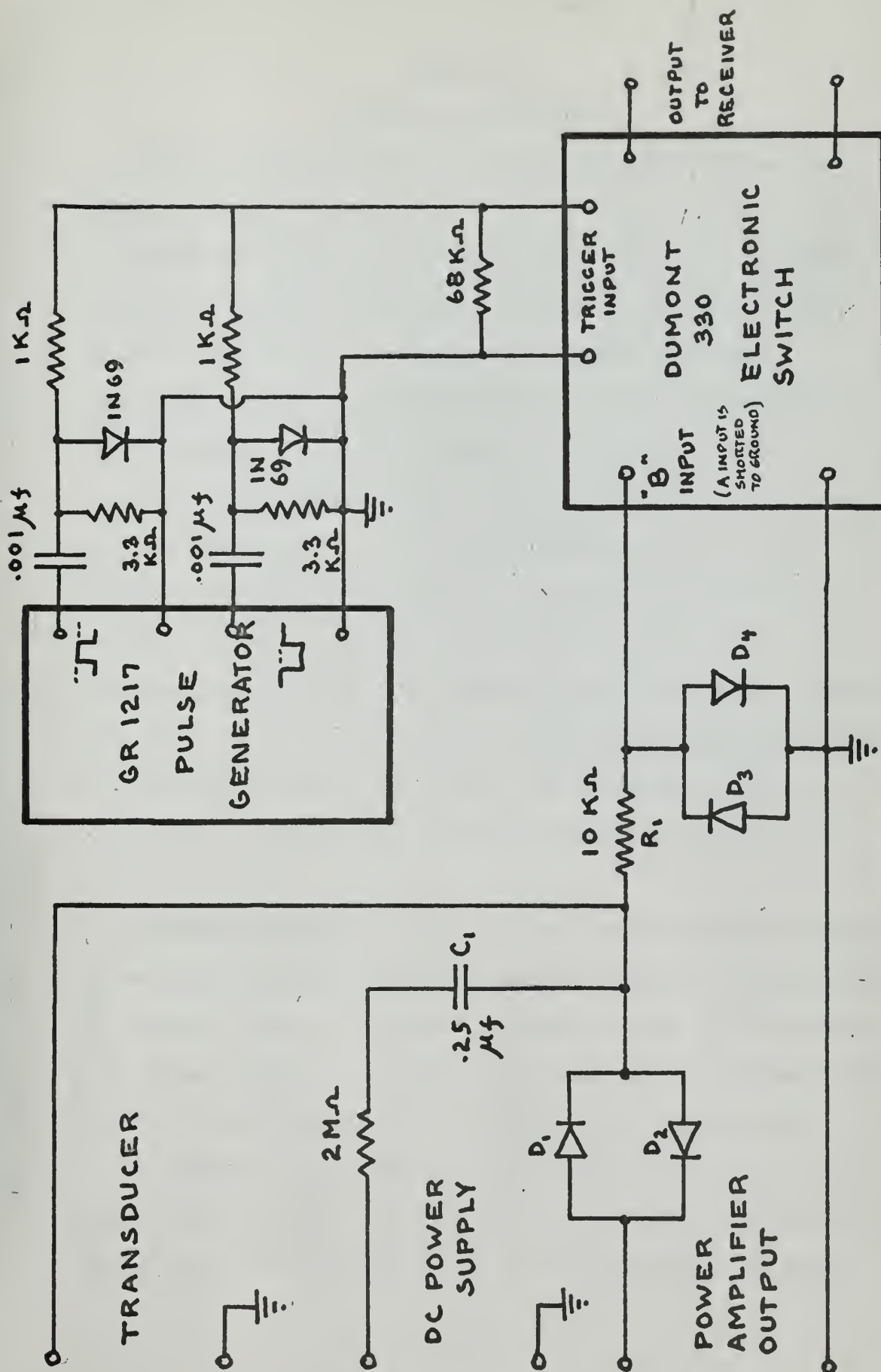


FIGURE III-1  
TRANSMIT-RECEIVE SWITCHING SECTION



## APPENDIX IV

### SYSTEM CHARACTERISTICS

Overall characteristics of the pulse echo system as one unit are presented below.

The usable frequency range is 16 Kcps to 200 Kcps. The upper frequency is limited by the band pass filter, and low electrical signal to noise ratio.. Power amplifier distortion at high frequencies was noticable but not serious. The low frequency is limited primarily by the divergence of the transducer beam.

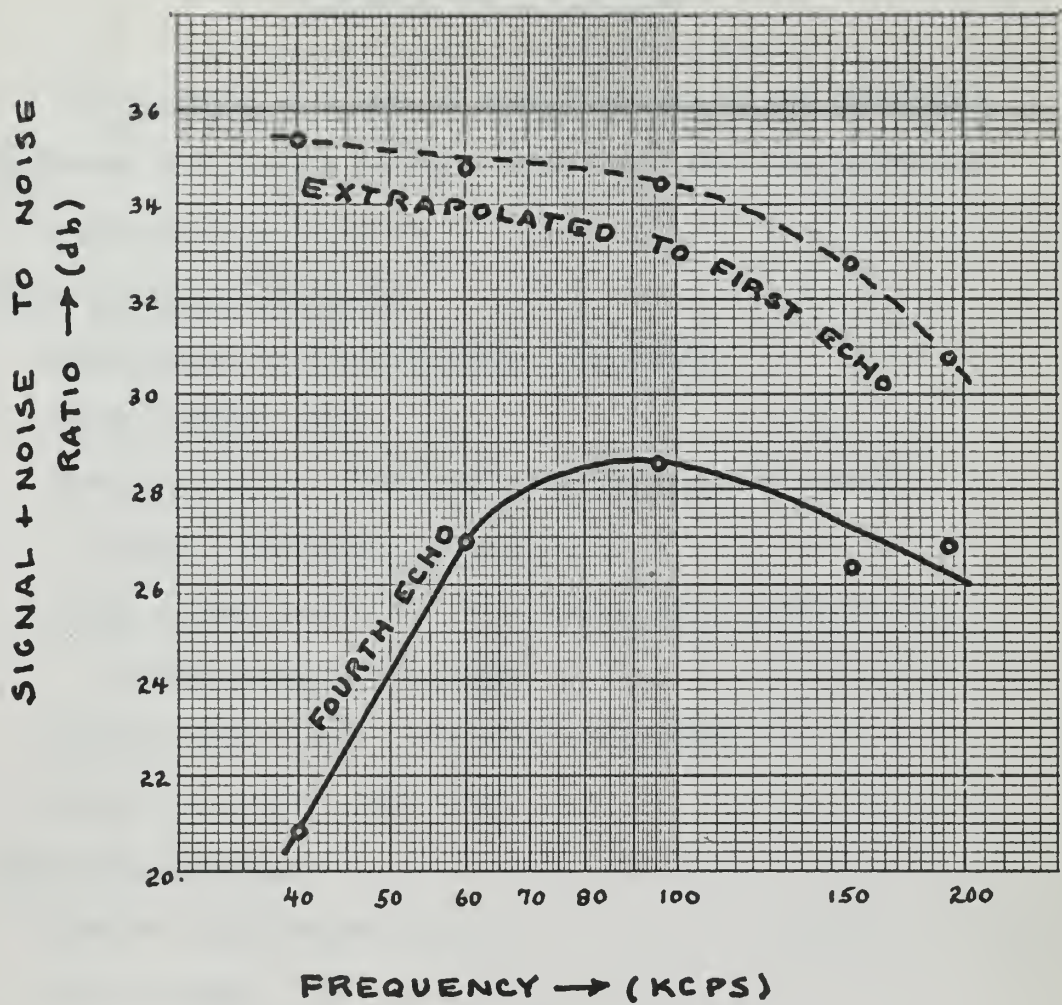
The received signal to noise ratio as a function of frequency is shown in Figure IV-1. Although the broken curve is a true indication of receiver performance, the solid curve is more an indication of system usefulness since the fourth echo was arbitrarily fixed as the first usable echo and it includes transducer divergence effects. The electronic switch was the primary offender in contributing noise to the system. The transmitted signal to noise ratio is greater than 90 db below 60 Kcps and greater than 80 db above 60 Kcps.

The maximum wave pulse width available for the system is limited by the tone burst generator to 128 cycles. The pulse repetition rate is controlled from the tone burst generator and may be varied from a continuous signal to one pulse in ten seconds. The minimum pulse width is five microseconds and is limited by the signal gate.

The receiver output deviates from linearity no more than about 0.25 db or 2.8 percent. This figure is approximately the order of the resolution of the instruments used in making the linearity check.







SIGNAL PLUS NOISE TO NOISE RATIO  
VS  
FREQUENCY

(AT FIRST AND FOURTH  
ECHOS)

FIGURE IV - 1



## APPENDIX V

### EQUIPMENT SPECIFICATIONS

The following is a list of specifications of the commercial equipment used in this project. Only those features pertaining to the project are included.

#### Audio Oscillator TS-382-DU

Manufactured by TRAV-LER Radio Corporation

Serial number: 1152

Frequency range: 20-200,000 CPS, continuously variable  
within four decade ranges

Output signal amplitude: 0-10 volts, continuously variable  
within seven decade ranges

Harmonic distortion: less than one percent

Output impedance: 1000 ohms

#### Tone Burst Generator

General Radio Company 1396-A

Serial Number: 397

Signal frequency range: DC-500 Kcps

Maximum input voltage:  $\pm$  seven volts

Input impedance: About 10 kilohms

Maximum voltage output:  $\pm$  seven volts

Total distortion: less than -60 db at 1 Kcps and 10 Kcps

On/off ratio: -40 db with maximum signal input

Output impedance: 600 ohms

Gating voltage output: 12 volts, gate open

-12 volts, gate closed



### Pulse Generator

General Radio Company 1217-B

Pulse repetition frequency: 2.5 CPS to 500 Kcps

internally generated. Externally controlled, DC to 1

MCPS. Output pulse is started by negative slope.

Output pulse duration: 100 nsec to 1 second in seven decade ranges

Rise and fall times: Less than 20 nsec.

Overshoot and noise: less than 5 percent of amplitude.

PRF stability: .05 percent

Pulse duration stability: .03 percent

### Power Amplifier

General Radio Company 1233-A

Serial number: 539

Frequency Range: 20 to 3 MC

Output power: 15 watts

Voltage output: .1 microsecond rise time, negligible overshoot.

Input voltage: .2 volt for full output

Input impedance: 100 K-ohms, 37 pf

Distortion: Less than three percent at rated output.

Noise: 70 db below 15 watts or .3 volt peak to peak.

Power consumption: 120 watts at zero output

### Electronic Switch

DuMont Laboratories type 330

Serial number: 1111

Input impedance: 2 megohms, 45 pf





Response: Flat to DC with 60 pf load, response down no more than 1 db at 10 MC.

Hum and noise level: 2.5 MV maximum exclusive of s switching transients.

Switching signal rise time: Two percent of square wave period

External trigger switching rate: Zero to 100 Kcps

Synchronizing Voltage: At least  $\pm 2$  volts peak with rise.

.02 V/ s.

Power consumed: 160 watts

#### Electronic Filter

Spencer-Kennedy model 302

Serial Number: 1483

Frequency limits: 20 CPS to 200 Kcps in four decade ranges

Rate of attenuation in rejection band: 18 db/octave per section

Maximum attenuation: 90 db

Input impedance: 2 megohms, 30 pf

Maximum input signal: Six volts peak

Output impedance: 300 ohms

Minimum external load for operation according to specification:

Ten K-ohms

Noise Level: 80 db below one volt (using detector bandwidth from zero to 40 Kcps)

Power consumed: 120 watts



## Amplifier

Hewlett-Packard model 450-A

Serial numbers: 228-06357 and 228-06379

Gain: 20 db  $\pm 1/8$  db or 40 db  $\pm 1/8$  db

Frequency response: 20 db gain: within  $\pm \frac{1}{2}$  db 5 to 1 MC

40 db gain: within  $\pm \frac{1}{2}$  db 10 to 1 MC

Maximum input voltage: 20 db gain: 1 volt

40 db gain: .1 volt

Input impedance: one megohm, 15 pf.

Output: Tenvolts maximum across 3000 ohms (or more)

Distortion: Less than one percent at rated output

Internal impedance: less than 150 ohms

Equivalent input noise level: 40 db gain: about 40 v

20 db gain: about 250 v

Power consumed: 55 watts





## APPENDIX VI

### TEST SITES

#### a) The U. S. Navy Electronics Laboratory Oceanographic Research Tower.

The Tower was chosen as the site for field work because it provided a stable platform [29] for the experimental equipment and was situated in water of known characteristics.

The Tower is located one mile off Mission Beach where the bottom is gently sloping rippled sand and the mean tidal depth is 56 feet. The dominant longshore current is from the north [30] so that water from Mission Bay or the flood control channel is unlikely to reach the Tower and the surrounding water is of almost constant salinity in the winter.

The electronic equipment was placed on the Main Deck in the room at the right hand side of Figure VI-1 with the transducers, reflector, temperature and oxygen sensors mounted on a car beneath Figure VI-2. This car was firmly mounted on railway tracks and could be lowered to the sea bottom so that it provided a stable platform at any desired depth.

The low self-noise of the Tower was an advantage which may have been somewhat offset by echoes from the structural members and marine growth shown in Figure VI-2.

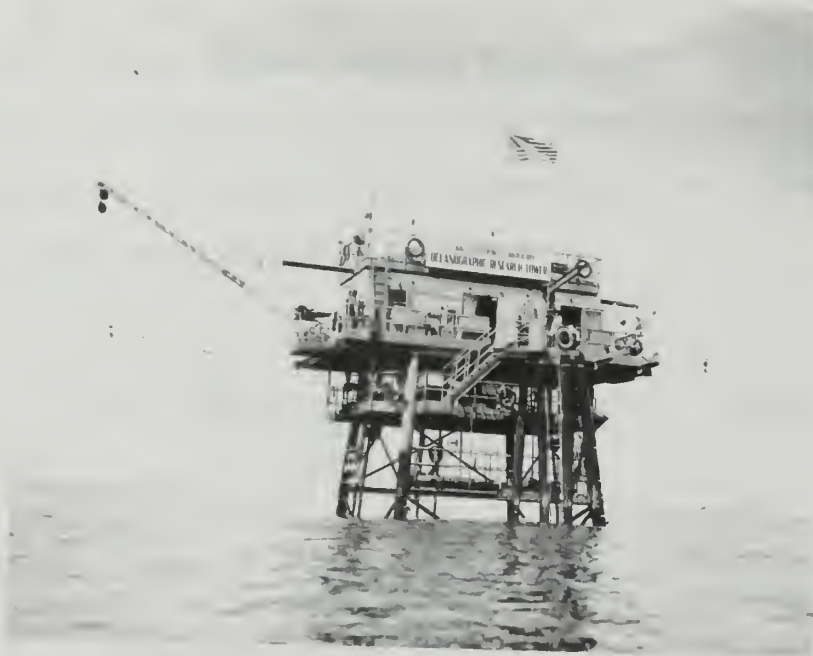
Full details of the construction and operation of the Tower will be given in a publication which is now being prepared by Dr. E. C. LaFond of NEL.



b) Monterey Bay

Experiments were performed in Monterey Bay using the USNPGS Oceanographic Research Vessel as platform. Engines were stopped while measurements were being made so that effects due to wake and screw action were minimised. The vessel was usually moored 300 yards off shore and 300 yards east of Monterey Municipal Wharf in 27 feet of water over a sandy bottom.





N.E.L. TOWER, LOOKING WEST , FIGURE VI-1

OFFICIAL  
PHOTOGRAPH  
U.S. NAVY



TRANSDUCER ASSEMBLY INSTALLED, N.E.L. TOWER  
FIGURE VI-2

OFFICIAL  
PHOTOGRAPH  
U.S. NAVY





## APPENDIX VII

### VELOCITY SHIFT COMPUTER PROGRAM

This computer program computes sound velocity shift as a function of frequency in sea water containing a distribution of bubble sizes. The basis of the computation is the expression for added compressibility due to bubbles

$$a' = \frac{3V}{\rho R^2 \omega_o^2} \frac{\frac{\omega_o^2}{\omega^2} - 1}{\left[\frac{\omega_o^2}{\omega^2} - 1\right]^2 + \left[d \frac{\omega_o}{\omega}\right]^2} \quad (5-4)$$

For a distribution of discrete bubble sizes the compressibilities will add obtaining at frequency  $\omega$ .

$$a'(\omega) = \sum_i \frac{3V_i}{\rho R_i^2 \omega_i^2} \frac{\frac{\omega_i^2}{\omega^2} - 1}{\left[\frac{\omega_i^2}{\omega^2} - 1\right]^2 + \left[d_i \frac{\omega_i}{\omega}\right]^2}$$

where  $i$  will be the index for each bubble size. The velocity at frequency,  $\omega$ , will then be:

$$v(\omega) = \frac{1}{\frac{1}{C_o^2} + a(\omega)}$$

The damping factor as a function of bubble resonant frequency has been approximated by

$$d_i = .027 \left[ \frac{\omega_i}{2\pi \times 10^3} \right]^{0.322} \quad (VII-1)$$



Equation VII-1 fits Devin's curve within about five percent below 200 Kcps. [4] .

The bubble resonant frequency as a function of bubble radius at one atmosphere has been approximated by

$$\omega_i = \frac{8 \pi \times 10^6}{R_i} \quad (\text{VII-2})$$

where  $R_i$  is in microns.

In equation VII-2 the bubble is assumed to behave adiabatically, surface tension is ignored and the external pressure is taken as standard sea level pressure.

The computer program provides a print out of volume concentration, formula coefficient, damping factor, and resonant frequency for each bubble size; and a print out of sound velocity shift from 1500 M/S, density times compressibility and frequency. The formula coefficient is

$$C_i = 3V_i/R_i^2\omega_o^2$$

The U. S. Naval Postgraduate School subroutine DRAW was utilized providing a graph of velocity shift versus frequency. [31]  
Figure VII-1 is a flow diagram for this program. Table VII-1 is a typical print out.

Several volume distributions were put into the program. Each will be described below.

Glotov, Kolobaev and Neuimin distribution.

For  $25 < R < 69 \mu$

$$V_i = B(.2067R_i - 5.17) \times 4.19 \times 10^{-18}R_i^3$$





For  $71 < R < 105 \mu$

$$V_i = B \times 1.91 \times 10^{-13} R_i$$

For  $107 < R < 325 \mu$

$$V_i = B \times 2.57 \times 10^{-7} / R_i^2$$

where

B = scaling factor

$V_i$  = volume concentration of all bubbles with radii one micron on either side of  $R_i$ .

The above formulas are derived from information given by Glotov et. al. in their paper. However the authors indicate that  $R_i^1$  should appear in the denominator of the third formula.  $R_i^2$  was used instead because  $R_i^1$  does not cause  $V_i$  to converge rapidly enough causing a large discontinuity at the target radius of 325 microns.

#### Distributions from attenuation data.

The folume concentrations derived from figure 3-12 were normalized to two micron increments. Two distributions were extracted from this data; the first utilizes all the data and the second utilizes the center portion of the distribution only.

First curve:

For  $16 < R < 26 \mu$

$$V_i = (.50R_i - 8.0) \times 10^{-10}$$

for  $28 < R < 60 \mu$

$$V_i = (.912R_i - 30.1) \times 10^{-10}$$

for  $62 < R < 84 \mu$

$$V_i = (.259R_i - 15.05) \times 10^{-10}$$



for  $86 < R < 110 \mu$

$$V_i = 4.3 \times 10^{-4} / R_i^3$$

for  $112 < R < 156 \mu$

$$V_i = (0.1R_i - 7.8) \times 10^{-10}$$

for  $158 < R < 416 \mu$

$$V_i = 3.05 \times 10^{-3} / R_i^3$$

Second Curve:

For  $58 < R < 84 \mu$

$$V_i = (.259R_i - 15.05) \times 10^{-10}$$

for  $86 < R < 458 \mu$

$$V_i = 4.3 \times 10^{-4} / R_i^3$$

#### Distribution from Scattering Data

The following formulas apply to Figure 6-2 and 6-4.

##### San Diego

For  $65 < R < 149 \mu$

$$V_i = (.283R_i - 18.3) \times 10^{-10}$$

for  $151 < R < 465 \mu$

$$V_i = 0.0080 / R_i^3$$

##### Monterey Bay

For  $65 < R < 135 \mu$

$$V_i = (0.1R_i - 6.5) \times 10^{-10}$$

for  $137 < R < 465 \mu$

$$V_i = 0.0017 / R_i^3$$



**FIGURE VII -1**  
**COMPUTER PROGRAM FLOW DIAGRAM**

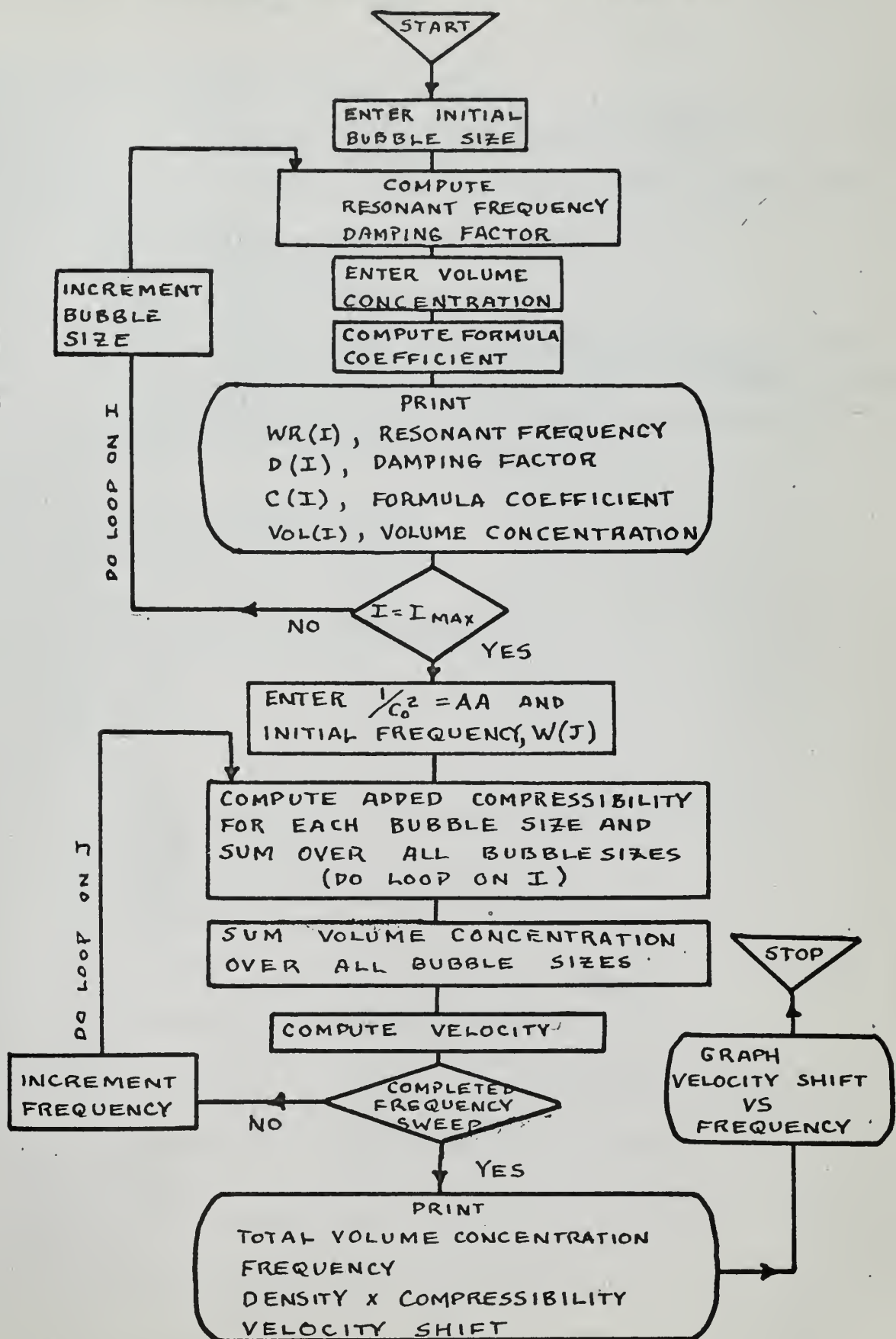






# TABLE VII - 1

```

C      PROGRAM SCAT A
C      THIS PROGRAM COMPUTES VELOCITY SHIFT
C      ACCORDING TO MCNEIL'S SCATTERING DATA
C      CURVE A
C      DIMENSION WR(201),R(201),D(201),C(201),W(201),A(201),
1      SUMA(201),V(201),ITITLE(12),EE(201),VOL(201)
C      PRINT 800
800    FORMAT(69H1      I      RESONANT FREQ.  DAMPING FACTOR  COEFFICIENT
1      VOLUME CONC.//)
C      R(I) = BUBBLE RADIUS
C      WR(I) = BUBBLE RESONANT FREQUENCY (RADIAN)
C      D(I) = BUBBLE DAMPING FACTOR
C      C(I) = FORMULA COEFFICIENT
C      VOL(I) = VOLUME CONCENTRATION FOR BUBBLE SIZE I
C      I = BUBBLE SIZE INDEX
C      W(J) = FREQUENCY AS INDEPENDANT VARIABLE (RADIAN)
C      A(I) = DENSITY X ADDED COMPRESSIBILITY DUE TO BUBBLES OF SIZE I
C      AA = DENSITY X COMPRESSIBILITY OF WATER WITHOUT BUBBLES
C      SUMA(J) = SUM OF ADDED COMPRESSIBILITIES OVER ALL BUBBLES SIZES
C      AT FREQUENCY W(J)
C      V(J) = SOUND VELOCITY SHIFT FROM 1500 M/S AT FREQUENCY W(J)
C      J = INDEPENDANT VARIABLE INDEX
C      EE(J) = FREQUENCY IN KCPS
C      R(1)=65.0
C      DO 50 I=1,200
10     WR(I)=8.0*3.1416*1000000.0/R(I)
C      D(I)=0.027*(WR(I)/6283.2)**0.322
C      IF(I-42)21,21,22
21     VOL(I)=(.283*R(I)-18.3)*1.0E-10
C      GO TO 30
22     VOL(I)=.0080/R(I)**3
30     C(I)=3.0*VOL(I)/((R(I)*1.0E-6*WR(I))**2)
C      PRINT 801,(I, WR(I),D(I),C(I),VOL(I))
801    FORMAT(15,1P4E16.7)
C      R(I+1)=R(I)+2.0
50     CONTINUE
C      AA=1.0/2250000.0
C      W(1)=6283.2
C      DO 40 J=1,200
C      SUMA(J)=0.0
C      SUMV=0.0
C      DO 101 I=1,200
C      A(I)=C(I)*((WR(I)/W(J))**2-1.)/(((WR(I)/W(J))**2-1.))**2
1      +(D(I)*WR(I)/W(J))**2)
C      SUMV=SUMV+VOL(I)
101    SUMA(J)=SUMA(J)+A(I)
C      V(J)=(1.0/SQRT(AA+SUMA(J)))-1500.0
C      EE(J)=W(J)/6283.2
C      W(J+1)=W(J)+6283.2
40     CONTINUE
C      PRINT 400, (SUMV)
400    FORMAT(30H TOTAL VOLUME CONCENTRATION = 1PE16.7)
12     PRINT 500
500    FORMAT(30H1VELOCITY SHIFT DUE TO BUBBLES/)
C      PRINT 501
501    FORMAT(26H      IN MCNEIL DISTRIBUTION//)
C      PRINT 600
600    FORMAT(54H FREQUENCY      RHO X COMPRESSIBILITY      VELOCITY SHIFT
1      //)
C      PRINT 700,(EE(J),SUMA(J),V(J),J=1,67)
700    FORMAT(0PF8.2,6H KC      1PE17.7,0PF18.7, 5H M/S)
C      PRINT 1000
1000   FORMAT(1H1///)
C      PRINT 600
C      PRINT 700,(EE(J),SUMA(J),V(J),J=68,134)
C      PRINT 1000
C      PRINT 600
C      PRINT 700,(EE(J),SUMA(J),V(J),J=135,200)

```



```

ITITLE(1)=8HSOUND
ITITLE(2)=8HVELCCITY
ITITLE(3)=8H    IN
ITITLE(4)=8HWATER
ITITLE(5)=8H WITH
ITITLE(6)=8HBUBBLES
ITITLE(7)=8H
ITITLE(8)=8HVERSUS
ITITLE(9)=8H FREQ.
ITITLE(10)=8H
ITITLE(11)=8H      R.H.
ITITLE(12)=8HMARKS
CALL DRAW(150,EE,V,0,0,4H ,ITITLE,C,0,4,0,2,2,9,8,1,LAST)
END
END

```

I	RESONANT FREQ.	DAMPING FACTOR	COEFFICIENT	VOLUME CCNC./
1	3.8665846E+05	1.0173467E-01	4.5119378E-14	9.5000000E-12
2	3.7511642E+05	1.0074674E-01	3.1393589E-13	6.6100000E-11
3	3.6424348E+05	9.9797043E-02	5.8275239E-13	1.2270000E-10
4	3.5398310E+05	9.8883059E-02	8.5156890E-13	1.7930000E-10
5	3.4428493E+05	9.8000249E-02	1.1203854E-12	2.3590000E-10
6	3.3510400E+05	9.7153255E-02	1.3892019E-12	2.9250000E-10
7	3.2640000E+05	9.6333440E-02	1.6580184E-12	3.4910000E-10
8	3.1813671E+05	9.5541303E-02	1.9268349E-12	4.0570000E-10
9	3.1028148E+05	9.4775243E-02	2.1956514E-12	4.6230000E-10
10	3.0280482E+05	9.4033789E-02	2.4644468E-12	5.1890000E-10
11	2.9568000E+05	9.3315586E-02	2.7332284E-12	5.7550000E-10
12	2.8888276E+05	9.2619383E-02	3.0022101E-12	6.3210000E-10
13	2.8239101E+05	9.1944022E-02	3.2709175E-12	6.8870000E-10
14	2.7618462E+05	9.1288433E-02	3.5397340E-12	7.4530000E-10
15	2.7024516E+05	9.0651620E-02	3.8085505E-12	8.0190000E-10
16	2.6455579E+05	9.0032660E-02	4.0773670E-12	8.5850000E-10
17	2.5910103E+05	8.9430690E-02	4.3461833E-12	9.1510000E-10
18	2.5386667E+05	8.8845059E-02	4.6150000E-12	9.7170000E-10
19	2.4883960E+05	8.8274568E-02	4.8838165E-12	1.0283000E-09
20	2.4400777E+05	8.7718964E-02	5.1526330E-12	1.0849000E-09
21	2.3936000E+05	8.7177443E-02	5.4214495E-12	1.1415000E-09
22	2.3488598E+05	8.6649338E-02	5.6902660E-12	1.1981000E-09
23	2.3057615E+05	8.6134225E-02	5.9590826E-12	1.2547000E-09
24	2.2642162E+05	8.5631407E-02	6.2278991E-12	1.3113000E-09
25	2.2241416E+05	8.5140427E-02	6.4967156E-12	1.3679000E-09
26	2.1854609E+05	8.4660802E-02	6.7655321E-12	1.4245000E-09
27	2.1481026E+05	8.4192079E-02	7.0343486E-12	1.4811000E-09
28	2.1120000E+05	8.3733831E-02	7.3031651E-12	1.5377000E-09
29	2.0770909E+05	8.3285652E-02	7.5719816E-12	1.5943000E-09
30	2.0433171E+05	8.2847162E-02	7.8407981E-12	1.6509000E-09
31	2.0106240E+05	8.2417597E-02	8.1096146E-12	1.7075000E-09
32	1.9789606E+05	8.1997816E-02	8.3784311E-12	1.7641000E-09
33	1.9482791E+05	8.1586292E-02	8.6472476E-12	1.8207000E-09
34	1.9185344E+05	8.1183117E-02	8.9160641E-12	1.8773000E-09
35	1.8896842E+05	8.0787599E-02	9.1848807E-12	1.9339000E-09
36	1.8616889E+05	8.0400659E-02	9.4536972E-12	1.9905000E-09
37	1.83345109E+05	8.0020831E-02	9.7225137E-12	2.0471000E-09
38	1.8081151E+05	7.9648264E-02	9.9913302E-12	2.1037000E-09
39	1.7824681E+05	7.9282717E-02	1.0260147E-11	2.1603000E-09
40	1.7575385E+05	7.8923562E-02	1.0528963E-11	2.2169000E-09
41	1.7332966E+05	7.8571779E-02	1.0797780E-11	2.2735000E-09
42	1.7097143E+05	7.8225560E-02	1.1066596E-11	2.3301000E-09
43	1.6867651E+05	7.7886305E-02	1.1486050E-11	2.4184170E-09
44	1.6644238E+05	7.7552625E-02	1.10635669E-11	2.3235881E-09
45	1.6426667E+05	7.7224737E-02	1.06085530E-11	2.2336529E-09
46	1.6214710E+05	7.6902467E-02	1.0203153E-11	2.1482998E-09
47	1.6008153E+05	7.6585648E-02	9.8181697E-12	2.0672406E-09





48	1.5806792E+05	7.6274120E-02	9.4523135E-12	1.9902087E-09
49	1.5610435E+05	7.5967730E-02	9.1044112E-12	1.9169556E-09
50	1.5418896E+05	7.5369781E-02	8.7733747E-12	1.8472564E-09
51	1.5232000E+05	7.5369781E-02	8.7733747E-12	1.7808994E-09
52	1.50049581E+05	7.5077945E-02	8.1579319E-12	1.7176733E-09
53	1.4871479E+05	7.4790694E-02	7.8717153E-12	1.6574097E-09
54	1.4697544E+05	7.4507902E-02	7.5987326E-12	1.5999322E-09
55	1.4527630E+05	7.4222944E-02	7.3382277E-12	1.5450825E-09
56	1.4361600E+05	7.3955521E-02	7.0894495E-12	1.4927114E-09
57	1.4199322E+05	7.3685102E-02	6.8518791E-12	1.4426806E-09
58	1.4040670E+05	7.3418598E-02	6.6247638E-12	1.3949486E-09
59	1.3888552E+05	7.3156780E-02	6.4075760E-12	1.3491314E-09
60	1.3733770E+05	7.2898572E-02	6.1997792E-12	1.3053731E-09
61	1.3585297E+05	7.2643671E-02	6.0008712E-12	1.2634987E-09
62	1.3440000E+05	7.2392585E-02	5.8103818E-12	1.2233907E-09
63	1.33297778E+05	7.2145024E-02	5.6278703E-12	1.1849926E-09
64	1.3158534E+05	7.1900902E-02	5.4529233E-12	1.1488126E-09
65	1.30022176E+05	7.1660136E-02	5.2851530E-12	1.1128024E-09
66	1.28888615E+05	7.1422646E-02	5.1241951E-12	1.0789123E-09
67	1.2757766E+05	7.1188355E-02	4.9697073E-12	1.0463845E-09
68	1.2629548E+05	7.0957187E-02	4.8213678E-12	1.0151513E-09
69	1.250303881E+05	7.0729071E-02	4.6786737E-12	9.8514876E-10
70	1.23806690E+05	7.0503353E-02	4.5419398E-12	9.5631699E-10
71	1.2259902E+05	7.0281713E-02	4.4102977E-12	9.2859941E-10
72	1.2141449E+05	7.0062339E-02	4.2836941E-12	9.0194271E-10
73	1.2025263E+05	6.9845749E-02	4.1618903E-12	8.7629660E-10
74	1.1911280E+05	6.9631182E-02	4.0446610E-12	8.5161490E-10
75	1.1799437E+05	6.9420678E-02	3.9317933E-12	8.2784909E-10
76	1.1689674E+05	6.9212079E-02	3.8223086E-12	8.0496057E-10
77	1.1581935E+05	6.9006031E-02	3.7183502E-12	7.8290810E-10
78	1.1476164E+05	6.8802477E-02	3.6174005E-12	7.6116204E-10
79	1.1372308E+05	6.8601267E-02	3.5200811E-12	7.4116204E-10
80	1.1270314E+05	6.8402648E-02	3.4262173E-12	7.2139877E-10
81	1.1170133E+05	6.8206272E-02	3.3356612E-12	7.0233319E-10
82	1.1071718E+05	6.8012189E-02	3.2482685E-12	6.8393120E-10
83	1.0975022E+05	6.7820355E-02	3.1639022E-12	6.6616765E-10
84	1.0880000E+05	6.7630722E-02	3.0822432E-12	6.4901397E-10
85	1.0786609E+05	6.7443248E-02	3.0037358E-12	6.3244421E-10
86	1.0694809E+05	6.7257889E-02	2.9276955E-12	6.1643374E-10
87	1.0604557E+05	6.7074603E-02	2.8542003E-12	6.0095595E-10
88	1.0515816E+05	6.6893352E-02	2.7831447E-12	5.8599820E-10
89	1.0428548E+05	6.6714094E-02	2.7144282E-12	5.7152377E-10
90	1.0342716E+05	6.6536792E-02	2.6479554E-12	5.5753375E-10
91	1.0258286E+05	6.6361410E-02	2.5836355E-12	5.4399910E-10
92	1.0175224E+05	6.6187909E-02	2.5213819E-12	5.3088338E-10
93	1.0093494E+05	6.6016256E-02	2.4611124E-12	5.1819348E-10
94	1.0013068E+05	6.5846416E-02	2.4027486E-12	5.0590048E-10
95	9.9339130E+04	6.5678356E-02	2.3464215E-12	4.9400168E-10
96	9.8560000E+04	6.5512043E-02	2.2914424E-12	4.8246904E-10
97	9.7792996E+04	6.5347446E-02	2.2383610E-12	4.7129260E-10
98	9.7037838E+04	6.5184533E-02	2.1869064E-12	4.6045871E-10
99	9.6294253E+04	6.5023275E-02	2.1370170E-12	4.4995436E-10
100	9.5561977E+04	6.4863642E-02	2.0886335E-12	4.3976711E-10
101	9.4840755E+04	6.4705666E-02	2.0416997E-12	4.2988507E-10
102	9.4130337E+04	6.4549139E-02	1.9961616E-12	4.2029692E-10
103	9.3430483E+04	6.4394214E-02	1.9519678E-12	4.1099179E-10
104	9.2740959E+04	6.4240804E-02	1.9090690E-12	4.0195933E-10
105	9.2061538E+04	6.4088884E-02	1.8674180E-12	3.9318962E-10
106	9.1392000E+04	6.3938428E-02	1.8269700E-12	3.8467031E-10
107	9.0732130E+04	6.3789412E-02	1.7876817E-12	3.7640092E-10
108	9.0081720E+04	6.3641811E-02	1.7495118E-12	3.6836417E-10
109	8.9440569E+04	6.3495602E-02	1.7124209E-12	3.6055459E-10
110	8.8808481E+04	6.3350763E-02	1.6763712E-12	3.5296842E-10
111	8.8185263E+04	6.3207270E-02	1.6413262E-12	3.4558542E-10
112	8.7570732E+04	6.3065103E-02	1.6072514E-12	3.3841086E-10
113	8.6964706E+04	6.2924240E-02	1.5741132E-12	3.3143354E-10
114	8.6367010E+04	6.2784659E-02	1.5418798E-12	3.2464672E-10
115	8.5777474E+04	6.2646341E-02	1.5105205E-12	3.1804394E-10



116	8.5195932E+04	6.2509265E-02	1.4800000E-12	3.116159C1E-10
117	8.422222E+04	6.2237341E-02	1.4503333E-12	3.0536597E-10
118	8.4056187E+04	6.2238764E-02	1.4213333E-12	2.9927912E-10
119	8.3349767E+04	6.2210533E-02	1.3933333E-12	2.9335298E-10
120	8.2946535E+04	6.1973300E-02	1.3655845E-12	2.8758227E-10
121	8.2186657E+04	6.1841859E-02	1.3393333E-12	2.8196170E-10
122	8.1865798E+04	6.1711844E-02	1.3133333E-12	2.7648309E-10
123	8.1335922E+04	6.1582514E-02	1.2877816E-12	2.7115530E-10
124	8.0861286E+04	6.1455514E-02	1.2633130E-12	2.6595540E-10
125	8.0296486E+04	6.1328424E-02	1.2399071E-12	2.6088972E-10
126	7.9786667E+04	6.1202771E-02	1.2156620E-12	2.5595518E-10
127	7.9283281E+04	6.1078168E-02	1.1927563E-12	2.5113787E-10
128	7.8786207E+04	6.0954599E-02	1.1704623E-12	2.4644382E-10
129	7.8295327E+04	6.0833205E-02	1.1487206E-12	2.4186604E-10
130	7.7810526E+04	6.0711050E-02	1.1275140E-12	2.3740003E-10
131	7.7331692E+04	6.0589556E-02	1.1068261E-12	2.3304006E-10
132	7.6858716E+04	6.0470381E-02	1.0866414E-12	2.2879511E-10
133	7.6391489E+04	6.0351769E-02	1.0666444E-12	2.2464786E-10
134	7.5929909E+04	6.0233406E-02	1.0477207E-12	2.2064093E-10
135	7.5473874E+04	6.0111737E-02	1.0285560E-12	2.1664933E-10
136	7.5023284E+04	6.0000157E-02	1.0106636E-12	2.1279213E-10
137	7.4578042E+04	5.9886682E-02	9.9274976E-13	2.0902599E-10
138	7.4138053E+04	5.9777266E-02	9.7528242E-13	2.0534820E-10
139	7.3703226E+04	5.9659977E-02	9.5822244E-13	2.0175618E-10
140	7.3273469E+04	5.9547341E-02	9.4155581E-13	1.9824746E-10
141	7.2848696E+04	5.9435567E-02	9.2527794E-13	1.9481962E-10
142	7.2428818E+04	5.9325443E-02	9.0933700E-13	1.9147336E-10
143	7.2013754E+04	5.9215758E-02	8.9382647E-13	1.8819744E-10
144	7.1603419E+04	5.9106901E-02	8.7863428E-13	1.8499868E-10
145	7.1197734E+04	5.8998861E-02	8.6378444E-13	1.8187201E-10
146	7.0796620E+04	5.8891627E-02	8.4926736E-13	1.7881540E-10
147	7.0400000E+04	5.8785189E-02	8.3500737E-13	1.7582691E-10
148	7.0007799E+04	5.8679536E-02	8.2119471E-13	1.7290464E-10
149	6.9619945E+04	5.8574658E-02	8.0762153E-13	1.7004677E-10
150	6.9236364E+04	5.8470546E-02	7.9434582E-13	1.6725153E-10
151	6.8856986E+04	5.8367189E-02	7.8135950E-13	1.6451723E-10
152	6.8481744E+04	5.8264578E-02	7.6865472E-13	1.6184221E-10
153	6.8110569E+04	5.8162704E-02	7.5622389E-13	1.5922486E-10
154	6.7743396E+04	5.8061558E-02	7.4400596E-13	1.5666366E-10
155	6.7380161E+04	5.7961129E-02	7.3215494E-13	1.5415709E-10
156	6.7020800E+04	5.7861410E-02	7.2050028E-13	1.5170037E-10
157	6.6665252E+04	5.7762392E-02	7.0909666E-13	1.4930211E-10
158	6.6313456E+04	5.7664065E-02	6.9792999E-13	1.4695094E-10
159	6.5965354E+04	5.7566422E-02	6.8699656E-13	1.4464887E-10
160	6.5620888E+04	5.7469455E-02	6.7629032E-13	1.4239465E-10
161	6.5280000E+04	5.7373154E-02	6.6580538E-13	1.4018702E-10
162	6.4942636E+04	5.7277513E-02	6.5553607E-13	1.3800247E-10
163	6.4608740E+04	5.7182523E-02	6.4554768E-13	1.3590680E-10
164	6.4278261E+04	5.7088176E-02	6.3562244E-13	1.3383192E-10
165	6.3951145E+04	5.6994465E-02	6.2596758E-13	1.3179907E-10
166	6.3627342E+04	5.6901382E-02	6.1650727E-13	1.2980718E-10
167	6.3306801E+04	5.6808921E-02	6.0723664E-13	1.2785522E-10
168	6.2989474E+04	5.6717073E-02	5.9815096E-13	1.2594221E-10
169	6.2675312E+04	5.6625832E-02	5.8924563E-13	1.2406717E-10
170	6.2364268E+04	5.6535190E-02	5.8051621E-13	1.2222917E-10
171	6.2056296E+04	5.6445141E-02	5.7195837E-13	1.2042729E-10
172	6.1751351E+04	5.6355678E-02	5.6355679E-13	1.1866066E-10
173	6.1449389E+04	5.6266795E-02	5.5534078E-13	1.1692842E-10
174	6.1150365E+04	5.6178484E-02	5.4727300E-13	1.1522972E-10
175	6.0854237E+04	5.6090739E-02	5.3936075E-13	1.13556378E-10





176	6.0560964E+04	5.6003555E-02	5.3160028E-13	1.1192979E-10
177	6.0270504E+04	5.5916554E-02	5.2398879E-13	1.1032270E-10
178	5.9982281E+04	5.5833064E-02	5.1655203E-13	1.1087546E-10
179	5.9697862E+04	5.5745029E-02	5.0919331E-13	1.0875467E-10
180	5.9415600E+04	5.5660229E-02	5.0200055E-13	1.0721207E-10
181	5.9136000E+04	5.5575566E-02	4.9499515E-13	1.0569851E-10
182	5.8859016E+04	5.5491863E-02	4.8802292E-13	1.0421311E-10
183	5.8584615E+04	5.5408429E-02	4.8123354E-13	1.0275580E-10
184	5.8312761E+04	5.5325507E-02	4.7455671E-13	1.0132233E-10
185	5.8043418E+04	5.5243309E-02	4.6800215E-13	9.9921332E-11
186	5.7776552E+04	5.5161179E-02	4.6159566E-13	9.8543318E-11
187	5.7512128E+04	5.5079983E-02	4.5528693E-13	9.7190142E-11
188	5.7250114E+04	5.4999883E-02	4.4909263E-13	9.5861821E-11
189	5.6990476E+04	5.4918539E-02	4.4301020E-13	9.4557597E-11
190	5.6733183E+04	5.4838439E-02	4.3703711E-13	9.3227652E-11
191	5.6478202E+04	5.4758955E-02	4.3117092E-13	9.2019275E-11
192	5.6225503E+04	5.4679944E-02	4.2540924E-13	9.0784134E-11
193	5.5975056E+04	5.4601339E-02	4.1974977E-13	8.9557059E-11
194	5.5726829E+04	5.4523113E-02	4.1419024E-13	8.8337633E-11
195	5.5480795E+04	5.4444568E-02	4.0872847E-13	8.7208810E-11
196	5.5236923E+04	5.4366850E-02	4.0336223E-13	8.6058819E-11
197	5.4995186E+04	5.4291778E-02	3.9808965E-13	8.4922955E-11
198	5.4755556E+04	5.4215491E-02	3.9290851E-13	8.3818790E-11
199	5.4518004E+04	5.4139642E-02	3.8781689E-13	8.2727887E-11
200	5.4282505E+04	5.4064228E-02	3.8281286E-13	8.1655832E-11
				8.0602222E-11

TOTAL VOLUME CONCENTRATION = 1.3114546E-07





# VELOCITY SHIFT DUE TO BUBBLES

## IN MCNEIL DISTRIBUTION

FREQUENCY		RHO X COMPRESSIBILITY	VELOCITY SHIFT	
1.00	KC	1.58C5603E-12	-.00C26672	M/S
2.00	KC	6.41339358E-12	-.0108234	M/S
3.00	KC	1.4796904E-11	-.0249692	M/S
4.00	KC	2.7309566E-11	-.0460828	M/S
5.00	KC	4.5006175E-11	-.0759422	M/S
6.00	KC	6.9907125E-11	-.1179544	M/S
7.00	KC	1.0658786E-10	-.1798347	M/S
8.00	KC	1.7038791E-10	-.2874469	M/S
9.00	KC	2.2668272E-10	-.3823808	M/S
10.00	KC	2.0659377E-10	-.3348505	M/S
11.00	KC	2.0567619E-10	-.3346958	M/S
12.00	KC	2.0813350E-10	-.3351102	M/S
13.00	KC	2.1027664E-10	-.3354716	M/S
14.00	KC	2.1049692E-10	-.3355087	M/S
15.00	KC	2.0777052E-10	-.3350489	M/S
16.00	KC	2.0126459E-10	-.3339518	M/S
17.00	KC	1.9018802E-10	-.3208393	M/S
18.00	KC	1.7371231E-10	-.2930536	M/S
19.00	KC	1.5091119E-10	-.2545978	M/S
20.00	KC	1.2069606E-10	-.2036332	M/S
21.00	KC	8.1730041E-11	-.1379004	M/S
22.00	KC	3.2297022E-11	-.0544983	M/S
23.00	KC	-2.9915002E-11	-.0504841	M/S
24.00	KC	-1.0819206E-10	-.1826074	M/S
25.00	KC	-2.0742440E-10	-.3501512	M/S
26.00	KC	-3.3431118E-10	-.5644686	M/S
27.00	KC	-4.8624115E-10	-.8212058	M/S
28.00	KC	-6.2075042E-10	1.0486149	M/S
29.00	KC	-7.1852852E-10	1.2139890	M/S
30.00	KC	-7.8912450E-10	1.3334235	M/S
31.00	KC	-8.4072293E-10	1.4207355	M/S
32.00	KC	-8.7863755E-10	1.4849029	M/S
33.00	KC	-9.0640521E-10	1.5319023	M/S
34.00	KC	-9.2647964E-10	1.5658830	M/S
35.00	KC	-9.4062358E-10	1.5898263	M/S
36.00	KC	-9.5013636E-10	1.6059304	M/S
37.00	KC	-9.5600018E-10	1.6158575	M/S
38.00	KC	-9.5896551E-10	1.6208778	M/S
39.00	KC	-9.5961931E-10	1.6219846	M/S
40.00	KC	-9.5841798E-10	1.6199508	M/S
41.00	KC	-9.5572699E-10	1.6153950	M/S
42.00	KC	-9.5183848E-10	1.6088120	M/S
43.00	KC	-9.4698572E-10	1.6000596	M/S
44.00	KC	-9.4135676E-10	1.5910674	M/S
45.00	KC	-9.3510402E-10	1.5804825	M/S
46.00	KC	-9.2835111E-10	1.5690510	M/S
47.00	KC	-9.2119815E-10	1.5569426	M/S
48.00	KC	-9.1372639E-10	1.5442949	M/S
49.00	KC	-9.0600184E-10	1.5312196	M/S
50.00	KC	-8.9807696E-10	1.5178055	M/S
51.00	KC	-8.8999037E-10	1.5041181	M/S
52.00	KC	-8.8176999E-10	1.4902046	M/S
53.00	KC	-8.7344152E-10	1.4761086	M/S
54.00	KC	-8.6502427E-10	1.4618627	M/S
55.00	KC	-8.5651873E-10	1.4474678	M/S
56.00	KC	-8.4792771E-10	1.4329287	M/S
57.00	KC	-8.3925645E-10	1.4182542	M/S
58.00	KC	-8.3048841E-10	1.4034163	M/S
59.00	KC	-8.2163118E-10	1.3884280	M/S
60.00	KC	-8.1269672E-10	1.3733094	M/S
61.00	KC	-8.0375212E-10	1.3581741	M/S
62.00	KC	-7.9495245E-10	1.3432845	M/S
63.00	KC	-7.8652497E-10	1.3290251	M/S
64.00	KC	-7.7861964E-10	1.3156495	M/S
65.00	KC	-7.7129255E-10	1.3032527	M/S
66.00	KC	-7.6453344E-10	1.2918171	M/S
67.00	KC	-7.5829973E-10	1.2812706	M/S



## FREQUENCY

## RHO X COMPRESSIBILITY

## VELOCITY SHIFT

68.00	KC	-7.5253968E-1C	1.2715257	M/S
69.00	KC	-7.4720296E-1C	1.2624971	M/S
70.00	KC	-7.4224420E-1C	1.2541081	M/S
71.00	KC	-7.3762367E-1C	1.2462915	M/S
72.00	KC	-7.3330692E-1C	1.2389888	M/S
73.00	KC	-7.2926411E-1C	1.2321497	M/S
74.00	KC	-7.2546934E-1C	1.2257303	M/S
75.00	KC	-7.2190000E-1C	1.2196922	M/S
76.00	KC	-7.1853630E-1C	1.2140022	M/S
77.00	KC	-7.1536079E-1C	1.2086305	M/S
78.00	KC	-7.1235805E-1C	1.2035512	M/S
79.00	KC	-7.0951439E-1C	1.1987410	M/S
80.00	KC	-7.0681755E-1C	1.1941791	M/S
81.00	KC	-7.0425657E-1C	1.1898472	M/S
82.00	KC	-7.0182160E-1C	1.1857284	M/S
83.00	KC	-6.9950373E-1C	1.1818077	M/S
84.00	KC	-6.9729491E-1C	1.1780716	M/S
85.00	KC	-6.9518782E-1C	1.1745074	M/S
86.00	KC	-6.9317579E-1C	1.1711042	M/S
87.00	KC	-6.9125275E-1C	1.1678515	M/S
88.00	KC	-6.8941313E-1C	1.1647399	M/S
89.00	KC	-6.8765182E-1C	1.1617607	M/S
90.00	KC	-6.8596414E-1C	1.1589061	M/S
91.00	KC	-6.8434574E-1C	1.1561688	M/S
92.00	KC	-6.8279266E-1C	1.1535419	M/S
93.00	KC	-6.8130120E-1C	1.1510192	M/S
94.00	KC	-6.7986794E-1C	1.1485951	M/S
95.00	KC	-6.7848972E-1C	1.1462640	M/S
96.00	KC	-6.7716359E-1C	1.1440210	M/S
97.00	KC	-6.7588683E-1C	1.1418615	M/S
98.00	KC	-6.7465687E-1C	1.1397812	M/S
99.00	KC	-6.7347134E-1C	1.1377761	M/S
100.00	KC	-6.7233280E-1C	1.1358423	M/S
101.00	KC	-6.7122482E-1C	1.1339765	M/S
102.00	KC	-6.7015982E-1C	1.1322175	M/S
103.00	KC	-6.6913117E-1C	1.1304354	M/S
104.00	KC	-6.6813717E-1C	1.1287543	M/S
105.00	KC	-6.6717622E-1C	1.1271290	M/S
106.00	KC	-6.6624680E-1C	1.1255571	M/S
107.00	KC	-6.6534749E-1C	1.1240361	M/S
108.00	KC	-6.6447695E-1C	1.1225637	M/S
109.00	KC	-6.6363392E-1C	1.1211379	M/S
110.00	KC	-6.6281720E-1C	1.1197566	M/S
111.00	KC	-6.6202568E-1C	1.1184179	M/S
112.00	KC	-6.6125829E-1C	1.1171201	M/S
113.00	KC	-6.6051402E-1C	1.1158613	M/S
114.00	KC	-6.5979192E-1C	1.1146400	M/S
115.00	KC	-6.5909109E-1C	1.1134548	M/S
116.00	KC	-6.5841067E-1C	1.1123040	M/S
117.00	KC	-6.5774985E-1C	1.1111864	M/S
118.00	KC	-6.5710787E-1C	1.1101007	M/S
119.00	KC	-6.5648399E-1C	1.1090455	M/S
120.00	KC	-6.5587751E-1C	1.1080198	M/S
121.00	KC	-6.5528779E-1C	1.1070224	M/S
122.00	KC	-6.5471417E-1C	1.1060523	M/S
123.00	KC	-6.5415608E-1C	1.1051084	M/S
124.00	KC	-6.5361293E-1C	1.1041898	M/S
125.00	KC	-6.5308418E-1C	1.1032956	M/S
126.00	KC	-6.5256932E-1C	1.1024249	M/S
127.00	KC	-6.5206785E-1C	1.1015767	M/S
128.00	KC	-6.5157929E-1C	1.1007505	M/S
129.00	KC	-6.5110321E-1C	1.0999453	M/S
130.00	KC	-6.5063915E-1C	1.0991605	M/S
131.00	KC	-6.5018672E-1C	1.0983954	M/S
132.00	KC	-6.4974552E-1C	1.0976492	M/S
133.00	KC	-6.4931517E-1C	1.0969214	M/S
134.00	KC	-6.4889531E-1C	1.0962113	M/S





# FREQUENCY

# RHO X COMPRESSIBILITY

# VELOCITY SHIFT

135.00	KC	-6.48483559E-10	1.0955184	M/S
136.00	KC	-6.4808569E-10	1.0948421	M/S
137.00	KC	-6.4769528E-10	1.0941818	M/S
138.00	KC	-6.4731406E-10	1.0935371	M/S
139.00	KC	-6.4694173E-10	1.0929075	M/S
140.00	KC	-6.4657803E-10	1.0922924	M/S
141.00	KC	-6.4622267E-10	1.0916914	M/S
142.00	KC	-6.45887540E-10	1.0911041	M/S
143.00	KC	-6.45553597E-10	1.0905300	M/S
144.00	KC	-6.45220414E-10	1.0899689	M/S
145.00	KC	-6.44887968E-10	1.0894202	M/S
146.00	KC	-6.44556238E-10	1.0888835	M/S
147.00	KC	-6.44225201E-10	1.0883586	M/S
148.00	KC	-6.43894483E-10	1.0878451	M/S
149.00	KC	-6.43565128E-10	1.0873427	M/S
150.00	KC	-6.43236053E-10	1.0868510	M/S
151.00	KC	-6.42907594E-10	1.0863697	M/S
152.00	KC	-6.42579734E-10	1.0858985	M/S
153.00	KC	-6.42252456E-10	1.0854372	M/S
154.00	KC	-6.41925744E-10	1.0849855	M/S
155.00	KC	-6.41599581E-10	1.0845430	M/S
156.00	KC	-6.41273953E-10	1.0841096	M/S
157.00	KC	-6.40948844E-10	1.0836850	M/S
158.00	KC	-6.40624241E-10	1.0832689	M/S
159.00	KC	-6.40300130E-10	1.0828612	M/S
160.00	KC	-6.40076498E-10	1.0824615	M/S
161.00	KC	-6.39853331E-10	1.0820697	M/S
162.00	KC	-6.39630618E-10	1.0816856	M/S
163.00	KC	-6.39408347E-10	1.0813090	M/S
164.00	KC	-6.39186506E-10	1.0809396	M/S
165.00	KC	-6.38965083E-10	1.0805773	M/S
166.00	KC	-6.38744069E-10	1.0802219	M/S
167.00	KC	-6.38523452E-10	1.0798733	M/S
168.00	KC	-6.38303223E-10	1.0795311	M/S
169.00	KC	-6.38083372E-10	1.0791954	M/S
170.00	KC	-6.37863889E-10	1.0788659	M/S
171.00	KC	-6.37644765E-10	1.0785426	M/S
172.00	KC	-6.37425991E-10	1.0782250	M/S
173.00	KC	-6.37207559E-10	1.0779133	M/S
174.00	KC	-6.36989460E-10	1.0776073	M/S
175.00	KC	-6.36771686E-10	1.0773067	M/S
176.00	KC	-6.36554230E-10	1.0770115	M/S
177.00	KC	-6.36337083E-10	1.0767215	M/S
178.00	KC	-6.36120239E-10	1.0764366	M/S
179.00	KC	-6.35903690E-10	1.0761567	M/S
180.00	KC	-6.35687429E-10	1.0758818	M/S
181.00	KC	-6.35471449E-10	1.0756115	M/S
182.00	KC	-6.35255745E-10	1.0753460	M/S
183.00	KC	-6.35040309E-10	1.0750849	M/S
184.00	KC	-6.34825136E-10	1.0748283	M/S
185.00	KC	-6.34610219E-10	1.0745761	M/S
186.00	KC	-6.34395553E-10	1.0743280	M/S
187.00	KC	-6.34181132E-10	1.0740842	M/S
188.00	KC	-6.33966951E-10	1.0738443	M/S
189.00	KC	-6.33753004E-10	1.0736085	M/S
190.00	KC	-6.33539285E-10	1.0733765	M/S
191.00	KC	-6.33325791E-10	1.0731483	M/S
192.00	KC	-6.33112516E-10	1.0729237	M/S
193.00	KC	-6.32899455E-10	1.0727029	M/S
194.00	KC	-6.32686604E-10	1.0724856	M/S
195.00	KC	-6.32473958E-10	1.0722717	M/S
196.00	KC	-6.32261513E-10	1.0720613	M/S
197.00	KC	-6.32049264E-10	1.0718541	M/S
198.00	KC	-6.31837208E-10	1.0716502	M/S
199.00	KC	-6.31625340E-10	1.0714495	M/S
200.00	KC	-6.31413656E-10	1.0712519	M/S

GRAPH TITLED . . SOUND VELOCITY IN WATER WITH BUBBLES  
 VERSUS FREQ. R.H. MARKS . . HAS  
 BEEN PLOTTED  
 TIME, 2 MINUTES AND 35 SECONDS



## APPENDIX VIII

### ENVELOPE DETECTOR AND ECHO COUNTER

This system starts a Beckman 7360 one megacycle counter at the start of the main bang and stops it at the beginning of a preselected echo. Figure (IX-2) is a circuit diagram of the system.

The system operation is as follows. The envelope detector passes the envelope of the echo train but does not pass the high frequency signal. The "and" circuit passes the echo train only between the main bang and the preselected echo for which we are measuring travel time. The amplifier and clipper convert the echo train into a rectangular pulse train with steep leading and trailing edges. The echo counter counts echos and sends a stop pulse to the one megacycle counter when the echo counter reaches the preselected count. At this time flip flop one is reset by this stop signal. The flip flop output turns off the clipper-amplifier. The next bang starts the one megacycle counter and the flip flo which in turn turns the amplifier-clipper back on. The process then repeats itself.

The system as shown is plagued by two sources of error. First, as frequency increases the rise time of the detected wave pulse decreases thus affecting the counter reading. Second, as attenuation increases the rise time of the detected wave pulse increases affecting the counter reading. The combination of these effects caused velocity variation of five percent from 15 KC to 100 KC over two round trips in the laboratory "non-dispersive" water.



By using a more elaborate clipping network with high sensitivity perhaps the above effects could be minimized. The wave shape of the detected pulse train limited the gain that could be used in the clipper as shown in figure (IX-1). This problem might be solved by using several clippers with different sensitivity. The most sensitive clipper would be turned on only when the last echo to be counted is received. This would enable later echos to be received. Receiving the 16th echo may decrease the variation of 0.6 percent and increasing the gain of this last echo may decrease the variation further. Figure (IX-3) is a possible block diagram of the proposed improved system. Time did not permit construction of the improved system.

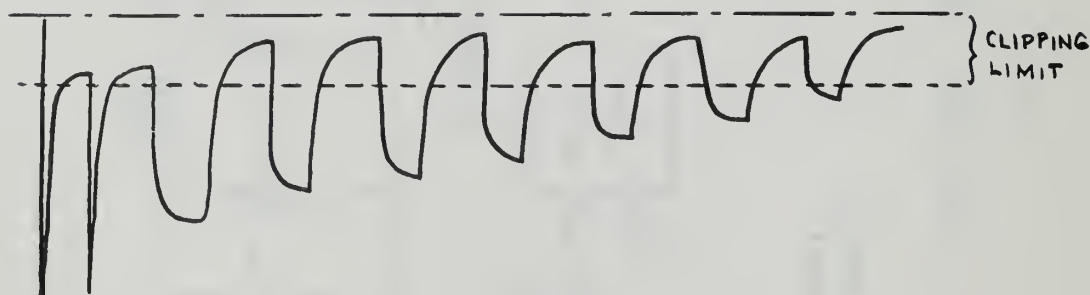


FIGURE VIII-1  
DETECTOR OUTPUT





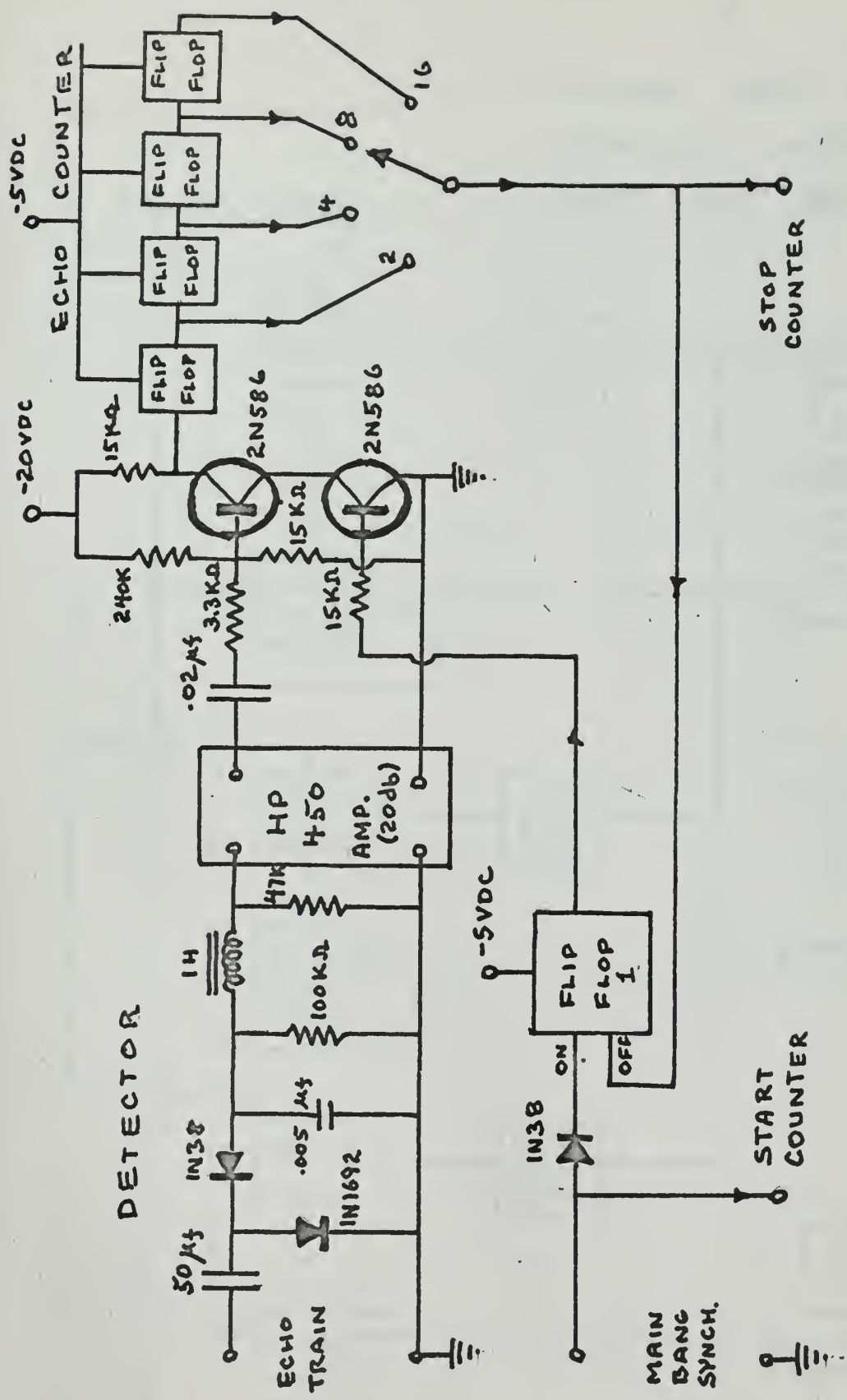
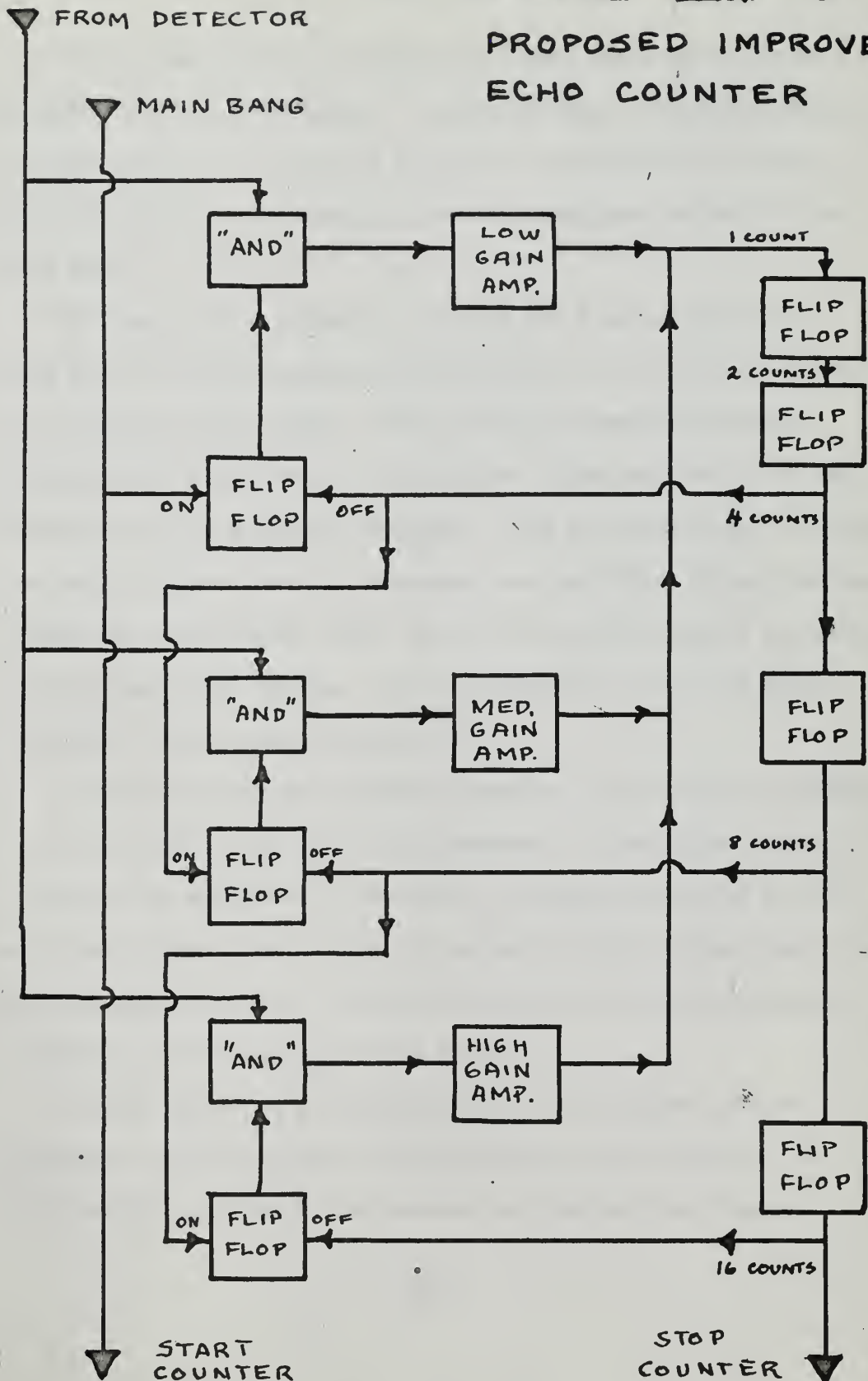


FIGURE VIII-2 ENVELOPE DETECTOR AND ECHO COUNTER



FIGURE VIII - 3  
PROPOSED IMPROVED  
ECHO COUNTER







## APPENDIX IX

### TIME MARKER

This system presents a display on a dual trace oscilloscope similar to a radar "A" scope. A selected echo is superimposed on a step voltage. The step can be moved to any point on the echo. This step stops a one megacycle counter which was started by the main bang.

The heart of the system is a DuMont 404 B pulse generator with delay. Delays from two microseconds to 12.5 milliseconds can be obtained in four ranges. With the dual trace oscilloscope synchronized to the start of the delayed pulse any echo up to the 11th echo can be displayed in detail. The pulse width can be finely controlled with a four inch diameter knob providing 100 microseconds change for a 360 degree turn. The rise and fall times of the pulse are 14 nanoseconds maximum. Pulse widths from .05 to 105 microseconds in three ranges are available.

The Beckman 7360 one megacycle counter is started by the gating voltage output of the tone burst generator. This gating voltage output has an amplitude of 24 volts, and width determined by the main bang width. The counter is stopped by the trailing edge of the pulse generator output. The counter can be started and stopped by a minimum plus or minus one volt pulse.

Overall error due to instabilities in the counter, pulse generator, and oscilloscope are indicated in figure (IX-1). A mean deviation of about .011 percent is obtained from Figure



(IX-1) when using the seventh echo for measurements and .0094 percent when using the eleventh echo. When taking actual measurements the error can be reduced by visual integration of the counter readout.





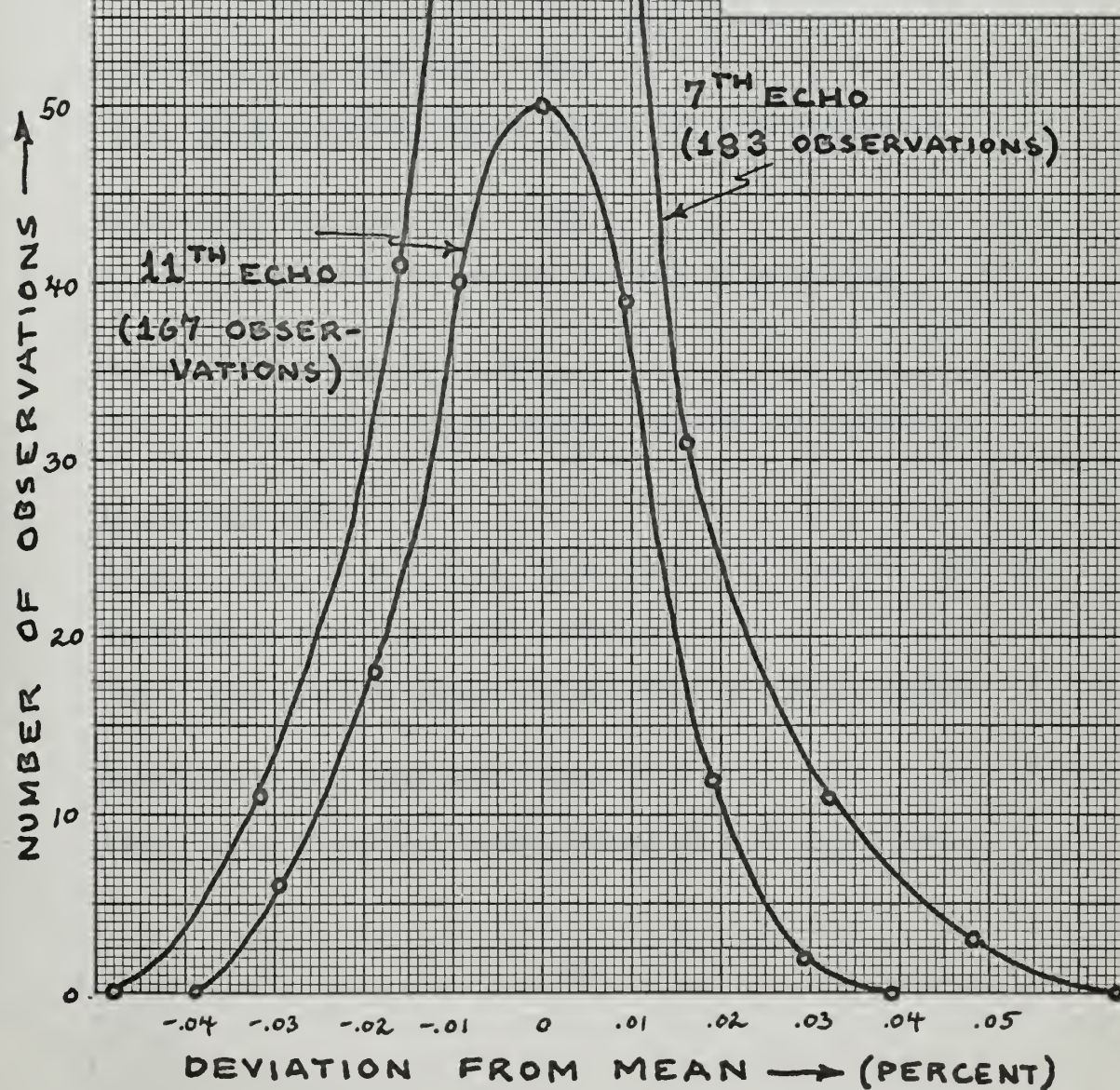
FIGURE IX-1

DISTRIBUTION OF  
TRAVEL TIME  
MEASUREMENTS

(NOTE: READING  
RESOLUTION OF  
ONE MEGACYCLE  
COUNTER

= .014%, 7<sup>TH</sup> ECHO

= .0096%, 11<sup>TH</sup> ECHO)







## APPENDIX X

Extracts from N.E.L. Tower log together with temperature and oxygen data.

### 10 February 1965

Tides: High 1746 at 3.2 ft.,; Lows 1119 at 0.2 ft., 2202 at 2.4 ft.

Wave Height:  $3\frac{1}{2}$  ft.; Water Clarity 15 ft., Slicks, None.

Wind: Speed 0-6 kts.; Direction from  $100^{\circ}$  to  $140^{\circ}$ .

Depth 10 ft., Time 1330 - 1614.

Temp.:  $13.2 \pm 0.1^{\circ}\text{C}$ ; Oxygen Content  $96 \pm 3\%$  saturation.

Depth 10-45 ft.; Time 1835 - 1855.

Temp.  $13.25 \pm 0.05^{\circ}\text{C}$ ; Oxygen Content  $101 \pm 5\%$  saturation

Depth 45-10 ft.; Time 1918 - 1958

Temp.  $13.3 \pm 0.1^{\circ}\text{C}$ ; Oxygen Content  $98 \pm 4\%$  saturation

Depth 10 ft.; Time 2141 - 2353.

Temp.  $13.4 \pm 0.1^{\circ}\text{C}$ ; Oxygen Content  $100.5 \pm 1.5\%$  saturation

### 12 February 1965

Water Clarity, 20 ft.; Wind, Speed 0-3 knots; Direction from  $095^{\circ}$

Depth 10-45 ft.; Time 1156 - 1218

Temp.  $13.2 \pm 0.1^{\circ}\text{C}$ ; Oxygen Content  $99.5 \pm 3.5\%$  saturation

Depth 45-10 ft.; Time 1224 - 1247.

Temp.  $13-15 \pm 0.05^{\circ}\text{C}$ ; Oxygen Content  $95 \pm 2\%$  saturation



15 February 1965

Tides; High 0805 at 7.2 ft.; Low 1512 at -1.9 ft.; High 2119 at 5.0 ft.

Wave Height 4 ft.; Water Clarity 20 ft.; Slicks - None

Wind; Speed 2 kts.; Direction from 020°

Depth 10-45 ft.; Time 0925 - 0942

Temp.  $12.85 \pm 0.05^{\circ}\text{C}.$ ; Oxygen Content  $98 \pm 2\%$  saturation

Depth 45-10 ft.; Time 0950 - 1008

Temp. Isothermal at  $12.9^{\circ}\text{C}.$ ; Oxygen Content  $94.5 \pm 3.5\%$  saturation

Depth 25 ft.; Time 1608 - 1639

Temp.  $13.05 \pm 0.5^{\circ}\text{C}.$ ; Oxygen Content  $94 \pm 1\%$  saturation

Oxygen data is not available after this time since the oxygen probe lead split and water entered the system.

16 February 1965

Tides; Low 0252 at 0.8 ft.; High 0849 at 7.0 ft.; Low 1549 at -1.7 ft.

Wave Height  $2\frac{1}{2}$  ft.; Water Clarity 12 ft.; Slicks, Some.

Wind; Speed 5 knots; Direction from 095°.





## APPENDIX XI

### Effect of Scatterer Position on Signal

Experimentation was carried out to determine the effect on backscattered sound from a 1.5 inch styrofoam sphere when it was placed in a number of positions within the region between the transducer and reflector.

The sphere was suspended in the space at the positions shown in Figure XI-4 and the set of accompanying photos were taken to show the backscatter. A partial analysis follows:

$$\text{Pulse length} = 75.0 \text{ cm} = 2.46 \text{ ft} = 0.5 \text{ msec}$$

$$\text{Cycles per pulse (at 49.05 KC)} = 24.5$$

The region is broken into 7 approximately equal intervals as shown in Figure XI-4. The distance from the transducer to the reflector is 76.4 cm or  $\approx$  pulse length.

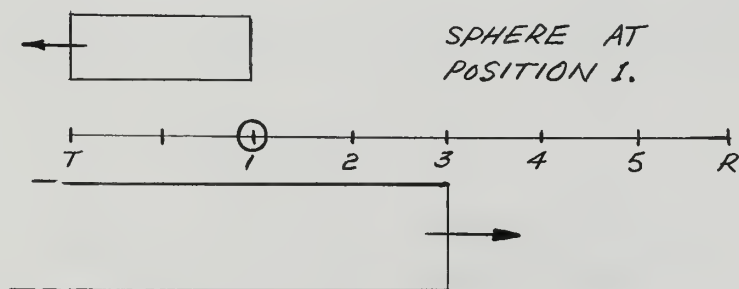


Figure XI-1

The first backscatter from sphere will appear at  $t = 4/7(25) = 14.3$  cycles having travelled to position 1 and back to the transducer but it will be blanked by the transmitted pulse for  $3/7(25) = 10.7$  cycles. Although the reflected pulse exists for a full 25 cycles it will be seen only after the source pulse has passed by the



sphere, that is it will be seen for only  $t = 4/7(25) = 14.3$  cycles. This is not completely seen in photo 1 because of the extra wide blanking pulse applied to the main bang interval. There is then a break of  $3/7(25) = 10.7$  cycles = 0.214 msec before the reflection from the reflector can be seen; this checks with photo 1. The reflector echo also lasts for 25 cycles. To be more exact, however, any echo will persist for a time equivalent to the length of the source pulse plus the length of or thickness of the insonified scatterer; that is the sphere echo will persist for  $75 + 2.54(15) = 78.1$  cm = 26 cycles. A breakdown of photo 1 is shown in Figure XI-2.

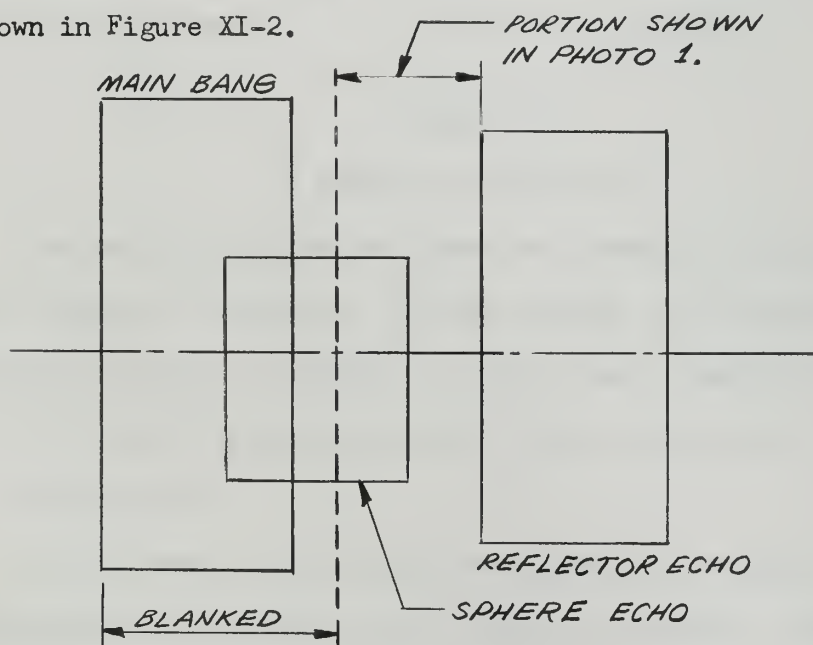


Figure XI-2

Analysis of Photo 1



Position 2:

At position 3 ( $3/7$  along the axis), the situation is shown in Figure XI-3.

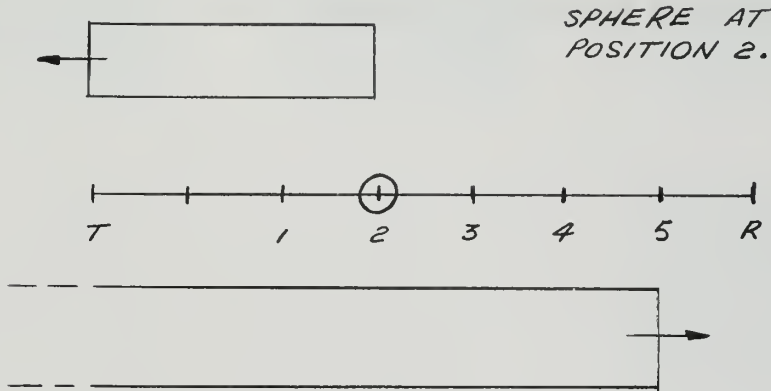


Figure XI-3

Sphere at Position 2

The scattering from the sphere will begin at  $6/7(25) = 21.4$  cycles = 0.429 msec. It will persist for 26 cycles as before and will be followed by a "no sound" interval of  $1/7(25) = 3.57$  cycles = 0.0715 msec; this checks with photo 2.

Position 3:

In this position ( $4/7$  along the axis), the backscattered sound begins at  $8/7(25) = 28.6$  cycles = 0.561 msec. There is no blanking by the source pulse since it terminated 0.0714 msec earlier. The scattered sound continues until  $15/7(0.5) = 1.07$  msec but will be overlapped from  $15/7(0.5) = 1.07$  msec or for the last 0.07 msec of the scattered pulse.

The analysis can be continued in a similar manner for positions 4 and 5.

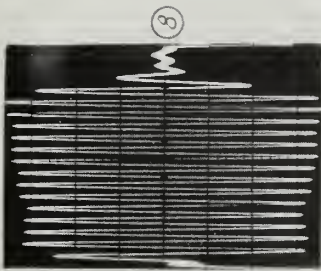




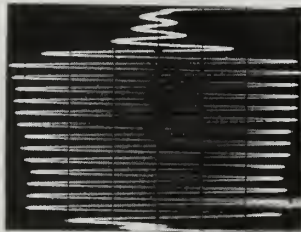
Photos 6 through 8 show the backscatter for corresponding positions of the sphere.

Taking the average amplitude of the scatter from position 3 as a reference it was found that for the data taken the total deviation from this value throughout the region was approximately 10%.





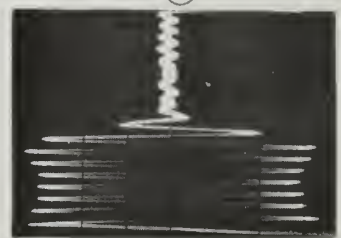
⑧



⑥



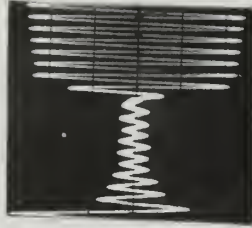
②



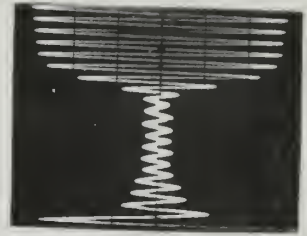
①



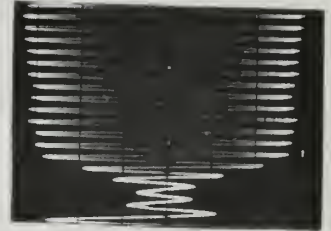
⑨



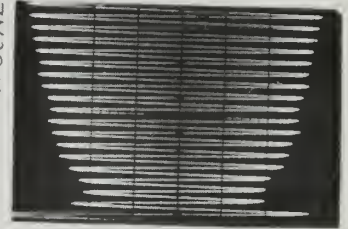
⑦



⑤



④



③

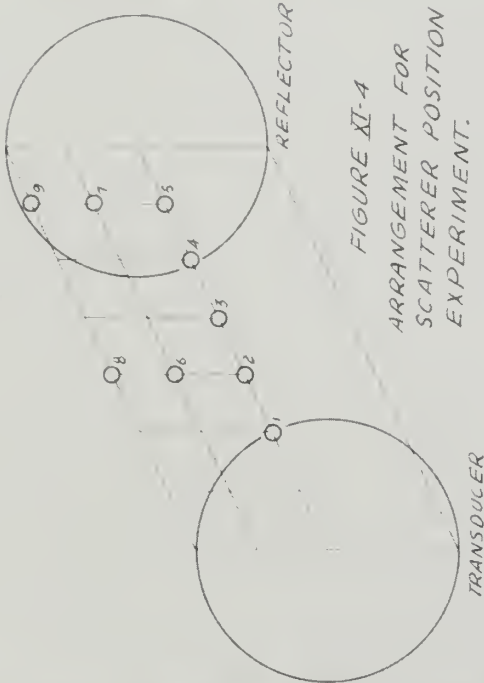


FIGURE XI-4  
ARRANGEMENT FOR  
SCATTERER POSITION  
EXPERIMENT.

TARGET - 15" DIAMETER STYROFOAM  
SPHERE.

FREQUENCY - 49.05 Kcps.

HORIZ. SCALE - 1 CM = 0.1 msec

VERT. SCALE - HELD CONSTANT.













24 AUG 65  
16 JUL 67  
16 JUN 81

BINDERY  
BINDERY  
S10000  
26560

Thesis  
B9518

Buxcey

79929

Acoustic detection  
of microbubbles and  
particulate matter  
near the sea surface.

16 JUL 65  
16 JUN 81

BINDERY  
S10000  
26560

79929

on  
d

Thesis  
B9518

Buxcey

79929

Acoustic detection  
of microbubbles and  
particulate matter  
near the sea surface.



thesB9518

Acoustic detection of microbubbles and p



3 2768 002 08875 9

DUDLEY KNOX LIBRARY